Rice University

Synthesis and Monitoring of Nanocars Bearing Different Wheel Types

by

Pinlei Chu

A THESIS SUBMITTED IN PARTIAL FULFILLMENT OF THE REQUIREMENTS FOR THE DEGREE

Doctor of Philosophy

APPROVED, THESIS COMMITTEE:

James Tour, Chair
Professor of Chemistry
Professor of Computer Science
Professor of Materials Science and NanoEngineering

Angel Marti
Associate Professor of Chemistry
Associate Professor of Bioengineering

Rafael Verduzco
Assistant Professor of Chemical and Biomolecular Engineering

Houston, Texas
February, 2016

Abstract

Synthesis and Monitoring of Nanocars Bearing Different Wheel Types

by

Pinlei Chu

Our group has developed different nanomachines over the years, while some of them are designed to perform in solution phase, a group of molecules termed nanocars were designed to specifically operate on solid surfaces. In this work, wheels, designed to yield better surface and molecule interaction for our studies is synthesized. In the past we have used mainly C_{60} fullerene wheels for our nanocars molecules. But after we decided to integrate a light activated motor into the nanocars, the fullerene wheels had to be phased out since the fullerene is known to quench the light energy used to actuate the motor. Our group then primarily utilized the p-carborane wheel as it does not show the same quenching effect with the motors. To improve the mobility and diffusion constant of the nanocars, a new generation of wheels was developed, featuring adamantane. A four-wheeled and a three-wheeled fluorescent nanocar was synthesized and monitored,

showing enhanced performance to the p-carborane wheeled analogue, which we attribute to the lower surface/wheel interactions. The adamantane wheels were then used to synthesize two nanocars with both a fluorescent 4,4-difluoro-4-bora-3a,4a-diaza-s-indacene (BODIPY) core and a MHz frequency light-activated unidirectional rotary motor, one molecule that is angular and expected to operate in circles and one that is straight and expected to primarily move in a single direction. Preliminary experiments have been conducted and show promising results. While the BODIPY core does quench some of the energy that was supposed to be directed to the motor, the motor still accelerates the nanocar to increase the diffusion constant. The same principle was used to synthesize a molecule with BODIPY core and motor (but without wheels) that could operate in solution. Finally, a two-wheeled nanocar was synthesized with a water soluble extension that could fit into cyclodextrin (CD) cavities and serve as wheels. This nanocar is expected to have very high surface interaction and could be used as to modify surface interactions and the resulting mobility and diffusion constants of nanocars on surfaces.

Acknowledgements

First I would like to thank my advisor Dr. James Tour, who has been guiding me along the path toward my PhD studies, writing, and presentation skills. I thank Dr. Angel Marti and Dr. Rafael Verduzco for serving on my thesis committee and also providing valuable input on my studies. Dr. Dustin James was always helpful during my need for opinions and suggestions. He proofreads and streamlines all my writing submitted for publications.

Dr. Jazmin Godoy and Dr. Guillaume Vives were extremely kind and helpful during my first tough few months when I joined the lab. They walked me through every basic synthetic technique and were patient with me when I made mistakes.

Dr. Pinn-Tsong Chiang is my good friend and taught me much on synthetic chemistry. I thank Victor Garcia Lopez for finishing my planned synthetic route to fluorescent motorized nanocars and he made the publication possible. I give particular thanks to all the Tour group members who have accompanied me in Dell Butcher Hall 300. The entire Tour group has been great colleagues and good friends.

I would like to thank my mother, Lien-Pin Pai, and my father, Shuni Chu, for supporting me emotionally during my PhD and also my sisters, Diana Chu and Vivian Chu, for helping me during tough times. I express my

sincere thanks to many members of Rice University, Rice Taiwanese Student Association, and my undergraduate classmates from abroad for their support over the course of my PhD studies. I give special thanks to Dr. Lin-Yung Wang who is a close friend and collaborator; without his work the imaging on adamantane wheeled nanocars would not have been possible.

I extend my gratitude to Dr. Ciceron Ayala Orozco for accompanying me on my path to Christianity this past year, although it was my advisor, Dr. James Tour, who first introduced me to the faith.

Table of Contents

List of Symbols and Abbreviations

Ac	Acetyl
AFM	atomic force microscopy
BODIPY	4,4-difluoro-4-bora-3a,4a-diaza-s-indacene
bp	boiling point
bpy	2,2'-bipyridine
br	broad (spectral)
Bu	butyl
calcd	calculated
°C	degree Celsius
CD	cyclodextrin
cm	centimeter(s)
cm^{-1}	wavenumbers
CNT	carbon nanotubes
CoMoCAT	cobalt-molybdenum catalyst
CTAB	cetyl hexadecyltrimethylammonium bromide
d	doublet
D	diffusion constant
δ	chemical shift in parts per million
dd	doublet of doublet

DMAP	4-(dimethylamino)pyridine
DMF	dimethylformamide
dppz	dipyrido[3,2-a:2’,3’-c]-phenazine
eq	equiv equation equivalence
Et	ethyl
FCS	fluorescence correlation spectroscopy
FRET	fluorescence resonance energy transfer
FTIR	Fourier transform infrared
g	gram(s)
h	hour(s)
HiPco	high-pressure CO conversion
HOMO	highest occupied molecular orbital
HRMS	high-resolution mass spectroscopy
Hz	hertz
IPA	isopropyl alcohol
J	coupling constant (in NMR spectroscopy)
L	liter(s)
λ_{abs}	maximum absorption wavelength
λ_{em}	maximum absorption wavelength
lit.	literature value

LUMO	lowest occupied molecular orbital
M	molar or moles per liter
m	meter(s); mili; multiplet
MALDI	matrix-assisted desorption ionization
MLCT	metal-ligand charge transfer
MWCNT	multi-walled carbon nanotubes
μ	micro
Me	methyl
mg	milligram(s)
min	minute(s)
mol	mole(s)
mp	melting point
m/z	mass-to-charge ratio
NIS	N-iodosuccinimide
nm	nanometer(s)
NMR	nuclear magnetic resonance
OPE	oligo(phenylene ethynylene)
Ph	phenyl
ppm	parts per million
%	percent

q	quartet (spectral
ΦF	quantum yield of fluorescence
rt	room temperature
s	second(s); singlet (spectral)
SMFM	single-molecule fluorescence microscopy
STM	scanning tunneling microscopy
SWCNT	single-walled carbon nanotubes
t	triplet (spectral)
TBACl	tetrabutylammonium chloride
TBAF	tetrabutylammonium fluoride
TEA	triethylamine
THF	tetrahydrofuran
TMS	trimethylsilyl
TMSA	trimethylsilyl acetylene
TOF	time-of-flight
TRITC	tetramethylrhodamine isothiocyanate
UV	ultraviolet
vis	visible

CHAPTER 1

Dipolar Nanocars

1.1 Introduction

Research groups over the world have used bottom-up synthesis methods to create various nanomachines such as switches,[1] turnstiles,[2] and shuttles[3] that are designed to mimic their macroscopic counterparts in appearance and function. Our group has specifically focused on nanocars, that are designed to behave as molecular cars with rotating wheels. We have synthesized a variety of nanocars over the years, including nanotrucks, nanoworm,[4] and fluorescent nanocars.[5, 6] The ultimate goal is to use bottom-up synthesis to produce a nanocar that can achieve the following three objectives:

1. Instead of random diffusion, the nanocar would have a motor to provide propulsion that can be actuated by light or other energy source
2. The nanocar's direction of translational motion could be controlled, either by an electrical or magnetic field
3. The nanocar could be controlled to pick up and deposit cargo

Objective 1 has been completed by other members of the group: nanocars **1** and **2** (Figure 1.1) that incorporate a molecular motor that is capable of rotation in the MHz range and uses UV light as an energy source, have been synthesized by Dr. Pinn-Tsong Chiang.[7]

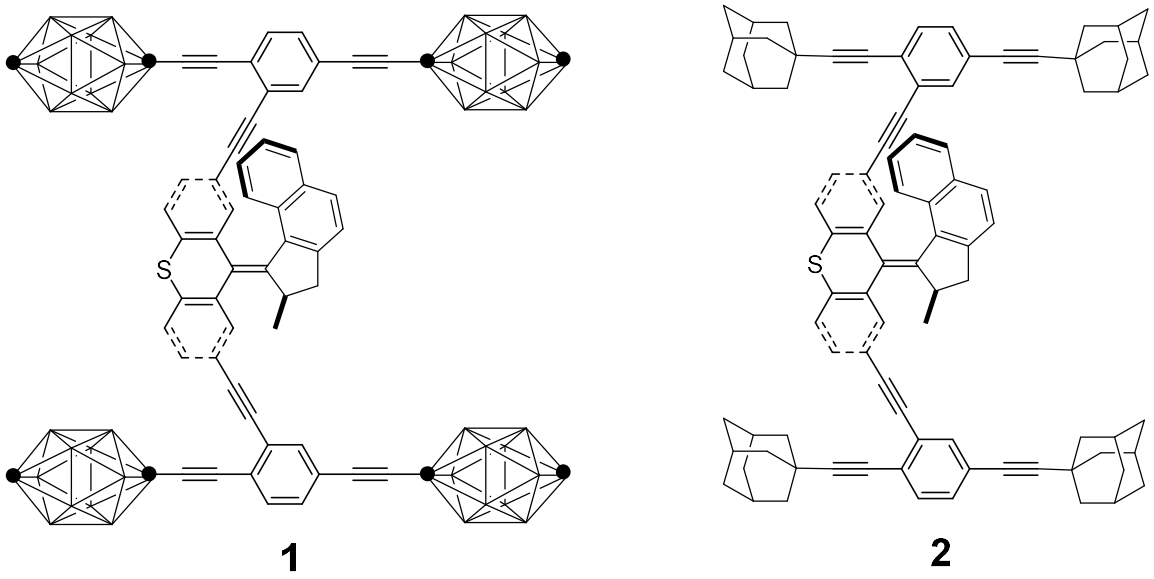

1 **2**

Figure 1.1. Nanocars **1** and **2**, with **1** bearing *p*-carborane wheels, the *p*-carboranes have BH at every intersection except at the points denoted by (•) which represents C and CH positions, *ipso* and *para*, respectively. Nanocar **2** bears adamantine wheels.[8]

Preliminary imaging studies have been done on both nanocars, which showed that although high resolution images (Figure 1.2) could be obtained on stationary cars via scanning-tunneling microscope (STM),[7] it is not possible with present technology to observe the effect of acceleration when UV light is shined upon the cars. Nanocar **1** is observed to be completely stationary, which we assume is due to the strong affinity of carborane to the gold surface, while **2** moves to the edge of the substrate before subsequent

imaging could be done, possibly because of the low surface interaction between the wheels and the substrate.

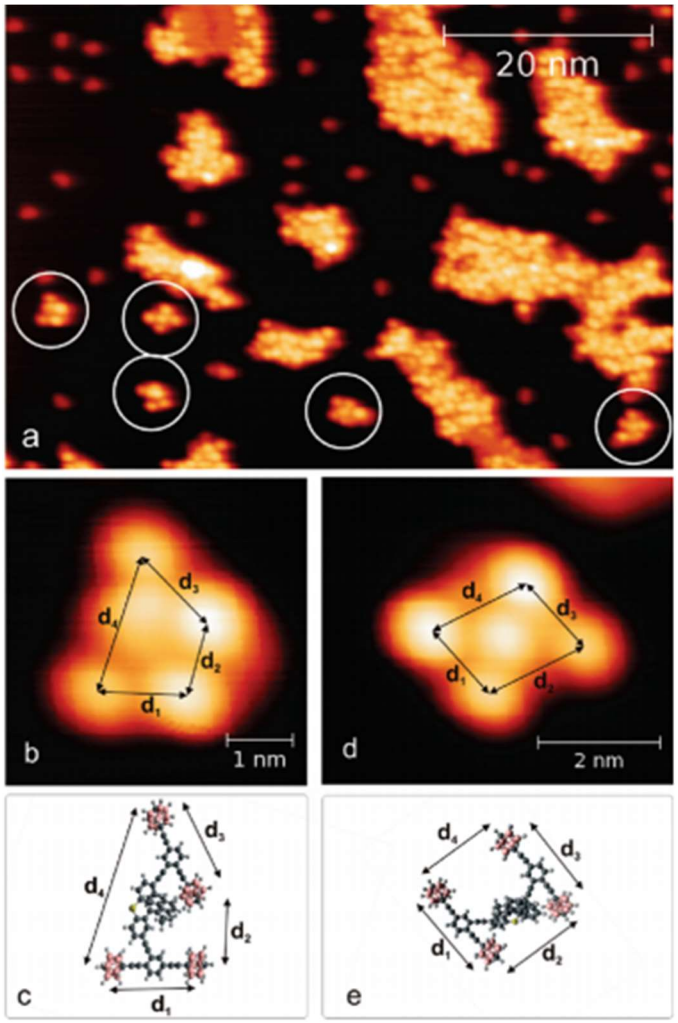

Figure 1.2.[7] STM images of nanocar **1** on Cu(111) and calculated gas phase structures (HyperChem 7 software). (a) Overview image of the surface (white circles indicate wheels and motors of single molecules, partially adsorbed at defects). Intramolecular dimensions, determined from STM images, are compared with the calculated gas phase structure. Crossed axes: d1 = 1.33 nm in the STM image (b) (and 1.38 nm in the calculation (c)), d2

= 1.10 nm (1.07 nm), d3 = 1.39 nm (1.38 nm), d4 = 2.15 nm (2.29 nm). Parallel axles (d,e): d1 = 1.38 nm in the STM image (d) (and 1.38 nm in the calculation (e)), d2 = 1.65 nm (1.42 nm), d3 = 1.37 nm (1.38 nm), d4 = 1.70 nm (1.51 nm).

Nanocar **3**, a compromise between **1** and **2** was also synthesized (Figure 1.3). While consisting of a molecular motor and adamantane wheels, it contains only one axle, which can prevent the nanocars from moving too fast. Experiments are undergoing to observe the accelerating effect of UV light on this particular nanocar.

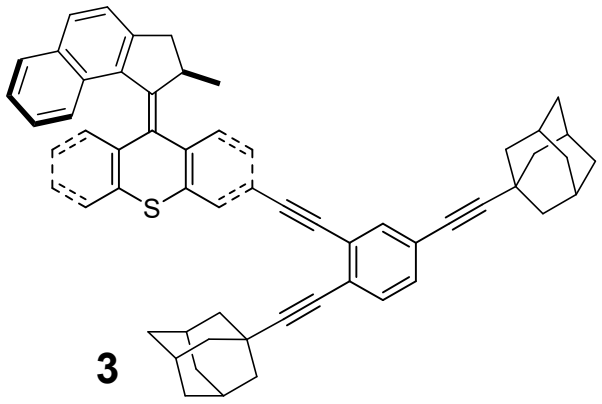

Figure 1.3. Nanocar **3**, bearing adamantine wheels and only one axle.

1.2 Dipolar Nanocars

Our next goal, objective 2, was to find a way to control the direction of translational motion of nanocars. We first considered the possibility of

utilizing a magnetic field to control the direction. As magnetic force is a cumulative force that involves an array of numerous atoms,[9] we quickly abandoned this idea, since each of our bottom-up synthesized nanocars contains at most 200 atoms, making it impossible for us to synthesize a nanocar that contains enough magnetic atoms to generate sufficient magnetic force.

The next option would be to use an electrical field as an inducing force, and in order to do so we need to synthesize a nanocar with enough dipole moment to make this possible. Dr. Takashi Sasaki synthesized a dipolar nanocar **4** (Figure 4) that contains a -NO_2 functional group as the electron withdrawing group at one end and a -NMe_2 as the electron donating group at the other end.[8]

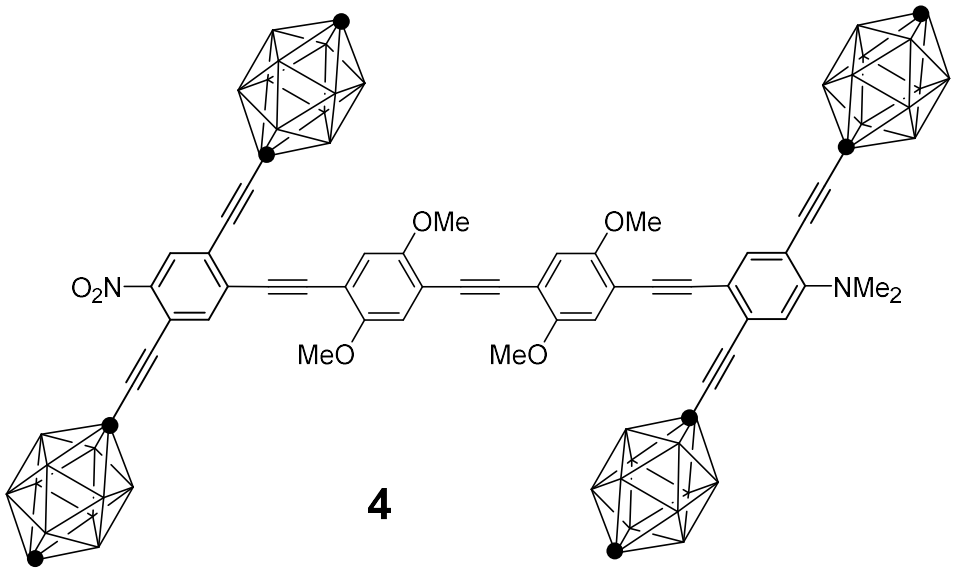

4

Figure 1.4 A dipolar nanocar with *p*-carborane wheels and electron withdrawing/donating functional groups at both ends.

Nanocar **4** was never observed under a microscope as our group could not find a collaborating group that specializes in STM at the time it was synthesized.

Because of the difficulties of STM imaging (requiring ultra-high vacuum and heat to deposit the molecules), we collaborated with Dr. Stephan Link at Rice University to employ an alternative method of imaging, single-molecule fluorescent microscopy (SMFM), which can be done in an ambient environment and rapidly yield data. In order to take advantage of this imaging technique, a crucial requirement is that the subject to be studied must be fluorescent. Dr. Jazmin Godoy in our lab synthesized **5** and **6** (Figure 1.5) that contain a 4,4-difluoro-4-bora-3a,4a-diaza-s-indacene (BODIPY) fluorescent core,[5] and extensive studies have been done on both molecules.[10-12]

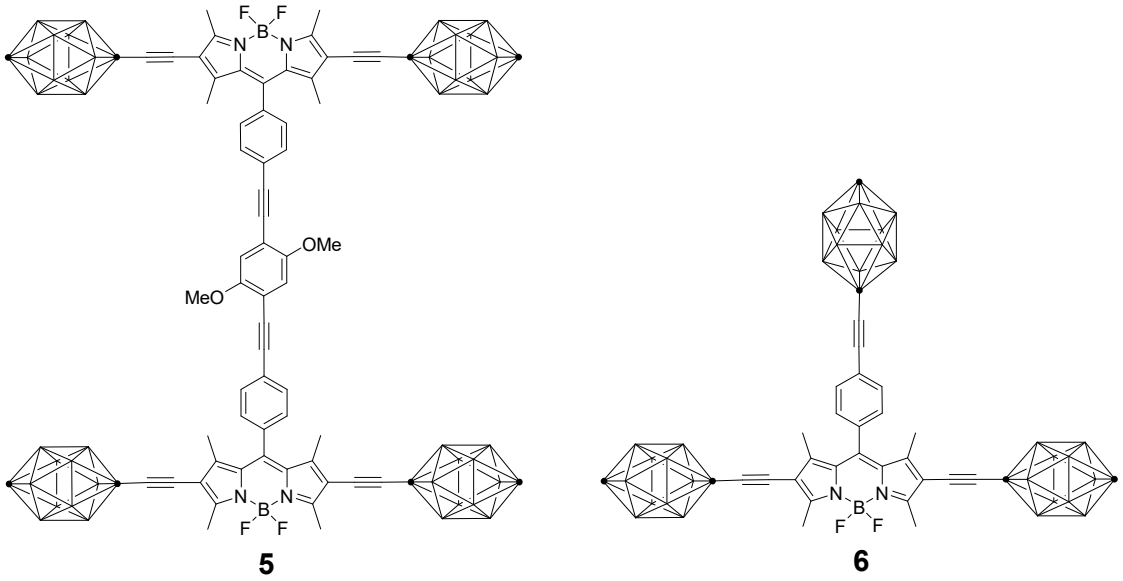

Figure 1.5. The fluorescent nanocar **5** and its three wheeled analogue **6**

1.2 Designing a Fluorescent Dipolar Nanocar

Our proposed experiment is to synthesize a fluorescent dipolar nanocar. When subjected to an electrical field, the electrical field would force the nanocar to align with the field direction as depicted in Figure 1.6.

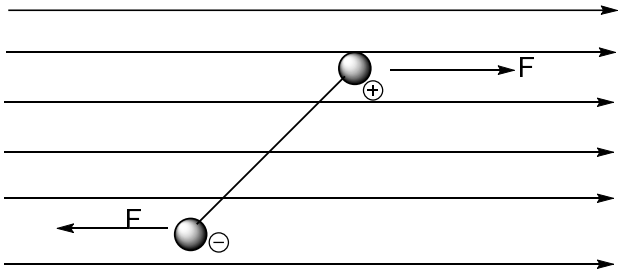

Figure 1.6. A dipole being aligned in a uniform electrical field.

The electric field generated cannot “drive” the nanocars, since the net force acting on a neutral object in a uniform electric field is 0. However, it can provide a net torque if the positive and negative charges are concentrated at different locations on the object, which means the electric field can only provide guidance to the direction of the nanocar’s translational motion. The strength of the guiding ability is determined both by the strength of the electric field and the dipole moment of the nanocar synthesized.

The first step involved in synthesizing the nanocar would be to calculate the net dipole moment of various structures. The first thing that came to our mind was to base our structure upon the already synthesized and well-studied nanocars **5**. We proposed to perform a nucleophilic displacement of the fluoride atoms on the boron with cyanide groups to form **7** as shown in Figure 1.7. Unfortunately, the calculated net dipole moment of this nanocar was less than 0.9 Debye, forcing us to look into alternative synthetic targets.

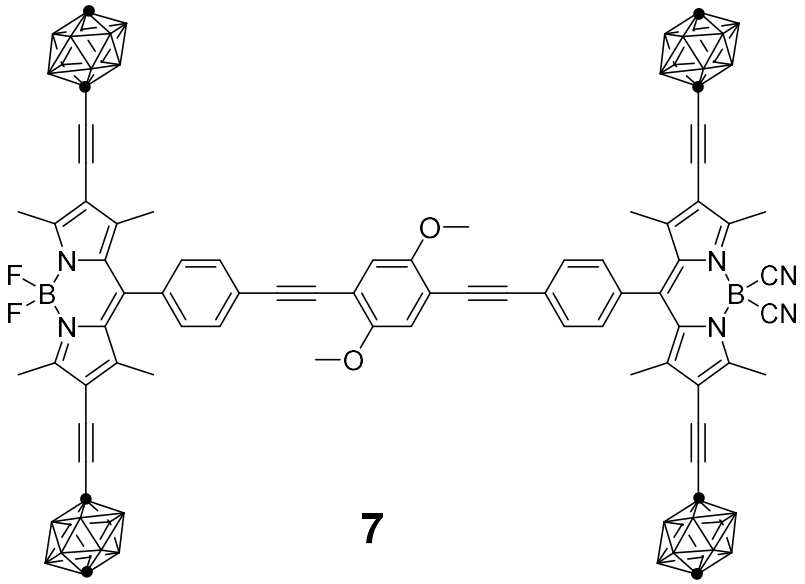

7

Figure 1.7. Nanocar **5** with 2 of the fluoride replaced with electron withdrawing cyanide groups.

The obvious candidates to serve as the electron withdrawing and electron donating groups would be nitro and amino groups, respectively, but unfortunately it has been shown that these two substituents quench the fluorescence of BODIPY thus drastically decreasing the quantum yield.[13]

Burgess's group has researched on BODIPY substituents,[14-18] and one of their papers, in which they synthesized both an electron withdrawing and an electron donating BODIPY **8** and **9** (Figure 1.8), provided the solution. The molecules which were prepared as in Scheme 1.1 according to literature.[19]

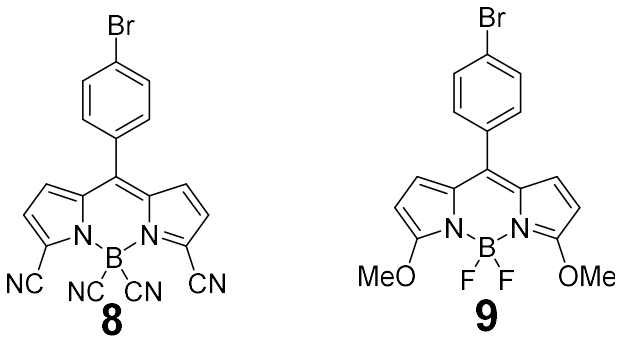

Figure 1.8. BODIPY **8** and **9**.

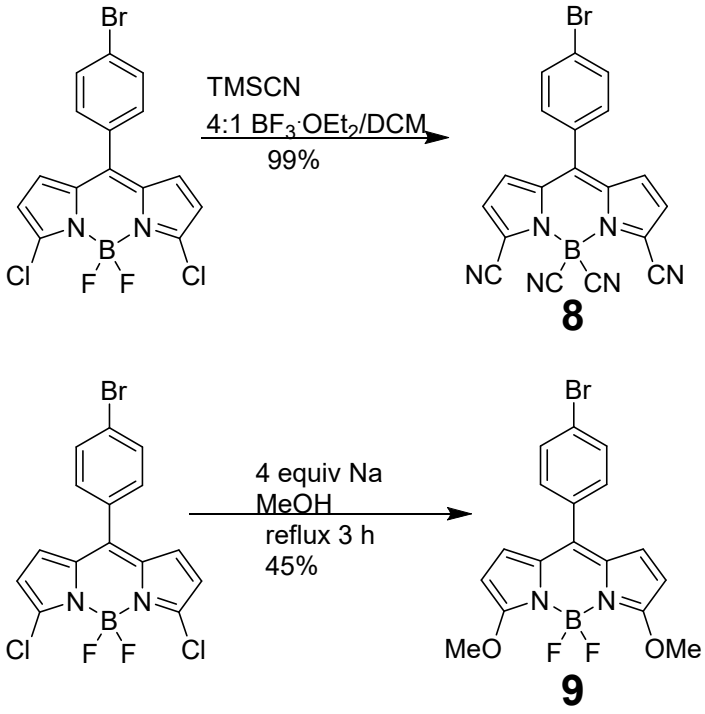

Scheme 1.1.

If we could attach the wheels, we could join the two halves together to form **10** (Figure 1.9) with a calculated dipole moment of 14.8 Debye, our proposed fluorescent dipolar nanocar.

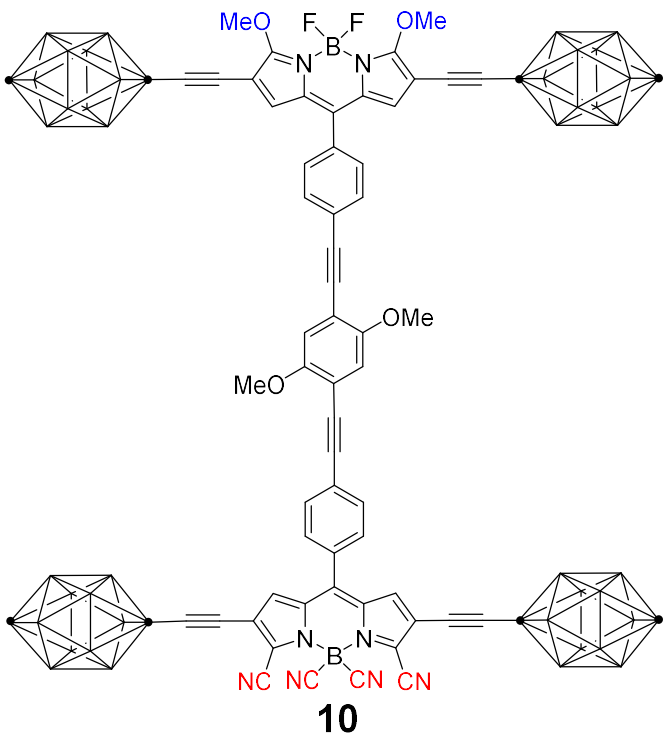

10

Figure 1.9. Proposed fluorescent dipolar nanocars **10**.

In order to attach the wheels utilizing Sonogashira coupling, we would need to iodinate BODIPY **8** and **9** at the 2,6-positions for future attachment of C-monoethynyl-*p*-carborane. We found this particularly difficult for **8** as the pyrrolic ring is extremely electron deficient since there are so many electron-withdrawing group. The iodination was very difficult regardless of iodination sources. ICl or N-iodosuccinimide (NIS) are analogues of I^+ and require an electron rich ring for a high yielding iodination. We tried various solvents such as DMF, THF, chloroform and acetonitrile (ACN) and temperature, running the reactions at the boiling

point of the solvents, of iodination with no success. A super-electrophilic iodonium was reported to successively iodinate electron deficient phenyl rings by using neat triflic acid as a solvent (Table 1.1).[20]

substrate	arene:NIS:acid ratio	product[ref]	yield[a]/%	bp/mmHg (mp, °C)	^{13}C NMR (ppm)	MS (70 eV), *m/e*
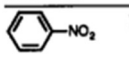	1.05:1:2	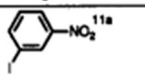 [11a]	86	(36–37)	93.4, 130.6, 132.3, 143.4, 148.4	249 (M$^+$, 100), 203 (70), 127 (15), 76 (71)
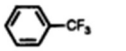	2:1:2	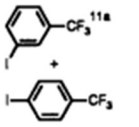 [11a] 94:6	91	82/25	93.8, 122.9 ($^1J_{C-F}$ = 272.3 Hz), 124.5 ($^3J_{C-F}$ = 3.7 Hz), 130.4, 132.4 ($^2J_{C-F}$ = 32.4 Hz), 134.2 ($^3J_{C-F}$ = 3.8 Hz), 140.9	272 (M$^+$, 100), 253 (10), 145 (84)
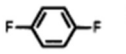	1:1:5	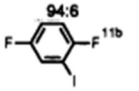 [11b]	79	81/16	80.7 ($^2J_{C-F}$ = 28.8 Hz, $^3J_{C-F}$ = 8.9 Hz), 115.9 ($^2J_{C-F}$ = 26.8 Hz, $^3J_{C-F}$ = 8.6 Hz), 116.5 ($^2J_{C-F}$ = 23.7 Hz, $^3J_{C-F}$ = 7.6 Hz), 125.8 ($^2J_{C-F}$ = 26.7 Hz, $^3J_{C-F}$ = 2.4 Hz), 158.3 ($^1J_{C-F}$ = 241.9 Hz, $^4J_{C-F}$ = 4.7 Hz), 158.4 ($^1J_{C-F}$ = 246.4 Hz, $^4J_{C-F}$ = 2.4 Hz)	240 (M$^+$, 100), 127 (19), 113 (33), 63 (21)
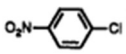	1:1:5	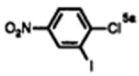 [5a]	79	(74–75)	97.9, 124.1, 129.5, 135.0, 145.8, 146.1	285 (M$^+$, 29), 283 (M$^+$, 100), 253 (9), 239 (11), 237 (36), 225 (19), 127 (10), 110 (36)

Table 1.1. Iodination of deactivated arenes with NIS as iodine source and triflic acid as solvent.[20] (Reprinted with permission from The American Chemical Society, 1993)

We tried this method, but **8** could not withstand the harsh conditions and thus decomposed. We then tried iodinating **9** with NIS using ACN as solvent, but the crude product decomposed as soon as it was exposed to oxygen and light. We assume this was due to the free pyrrolic positions that are not capped with methyl groups such as the case in **5** and **6**, leading to rapid decomposition when light and oxygen is present.

1.3 Calculations

Before we invested more time into this project, we asked Jun Yao from our group to perform a crude calculation as to whether this project was feasible or not. The model used in the calculation is shown in Figure 1.10.

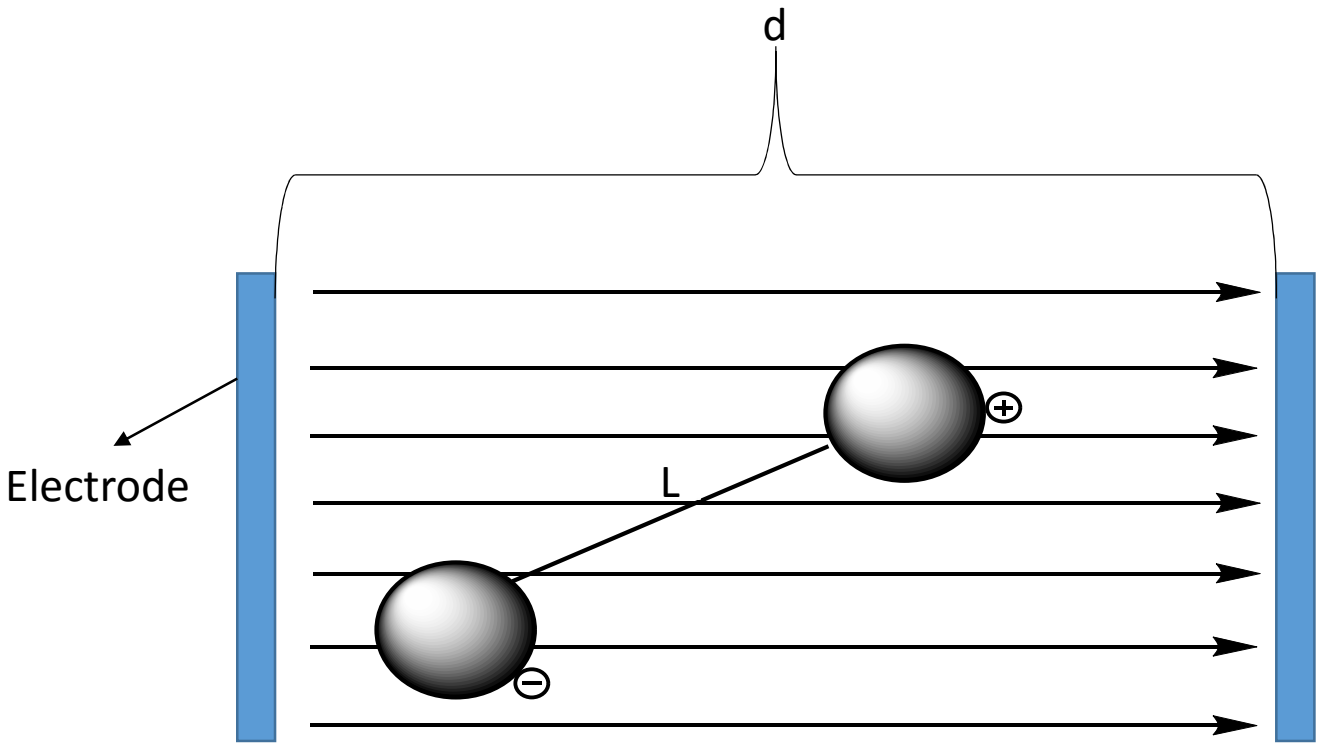

Figure 1.10. A dipolar molecule that is at a 45° angle with the electric field

We assume that the dipolar molecule is at a 45° angle with the electric field, the distance between the two electrodes = d = 15 μm. The molecule's length= L= 2 nm. The molecule's dipole is:

$$14D = 14 \times 3.36 \times 10^{-30} C \cdot m$$

The energy needed to be conquered in 298 K (room temperature) is:

$k \cdot T = 26meV = 4.1 \times 10^{-21} J$ (k = Boltzmann constant)

The energy difference between the dipole that is in a 45° angle with the electric field and the dipole that is aligned with the electric field must be equal or larger than kT ($\Delta E \geq kT$). We know that:

$\Delta E = [1 - \cos(45°)] \times 14D \times E_f \geq kT$ (E_f= electric field)

We obtain $E_f \geq 3 \times 10^8$, and since $E_f = \frac{V}{d}$, $V \geq 4500$.

In order to overcome the thermal energy alone would take 4500 V between two electrodes placed 15 μm apart, which would form an arc in the atmosphere. If the two electrodes were placed 150 nm apart, we would still need 45 V, which can be achieved but is not compatible with the resolution of the fluorescent microscope. From the calculations alone we found out the project would not work, and it has since been abandoned.

1.4 References

1. Chiang, P. T.; Cheng, P. N.; Lin, C. F.; Liu, Y. H.; Lai, C. C.; Peng, S. M.; Chiu, S. H. A Macrocycle/Molecular-Clip Complex That Functions as a Quadruply Controllable Molecular Switch. *Chem. Eur. J.* **2006**, *12*, 865-876.

2. Bedard, T. C.; Moore, J. S. Design and Synthesis of a Molecular Turnstile. *J. Am. Chem. Soc.* **1995**, *117*, 10662-10671.

3. Hess, H.; Clemmens, J.; Qin, D.; Howard, J.; Vogel, V. Light-Controlled Molecular Shuttles Made from Motor Proteins Carrying Cargo on Engineered Surfaces. *Nano Lett.* **2001**, *1*, 235-239.

4. Vives, G.; Tour, J. M. Synthesis of Single-Molecule Nanocars. *Acc. Chem. Res.* **2009**, *42*, 473-487.

5. Godoy, J.; Vives, G.; Tour, J. M. Synthesis of Highly Fluorescent Bodipy-Based Nanocars. *Org. Lett.* **2010**, *12*, 1464-1467.

6. Vives, G.; Guerrero, J. M.; Godoy, J.; Khatua, S.; Wang, Y. P.; Kiappes, J. L.; Link, S.; Tour, J. M. Synthesis of Fluorescent Dye-Tagged Nanomachines for Single-Molecule Fluorescence Spectroscopy. *J. Org. Chem.* **2010**, *75*, 6631-6643.

7. Chiang, P. T.; Mielke, J.; Godoy, J.; Guerrero, J. M.; Alemany, L. B.; Villagomez, C. J.; Saywell, A.; Grill, L.; Tour, J. M. Toward a Light-Driven Motorized Nanocar: Synthesis and Initial Imaging of Single Molecules. *ACS Nano* **2012**, *6*, 592-597.

8. Sasaki, T.; Tour, J. M. Synthesis of a Dipolar Nanocar. *Tetrahedron Lett.* **2007**, *48*, 5821-5824.

9. Reichel, J.; Vuletic, V. Atom Chips. John Wiley & Sons, Ltd.,: Hoboken, **2011**; p. 1 online resource (447 p.).

10. Claytor, K.; Khatua, S.; Guerrero, J. M.; Tcherniak, A.; Tour, J. M.; Link, S. Accurately Determining Single Molecule Trajectories of Molecular Motion on Surfaces. *J. Chem. Phys.* **2009**, *130*.

11. Khatua, S.; Godoy, J.; Tour, J. M.; Link, S. Influence of the Substrate on the Mobility of Individual Nanocars. *J. Phys. Chem. Lett.* **2010**, *1*, 3288-3291.

12. Khatua, S.; Guerrero, J. M.; Claytor, K.; Vives, G.; Kolomeisky, A. B.; Tour, J. M.; Link, S. Micrometer-Scale Translation and Monitoring of Individual Nanocars on Glass. *ACS Nano* **2009**, *3*, 351-356.

13. Esnal, I.; Banuelos, J.; Lopez Arbeloa, I.; Costela, A.; Garcia-Moreno, I.; Garzon, M.; Agarrabeitia, A. R.; Jose Ortiz, M. Nitro and Amino Bodipys: Crucial Substituents to Modulate Their Photonic Behavior. *RSC Advances* **2013**, *3*, 1547-1556.

14. Burghart, A.; Kim, H. J.; Welch, M. B.; Thoresen, L. H.; Reibenspies, J.; Burgess, K.; Bergstrom, F.; Johansson, L. B. A. 3,5-Diaryl-4,4-Difluoro-4-Bora-3a,4a-Diaza-S-Indacene (Bodipy) Dyes: Synthesis, Spectroscopic, Electrochemical, and Structural Properties. *J. Org. Chem.* **1999**, *64*, 7813-7819.

15. Kamkaew, A.; Burgess, K. Aza-Bodipy Dyes with Enhanced Hydrophilicity. *Chem. Commun. (Cambridge, U. K.)* **2015**, *51*, 10664-10667.

16. Kim, H.; Burghart, A.; Welch, M. B.; Reibenspies, J.; Burgess, K. Synthesis and Spectroscopic Properties of a New 4-Bora-3a,4a-Diaza-S-Indacene (Bodipy (R)) Dye. *Chem. Commun. (Cambridge, U. K.)* **1999**, 1889-1890.

17. Loudet, A.; Burgess, K. Bodipy Dyes and Their Derivatives: Syntheses and Spectroscopic Properties. *Chem. Rev.* **2007**, *107*, 4891-4932.

18. Thoresen, L. H.; Kim, H.; Welch, M. B.; Burghart, A.; Burgess, K. Synthesis of 3,5-Diaryl-4,4-Difluoro-4-Bora-3a,4a-Diaza-S-Indacene (Bodipy (R)) Dyes (Pg 1276, 1998). *Synlett* **1998**, 1461-+.

19. Li, L.; Nguyen, B.; Burgess, K. Functionalization of the 4,4-Difluoro-4-Bora-3a, 4a-Diaza-S-Indacene (Bodipy) Core. *Bioorg. Med. Chem. Lett.* **2008**, *18*, 3112-3116.

20. Olah, G. A.; Wang, Q.; Sandford, G.; Prakash, G. K. S. Iodination of Deactivated Aromatics with N-Iodosuccinimide in Trifluoromethanesulfonic Acid (Nis-Cf3so3h) Via in Situ Generated Superelectrophilic Iodine(I) Trifluoromethanesulfonate. *J. Org. Chem.* **1993**, *58*, 3194-3195.

CHAPTER 2

Synthesis and Single-Molecule Imaging of Highly Mobile Adamantane-Wheeled Nanocars

2.1 Introduction

Miniaturizing devices and machines such as motors,[1, 2] switches,[3] turnstiles[4] and barrows[5] to the molecular level has been accomplished by means of organic synthesis. These nanomachines were inspired by their macroscopic counterparts. A family of nanovehicles[6] termed nanocars was developed to translate on surfaces with controlled directionality. These nanocars are akin to their macroscopic analogues in the sense that they consist of a chassis, axles and wheels. The ultimate goal would be to utilize nanocars to transport cargo from one place to another, [7] with the nanocars incorporating a device that imitates an engine, providing translational motion from an external energy source.[7-9] The first generation of nanocars were equipped with carbon-based C60 wheels.[10, 11] These nanocars demonstrated directional movement on a gold surface using a STM-tip to electrically induce the motion. However, when trying to integrate a light-driven molecular motor that can convert light energy into rotational motion, it was found that the C60 wheels quenched the photoisomerization process of the molecular motor.[12-14] For this reason, p-carborane wheels were used which are also spherical and can rotate symmetrically along a single bond. A series of *p*-carborane wheeled nanocars with different functionalities have been synthesized, including a dipolar nanocar,[15] self-assembled nanocars,[16]

nanotrains,[17] and a motorized nanocar.[7] Most of these nanocars were intended to be studied using scanning tunneling microscopy (STM) because this technique offers excellent atomic resolution. However, only few of them have been successfully imaged using STM, in large part due to the lengthy time periods often required to acquire high quality STM images. Seeking an alternative imaging method, single-molecule fluorescent microscopy (SMFM) was chosen to track individual nanocars and calculate their mobility on conductive substrates.[18, 19] Even though this method does not provide the atomic resolution offered by STM, it allows localization of individual fluorophores within a few nanometers and also yields rapid results, two crucial requirements for progress in the field.

2.2 TRITC Tagged Nanocar

Our group first synthesized a nanocar with fluorescent dye Tetramethylrhodamine (TRITC) attached as a marker [20] (**5** shown in Figure 2.1). This is the very first attempt to visualize nanocars on glass using SMFM. Unlike imaging done using STM, this method is carried out in atmosphere (STM requires an ultra-high vacuum chamber), and no thermal activation of the molecules is necessary to achieve movements from the nanocar. The nanocars are observed to have a significant displacement, which is achieved by a tracking program developed by Dr. Stephan Link's

group in MATLAB. The way the program tracks the individual nanocar is by comparing images taken subsequently (each image scan is 30 s, total length of time is 5 min),[21] If one fluorophore, which in this case is the nanocar, is found at in the same spot or within a predefined search area, they are associated with the corresponding one in the previous image, then the displacement is calculated and recorded for each nanocar. If a large displacement or premature (before the 5 min timeframe) photobleaching occurs, the data for that nanocar is discarded and excluded for further analysis.

In order to confirm that if translational motion occurs, it would be originated from the free rotation of the C-C triple bond and hence the rolling of the wheels, a standalone TRITC dye was tested and found no significant displacement in subsequent images.

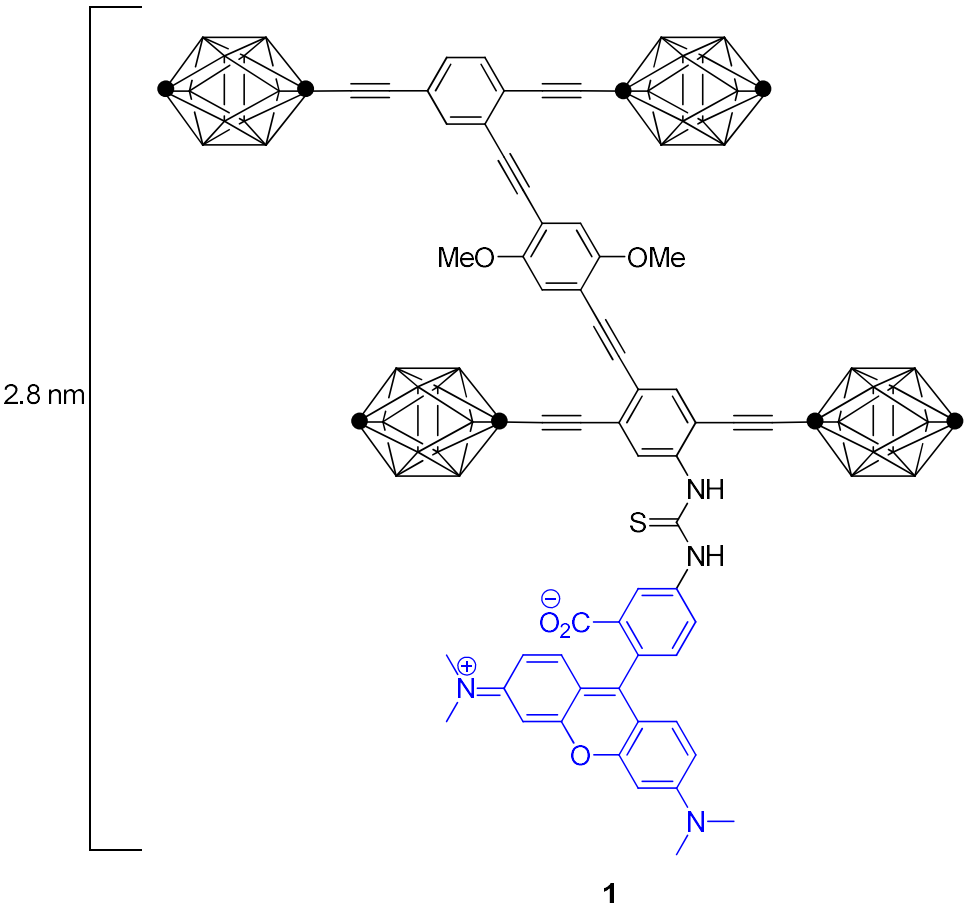

Figure 2.1 The TRITC tagged nanocar, TRITC colored in blue

It is important to note that of all the identified nanocars, not all of them moved. In fact only 25% (46 out of 191 molecules) demonstrated significant displacement and translational motion.

These nanocars showed a low mobility (percentage of moving nanocars), and this could be attributed to the following reasons:

1. The strong electronic interactions[21, 22] between TRITC and the glass surfaces

2. The surface roughness of the glass substrate, as the glass is not atomically flat and contains a lot of defects that is huge compared to the nanocar which is only a few nanometers in length.
3. As the laser hits the molecules, some decomposition may occur, when the molecules lose fluorescence it is called photobleaching. However if the fluorescence tag is simply cleaved from the car, the microscope cannot tell since it only senses the fluorophores, and determines that there is no displacement at all.

The TRITC trailer tag acts as an anchor and inhibits translational motion.

2.3 Intrinsically Fluorescent Nanocars

In order to solve the short comings of the trailer typed fluorescent tag, our group developed another fluorescent nanocar (**2** shown in Figure 2.2).

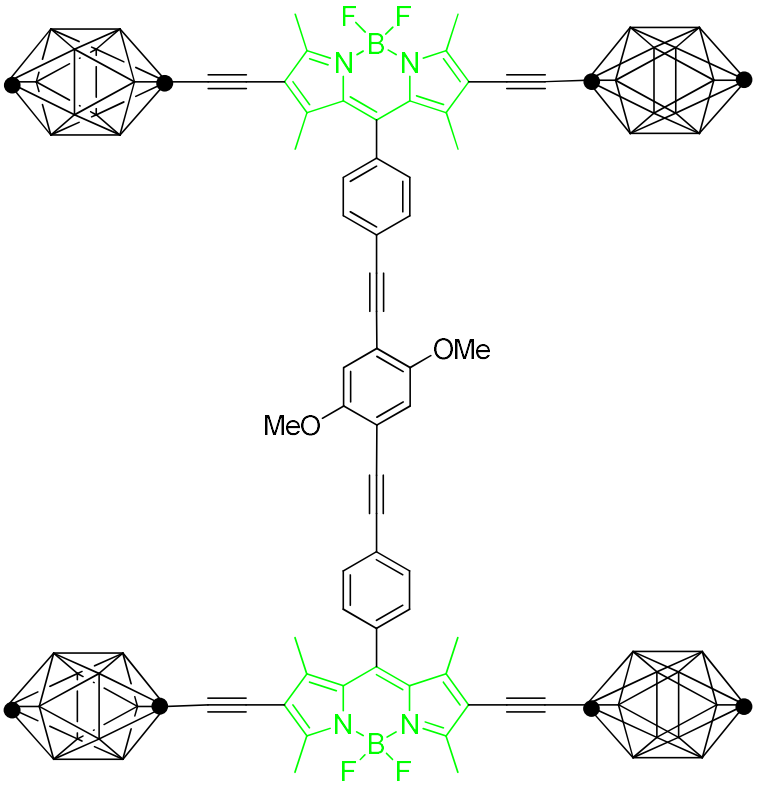

2

Figure 2.2 The BODIPY nanocar, BODIPY core highlighted in green

This fluorescent nanocar also has *p*-carborane as wheels yet the fluorescent properties of the molecule lies within the 4,4-difluoro-4-bora-3a,4a-diaza-s-indacene (BODIPY) core which is part of the axle/chassis, and does not rely on an outlying moiety such as TRITC to impart fluorescence. Testing of this nanocar finds that the mobility has increased to 45%,[18, 20] a significant improvement. Further testing of this nanocar on different glass surfaces (Vectabond-treated and amine terminated glass) suggests that

surface roughness and the interaction strength of wheels versus substrate both play a part in the mobility and diffusion constant of nanocars on surfaces.

2.4 Design of the Adamantane Wheeled Nanocar

Although the intrinsically fluorescent nanocar **2** has already increased the mobility of the nanocar almost 2-fold, half of the nanocars remain stationary. Since the ultimate goal is to use nanocars to transport nanocargo, it is desirable to maximize the number of moving molecules.

It was already deduced from previous experiments that modifying the substrate to provide stronger interactions between wheels and substrate, we need to think of a way to decrease the interactions rather than increasing it. One option would be to alkylate the glass to provide a substrate that has less hydrogen bond interactions with the wheels, while the other option would be to modify the wheels itself. The geometry of the candidate should preferably be of comparable size to the nanocar, relatively spherical and symmetrical. Adamantane was chosen in the present work since it fulfills those requirements. Most importantly, it was hypothesized that the negligible polarity of its C-H bonds would lessen the interactions between the nanocar and the glass surface, thereby increasing the mobility of the nanocars. A size

and shape comparison of three of our studied wheel systems, C_{60}, *p*-carborane, and adamantane, is shown on Figure 2.3.

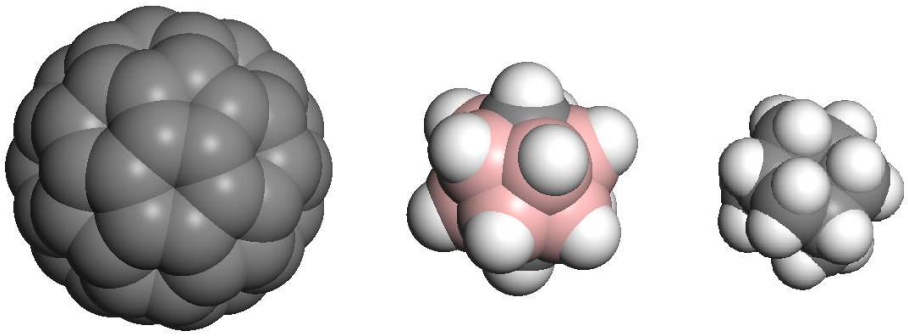

Figure 2.3 Space-filling models of C_{60}, *p*-carborane, and adamantane (from left to right).

Capitalizing upon the adamantane-wheeled systems, nanocar **3** in Scheme 2.1 was designed to move in a straight line on surfaces while the three-wheeled analogue **4** in Scheme 2.2 is expected to exhibit little or no motion given that only two of its three adamantane wheels are aligned.

To synthesize **3**, TMS-protected diiodide **5** was coupled with ethynyladamantane (**6**)[23] to form **7**. After TMS deprotection, adamantane-wheel-axle **8** was obtained. Then two units of the terminal alkyne axle **8** were coupled with 1,4-diiodo-2,5-dimethoxybenzene (**9**)[24] to give **3**.

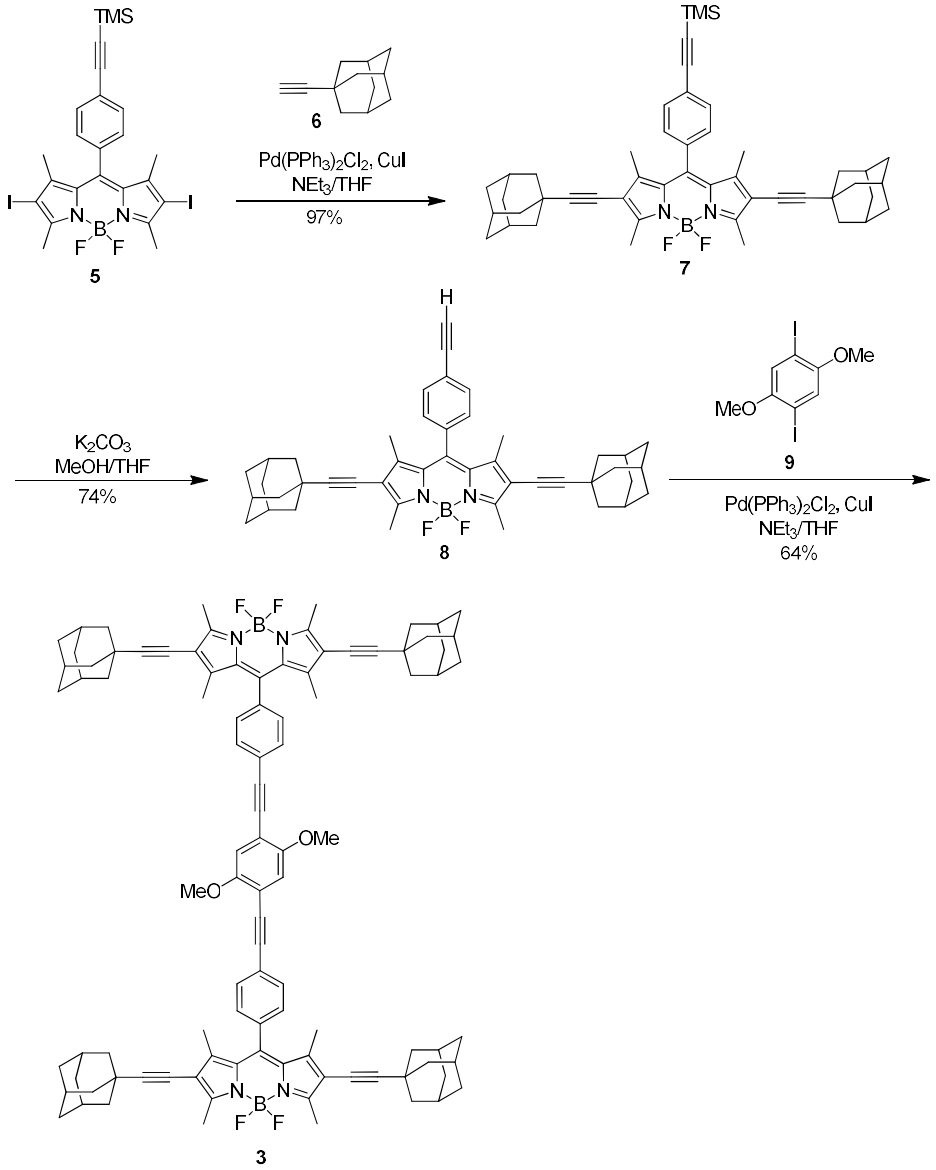

Scheme 2.1 Synthesis of adamantane-wheeled nanocar **3**.

Trimer **4** was prepared through a Sonogashira coupling between triiodide BODIPY **10** and terminal alkyne **6** (Scheme 2.2). It is noteworthy that the reaction was very efficient given that it was a triple coupling.

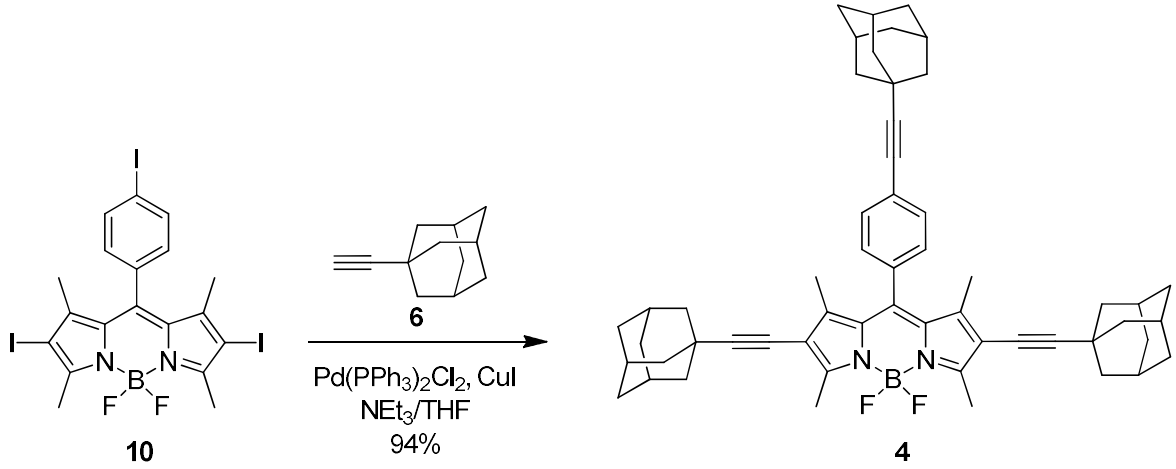

Scheme 2.2 Synthesis of adamantane-wheeled trimer **4**

In order to make a more comprehensive comparison, we wanted to synthesize a molecule where no two wheels are aligned. The proposed molecule **12** is shown in Scheme 2.3, where I attempt to do a triple Sonogashira coupling with the literature reported BODIPY **11.**

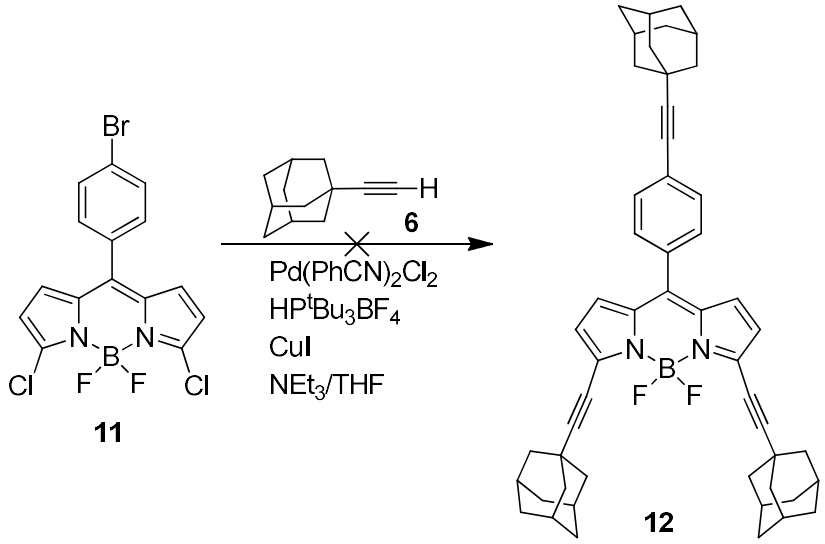

Scheme 2.3 Proposed Y-Shaped molecule synthesis.

The attempted coupling failed as there is no desired compound **12** found in the fractions of column chromatography. The chloride on the pyrrolic ring in BODIPY **11** was shown in literature to be reactive towards palladium catalyzed reactions,[25, 26] despite being a usually nonreactive and undesired halogen chloride, while the reactivity on the bromide is unknown. Since the desired molecule could not be obtained, we excluded **12** from our experiments.

2.5 Materials and Methods

Glass coverslips (Fisher Scientific 12-545-F 24X50-1) were used as the substrate. They were first cleaned by sonication in soap (LIQUIDNOX™, ALCONOX) for 15 min, rinsed with DI water, and then dried with nitrogen. The cleaning steps were repeated three times before oxygen plasma cleaning with a PDC-32G, HARRICK PLASMA at ~200 mTorr for 2 min. The cleaned coverslips were stored in DI water until used. Single-molecule fluorescence imaging was carried out on a home-built sample scanning fluoresecnce microscope that is schematically illustrated in Figure 2.4. Circularly polarized 514 nm excitation was provided by an Ar^+ laser (Modu-Lasser Stellar-Pro). The laser beam was expanded before entering an inverted microscope (Zeiss Axiovert 200) to achieve a diffraction-limited excitation spot. Fluorescence was collected in an epi-

illumination geometry by an oil-immersion objective (Zeiss Fluar) and then directed to an avanlanche photodiode detector (Perkin-Elmer SPCM-AQR-15). A dichroic mirror and a notch filter were used to separate the fluorescence from the excitation beam. The samples were placed on a XYZ piezo-electric scanning stage (Physik Instrumente P-517.3CL), which was controlled by a surface probe controller (RHK Technology SPM 1000). Images with dimensions of 10 µm × 10 µm consisting of 128 × 128 pixels were acquired by moving the sample across the excitation spot with a scanning speed of 1 pixel/ms. Typical excitation powers at the sample were 500 nW. All measurements were carried out at room temperature and in an ambient air atmosphere.

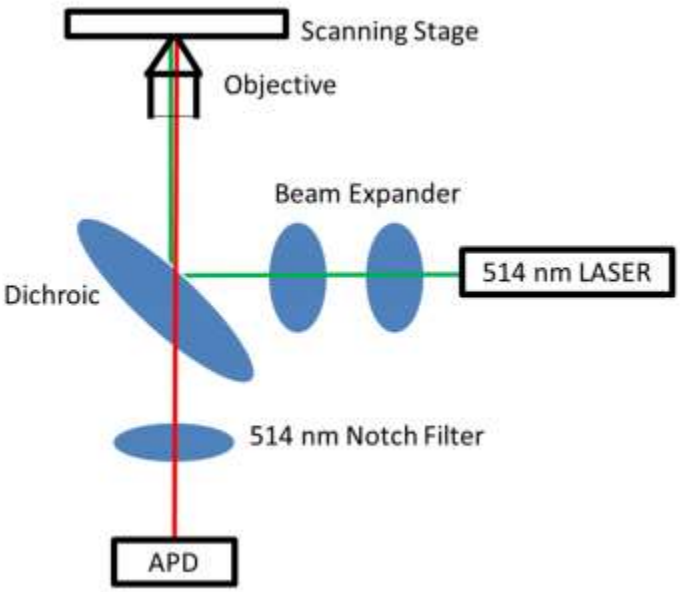

Figure 2.4 Schematic of the scanning fluorescence microscope that uses an avalanche photodiode detector (APD) to gather data.

2.6 Results and Discussion

The mobility of three different nanocars was investigated by single-molecule fluorescence imaging: The 4- and 3-wheeled adamantane nanocars 3 and 4, shown in Figure 3, and the 4-wheeled p-carborane nanocar 2, shown in Figure 2. The latter has been studied previously and was measured here again for direct comparison between nanocars with the same chassis, but different wheels.[18] An example of the fluorescence imaging is shown for 3 in Figure 2.5. The mobility of the nanocars was determined from fluorescence images taken as a function of time. Each series of time-lapsed images contained 20 frames and was analyzed using a Matlab particle-tracking program, which can account for photoblinking and photobleaching of fluorescent molecules.[22] Specifically, the bright spots in the fluorescence image in Figure 2.5A represent individual nanocar molecules, which were identified based on an intensity threshold and the shape of the fluorescent spot. A two-dimensional Gaussian function was fit to each spot in the first image frame taken. The centroids of the Gaussian functions were regarded as the starting positions of the nanocars. Nanocars identified in subsequent

frames were associated with those in previous frames, creating trajectories of position vs. time for each individual molecule. To visually illustrate this, Figure 2.5B-2.5E show a time-series of frames at a higher magnification for the red square marked in Figure 2.5A. The movement of individual nanocars is clearly seen in these images: the two nanocars in the upper and lower right quadrants move towards the outermost corners of their respective quadrants, while the bright spot in the upper left quadrant remains stationary and serves as a reference point. In Figure 2.5F, a single molecule trajectory is provided as calculated from 10 fluorescence images until photobleaching occurred.

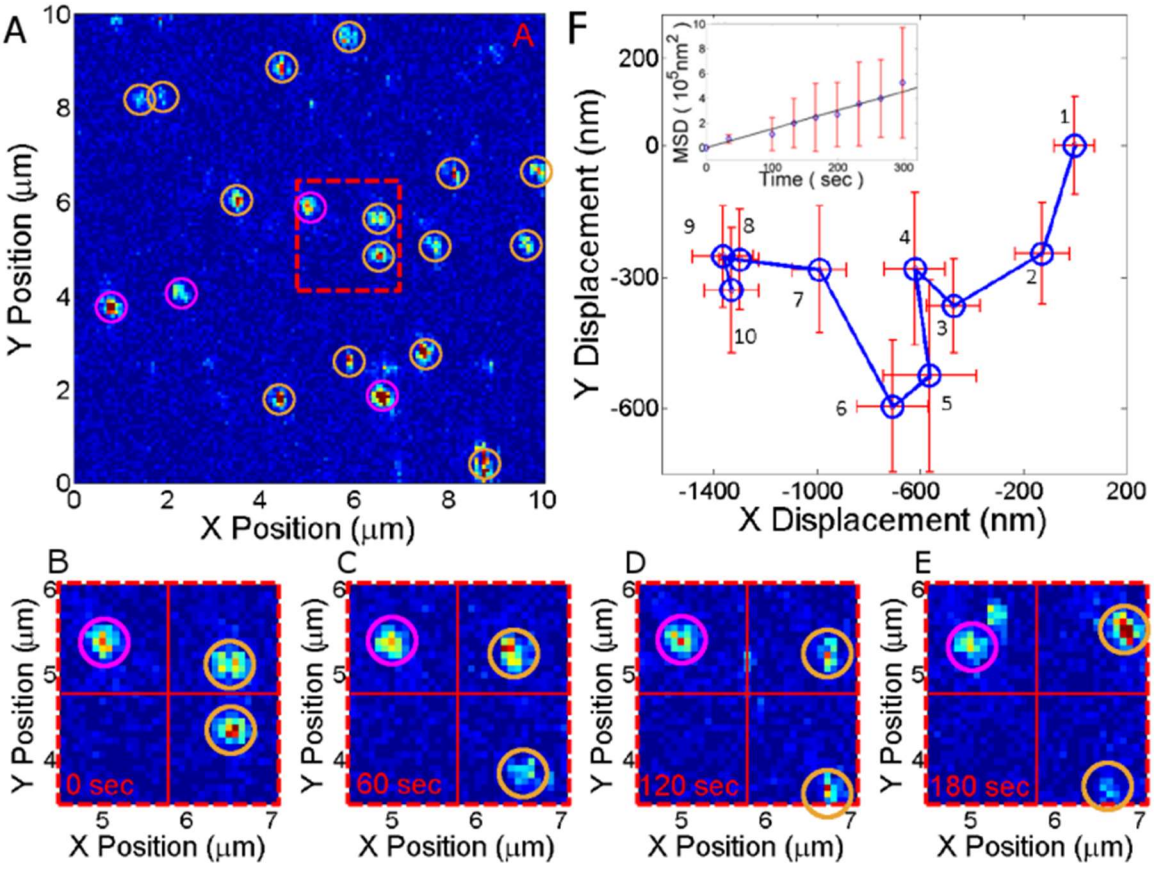

Figure 2.5 (A) Fluorescence image of **3**. The yellow circles indicate moving nanocars whereas the stationary nanocars are highlighted by magenta circles. (B-E) Time-lapsed images (2 μm × 2 μm) of the nanocars in the red dotted square in (A). The red cross at the center provides a reference frame to visualize the displacement of the two nanocars in the upper and lower right quadrants. (F) Single molecule trajectory of **3**. The error bars represent the x-y localization uncertainties determined from fitting a 2-dimensional Gaussian function to the fluorescence spot in each image. The inset shows the mean square displacement as calculated from the trajectory as a function of time. The linear fit yields the diffusion constant.

Molecules were categorized into 'moving' and 'stationary' nanocars based on the displacement compared to the localization error obtained from the Gaussian fit. If the displacement in at least two frames was larger than twice the localization error, the nanocars were considered to be moving. The ratio of moving nanocars marked by the yellow circles and stationary nanocars indicated by the violet circles is 15:4 for **3** (Figure 2.5). It should be noted that the threshold for identifying the moving nanocars was increased by a factor of 2 compared to earlier studies as we found that this threshold change allowed for a better distinction between moving and

stationary nanocars, but otherwise this threshold change had no significant effect on the results.

Two-dimensional diffusion constants for individual nanocars were calculated from single molecule trajectories using a mean square displacement (MSD) analysis.[27, 28] We have previously used an analysis that did not average the displacements for a given time interval, but instead gave each time step an equal weight.[19, 21, 22] Because recent simulations demonstrated that the MSD analysis generally yields a smaller uncertainty in the calculated diffusion constants,[27] we adopted this analysis for the current study. The MSD analysis for the single molecule trajectory in Figure 2.5F is shown in the inset. By applying this procedure to all moving nanocars, their diffusion constants were calculated. The distributions of diffusion constants for all three nanocars studied here are summarized in Figure 2.6A, which also lists the average diffusion constants and percentages of moving nanocars. Errors for the average diffusion constant and the percentage of moving nanocars were calculated based on three independent measurements of at least 100 molecules each. Importantly, we tested the effects of all changes in the analysis procedure on the previously studied *p*-carborane-wheeled nanocar and found that the average diffusion constants and

percentage of moving nanocars were comparable within the error of the measurement.

Comparing the two 4-wheeled nanocars, which only differed by the type of wheel attached to the BODIPY-based chassis, we found that the new adamantane-wheeled nanocars **3** have a slightly larger diffusion constant (Figure 2.6A) compared to the *p*-carborane nanocars **2**. This result can be explained by the different interaction energies between the glass surface and the two different types of wheels. The adamantane wheels are hydrocarbons that interact with the glass *via* weak van der Waals forces. Such interactions are significantly smaller than the B-H--O hydrogen bonding between the *p*-carborane wheels with the oxygen of the glass substrate.[18, 19, 21]

Assuming an energy activated process for the nanocar movement, the fraction of moving nanocars is also an important characteristic of the nanocar mobility in experiments with finite measurement times, in addition to the diffusion constant, and should increase with increasing diffusion constant. This is indeed observed as illustrated by the integrated area under the histograms in Figure 2.6A, which also summarizes the values for the diffusion constant and fraction of moving nanocars. These results demonstrate our ability to tune the mobility of the nanocars through the interaction between the nanocar wheels and the substrate. While we

previously changed the chemistry of the substrate,[18] here we have manipulated the nanocar movement by changing the wheels.

We can furthermore theoretically explain the relationship between the diffusion constant and the percentage of moving nanocars by a two-dimensional diffusion model that is based on the random walk theory. The probability $P(r,t)$ of finding a diffusing molecule on a two-dimensional surface can be expressed as eq 1:

$$P(r,t) = \frac{e^{-\frac{r^2}{8Dt}}}{\sqrt{8\pi Dt}} \qquad \text{(eq 1)}$$

where r is the radial distance from the starting position, t is the time, and $D$is the diffusion constant. Experimentally, the moving nanocars are those which move by more than twice the localization error Λ within the 30 s it takes to acquire an image. The fraction of moving nanocars P_{moving} can then be obtained by integrating $P(r,t)$ from $r = \Lambda$ to $r = \infty$, yielding eq 2:

$$P_{moving} = e^{-\Lambda^2/8Dt} \qquad \text{(eq 2)}$$

Based on this model, the fraction of moving nanocars is therefore directly related to the diffusion constant, in excellent agreement with our single molecule imaging results. Using an average experimental localization error of Λ_{exp} = 200 nm, Figure 2.5B illustrates the relationship given by eq 2. The experimental data points for the three nanocars discussed here and

summarized in Figure 5A are in excellent agreement with this model. Furthermore, we have included the data from our previous work on BODIPY based *p*-carborane nanocars on different surfaces and a TRITC-tagged nanocar.[18, 21] Only the latter deviates from the predicted behavior, which is understandable considering that the TRITC dye was attached at the end of the nanocar chassis and likely impeded the movement of some nanocars by acting as a local surface anchor, thereby reducing the fraction of moving nanocars while not affecting the diffusion constant for the mobile nanocars. In addition, a fit of the data points to eq 2 yields a localization error of Λ_{fit} = 213 nm, in excellent agreement with the experimentally estimated value for Λ.

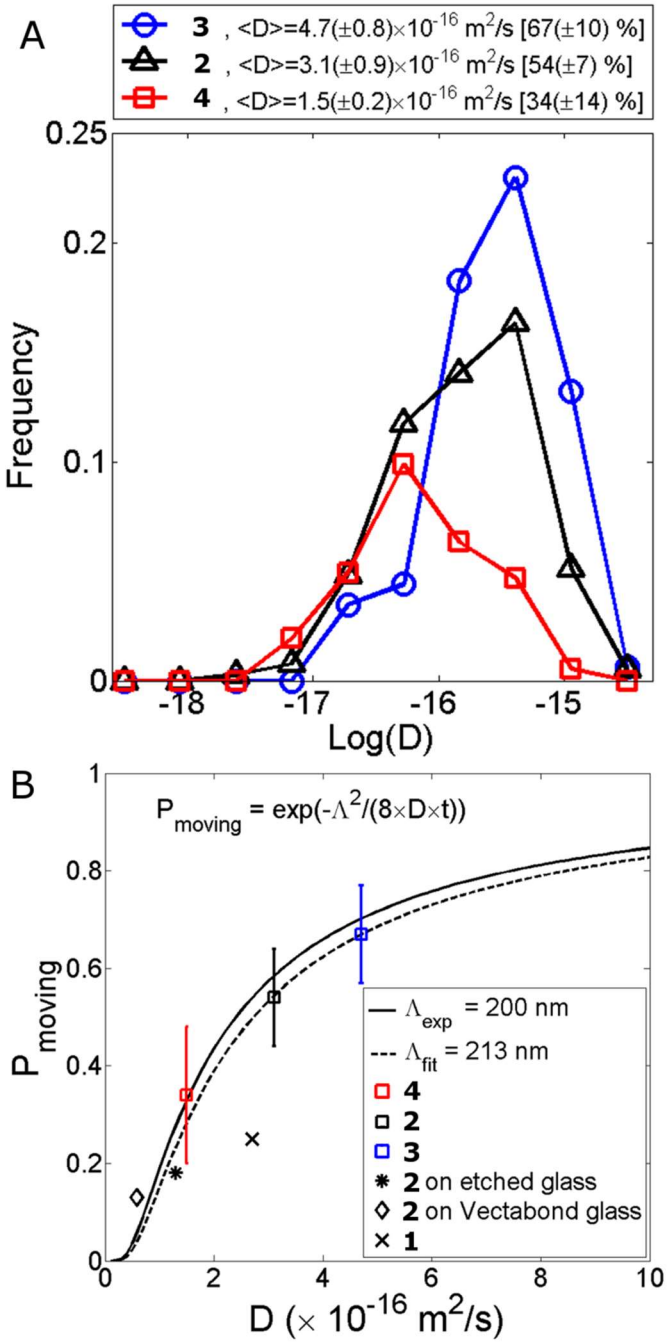

Figure 2.6 (A) Distribution of diffusion constants of the 4-wheeled adamantane nanocar **3**, 3-wheeled adamantane trimer **4**, and the BODIPY based 4-wheeled *p*-carborane nanocar **2**. The average diffusion constants of the nanocars are shown in the legend. Percentages in the legend correspond

to the fraction of moving nanocars and are proportional to the areas under the curves. (B) Fraction of moving nanocars P_{moving} as a function of the experimentally determined diffusion constant D. The data points also include previous measurements of the 4-wheeled *p*-carborane nanocar **2** on different surfaces and a TRITC-tagged *p*-carborane nanocar **1**.[18,20] The colored symbols in (B) correspond to the analogously colored lines shown in (A). The solid line was calculated from the two-dimensional random walk model (eq 2) with average experimental localization error of Λ_{exp} = 200 nm. The dashed line is calculated by fitting the data points to eq 2 instead, yielding a localization error of Λ_{fit} = 213 nm, which is in excellent agreement with experiments. Within experimental error, there is also excellent agreement between the measurements for **3** reported here and our earlier results, which were carried out independently from each other.

Comparing the mobility of **3** vs. **4** allowed us to again address the mechanism of the nanocar movement. **4** shows some mobility, but the diffusion constant and the percentage of moving nanocars decreased significantly compared to **3** (Figure 2.6). If the nanocars were only hopping or sliding on the surface, we would expect that the trimer **4** would show a higher mobility because they have one fewer wheel and thus reduced

interaction energy with the substrate. However, we observed the opposite as **3** has a higher mobility than **4**. The small but non-zero mobility of **4** could be explained assuming that some of those nanocars move using only the two wheels aligned 180˚ while the third wheel projects upward and occasionally acts as a brake when surface-bound. These results are therefore in excellent agreement with previous experimental studies and molecular dynamics simulations, which showed a wheel-assisted moving mechanism of nanocars.[11, 21, 29]

2.7 Conclusions

Our single-molecule measurements presented here not only support our previous study, which concluded that the interaction energy between the nanocar wheels and the glass substrate determines the mobility of the nanocars,[18, 19] but also successfully demonstrate the feasibility of changing the wheels to further improve the mobility of nanocars, giving guidance for the future molecular design of efficient nano-transporters. The comparison of the diffusion constants and percentage of moving nanocars between the 4-wheeled nanocar **3** and the 3-wheeled nanocar **4** furthermore validates the wheel-like rolling mechanism suggested for the movement of these molecular machines.

2.8 Experimental Section

Experimental data for compounds 3, 4, 7, 8

General Methods. ^{1}H NMR and ^{13}C NMR spectra were recorded at 400 or 500and 100 or 125 MHZ respectively. Chemical shift (δ) are reported in ppm from TMS=0 ppm. FTIR spectra were recorded using a FTIR Infrared microscope with ATR objective with 2 cm^{-1} resolution. All glassware was oven-dried (150 °C) and then vacuum cooled prior to use. Tetrahydrofuran (THF) was distilled from sodium benzophenoneketyl under N_2 atmosphere. Triethyamine (NEt_3), dichloromethane (CH_2Cl_2), N,N'-dimethylformamide (DMF), pyrrole, and 2,4-dimethylpyrrole were distilled from calcium hydride (CaH_2) under N_2 atmosphere. THF and NEt_3 were degassed with a stream of argon for 30 min before being used in Sonogashira coupling reactions. All reactions were carried out under N_2 atmosphere unless otherwise noted. All chemicals were purchased from commercial suppliers and used without further purification. Flash column chromatography was performed using 230-400 mesh silica gel from EM science. Thin layer chromatography (TLC) was performed using glass plates pre-coated with silica gel 40 F_{254} 0.25 mm layer thickness purchased from EM Science.

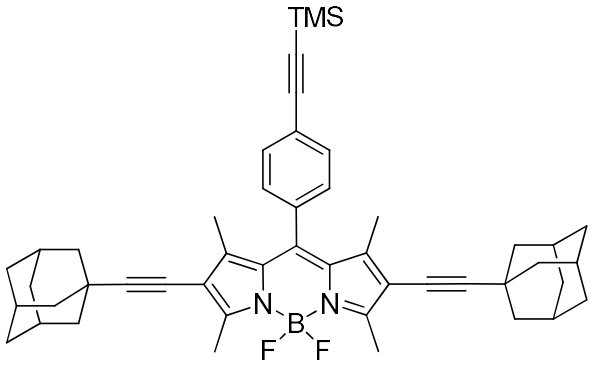

BODIPY Axle 7. An oven-dried 10 mL Schlenk tube equipped with a stir bar was charged with TMS-protected diiodide **5** (100 mg, 0.149 mmol), **6** (53 mg, 0.33 mmol), $Pd(PPh_3)_2Cl_2$ (10.4 mg, 14.8 μmol), and CuI (5.7 mg, 30 μmol) to which were added Et_3N (2 mL) and THF (1 mL). The reaction mixture was stirred at 70 °C overnight. The mixture was quenched with saturated NH_4Cl (20 mL) and extracted with dichloromethane (60 mL). The organic phase was washed with water (30 mL), dried over anhydrous $MgSO_4$, filtered, and the filtrate was concentrated under vacuum. The crude product was purified by column chromatography (silica gel, 5% EtOAc in hexanes) to yield **7** as a red solid (106 mg, 97%). FTIR (neat) 2904, 2848, 2162, 1616, 1526, 1475, 1390, 1310, 1220, 1175, 1077 cm^{-1}; ^1H NMR (500 MHz, $CDCl_3$) δ 7.60 (d, J = 8.5 Hz, 2H), 7.18 (d, J = 8.5 Hz, 2H), 2.59 (s, 6H), 1.96 (M, 6H), 1.90 (d, J = 2.9 Hz, 12H), 1.69 (t, J = 3.0 Hz, 12H), 1.42 (s, 6H), 0.28 (s, 9H); ^{13}C NMR (125 MHz, $CDCl_3$) δ 158.10, 142.91 , 140.68 , 134.94 , 132.72 , 130.60 , 128.02 , 124.05 , 116.86 , 105.91 , 104.13 , 95.93

, 77.25 , 77.00, 76.75 , 70.91 , 43.07 , 36.32 , 30.43 , 27.98 , 13.46, 13.42; HRMS (APCI) *m/z* calcd for $[M+H]^+$ $C_{48}H_{55}N_2BF_2Si$ 737.4277, found 737.4306.

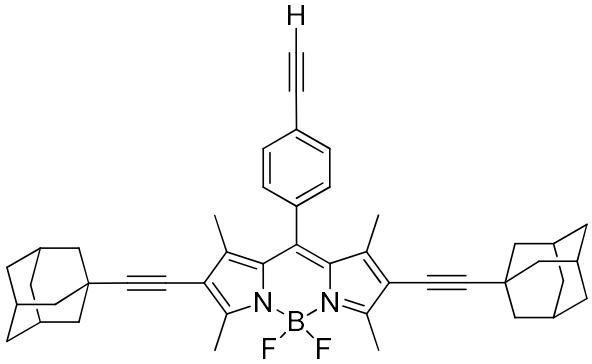

BODIPY Axle 8 An oven-dried 25 mL round bottom flask equipped with a stir bar was charged with **7** (100 mg, 0.136 mmol) and K_2CO_3 (94 mg, 0.68 mmol), to which were added MeOH (5 mL) and THF (5 mL). The reaction mixture was stirred at room temperature for 90 min. The mixture was quenched with water and extracted with dichloromethane (50 mL). The organic phase was washed with water (30 mL), dried over anhydrous $MgSO_4$, filtered, and the filtrate was concentrated under vacuum. The crude product was purified by column chromatography (silica gel, 5% EtOAc in hexanes) to yield **8** as a dark red solid (67 mg, 74%). FTIR (neat) 3263, 2901, 2850, 1616, 1536, 1475, 1400, 1305, 1225, 1170, 1077 cm^{-1}; ^1H NMR (500 MHz, $CDCl_3$) δ 7.62 (d, *J* = 8.3 Hz, 2H), 7.21 (d, *J* = 8.5 Hz, 2H), 3.19 (s, 1H), 2.59 (s, 6H), 1.96 (s, 6H), 1.90 (d, *J* = 2.9 Hz, 12H), 1.69 (d, *J* = 3.0

Hz, 12H), 1.42 (s, 6H); ^{13}C NMR (125 MHz, $CDCl_3$) δ 158.17, 142.89, 140.47, 135.33, 132.86, 130.58, 128.16, 123.08, 116.92, 105.94, 82.82, 78.64, 70.90, 43.07, 36.32, 30.43, 27.98, 13.47, 13.40; HRMS (APCI) *m/z* calcd for $[M+H]^+$ $C_{45}H_{47}BF_2N_2$ 665.3879, found 665.3909.

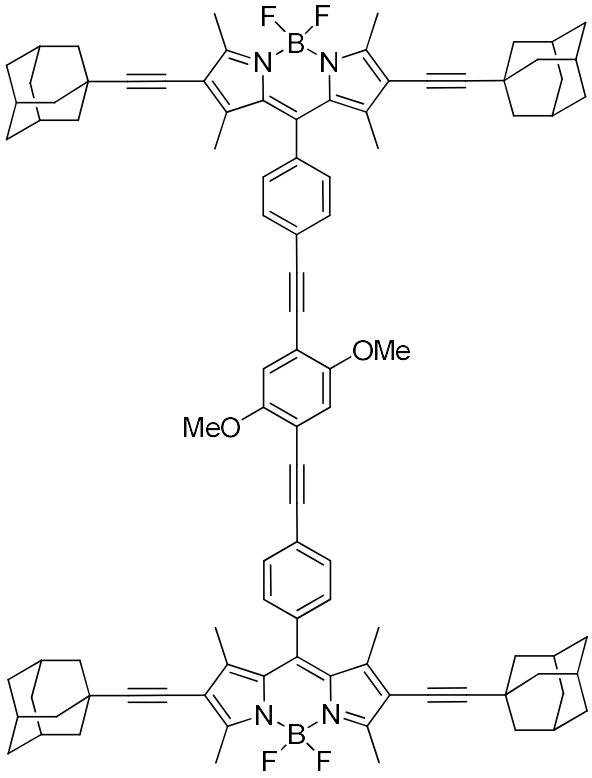

Four Wheeled Nanocar 3. An oven-dried 10 mL Schlenk tube equipped with a stir bar was charged with **8** (50 mg, 0.075 mmol), **9** (13.4 mg, 0.034 mmol), $Pd(PPh_3)_2Cl_2$ (5.3 mg, 7.6 μmol), and CuI (2.9 mg, 15 μmol) to which were added Et_3N (1 mL) and THF (1 mL). The reaction mixture was stirred at room temperature overnight. The mixture was quenched with saturated NH_4Cl (10 mL) and extracted with dichloromethane (30 mL). The organic phase was washed with water (20 mL), dried over anhydrous

$MgSO_4$, filtered, and the filtrate was concentrated under vacuum. The crude product was purified by column chromatography (silica gel, 30% chloroform in hexanes) to yield **3** as a purple solid (70.4 mg, 64%). FTIR (neat) 2900, 2850, 1616, 1530, 1480, 1450, 1392, 1310, 1225, 1172, 1075 cm^{-1}; ^1H NMR (400 MHz, CD_2Cl_2) δ 7.69 (d, J = 7.9 Hz, 4H), 7.28 (d, J = 7.8 Hz, 4H), 7.09 (s, 2H), 3.91 (s, 6H), 2.54 (s, 12H), 1.94 (M, 12H), 1.90 (M, 24H), 1.69 (M, 24H), 1.46 (s, 12H); ^{13}C NMR (125 MHz, $CDCl_3$) δ 158.15, 153.96, 142.86, 132.44, 130.64, 128.15, 116.89, 115.53, 105.93, 77.25, 77.00, 76.75, 70.92, 56.48, 43.07, 36.32, 30.44, 27.98, 13.47, 13.44; MALDI *m/z* calcd for $[M+K]^+$ $C_{98}H_{100}B_2F_4N_4O_2$ 1502.8, found 1502.7

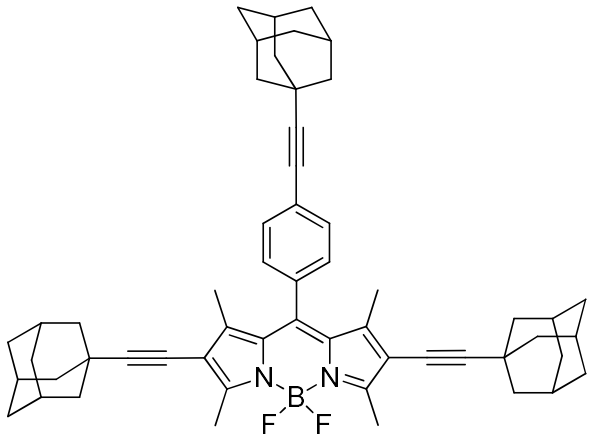

Three Wheeled Nanocar 3. An oven-dried 10 mL Schlenk tube equipped with a stir bar was charged with triiodide BODIPY **10** (200 mg, 0.285 mmol), **6** (160 mg, 1.0 mmol), $Pd(PPh_3)_2Cl_2$ (30 mg, 0.043 mmol), and CuI (16.3 mg, 0.086 mmol) to which were added Et_3N (2 mL) and THF (2 mL). The reaction mixture was stirred at room temperature overnight. The mixture

was quenched with saturated NH_4Cl (25 mL) and extracted with dichloromethane (100 mL). The organic phase was washed with water (50 mL), dried over anhydrous $MgSO_4$, filtered, and the filtrate was concentrated under vacuum. The crude product was purified by column chromatography (silica gel, 10% EtOAc in hexanes) to yield **4** as a red solid (214.3 mg, 94%). FTIR (neat) 2900, 2848, 1616, 1530, 1450, 1391, 1309, 1225, 1175, 1075 cm^{-1}; ^1H NMR (500 MHz, $CDCl_3$) δ 7.51 (d, J = 8.5 Hz, 2H), 7.14 (d, J = 8.5 Hz, 2H), 2.59 (s, 6H), 2.08 – 1.61 (m, 45H), 1.43 (s, 6H); ^{13}C NMR (125 MHz, $CDCl_3$) δ 157.93, 143.05, 141.15, 133.72, 132.39, 130.72, 127.84, 125.08, 116.74, 105.82, 99.86, 78.81, 70.97, 43.09, 42.73, 36.34, 30.44, 30.17, 28.00, 27.96, 13.48, 13.46; HRMS (APCI) *m/z* calcd for $[M+H]^+$ $C_{55}H_{61}BF_2N_2$ 799.4978, found 799.4966.

2.9 Contributions

I finished and optimized all synthetic tasks on the adamantane wheeled nanocars based on the previous work of Jazmin Godoy. Dr. Stephan Link and Lin-Yung Wang did the imaging on the various molecules synthesized. Dr. Anatoly Kolomeisky came up with the theory of fitting the data into a 2-D random walk model.

2.10 Acknowledgements

J. M. T. acknowledges support from the National Science Foundation (CHE-1007483). We thank Drs. I. Chester of FAR Research, Inc. and R. Awartari of Petra Research, Inc. for providing trimethylsilyacetylene.

2.11 References

1. Klok, M.; Boyle, N.; Pryce, M. T.; Meetsma, A.; Browne, W. R.; Feringa, B. L. Mhz Unidirectional Rotation of Molecular Rotary Motors. *J. Am. Chem. Soc.* **2008**, *130*, 10484-10485.

2. Kulago, A. A.; Mes, E. M.; Klok, M.; Meetsma, A.; Brouwer, A. M.; Feringa, B. L. Ultrafast Light-Driven Nanomotors Based on an Acridane Stator. *J. Org. Chem.* **2010**, *75*, 666-679.

3. Chiang, P. T.; Cheng, P. N.; Lin, C. F.; Liu, Y. H.; Lai, C. C.; Peng, S. M.; Chiu, S. H. A Macrocycle/Molecular-Clip Complex That Functions as a Quadruply Controllable Molecular Switch. *Chem. Eur. J.* **2006**, *12*, 865-876.

4. Bedard, T. C.; Moore, J. S. Design and Synthesis of a Molecular Turnstile. *J. Am. Chem. Soc.* **1995**, *117*, 10662-10671.

5. Rapenne, G.; Jimenez-Bueno, G. Molecular Machines: Synthesis and Characterization of Two Prototypes of Molecular Wheelbarrows. *Tetrahedron* **2007**, *63*, 7018-7026.

6. Shirai, Y.; Morin, J. F.; Sasaki, T.; Guerrero, J. M.; Tour, J. M. Recent Progress on Nanovehicles. *Chem. Soc. Rev.* **2006**, *35*, 1043-1055.

7. Chiang, P. T.; Mielke, J.; Godoy, J.; Guerrero, J. M.; Alemany, L. B.; Villagomez, C. J.; Saywell, A.; Grill, L.; Tour, J. M. Toward a Light-Driven Motorized Nanocar: Synthesis and Initial Imaging of Single Molecules. *ACS Nano* **2012**, *6*, 592-597.

8. Godoy, J.; Vives, G.; Tour, J. M. Toward Chemical Propulsion: Synthesis of Romp-Propelled Nanocars. *ACS Nano* **2011**, *5*, 85-90.

9. Kudernac, T.; Ruangsupapichat, N.; Parschau, M.; Macia, B.; Katsonis, N.; Harutyunyan, S. R.; Ernst, K. H.; Feringa, B. L. Electrically Driven Directional Motion of a Four-Wheeled Molecule on a Metal Surface. *Nature* **2011**, *479*, 208-211.

10. Shirai, Y.; Osgood, A. J.; Zhao, Y. M.; Yao, Y. X.; Saudan, L.; Yang, H. B.; Chiu, Y. H.; Alemany, L. B.; Sasaki, T.; Morin, J. F.; Guerrero, J. M.; Kelly, K. F.; Tour, J. M. Surface-Rolling Molecules. *J. Am. Chem. Soc.* **2006**, *128*, 4854-4864.

11. Shirai, Y.; Osgood, A. J.; Zhao, Y. M.; Kelly, K. F.; Tour, J. M. Directional Control in Thermally Driven Single-Molecule Nanocars. *Nano Lett.* **2005**, *5*, 2330-2334.

12. Shirai, Y.; Sasaki, T.; Guerrero, J. M.; Yu, B. C.; Hodge, P.; Tour, J. M. Synthesis and Photo Isomerization of Fullerene- and Oligo(Phenylene Ethynylene) - Azobenzene Derivatives. *ACS Nano* **2008**, *2*, 97-106.

13. Sasaki, T.; Tour, J. M. Synthesis of a New Photoactive Nanovehicle: A Nanoworm. *Org. Lett.* **2008**, *10*, 897-900.

14. Morin, J. F.; Shirai, Y.; Tour, J. M. En Route to a Motorized Nanocar. *Org. Lett.* **2006**, *8*, 1713-1716.

15. Sasaki, T.; Tour, J. M. Synthesis of a Dipolar Nanocar. *Tetrahedron Lett.* **2007**, *48*, 5821-5824.

16. Sasaki, T.; Guerrero, J. M.; Tour, J. M. The Assembly Line: Self-Assembling Nanocars. *Tetrahedron* **2008**, *64*, 8522-8529.

17. Sasaki, T.; Guerrero, J. M.; Leonard, A. D.; Tour, J. M. Nanotrains and Self-Assembled Two-Dimensional Arrays Built from Carboranes Linked by Hydrogen Bonding of Dipyridones. *Nano Research* **2008**, *1*, 412-419.

18. Khatua, S.; Godoy, J.; Tour, J. M.; Link, S. Influence of the Substrate on the Mobility of Individual Nanocars. *J. Phys. Chem. Lett.* **2010**, *1*, 3288-3291.

19. Kupchenko, I. V.; Moskovsky, A. A.; Nemukhin, A. V.; Kolomeisky, A. B. On the Mechanism of Carborane Diffusion on a Hydrated Silica Surface. *J. Phys. Chem. C* **2011**, *115*, 108-111.

20. Vives, G.; Guerrero, J. M.; Godoy, J.; Khatua, S.; Wang, Y. P.; Kiappes, J. L.; Link, S.; Tour, J. M. Synthesis of Fluorescent Dye-Tagged Nanomachines for Single-Molecule Fluorescence Spectroscopy. *J. Org. Chem.* **2010**, *75*, 6631-6643.

21. Khatua, S.; Guerrero, J. M.; Claytor, K.; Vives, G.; Kolomeisky, A. B.; Tour, J. M.; Link, S. Micrometer-Scale Translation and Monitoring of Individual Nanocars on Glass. *ACS Nano* **2009**, *3*, 351-356.

22. Claytor, K.; Khatua, S.; Guerrero, J. M.; Tcherniak, A.; Tour, J. M.; Link, S. Accurately Determining Single Molecule Trajectories of Molecular Motion on Surfaces. *J. Chem. Phys.* **2009**, *130*.

23. Archibald, T. G.; Malik, A. A.; Baum, K. Thermally Stable Acetylenic Adamantane Polymers. *Macromolecules* **1991**, *24*, 5261-5265.

24. Waybright, S. M.; Singleton, C. P.; Wachter, K.; Murphy, C. J.; Bunz, U. H. F. Oligonucleotide-Directed Assembly of Materials: Defined Oligomers. *J. Am. Chem. Soc.* **2001**, *123*, 1828-1833.

25. Rohand, T.; Qin, W. W.; Boens, N.; Dehaen, W. Palladium-Catalyzed Coupling Reactions for the Functionalization of Bodipy Dyes with

Fluorescence Spanning the Visible Spectrum. *Eur. J. Org. Chem.* **2006**, 4658-4663.

26. Li, L.; Nguyen, B.; Burgess, K. Functionalization of the 4,4-Difluoro-4-Bora-3a,4a-Diaza-S-Indacene (Bodipy) Core. *Bioorg. Med. Chem. Lett.* **2008**, *18*, 3112-3116.

27. Michalet, X. Mean Square Displacement Analysis of Single-Particle Trajectories with Localization Error: Brownian Motion in an Isotropic Medium. *Physical Review E* **2010**, *82*.

28. Savin, T.; Doyle, P. S. Static and Dynamic Errors in Particle Tracking Microrheology. *Biophys. J.* **2005**, *88*, 623-638.

29. Akimov, A. V.; Nemukhin, A. V.; Moskovsky, A. A.; Kolomeisky, A. B.; Tour, J. M. Molecular Dynamics of Surface-Moving Thermally Driven Nanocars. *J. Chem. Theory Comput.* **2008**, *4*, 652-656.

^{1}H NMR of **7**

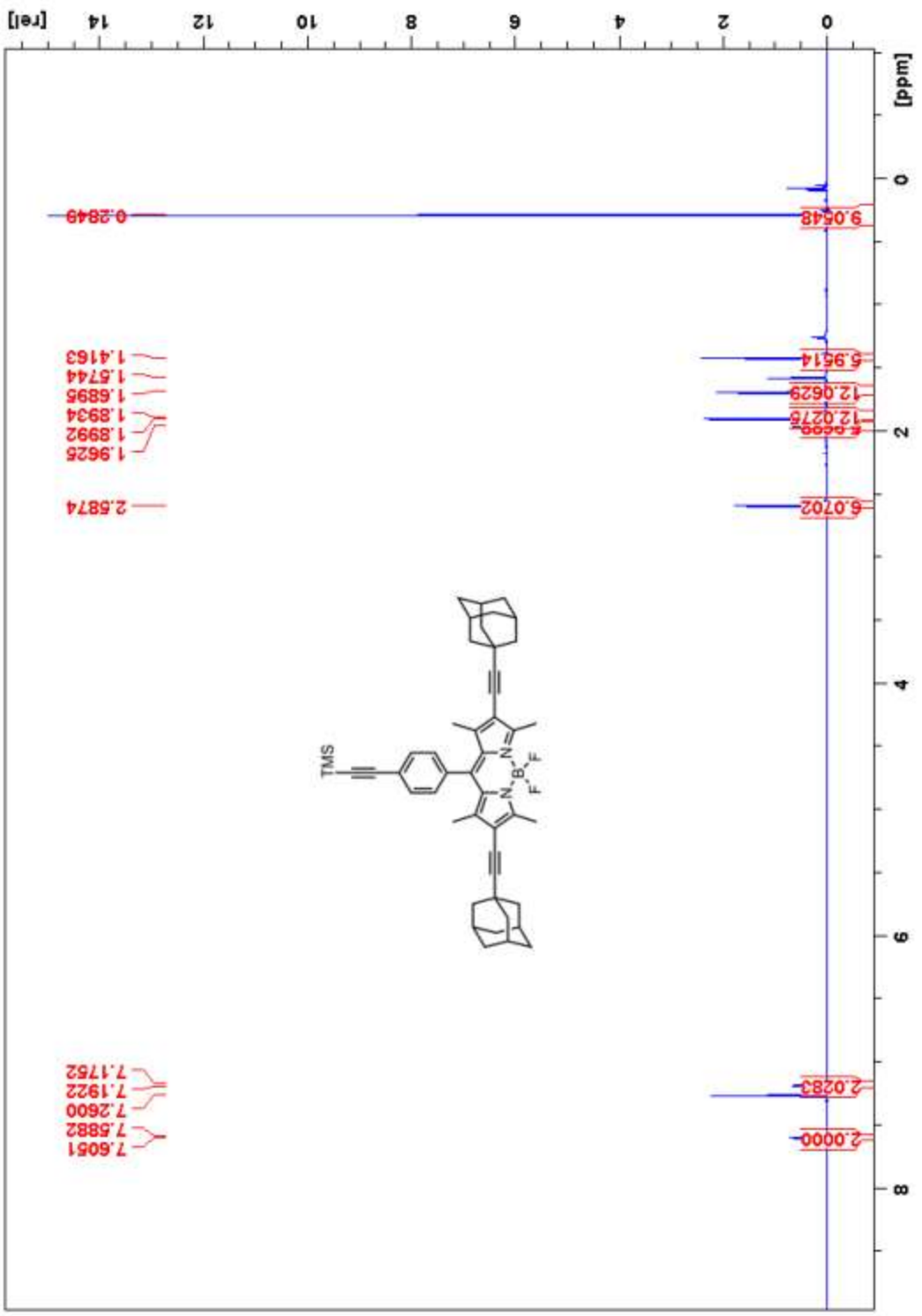
[rel]
14
12
10
8
6
4
2
0
[ppm]
0.2849
9.0548
1.4163
1.5744
1.6895
1.8934
1.8992
1.9625
2.5874
5.9514
12.0629
12.0278
6.0702
TMS
7.1752
7.1922
7.2600
7.5882
7.6051
2.0283
2.0000

Amplification of ^{1}H NMR of **7**

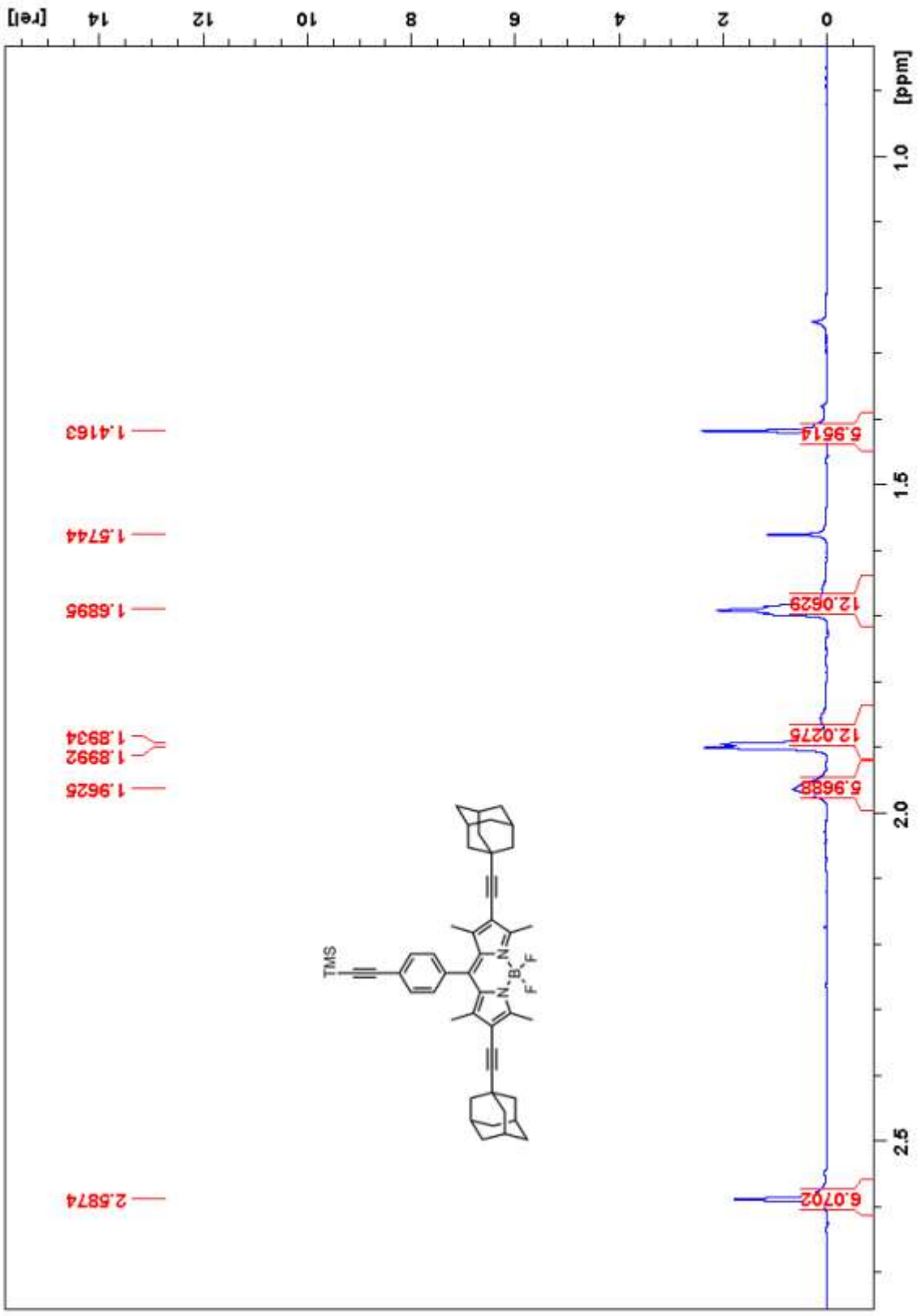

^{13}C NMR of **7**

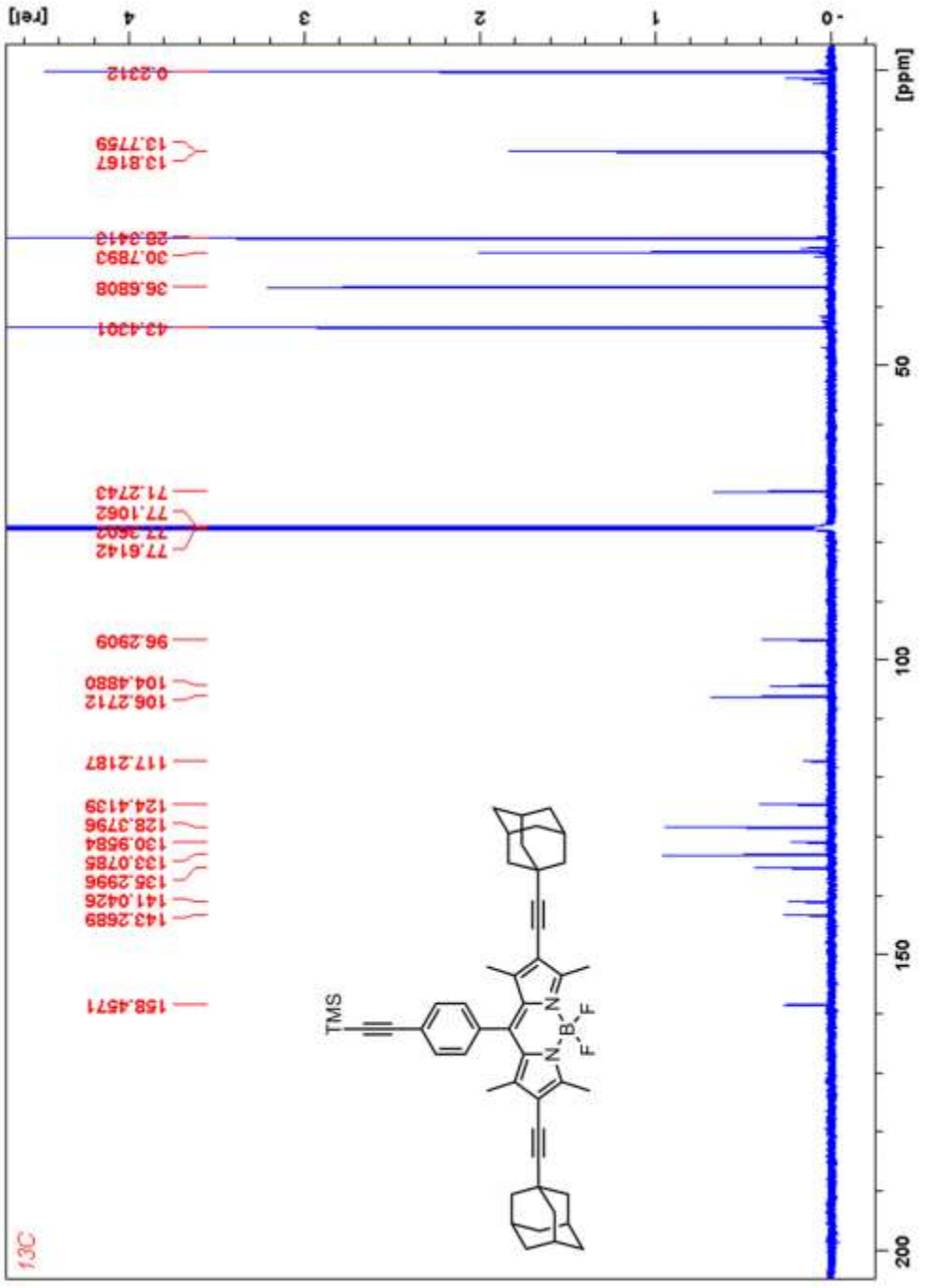
[rel]
4
3
2
1
0
[ppm]
50
100
150
200
0.2312
13.8167
13.7759
28.3413
30.7893
36.6808
43.4301
71.2743
77.1062
77.6142
96.2909
104.4880
106.2712
117.2187
124.4139
128.3796
130.9584
133.0785
135.2996
141.0426
143.2689
158.4571
TMS
N
B
F
F
13C

^{1}H NMR of **8**

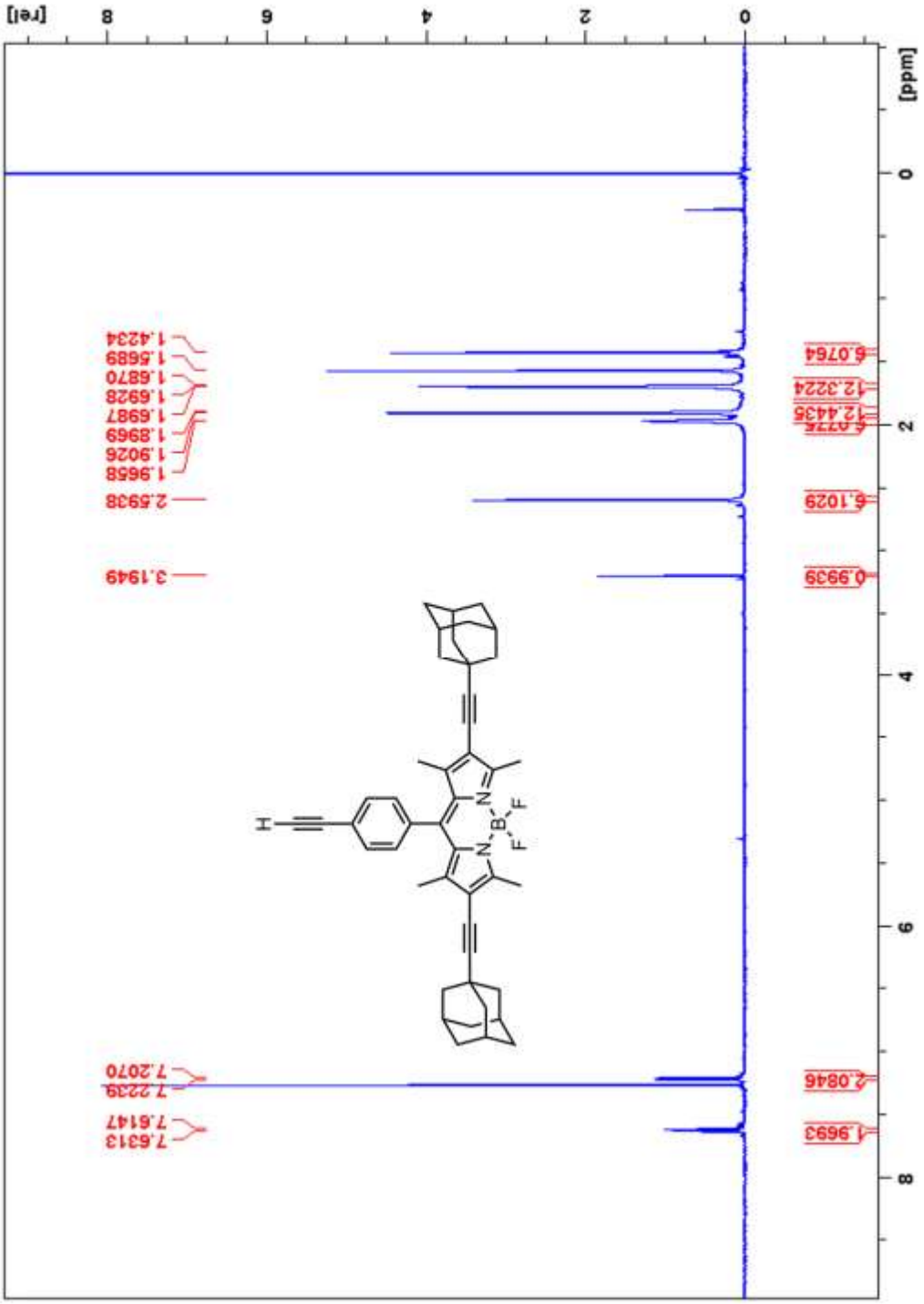
[rel]
8
6
4
2
0
[ppm]
0
2
4
6
8
1.4234
1.5689
1.6870
1.6928
1.6987
1.8969
1.9026
1.9658
2.5938
3.1949
7.2070
7.2239
7.6147
7.6313
6.0764
12.3224
12.4435
6.0276
6.1029
0.9939
2.0846
1.9693
H
N
B
F
F

Amplification of ^{1}H NMR of **8**

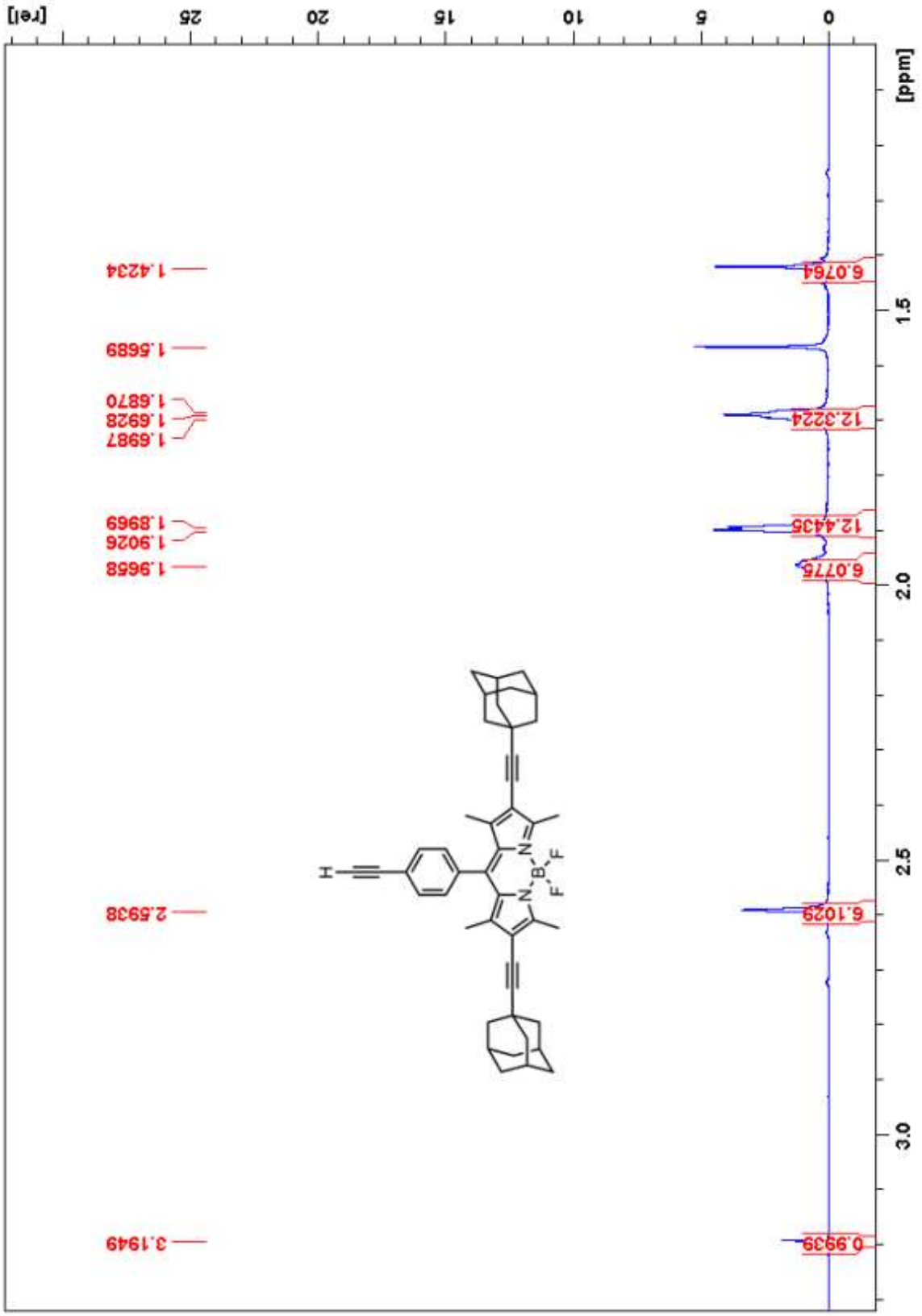

^{13}C NMR of **8**

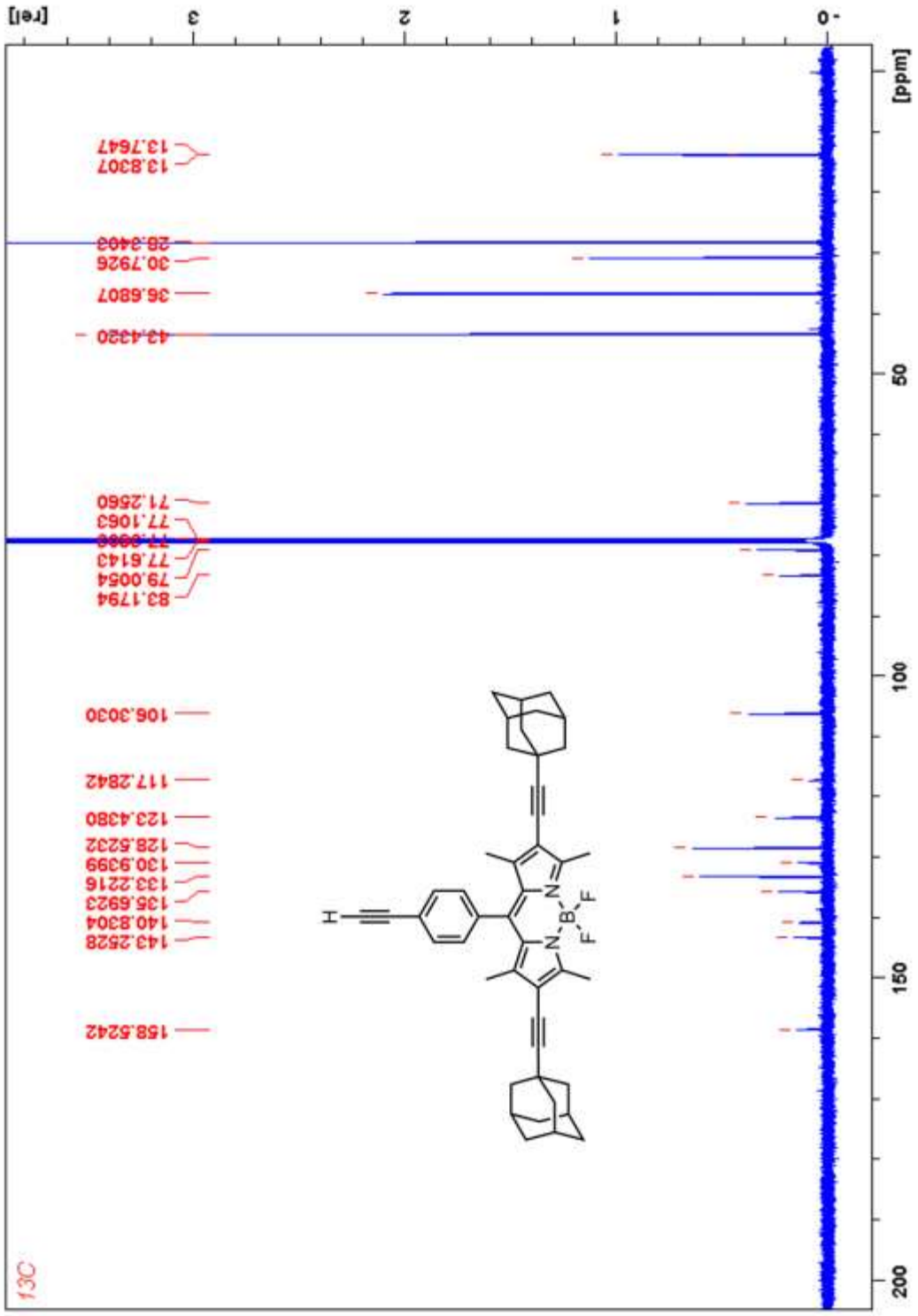
13.7647
13.8307
28.3403
30.7926
36.6807
43.4320
71.2560
77.1063
77.6143
79.0054
83.1794
106.3030
117.2842
123.4380
128.5232
130.9399
133.2216
135.6923
140.8304
143.2528
158.5242
13C
[ppm]
[rel]
F
F
B
N
N
H

^{13}C NMR of **3**

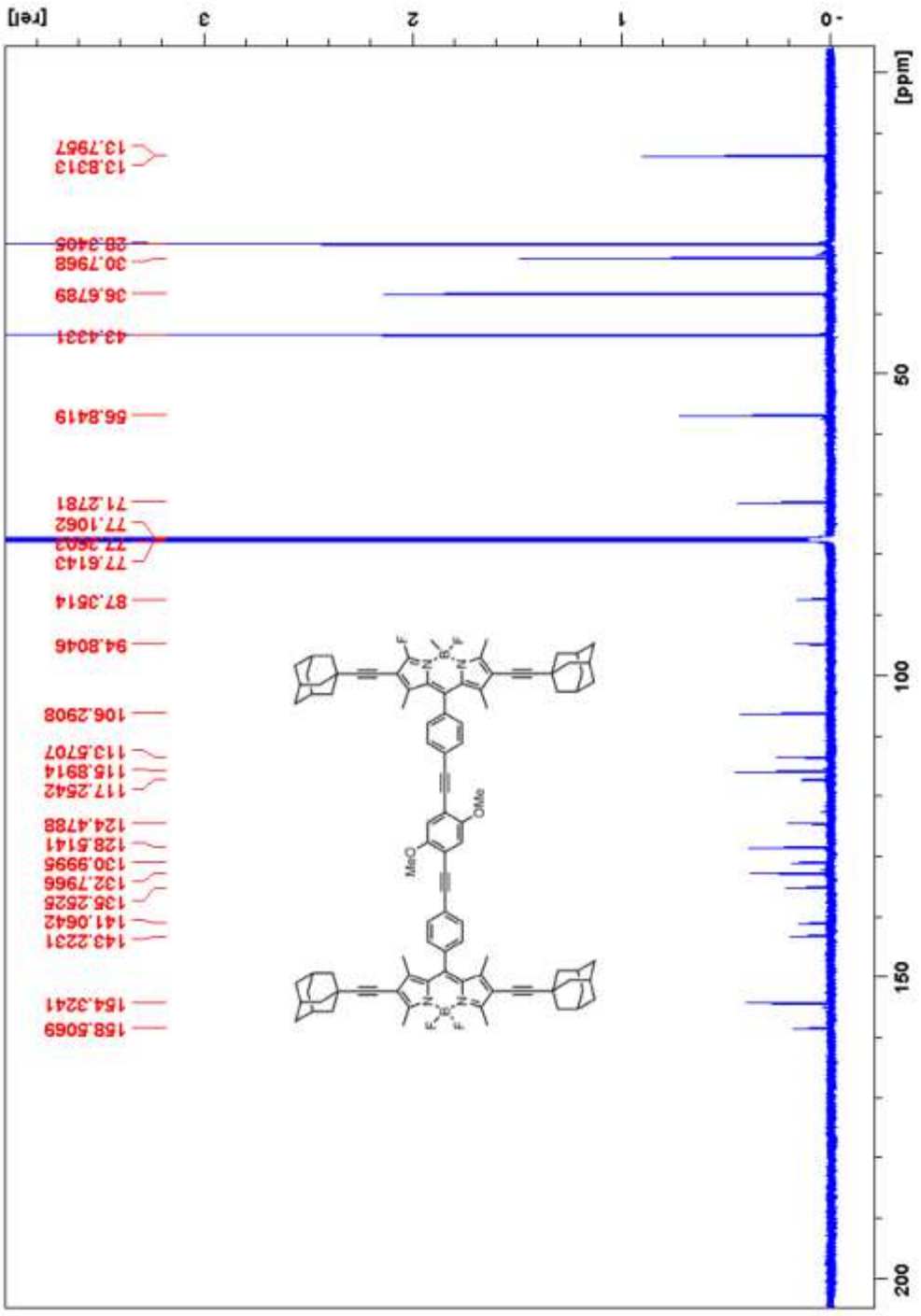
[rel]
3
2
1
0
[ppm]
50
100
150
200
13.7957
13.8313
28.3405
30.7968
36.6789
43.4331
56.8419
71.2781
77.1062
77.3503
77.6143
87.3514
94.8046
106.2908
113.5707
115.8914
117.2542
124.4788
128.5141
130.9995
132.7966
135.2525
141.0642
143.2231
154.3241
158.5069
MeO
OMe

^{1}H NMR of **3**

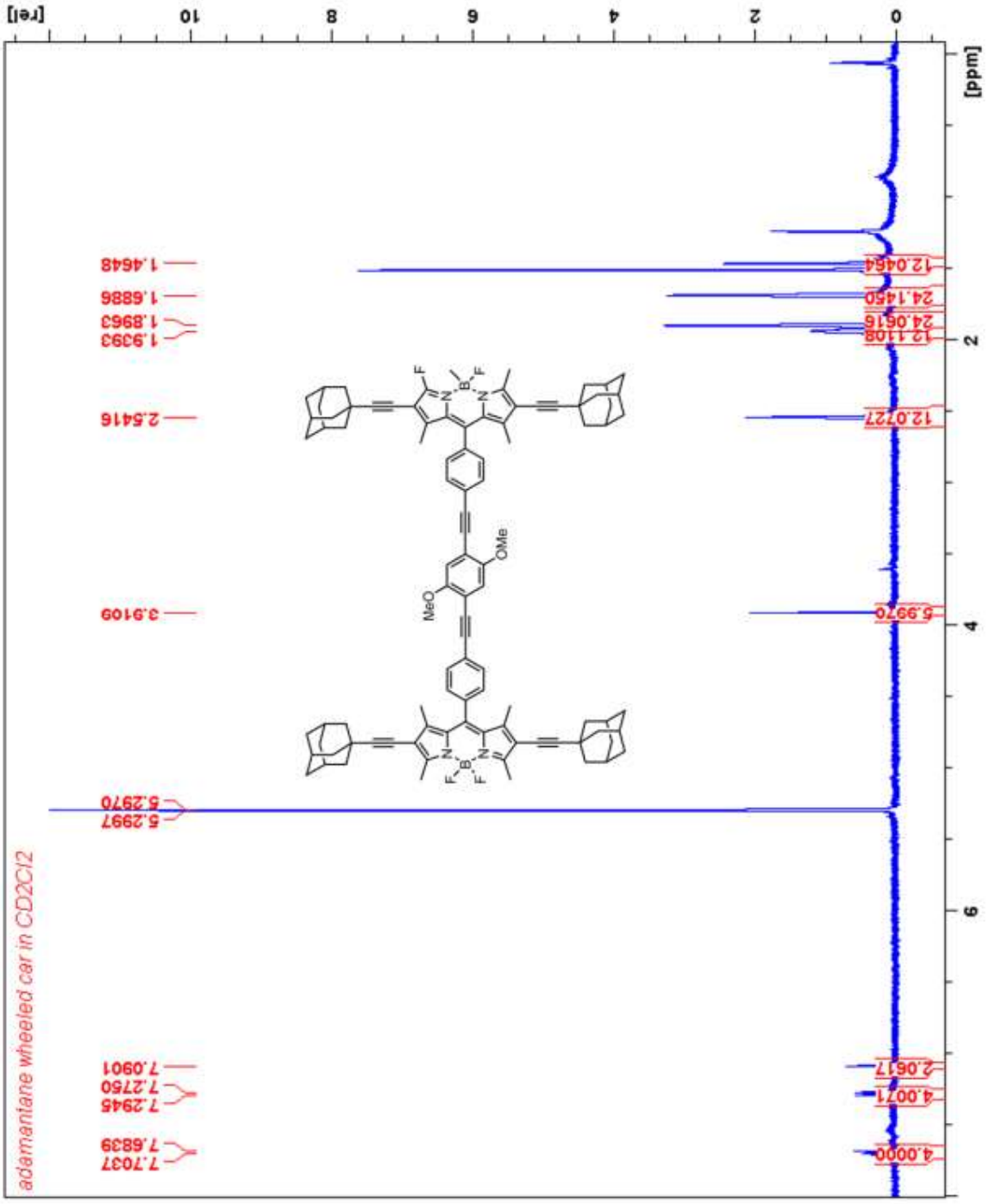
adamantane wheeled car in CD2Cl2
[ppm]
[rel]
12.0464
24.1450
24.0616
12.1108
12.0727
5.9970
4.0000
4.0071
2.0617
7.7037
7.6839
7.2945
7.2750
7.0901
5.2997
5.2970
3.9109
2.5416
1.9393
1.8963
1.6886
1.4648
OMe
MeO

CHAPTER 3

Carbon Nanotubes Dispersed in Aqueous Solution by Ruthenium(II) Polypyridyl Complexes

This chapter is copied from a submission to Chemical Sciences

3.1 Introduction

Carbon nanotubes (CNTs) are one-dimensional cylindrical structures of wrapped graphene sheets forming tubular architectures. Single-walled carbon nanotubes (SWCNT) are formed by one of such rolled sheets, while multi-walled carbon nanotubes (MWCNT) contain several graphene sheets leading to multiple concentric tubes of different sizes.[1] In the past two decades, SWCNTs have emerged as an intensive research topic for applications in solar cells,[2-4] electronic devices,[5, 6] transparent conductive films,[7-9] strong conductive fibers,[10, 11] and hydrogen storage,[12] among others. However, as-synthesized SWCNTs form bundles due to strong van der Waals attractions between them. Bulk bundled SWCNTs require to be individualized in order to fully exploit their mechanical, electronic, and optical properties.[13-16] A general approach to debundle SWCNTs is introducing repulsive interactions between them to counterbalance short-range attractions. To date, myriad approaches have been developed to individualize carbon nanotubes and most of them are simply divided into two categories, that is, covalent functionalization,[17, 18] versus non-covalent functionalization.[16, 19, 20]

On one hand, covalent functionalization is an effective approach for attaching functional groups to the sidewalls of carbon nanotubes. In turns, it enables their dispersion in different solvents, but the process involves the chemical modification of SWCNTs. The conversion of, for example, sp^2 carbons to sp^3 carbons leads to the destruction of the extended π-system and, therefore, to changes in the resulting electronic properties. On the other hand, non-covalent interactions with molecular building blocks such as surfactants, which contain hydrophobic and hydrophilic domains, keep the carbon backbone of SWCNTs intact and preserve their electronic properties. The design of photoactive molecular building blocks capable of dispersing SWCNTs, while maintaining their delocalized π-electron systems intact, is of great importance, especially in the context of their use in solar energy conversion.[13]

Marti's group has previously reported on the use of ruthenium polypyridyl complex with extended π-systems such as $[Ru(bpy)_2(dppz)]^{2+}$ (bpy = 2,2'-bipyridine; dppz = dipyrido[3,2-a:2'.3'-c]-phenazine) to non-covalently disperse SWCNTs in aqueous media.[16] Although high concentration of SWCNTs are dispersable in aqueous solutions using $[Ru(bpy)_2(dppz)]^{2+}$, its short lived non-emissive excited state in aqueous solution limits the excited state interactions between the metal complex and

the CNTs.[21, 22] In this study, we synthesized two ruthenium complexes containing pyrene-anchoring groups – Scheme 3.1. These complexes are photoluminescent in water with reasonably long photoluminescence lifetimes.[23] Non-covalent π-stacking interactions between SWCNTs and pyrene are responsible for the physisorption of the photoluminescent complexes onto carbon nanotubes. The non-covalent attachment of pyrene derivatives onto SWCNTs not only keeps their electronic structure intact, but also its easy modification allows the attachment of a variety of molecules to carbon nanotubes.[2, 24-28] In this manuscript, we demonstrate that ruthenium complexes containing pyrene-anchoring groups are efficient dispersers for SWCNTs in water. Using different spectroscopic techniques such as steady-state and time-resolved photoluminescence spectroscopy as well as transient absorption spectroscopy we probed the excited state of ruthenium complexes/SWCNTs composites in aqueous solution. The spectroscopic results obtained are in line with quenching of the excited state by Förster Resonance Energy Transfer (FRET) from the ruthenium complexes to SWCNTs.

3.2 Results and Discussion

Ruthenium complexes with pyrene anchoring groups (**RuPy**) were synthesized by multi-step reactions – see Schemes 3.2 and 3.3 in the experimental section – followed by ion exchange of the hexafluorophosphate salts with water-soluble chloride anions. Two molecules were synthesized labeled **RuPy1** and **RuPy2** as depicted in Scheme 3.1. The difference between **RuPy1** and **RuPy2** is the respective linker between the phenanthroline and the pyrene – for **RuPy1** the linker is an alkyne group, while for **RuPy2** the linker is an alkane group.

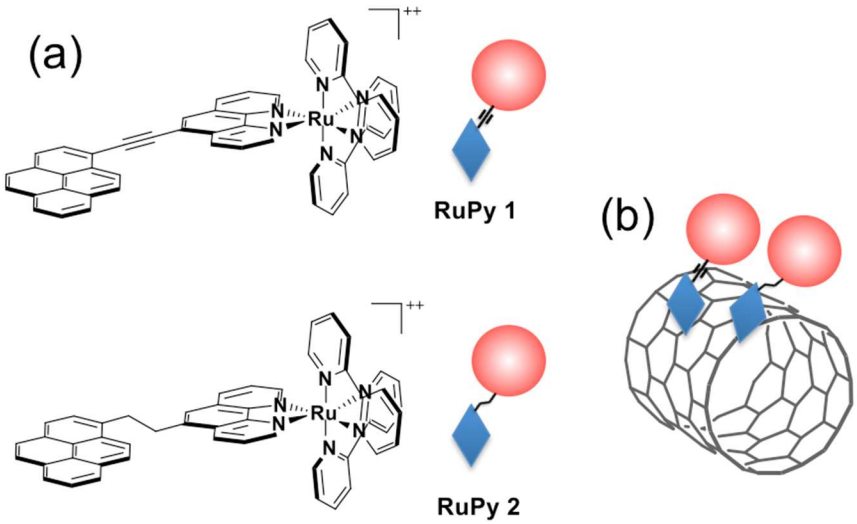

Scheme 3.1. a) Structures of RuPy1 and RuPy2; b) Pictorial illustration of the interactions of RuPy1 and RuPy2 with SWCNTs.

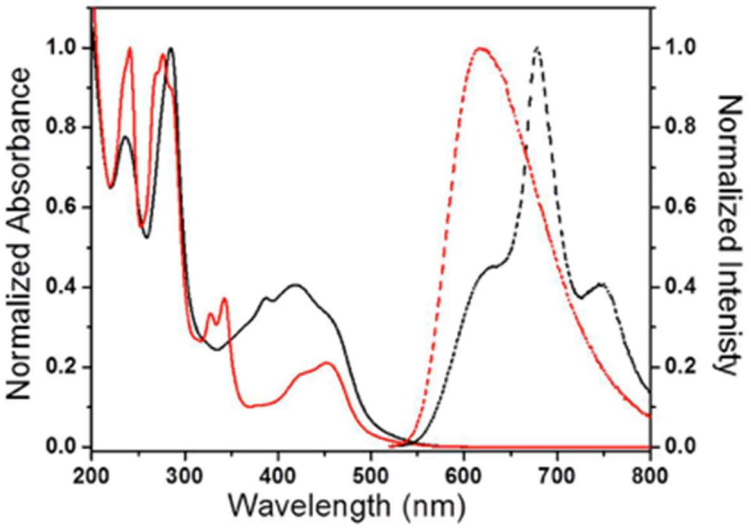

Figure 3.1. Normalized absorption and emission spectra of RuPy1 (black spectra) and RuPy2 (red spectra) in nitrogen purged aqueous solution.

The absorption and emission of **RuPy1** and **RuPy2** were studied in nitrogen purged aqueous solutions. The absorption spectrum of **RuPy1** in Figure 3.1 exhibits a broad absorption band with a maximum at 420 nm, which possesses MLCT (metal-to-ligand charge transfer) as well as IL character, and bands at 235 and 285 nm, which correspond to ligand-centered transitions in line with a previous report of a similar complex.[29] The existence of electronic communication between phenanthroline and pyrene via the triple bond conjugation in **RuPy1** is the origin for a structured red-shifted emission with a maximum at 680 nm. Interestingly, its emission lifetime in water reaches 665 μs. In accordance with previous studies, this phenomenon is attributed to the emission from ^{3}IL/^{3}LLCT excited states.[29, 30]

RuPy2 shows an MLCT band with maximum at 452 nm and distinguishable LC bands at higher energies. Reducing the acetylene group linking the phenanthroline and pyrene in **RuPy2** disrupts the extended conjugation of the ligand and restores the typical shape of the MLCT seen in polypyridyl ruthenium complexes.[31, 32] A point to note is that **RuPy2** has distinguishable peaks around 340 nm, which resemble those of pyrene, and, which arise likely due to the disruption of conjugation upon reduction of the alkyne group. **RuPy2** shows an unstructured emission at 615 nm consistent with the emission of $[Ru(bpy)_2(phen)]^{2+}$ in water and an emission lifetime of 12 μs (Table S1). The latter exceeds that of $[Ru(bpy)_2(phen)]^{2+}$, which is consistent with a triplet-triplet excited state equilibrium between the ^{3}MLCT and pyrene centered ^{3}IL states.[33-36]

To study the interaction of **RuPy** complexes with a variety of nanotubes types (chiralities) we employed High-Pressure CO Conversion (HiPco) nanotubes. SWCNTs were dispersed in D_2O solutions of either **RuPy1** or **RuPy2** with different initial amounts of HiPco SWCNTs. The resulting dispersions were sonicated followed by centrifugation to remove non-dispersed bundled SWCNTs. Then, the supernatant was collected to isolate dispersions of **RuPy**/HiPco SWCNT hybrids. Hybrids of **RuPy** Co-Mo catalyst (CoMoCat) SWCNTs were prepared in the same way. The

absorption spectra of HiPco SWCNTs dispersed with **RuPy1** are shown in Figure 3.2, while those for **RuPy2** are found in Supporting information, Figure S2. Consistent with Figure 3.1, there is no appreciable absorption for **RuPy1** above 550 nm. On the contrary, for **RuPy1**/HiPco SWCNT hybrids, an increase in the absorption above 550 is noted (Figure 3.2a), which shows the typical SWCNT centered van Hove transitions. We note in Figure 3.2a that the absorbance at 420 nm decreases as the initial concentration of SWCNT increases, which implies the decrease of the **RuPy1** concentration in solution. This phenomenon is attributed to the immobilization of **RuPy1** onto undispersed SWCNTs following tip sonication and centrifugation. From analyses of Figure 3.2a, we concluded that the optimum dispersion conditions for SWCNTs with **RuPy1** include an initial concentration of 2 mg/mL. Similar dispersion results are found for CoMoCat SWCNTs, which are enriched in (6,5) SWCNTs (Figure S3).

In order to study dispersed SWCNTs with minimum interference from free **RuPy1** and / or **RuPy2**, the solutions were dialyzed using nominal 2000 MW membranes. After dialysis, the absorption spectra of the resulting dispersions (Figure 3.2b) give rise to a reduced amount of **RuPy1** and / or **RuPy2** as corroboration for the removal of free RuPy. In the near infrared, the absorption spectra of HiPco SWCNTs show discernable van-Hove

singularities, which is indicative for SWCNT individualization, and, which underlines that 2 mg/mL is indeed the optimum initial concentration of SWCNTs when dispersed with **RuPy1** (Figure 3.2c). This confirms that dialysis for a controlled time period is a viable strategy for removing free **RuPy1**. If the dialysis continues beyond 24 h, the dispersion is, however, rather unstable leading to the precipitation of SWCNTs. If the dialysis is stopped before or at the 24 h limit the dispersions are stable for days. Notable, dispersions featuring lower concentrations of SWCNTs are dialyzable for more than 24h without showing significant precipitation. Absorption spectra of **RuPy2**/HiPco SWCNTs are similar to those shown in Figure 2 (Figures S2b and S2c). Qualitatively, the absorption spectra in Figure 3.2c and S2c seems to indicate that **RuPy1** and is slightly better dispersant for HiPco SWCNTs that **RuPy2** in spite of its more rigid structure.

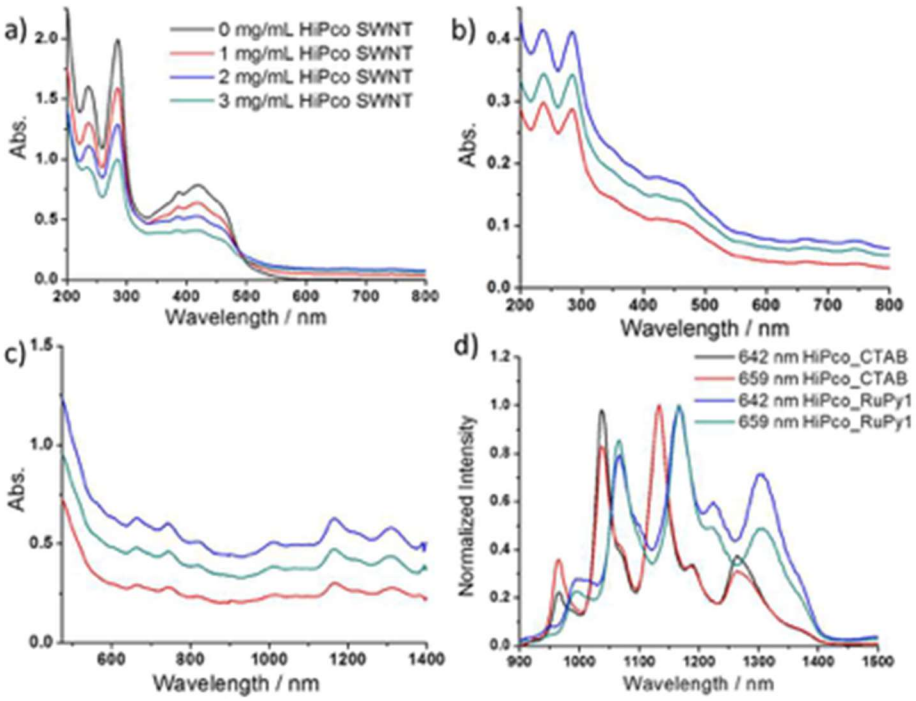

Figure 3.2. Absorption spectra of **RuPy1** and HiPco SWCNT hybrids in aqueous solutions before (a) and after (b) dialysis for 16 h using a nominal 2000 MW membrane. Dispersions were prepared with 1 mg/mL **RuPy1**, with initial concentration of 0 mg/mL (black line), 1 mg/mL (red line), 2 mg/mL (blue line), and 3 mg/mL (cyan line) of HiPco SWCNTs, respectively (40x dilution before taking the spectra); c) Absorption spectra of **RuPy1** and HiPco SWCNT hybrids in aqueous solution (5x dilution before taking the spectra); d) Comparison of photoluminescence spectra of HiPco SWCNTs dispersed in **RuPy1** aqueous solution and CTAB surfactants.

The individualization of SWCNTs in the dispersions is probed by the NIR emission of SWCNTs. Individualized semiconducting SWCNTs give

rise to narrow emissions, whereas the emission is quenched in bundled SWCNTs possibly due to energy transfer to metallic nanotubes present in the bundles.[37, 38] Figure 3.2d shows NIR emission of SWCNTs dispersed by **RuPy1** and by cetyl hexadecyltrimethylammonium bromide (CTAB) and either excited at 642 nm or at 659 nm in aqueous solutions. Again, the presence of emission peaks in the near infrared region attests their individualization. Substantial red-shifts – in the order of 30 nm –in the emission maxima and line broadening were observed in **RuPy1**/HiPco SWCNTs when compared with CTAB/HiPco SWCNTs. This can be attributed to π-π stacking of the pyrene anchors of **RuPy1** onto the sidewalls of SWCNTs.[16] Experiments using **RuPy2** and SWCNTs show similar results (Supporting information, Figures S2d). Contour plots of the photoluminescence of dispersions of SWCNTs with **RuPy1 and RuPy2** at different excitation wavelengths are shown in Figure S5.

Debundling of SWCNTs was independently confirmed by microscopy techniques. Figure 3.3a shows representative AFM images of **RuPy1**/HiPco SWCNTs deposited on mica. The average height of SWCNTs was estimated to be around 2.1 nm, which corresponds to diameters of individual or mostly debundled HiPco SWCNTs covered with **RuPy1**. The morphology of **RuPy1**/HiPco SWCNTs was further visualized by TEM

(Figures 3.5b) More images can be seen in Supporting Information Figure S6. TEM images show two to three individual SWCNTs wrapped with an amorphous material, which suggests the immobilization of **RuPy1** onto SWCNTs. TEM images of **RuPy2**/HiPco and **RuPy1**/CoMoCat SWCNTs show similar features (Figures S7 - S9, respectively).

In light of the fact that sonication induces defects on the sidewalls of SWCNTs, it is crucial to monitor the defects of dispersed SWCNTs. To this end, the G/D ratios in Raman spectra taken for SWCNTs are a qualitative approach to assess defects. Raman spectra of HiPco and CoMoCat SWCNTs dispersed with **RuPy1** were obtained by dropcasting and drying the dispersions on silicon wafers (Figure S10). In the spectra, G- and D-bands evolve at 1592 and 1300 cm^{-1}, respectively. The relative intensity ratios of the G/D bands is 11.1, which infers only slight damaging of the SWCNT sidewalls. In the literature, pristine SWCNTs feature G/D in the range from 17 to 20.[8]

To probe excited state interactions between SWCNTs and **RuPy1** or **RuPy2** we employed first steady-state emission spectroscopy. The effect of **RuPy1** on the emission of HiPco SWCNTs was assessed by diluting dispersions of **RuPy1**/HiPco SWCNTs and CTAB/HiPco SWCNTs to the same absorption at 642 nm. CTAB is a cationic surfactant, which should

have minimum excited state interactions with SWCNTs. The NIR emission of SWCNTs excited at 642 was obtained and shows a 70% quenching of the HiPco SWCNT emissions when dispersed with **RuPy1,** accompanied by a 30 nm red-shift in the emission maxima – Figure 4a. The same experiments yield for **RuPy2** a 94% quenching of the HiPco SWCNTs centered features – Figure S11a. The quenching of the SWCNTs photoluminescence is consistent with quenching of the excited state by heavy atom effect due to the close proximity of the ruthenium complexes. Actually, it is possible that the stronger quenching of SWCNT photoluminescence by **RuPy2** is associated with a closer distance of this complex to the nanotube due to its flexible linker.

To study the effect of SWCNTs on the excited state emission of **RuPy1**, we prepared a **RuPy1**/HiPco SWCNTs dispersion with an absorbance of less than 0.05 at 440 nm to minimize inner filter effects. Then, we prepared a CTAB/HiPco SWCNTs dispersion and diluted it to match the absorption of **RuPy1**/HiPco SWCNTs at 642 nm (this is done to estimate the contribution of SWCNT to the absorption spectrum of **RuPy1**/HiPco). Implicit in the subtraction of these two spectra is the amount of **RuPy1** used to disperse the HiPco SWCNTs. Then, we prepared a solution of **RuPy1** with the same absorption at 420 nm as the spectra

obtained by subtraction of the **RuPy1** and **RuPy1**/SWCNTs spectra. This is carried out to guarantee the same concentrations of **RuPy1** in both solutions. The emission of **RuPy1** and **RuPy1**/SWCNTs were then recorded showing a 92% decrease in intensity in the case of the later – Figure 4b. The experiment for **RuPy2** yields a 75% emission quenching in the presence of HiPco SWCNTs – Supporting information, Figure S11b.

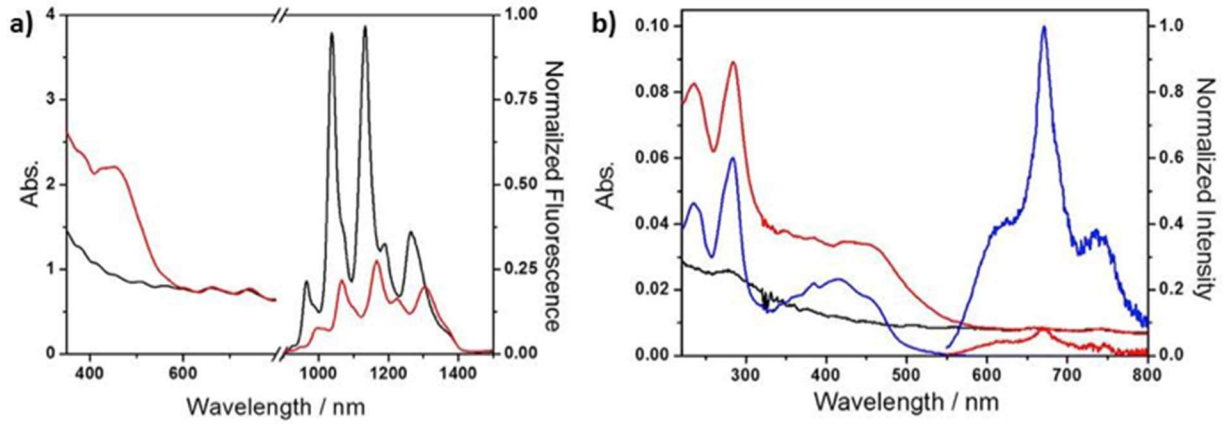

Figure 3.4. (a) Absorption and NIR emission spectra of CTAB/HiPco SWCNT (black spectra) and **RuPy1**/HiPco SWCNT (red spectra) in aqueous solution upon 642 nm photoexcitation; (b) Absorption and emission spectra of CTAB/HiPco SWCNT (black spectra), **RuPy1**/HiPco SWCNT (red spectra), and **RuPy1** (blue spectra) in aqueous solutions upon 420 nm photoexcitation.

The stronger quenching, as it is observed for **RuPy1** with SWCNTs, is likely to be a consequence of its longer photoluminescence lifetime in

comparison with **RuPy2** – vide infra. The nature of this quenching will be discussed in more detail below.

Emission lifetime analysis for **RuPy1** also shows a decrease when SWCNTs are present, namely from 665 to 382 μs, when used to disperse HiPco SWCNTs (Table S1). For **RuPy2**, the change in lifetime was from 12.2 to 6.8 μs. It is, however, important to mention that the quenching based on lifetime values is smaller (~55%) than what would be expected based on the steady state photoluminescence (>75%, previous paragraph). As such, a static component must contribute to the quenching of the **RuPy1 and 2** emission in the presence of SWCNTs.

To further explore the nature of the SWCNTs and **RuPy1** and / or **RuPy2** interactions, pump-probe experiments were performed. Control pump-probe experiments of **RuPy1** in D_2O show bleaching of the MLCT, which recovers biexponentially with lifetimes of 8.5 and 102.5 ps – Figure S12. This bleach is followed by the emergence of a long-lived positive transient with maxima at 439 and ~500 nm, which are likely associated with triplet-triplet absorptions of pyrene.[29] The differential absorption spectra for **RuPy2** are similar to that of **RuPy1**. The only notable difference is the recovery of the MLCT bleaching, which exhibits lifetimes of 81.8 and 698.7 ps – Figure S13. The MLCT bleaching is followed by the formation of

positive transients with maxima at 490 and 515 nm as well as a negative transient at ~630 nm, which can be attributed to emission.

The pump-probe experiments for HiPco SWCNTs dispersed by CTAB were also obtained as control experiments and are shown in Figure 3.5a. Two major features are observed in the pump-probe experiments: transient bleachings and transient absorption. Transient bleachings are due to pump laser excitation which creates E_{ii} excitons that relax to E_{11} within 100 fs.[49] This produces a depletion of the ground state that is observed as a bleaching in the van Hoff transitions. Transient absorption features have been attributed to several factors such as population of a biexciton manifold ($E_{11} + E_{22}$) from E_{11} and photoexcited bound excitons,[49] e.g. E_{22}-E_{11} or E_{33}-E_{11}.[50]

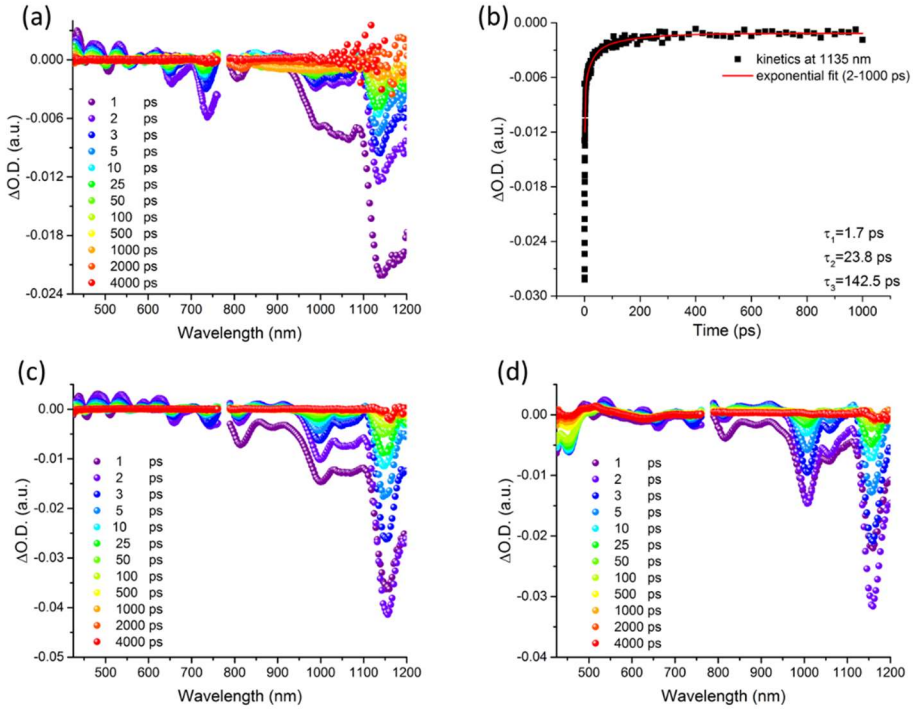

Figure 3.5. Differential absorption spectra obtained upon femtosecond pump probe experiments (387 nm) of (a) CTAB/HiPco SWCNTs in D_2O with its time decay profile at 1135. Differential absorption spectra for (c) **RuPy1**/HiPco SWCNTs and (d) **RuPy2**/HiPco SWCNTs in D_2O.

Transient bleachings are observed at 988, 1030, 1060, and 1140 nm, which are consistent with bleaching of the ground state of (6,5), (7,5), (10,2), and (7,6) SWCNTs, respectively. These bleachings are red shifted in relation with HiPco nanotubes dispersed with SDBS.[20] Exponential fits (from 2-1000 ps) let to dynamics in the picosecond range of ~2, 23, and 142 ps – Table S3. Previous studies have suggested that short component lifetimes (≤

2 ps) are due to relaxation of SWCNTs in bundles,[50, 51] while longer components from tens to hundreds of nanoseconds can be assigned band edge relaxation.[51, 52] It is important however to point out that exciton relaxation transitions in SWCNTs depend on a variety of factors such as defects, length and dispersant.[50]

Pump-probe experiments for **RuPy1**/HiPco show transient bleachings at 1000, 1050 nm (not prominent), and 1152 nm with similar lifetimes of ~2, 36, and 169 ps – Figure 3.5c and Table S3. For **RuPy2**/HiPco SWCNTs, the minima are further red shifted to 1005, 1055, 1156 nm – Figure 5d – and with lifetimes as detailed in Table S3. Nonetheless, we did not observe any significant changes in the bi-exponential lifetimes in the excited state decay profile of **RuPy1**/HiPco SWCNTs and **RuPy2**/HiPco SWCNTs when compared to the analogous HiPco SWCNTs dispersion. Notable is that the transient absorption experiment for **RuPy2**/HiPco SWCNTs (Figure 3.5d) show features that are consistent with free **RuPy2** as discussed in the previous paragraph. This is because the samples for transient absorption experiments were not dialyzed in order to increase their stability during the transient absorption experiments (see experimental section). These features are not obvious in the **RuPy1**/HiPco SWCNTs transient absorption experiments (Figure 3.5c) due

to the better interaction between **RuPy1** and SWCNTs, which results in less free **RuPy1.**

In order to identify any potential new bands due to charge transfer interactions, we performed spectroelectrochemistry of **RuPy1** and **RuPy2.** Figures S12-S13, supporting information, illustrate UV-Vis for the oxidation and reduction of **RuPy1** and **RuPy2** upon applying variable potentials, respectively. On one hand, under oxidative and reductive conditions, attenuation of the MLCT related transitions is expressed in terms of negative differential absorption changes between 400 and 500 nm. Once oxidized, the tendency to transfer metal t_{2g} electrons to ligand π^* orbitals is eliminated. On the other hand, weak positive differential absorption changes in the range from 500 to 900 nm are in line with recent reports assigned to LMCT transitions. Unfortunately, the differential absorption bands seen at different reduction potentials resemble those of the control transient absorption experiments of the complexes in solution with no nanotubes (Figures S12 and S13). Comparison of Figure 5c and d with Figure 5a, indicate small shifts in maxima and intensities of the peaks but no new spectral bands which could be unambiguously associated with charge transfer processes (Figure 3.5).

To overcome the heterogeneity of HiPco SWCNT, we performed transient absorption experiments with CoMoCat SWCNTs. The advantage of using CoMoCat SWCNTs is that they are enriched in (6,5) nanotubes, allowing to obtain simpler signals in the transient absorption experiment. Figure 6a shows transient absorption spectra with minima at 993 and 1149 nm in the NIR range corresponding to (6,5) and (7,6) enriched nanotubes dispersed via CTAB in D_2O. This ground state bleaching at, for example, 993 nm is fit to a triexponential decay with lifetimes of 2, 26, and 175 ps. Transient minima in visible range at 464, 513, 571, 652, also corresponds to ground state bleaching, which match with the steady-state absorption spectrum. Transient maxima appear at 479, 530, 607, 902, 936, and 1093 nm and are in sound agreement with previous reports.[20] The transient absorption spectra of CoMoCat SWCNTs dispersed by means of **RuPy1** are shown in Figure 3.6c upon 387 nm excitation.

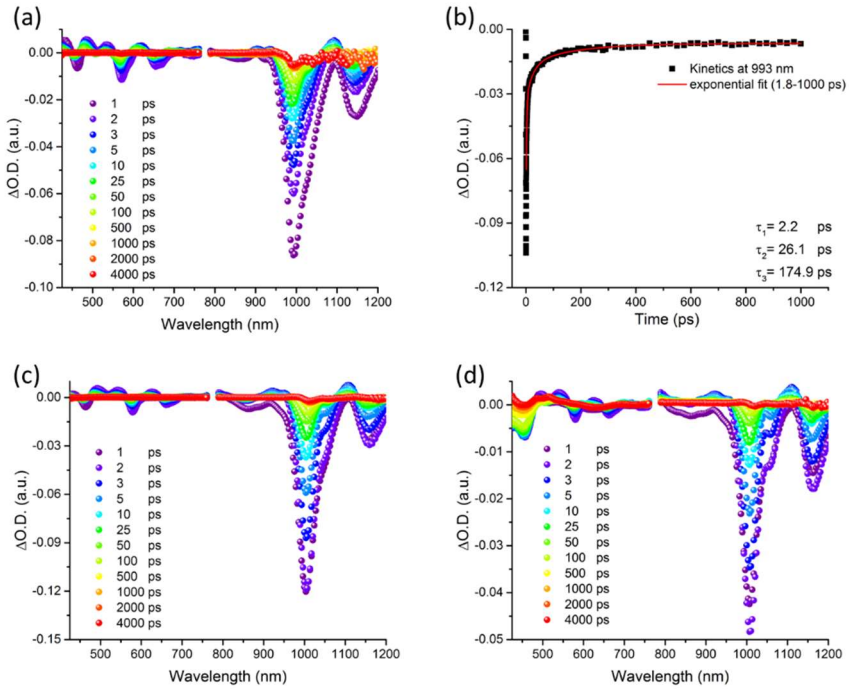

Figure 3.6. Differential absorption spectra obtained upon femtosecond pump probe experiments (387 nm) of (a) CTAB/CoMoCat in D_2O with its time-decay profile at 993 nm. Differential absorption spectra for (c) **RuPy1**/CoMoCat in D_2O, and (d) **RuPy2**/CoMoCat in D_2O.

Minima were observed in this case at 1003 and 1156 nm, which correlate to ground state absorptions of (6,5) and (7,6) SWCNTs, respectively, and that are red-shifted in comparison with CoMoCat SWCNTs. Exponential fitting of the dynamics resulted in three major lifetimes, namely 2, 19, and 136 ps for (6,5) chilarlity. Interestingly, shorter biexponential decay was observed for (7,6) tubes – Table S3. In comparison,

the minima in **RuPy 2**/CoMoCat are slightly red shifted to 1006 nm and 1163 nm (Figure 3.6d) with 2, 17, and 95 ps emerged as lifetimes for (6,5). The red shifts observed for **RuPy** with SWCNTs are reminiscent of the red shifts observed in the photoluminescence spectra and are likely due to π-π stacking.

Interestingly, in past works, both oxidation and reduction of SWCNTs in the presence of ruthenium polypyridyl complexes have been inferred based on photoconductivity, photovoltaics performance, and FET studies.[39-41] Notably, these studies have been performed in dry films, in which the orientation of ruthenium complexes relative to SWCNTs and / or the solvent reorganization energy is likely to play a role in the direction of electron density shift. Thus, both directions of photo-excited electron transfer are in theory, thermodynamically feasible in **RuPy**/SWCNT hybrids as mentioned by et al.[39] Nonetheless, as discussed above for **RuPy1** and **2** with HiPco and CoMoCat SWCNTs, no new features were observed in the transient absorption spectra, that would indicate photoredox chemistry, and thus the reason for the high degree of quenching of the metal complexes cannot be unambiguously identified.

A possibility so far unaddressed is that quenching of RuPy by SWCNTs could be due to FRET. Since the emission from **RuPy1** and **2**

comes from an excited state with strong triplet character, FRET is spin-forbidden and thus it was expected to have minimum contribution to quenching. Nonetheless, calculations of the theoretical quenching efficiency between **RuPy1** and (6,5) SWCNTs as a function of the distance using FRETView[42] (details in appendix 1, supporting information) shows that FRET is quite efficient when the distance between **RuPy1** and SWCNT is close (Table S4). From structural models we anticipate that the distance between the ruthenium cation and the center of a (6,5) SWCNTs is about 1.25 nm (Figure S14), which correspond to an estimated FRET efficiency of unity.

Considering that the emission spectra of **RuPy 1** and **2** are broad, overlapping with the absorption spectra of a variety of SWCNTs, and that the distance between these metal complexes and SWCNTs are expected to be very small, it is reasonable to think that quenching of the photoluminescence of **RuPy1** and **2** is due to FRET rather than electron transfer. Still, we must also point out that the expected FRET rate for **RuPy1** to (6,5) SWCNTs is slow ($10^7 – 10^8$ s^{-1}), which should yield an excited state lifetime component tens of nanoseconds long. Such long component was not detected in our transient absorption experiments, which could be taken as an argument against FRET. Nonetheless, it is likely that we are overestimating the

distance between **RuPy 1** and (6,5) SWCNTS in our calculation, which are really in van der Waals contact, and that would result in faster FRET rates. Finally a concerted electron exchanged mechanism (Dexter energy transfer) is also possible due to the close contact between the **RuPy** and SWCNTs. This kind of mechanism, would leave the lifetimes of SWCNTs unchanged and will not produce any new features in the transient absorption spectra consistent with the experimental data.[43]

3.3 Conclusions

In conclusion, we have synthesized ruthenium complexes capable of dispersing SWCNTs in solution. SWCNT emission and microscopy suggest a great degree of individualization in the dispersions. Upon immobilization onto SWCNTs, the emission of RuPy decreases by up to 92%. Transient absorption experiments show features consistent with **RuPy** and SWCNT excitation, but no new bands corresponding to photoinduced redox species where unambiguously identified. Thus, we concluded that the quenching of **RuPy** in the presence of SWCNTs is likely due to energy transfer, although photoinduced electron transfer cannot be completely ruled out. Due to the large body of research on ruthenium polypyridine complexes donor-acceptor systems for solar energy conversion and water splitting,[31, 32, 44, 45] the creation

of water-soluble **RuPy**/SWCNTs present interesting systems with potential use in artificial photochemistry schemes. Since the proximity of the pyrene group to the Ru(II) complex produces a very short lived MLCT, future work will include creating ruthenium complexes containing long aliphatic chains instead of pyrene groups, which will allow a better monitoring of the long-lived MLCT band in the transient absorption spectrum and a more concise study of the photoredox chemistry of these systems.

3.4 Experimental Section

3.4.1 Schemes and Instruments

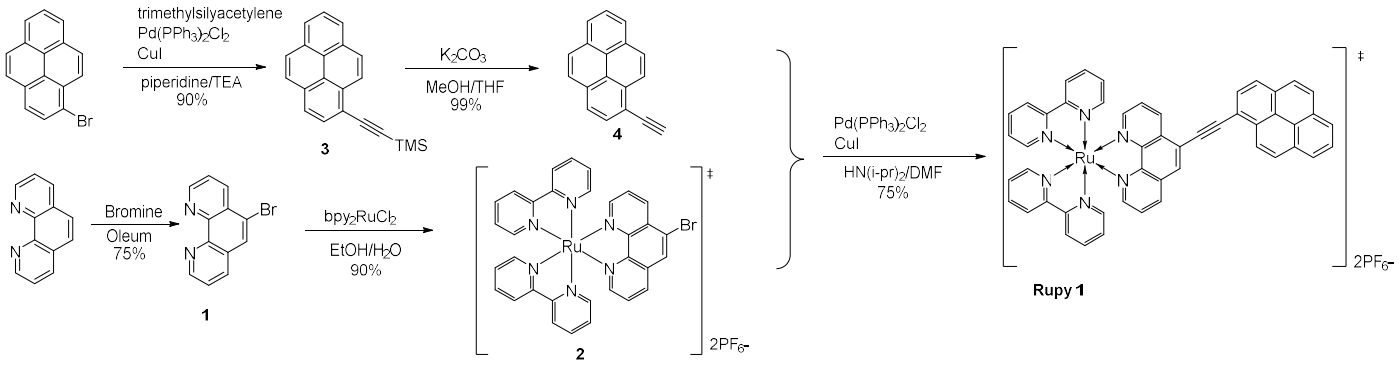

Scheme 3.2. Scheme for the synthesis of **Rupy 1**

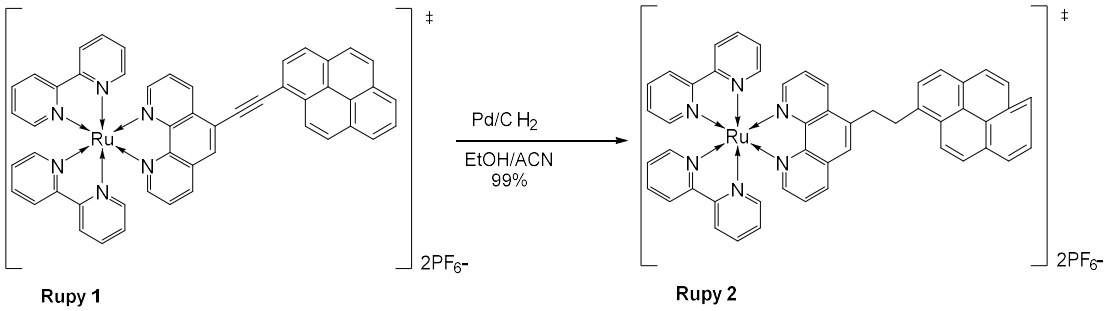

Rupy 1 Rupy 2

Scheme 3.3. Scheme for the synthesis of compound **RuPy2.**

^{1}H NMR spectra were recorded with a Bruker 400 MHz NMR spectrometer. Electrospray ionization mass spectra (ESI-MS) were measured on a Bruker MicroTOF system. UV-Visible spectra were recorded on a Shimadzu UV-2450 UV-Vis spectrophotometer. Steady-state photoluminescence spectra (in the visible region of the spectrum) were obtained in a HORIBA JovinYvonFluorolog 3. Time-resolved studies where performed using an Edinburgh Instruments OD470 single-photon counting spectrometer with a blue detector and μF 920H lamp with excitation at 420 nm for **RuPy1**, while a 440 nm picosecond pulse diode laser and a high speed red detector was used for **RuPy2**. 2D steady-state photoluminescence spectra (in the NIR detection) were measured with a model NS1 Nanospectralyzer (Applied NanoFluorescence) with fixed excitation lasers at 642, and 659 nm. Cyclic voltammetry and square wave voltammetry were

performed by using a FRA 2 μ Autplab type III (METROHM) potentiostat, in a conventional three-electrode electrochemical cell. A glass carbon disk (1 mm diameter) was used as working electrode, a Pt wire electrode served as the counter electrode, an Ag wire was used as the quasi reference electrode while $(n\text{-}Bu)_4NPF_6$ was used as the supporting electrolyte. All potentials were referenced to ferrocenium/ferrocene (Fc^+/Fc). All electrochemical measurements were performed after purging with argon at ambient temperature. Spectroelectrochemistry experiments were performed also with a three-electrode setup in a home-built cell – a transparent platinum gauze as working electrode, a Pt wire as the counter electrode, and a Ag wire as reference electrode. The variable potentials were applied with PGSTAT 101 and the results were shown as differential spectra – spectrum with and without applied potential. The spectra were monitored with a Cary 5000 (VARIAN) UV/vis/NIR spectrometer. In case of **RuPy**/CoMoCaT, NaCl is used as supporting electrolyte whereas conventional $(n\text{-}Bu)_4NPF_6$ is used for spectroelectrochemistry measurements of **RuPy1** and **2** complexes. Raman spectra were obtained using a Renishaw inVia MicroRaman spectrometer. AFM images were taken on a scanning probe microscope, Digital instrument nanoscope III. TEM images were obtained from JEOL 2100 FEG TEM (200 kV, high resolution) and LEO 912 OMEGA transmission electron

microscope (80 kV). Femtosecond transient absorption studies were performed with 387 nm laser pump pulses (1 kHz, 150 fs pulse width-output: 775 nm) from an amplified Ti-sapphire laser system (CPA 2110 Laser, Clark-MXR Inc.). Transient absorption spectra were monitored in 2 mm cuvettes with Helios from Ultrafast Systems. 3D steady-state photoluminescence spectra (in the NIR detection) were taken with a FluroLog3 spectrometer (Horiba) with InGaAs detectors (IGA Symphony 800 to 1700 nm 512 × 1 × 1 μm).

3.4.2 Synthetic Procedures

All reagents and chemicals were obtained from commercial sources and used as received without purification. Cis-Dichlorobis(2,2'-bipyridine)ruthenium(II) dehydrate was purchased from Strem Chemicals. 1-bromopyrene, 1,10-phenanthroline, (trimethylsilyl)acetylene were purchased from Alfa Aesar, USA. Potassium hexafluorophosphate was purchased from TCI America. All other chemicals were purchased from Sigma-Aldrich. Dialysis membranes with Nominal MWCO 2000 were purchased from Membrane Filtration Products, Inc.

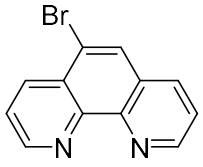

Synthesis of compound 1: This compound was synthesized based on literature methods.[46] 2.4 g of 1,10-phenanthroline were placed in a heavy wall glass reaction tube with a Teflon screw top fitted with a Viton-O-ring. The reaction vessel was placed in an ice bath, and 8 mL of oleum (18%) and 0.4 mL of bromine were added. The reaction tube was placed in a silicon oil bath, and the temperature was slowly raised to 135 ºC. After 24 hrs, the reaction mixture was cooled to room temperature, poured over ice, and neutralized with ammonium hydroxide. The mixture was extracted with chloroform. The red extracts were stirred with charcoal and then dried over sodium sulfate. The crude product was recrystallized from hot diethyl ether with a little amount of dichloromethane. 75% ^{1}H NMR (400 MHz, $CDCl_3$) δ (ppm) 9.214 (t, J = 4.8, 2H), 8.675 (d, J = 8.4, 1H), 8.184 (d, J = 8.0, 1H), 8.150 (s, 1H), 7.750 (dd, J = 4.4, 1H), 7.652 (dd, J = 4.4, 1H).

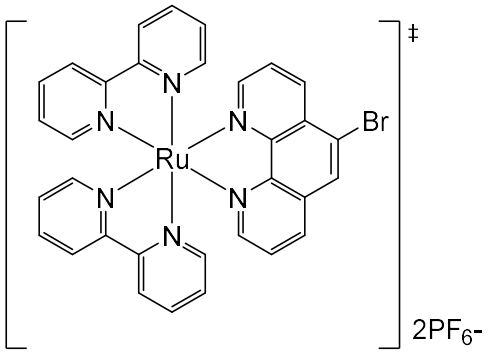

Synthesis of compound 2: This compound was synthesized based on literature methods.[47] The mixture of cis-dichlorobis(2,2'-bipyridine)ruthenium(II) dehydrate (0.260 g) and compound **1** (0.130 mg) in ethanol and water mixture solvent (v/v, 1/1) was heated to reflux for 2 h. After this, it was cooled down to room temperature and 150 mg of potassium hexafluorophosphate were added. The solvent was removed by rotovap and the crude product was purified by column chromatography in 90% yield. ^{1}H NMR (400 MHz, CD_3CN) δ (ppm) 8.742 (d, J = 8.4, 1H), 8.742 (d, J = 8.4, 1H), 8.602 – 8.538 (overlapping m, 6H), 8.202 (dd, J = 6.8, 2H), 8.116 (t, J = 8.0, 2H), 8.024 (t, J = 8.4, 2H), 7.903 (m, 2H), 7.850 (dd, J = 5.2, 1H), 7.781 (dd, J = 5.2, 1H), 7.610 (m, 2H), 7.489 (t, J = 6.4, 2H), 7.280 (m, 2H). ESI-MS: m/e 817.0 (M - PF_6^-), 337.0 ([M - $2PF_6^-$]/2).

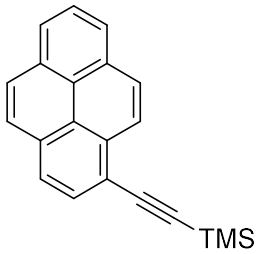

Synthesis of compound 3: This compound was synthesized based on literature methods.[48] A mixture of 1-bromopyrene (560 mg), $Pd(PPh_3)_2Cl_2$ (175 mg), CuI (50 mg) and piperidine (4 mL) in 30 mL triethylamine was bubbled with nitrogen for 20 min. Then, the trimethylsilylacetylene was added and the resulting solution was heated at 110 °C overnight under

nitrogen protection. The mixture was evaporated by rotovap and the residue was subjected to column chromatography on silica gel, eluting with hexane to yield a yellow crystalline product. 90%. ^{1}H NMR (400 MHz, $CDCl_3$) δ (ppm) 8.567 (d, J = 9.2, 1H), 8.228 – 8.002 (overlapping m, 8H), 0.395 (s, 9H).

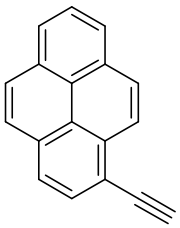

Synthesis of compound 4: This compound was synthesized based on literature methods.[48] The mixture solution of compound **3** (300 mg) and potassium bicarbonate (690 mg) was stirred at room temperature for one hour, the solvent removed, and the crude compound further purified by column chromatography on silica gel, eluting with hexane and dichloromethane mixture (v/v, 10/1). 99%. Since compound **4** is oxygen and light sensitive, it was used directly for next step without any storage.

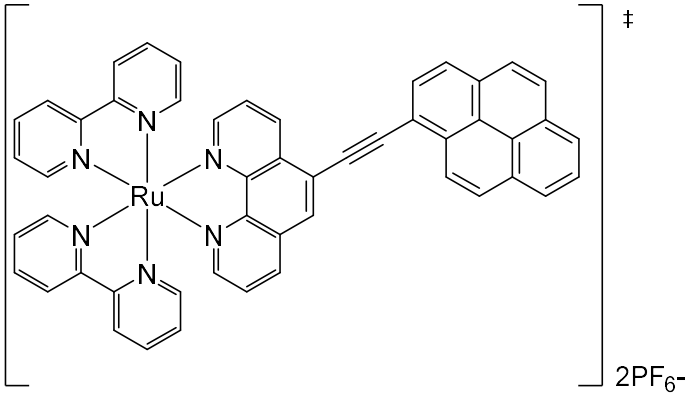

Synthesis of compound RuPy1: This compound was synthesized based on literature methods.[29] Compound **2** (100mg), compound **4** (46 mg), $Pd(PPh_3)_2Cl_2$ (35 mg) and CuI (9.8 mg) were added to a 50 mL round bottom flask. To this flask a mixture of DMF and $HN(i\text{-}Pr)_2$ (10 mL, v/v, 3/2) that has been purged for 2 h with N_2 was added. The solution was stirred under nitrogen protection at room temperature for 24 h. After that, the mixture was filtered and the liquid filtrate was concentrated under reduced pressure. The crude compound was further purified by column chromatography on silica gel with acetonitrile and dichloromethane mixture (v/v, 1/4) as eluent. 75%. ^1H NMR (400 MHz, CD3CN) δ (ppm) 9.130 (d, J = 8.0, 1H), 8.750 (d, J = 9.2, 1H), 8.628~8.527 (m, 6H), 8.393 (m, 3H), 8.297 (d, J = 8.0, 1H), 8.267 (d, J = 7.6, 1H), 8.209 (d, J = 5.2, 1H), 8.167 - 8.020 (overlapping m, 8H), 7.906 (m, 3H), 7.793 (dd, J = 8.4; 5.6 , 1H), 7.680 (d, J = 5.6, 1H), 7.621 (d, J = 6.0, 1H), 7.499 (t, J = 6.4, 2H), 7.303 (quint, 2H). ESI-MS: m/e 963.1 (M - PF6-), 409.1 ([M - 2PF6-]/2). High-Resolution MS: m/e 963.1379 (M - PF6-), 409.0868 ([M - 2PF6-]/2).

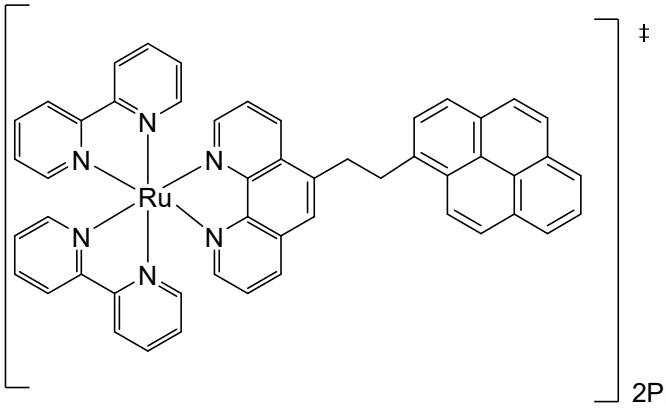

Synthesis of compound RuPy2: RuPy1 (100 mg) and Pd/C (20 mg) as catalyst were added to a 100 mL three-necked round bottom flask under a hydrogen atmosphere. Then, a 2-hour Argon purged ethanol and acetonitrile mixture solvent (v/v, 1/4) were added. The solution was stirred at room temperature for 24 h under hydrogen. After that, the precipitate was removed by filtration (twice) and the liquid filtrate was collected under reduced pressure. The same reduction process was repeated twice to make sure all the **RuPy1** turn to into **RuPy2**. 99%. The product was used directly for ionic exchange. ^{1}H NMR (400 MHz, CD_3CN) δ (ppm) 8.664 (d, *J* = 8.8, 1H), 8.531 (m, 4H), 8.392 (d, *J* = 8.0, 1H), 8.328 (d, *J* = 9.2, 1H), 8.238 (t, *J* = 6.8, 2H), 8.132 – 8.017 (overlapping m, 12H), 7.856 (d, *J* = 5.6, 2H), 7.825 (d, *J* = 8.0, 1H), 7.661 (q, 1H), 7.578 (q, 1H), 7.521 (t, *J* = 6.4, 2H), 7.461 (t, *J* = 7.2, 2H), 7.255 (m, 2H), 3.909 (t, 2H), 3.822 (t, 2H). ESI-MS: m/e 967.1 (M - $PF6^-$), 411.1 ([M - $2PF_6^-$]/2).

Ion exchange of the RuPy1 and 2 hexafluorophosphate salts to chloride salts: The PF_6 salts were dissolved in acetone as concentrated as possible, followed by dropwise addition of a saturated solution of tetra-nbutylammonium chloride (TBACl) in acetone. The orange-red chloride salts was precipitated, collected by centrifuging in several 1.5 mL centrifuge tubes, and washed with large amounts of ethyl acetate to wash away extra TBACl.

Dispersion of SWCNTs: Raw SWCNTs were purified as reported elsewhere.[49] Different amount of purified HiPco (Batch # 195.1) and CoMoCat (Sigman-Aldrich) SWCNTs were weighted in separate vials, followed by addition of 1mg/mL **RuPy1** aqueous solution to give different initial concentration of the nanotube in solution. The resultant mixture was sonicated with a probe sonicator (Sartorius, LABSONIC® M) for 30 min and then centrifuged (VWR centrifugator) for 45 min at 12000 g. The supernatant was collected carefully and diluted for further analysis.

For transient absorption measurements, ~ 0.2-0.3 mg of HiPco and CoMoCat tubes were added to **RuPy1** (2.5×10^{-4} M) and **RuPy2** (5×10^{-4} M) solutions in D_2O respectively. The resulting mixtures were kept in a

temperature-controlled ultrasonic bath for 20 min at 37 kHZ (Elmasonic P120 H, pulse mode). The dispersions were centrifuged at 12000 g for 45 min to remove large bundles. The sonication/centrifugation steps were repeated once again with the addition of nanotubes to enrich the amount of dispersed SWCNTs as previously described.[20] Finally, the dispersion of centrifuged nanotubes was used for transient absorption measurements. Transmission electron microscopy measurement showed debundled SWCNTs of comparable diameter (ca. 2.1-2.4 nm) by both tip sonication and bath sonication procedures.

Dialysis: For UV-Vis and fluorescence experiments the free ruthenium complexes were removed by dialysis. The dialysis procedure was performed using Nominal MWCO 2000 membranes (Cellu Sep H1 and part # 5-0250-28). 3 mL of the dispersed nanotubes solution were added to the dialysis membrane. Either side of the membrane was sealed by a dialysis tubing clip. The membrane bag was stirred gently in HPLC grade water, which was changed every 8 h. After 24 h, the **RuPy 1**/SWCNT composites solution was removed from the dialysis membrane and centrifuged again for 45 minutes at 12000 g. The supernatant was collected and used in the experiments.

AFM and TEM Sample Preparation: For AFM (Digital instrument nanoscope) a **RuPy1**/SWCNT composites solution (HiPco and CoMoCat) was diluted 10 times and 10 μL of the solution was drop casted on freshly cleaved mica and spin coated at 4000 rpm for 15 min. During spinning, the sample was washed with 4-5 drops of methanol to remove excess Ru-complexes. To prepare the TEM sample, diluted **RuPy1**/SWCNT solutions were drop casted on lacey carbon grid and dried overnight. Jeol 2100 field emission gun (FEG) TEM was used to visualize the nanotubes.

4.5 Supporting Information

3.5.1 Characterization data

Figure S1. 1mg/mL **RuPy1** and **RuPy2** aqueous solutions and dispersions with SWNCTs. (1) 1 mg/mL **RuPy1** in water solution; (2) 1 mg/mL **RuPy1** with 1 mg/mL HiPco SWCNTs in water solution before dialysis; (3) 1 mg/mL **RuPy1** and 1 mg/mL HiPco SWCNTs in water solution after dialysis for 16 h; (4) 1 mg/mL **RuPy2** in water solution; (5) 1 mg/mL **RuPy2** and 1 mg/mL HiPco SWCNTs in water solution before dialysis; (6) 1 mg/mL **RuPy2** and 1 mg/mL HiPco SWCNTs in water solution after dialysis for 16 h.

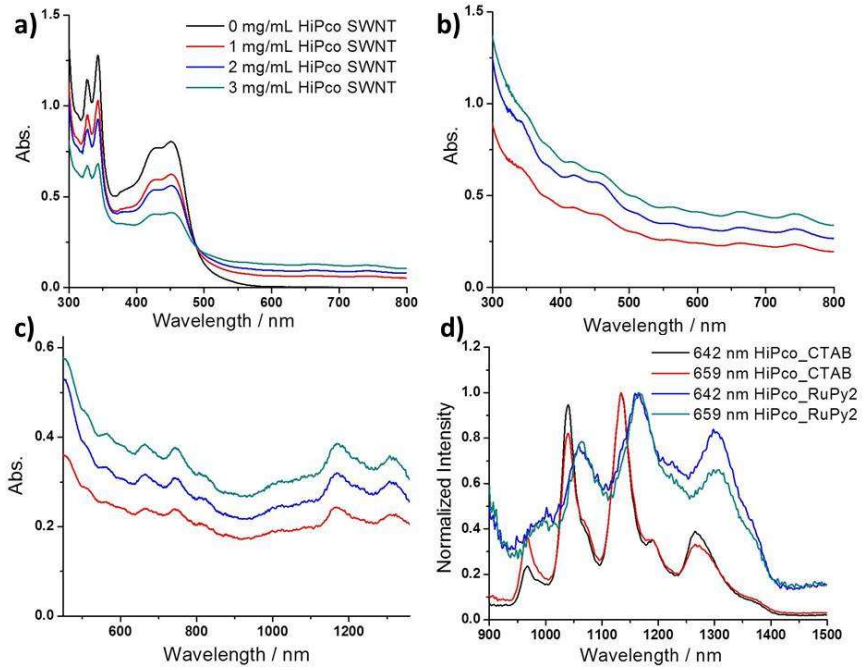

Figure S2. UV-Vis absorption spectra of **RuPy2** and HiPco SWCNT composites in aqueous solution before (a) and after (b) dialysis for 16 h using nominal 2000 MW membrane. Dispersion solutions were prepared by 1 mg/mL **RuPy2** with initial concentration of HiPco 0 mg/mL (black line), 1 mg/mL (red spectra), 2 mg/mL (blue spectra) and 3 mg/mL (cyan spectra), HiPco SWCNTs respectively (20× dilution for (a) and 5× dilution for (b) before taking the spectra); c) Visible-NIR absorption spectra of **RuPy2** and HiPco SWCNT composites in aqueous solution (5× dilution before taking the spectra). d) Normalized NIR-photoluminescence spectra of HiPco SWCNTs dispersed using **RuPy2** aqueous solution and CTAB surfactants.

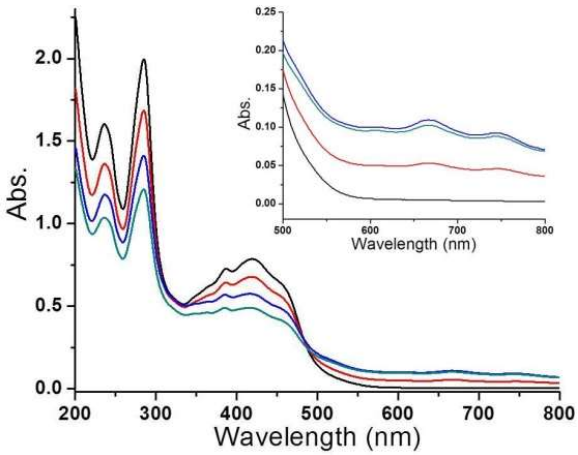

Figure S3. UV-Vis absorption spectra of **RuPy1** and CoMoCat SWCNTs composites in aqueous solution. Dispersion were prepared by using 1 mg/mL **RuPy1** with initial concentration of 0 (black spectra), 1mg/mL (red spectra), 2 mg/mL (blue spectra) and 3 mg/mL (cyan spectra), CoMoCat SWCNTs respectively. All the solutions were diluted to 2.5% before taking the spectra.

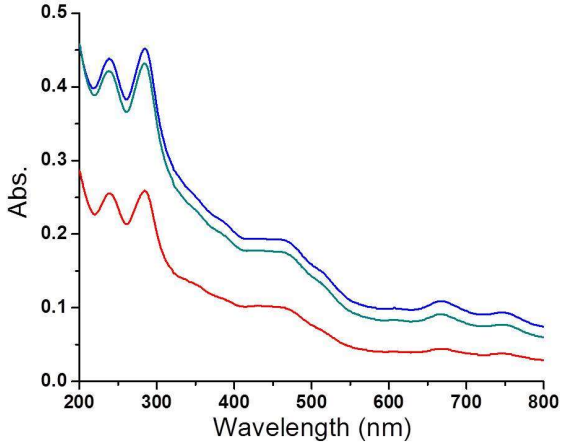

Figure S4. UV-Vis absorption spectra of **RuPy1** and CoMoCat SWCNTs composites in aqueous solution after dialysis for 16 h using nominal 2000 MW membrane. Dispersions were prepared by using 1 mg/mL **RuPy1** with initial amounts of 1 mg/mL (red spectra), 2 mg/mL (blue spectra) and 3 mg/mL (cyan

spectra), of CoMoCat SWCNTs respectively. All the solutions were diluted to 2.5% before taking the spectra.

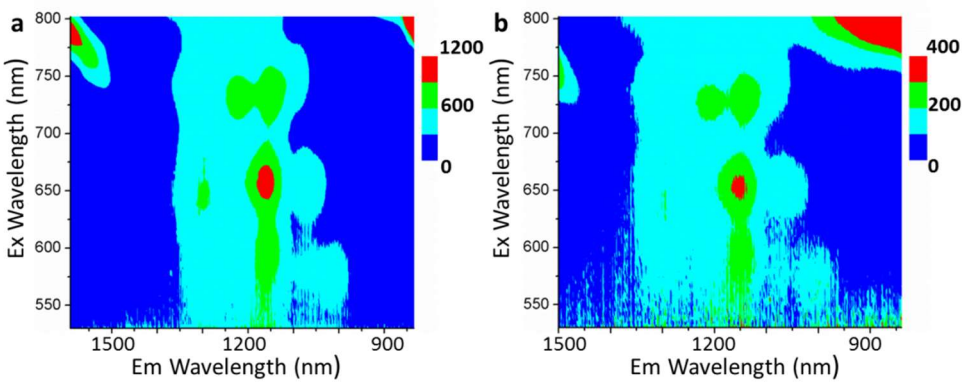

Figure S5. 3D steady-state photoluminescence spectra of (a) **RuPy1**/HiPco SWCNTs, (b) **RuPy2**/ HiPco SWCNTs in D_2O.

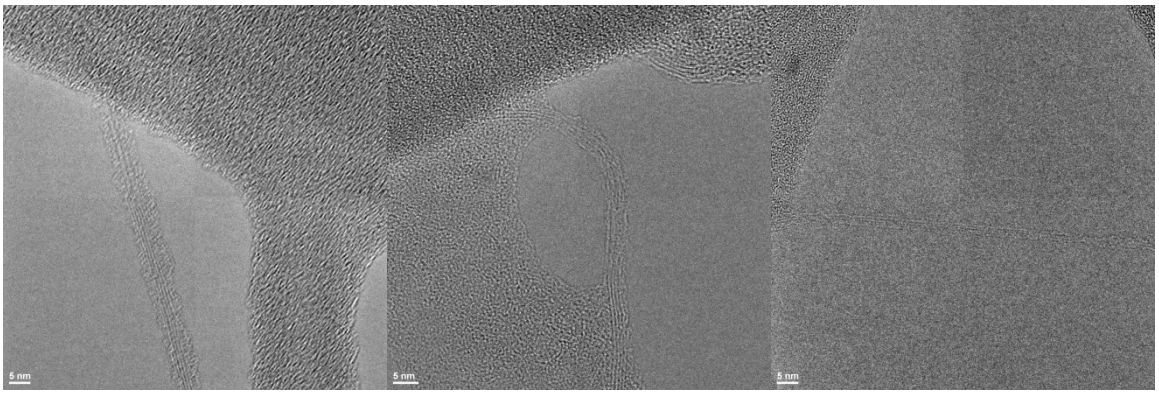

Figure S6. Representative TEM images of HiPco SWCNTs dispersed in **RuPy1** aqueous solution.

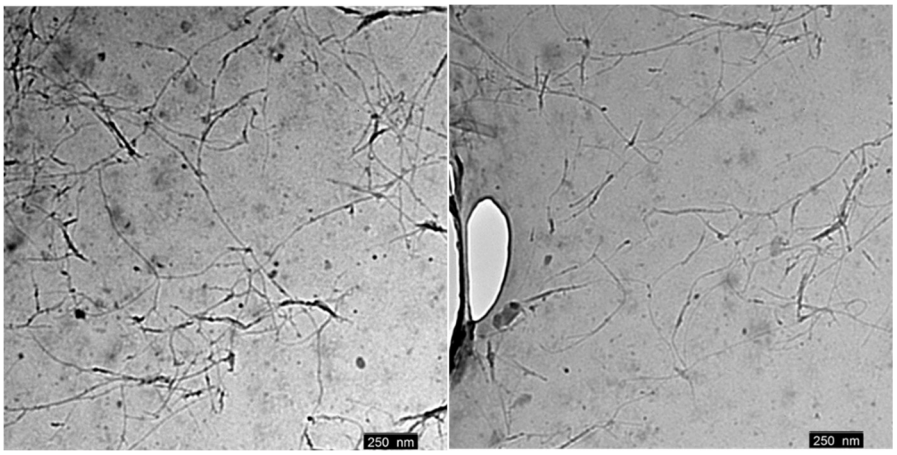

Figure S7. Representative TEM images of HiPco SWCNTs dispersed in **RuPy2** aqueous solution.

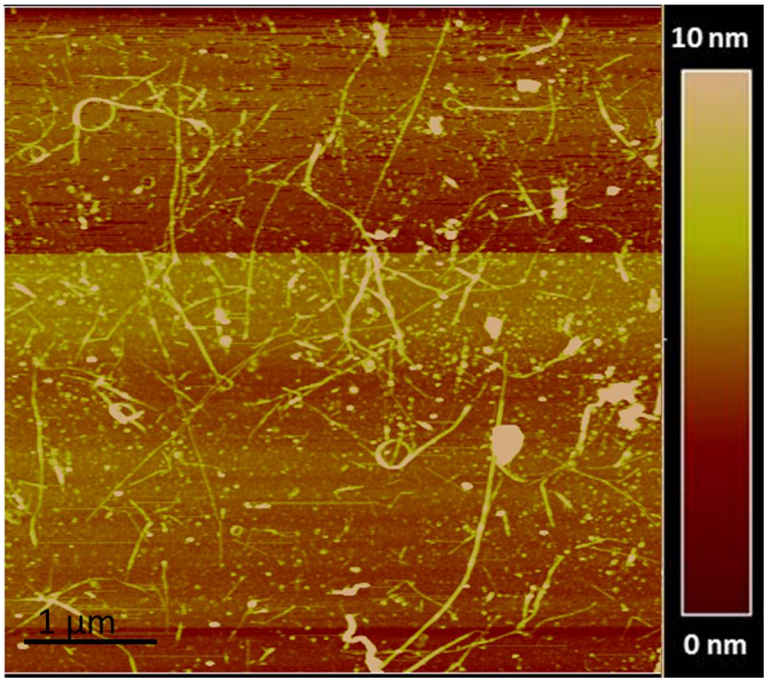

Figure S8. Representative AFM images of CoMoCat SWCNTs dispersed in **RuPy1** aqueous solution.

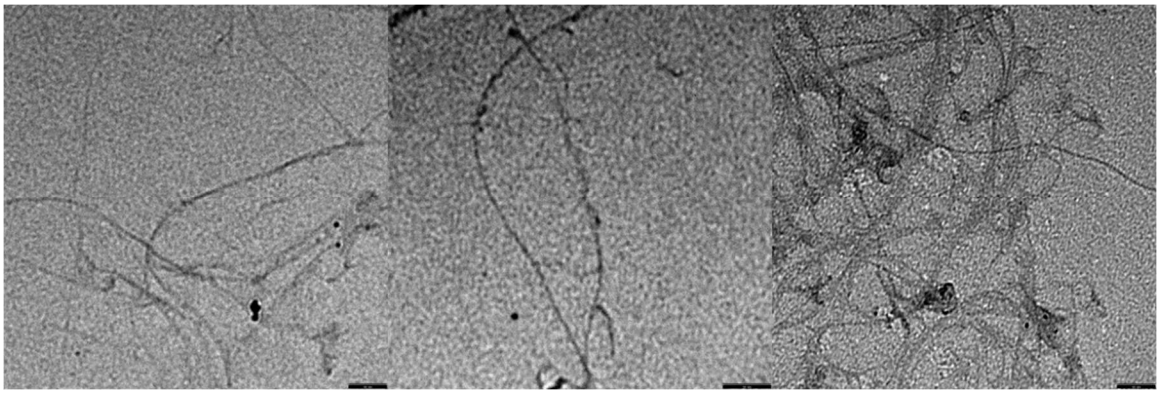

Figure S9. Representative TEM images of CoMoCat SWCNTs dispersed in **RuPy1** aqueous solution.

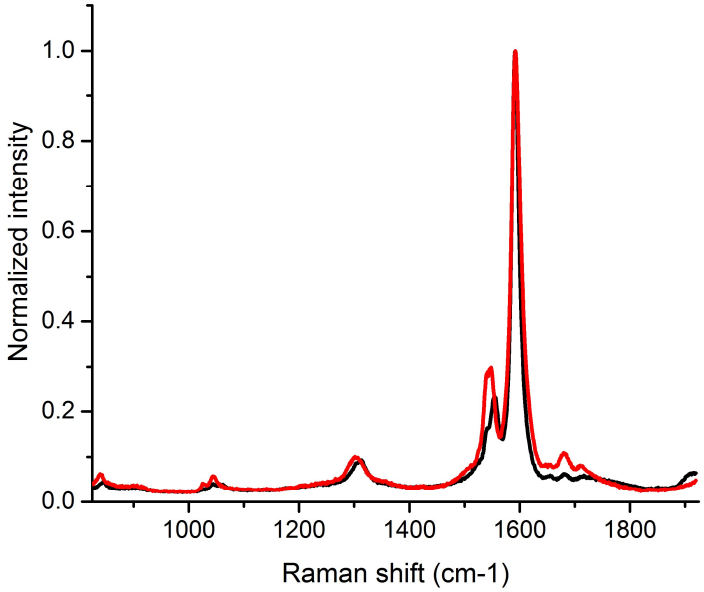

Figure S10. (a) Representative Raman spectra of **RuPy1**/HiPco SWCNTs (black spectrum) and **RuPy1**/CoMoCat SWCNTs (red spectrum) on silicon wafer. Spectra were taken upon 633 nm excitation.

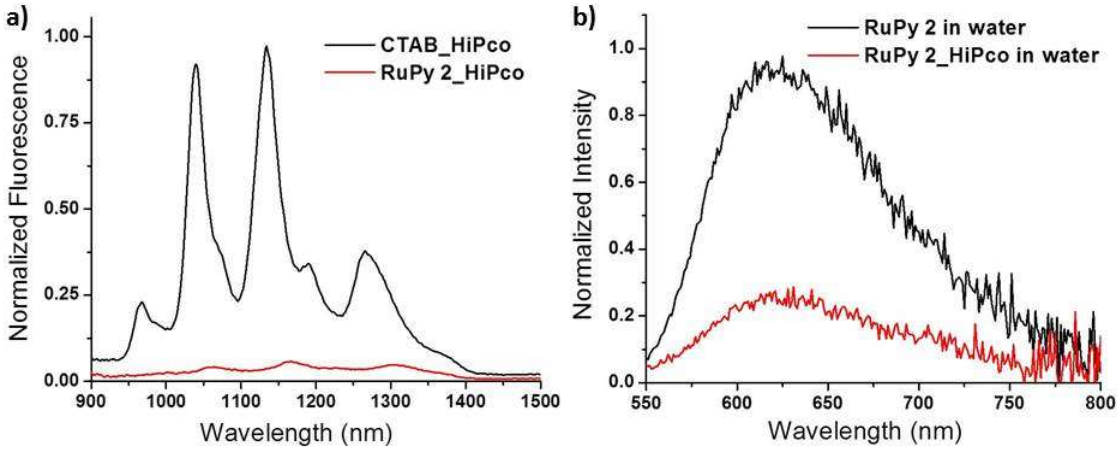

Figure S11. (a) The NIR photoluminescence of CTAB/HiPco SWCNTs (black line) and **RuPy2**/HiPco SWCNTs (red line) in aqueous solution (same concentration of HiPco in water, λ_{ex} = 642 nm); (b) The steady-state photoluminescence of **RuPy2** (black line), **RuPy2**/HiPco SWCNTs (red line) in aqueous solution (same concentration of **RuPy2** in water, λ_{ex} = 420 nm).

3.5.2 Time-resolved photoluminescence, Transient Absorption and Spectroelectrochemical data

Table S1. Photophysical properties of **RuPy1** and **RuPy2** complexes.

	λ_{abs}/nm	λ_{em}/nm	$\varepsilon/M^{-1}cm^{-1}$	$\tau/\mu s$
RuPy1	419	628, 679, 744	33407	665.1[a]
RuPy2	452	616	16009	12.23[b]

a. Results were obtained in deaerated aqueous solution using µF 920H lamp with excitation at 420 nm and un-Cooled Blue as detector for **RuPy1.** Average lifetime, lifetime distributions of **RuPy1**: 734.6 µs (90.18%), 38.6µs (6.65%), 1.8 µs (3.17%).

b. Results was obtained in deaerated aqueous solution using a 440 nm picosecond pulse diode laser and a high speed red detector for **RuPy2**. Average lifetime, lifetime distributions of **RuPy2**: 12826.90 ns (94.88%), 1142.11 ns (5.12%).

Table S2. Lifetime of 1mg/mL **RuPy1** complexes with different concentration of HiPco SWCNTs in deaerated water solution before and after dialysis.

	Lifetime/μs	
Initial HiPco Conc.	Before Dialyais	After Dialysis
0 mg/mL	665.1 (average)	
	734.6 (90.18%) 38.6 (6.65%) 1.8 (3.17%)	
1 mg/mL	615.9 (average)	532.6 (average)
	665.6 (92.20%) 37.8 (6.08%) 1.9 (1.72%)	605.4 (87.83%) 12.9 (5.67%) 1.3 (6.50%)
2 mg/mL	760.7 (average)	382.8 (average)
	826.7 (91.65%) 42.5 (7.02%) 2.0 (1.33%)	442.1 (86.36%) 16.8 (4.96%) 1.8 (8.68%)
3 mg/mL	792.6 (average)	513.7 (average)
	870.9 (90.59%)	599.3 (85.54%)

	44.8 (8.22%) 2.4 (1.19%)	13.5 (7.05%) 1.4 (7.40%)

Table S3. Lifetime of ground state bleaching of - HiPco and CoMoCat SWCNTs (in NIR region) dispersed by CTAB, **RuPy1**, and **RuPy2** in deaerated D_2O, from femto-second pump probe experiments (percentage of each component shown in parenthesis).

	Wavelength (nm)	τ_1 (ps)	τ_2 (ps)	τ_3 (ps)
CTAB/HiPco	989	3.5 (5.4%)	15.4 (15.6%)	166.1(79.0%)
	1135	1.7 (6.4%)	23.8 (22.5%)	142.5 (71.1%)
CTAB/CoMoCat	993	2.2 (6.8%)	26.1 (19.2%)	174.9 (74.0%)
	1149	3.1 (12.6%)	45.5 (49.5%)	170.5 (37.9%)
RuPy1/HiPco	1000	2.3 (12.5%)	25.3 (27.1%)	136.1 (60.4%)
	1149	2.6 (12.1%)	36.4 (39.1%)	169.6 (48.8%)
RuPy2/HiPco	1000	2.3 (45.3%)	29.8 (36.1%)	102.0 (18.6%)
	1149	3.8 (19.1%)	36.1 (54.1%)	81.9 (26.8%)
RuPy1/CoMoCat	1010	2.4 (13.5%)	18.7 (21.3%)	136.5 (65.2%)
	1149	2.6 (24.9%)	44.3 (75.1%)	-
RuPy2/CoMoCat	1010	2.4 (19.6%)	17.1 (29.3%)	95.6 (51.1%)
	1149	2.0 (25.6%)	44.1 (74.4%)	-

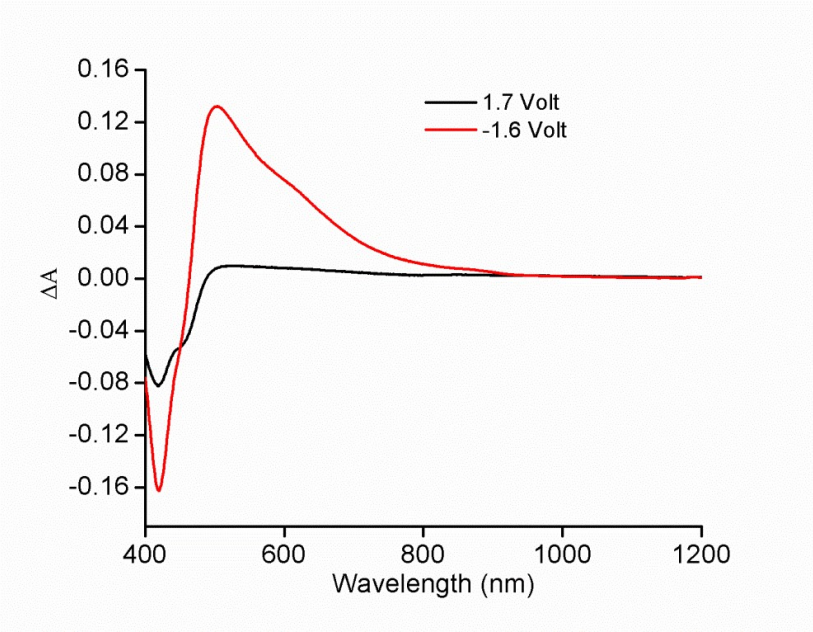

Figure S12. Differential absorption changes upon oxidation (black spectrum) and reduction (red spectrum) of **RuPy 1** in D_2O (0.2 M tetrabutylammonium hexafluorophosphate supporting electrolyte, potentials with regards to Ag wire).

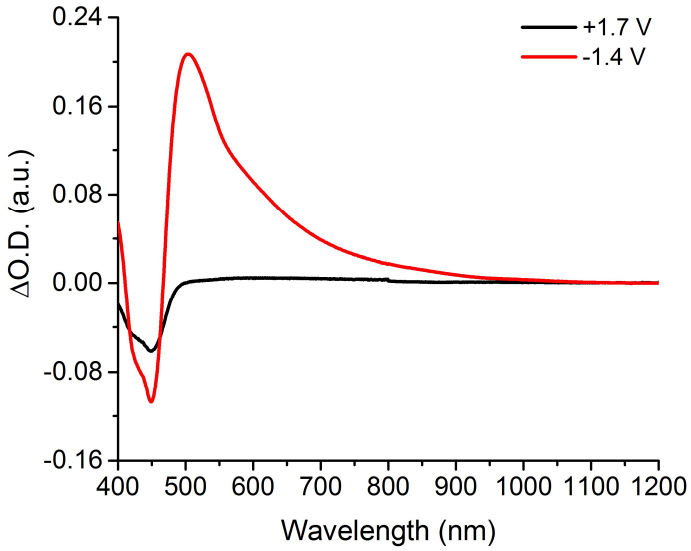

Figure S13. Differential absorption changes upon oxidation (black spectrum) and reduction (red spectrum) of **RuPy 2** in D_2O (0.2 M tetrabutylammonium hexafluorophosphate supporting electrolyte, potentials with regards to Ag wire).

3.5.3 Appendix 1. FRET efficiency for the FRET couple RuPy 1 and (6,5) SWCNTs.

To answer the question of whether quenching is due to FRET or electron transfer one can calculate the rate of FRET. This can be done by making some assumptions about our system. FRET rate constant can be calculated from:

$$k_{FRET}(r) = \frac{1}{\tau_D}\left(\frac{R_0}{r}\right)^6 \qquad (1)$$

where τ_D is the donor's lifetime, r is the distance between the donor and acceptor and R_0 is given by:

$$R_0^6 = \frac{9000(\ln 10)\kappa^2\phi J}{128\pi^5\eta^4 N_{Av}} \qquad (2)$$

R_0 is the Förster distance (the distance at which half of the donor excitation is transferred to the acceptor), κ^2 is the orientation factor (usually 2/3 for free molecules in solution), ϕ is the quantum yield of the donor, J is the spectral overlap constant, which describes the overlap between the donor emission spectrum and the acceptor absorption spectrum, N_{Av} is the Avogadro's number and η is the refractive index of the medium (~1.3).

Thus, the first we need to estimate is the distance between RuPy1 and the carbon nanotube, in this case a (6,5) CoMoCat SWCNT. Since the Ruthenium polypyridine part of the molecule has a charge of +2, it is reasonable to think that it will try to stay as retired from the hydrophobic surface of the carbon nanotube as possible. Also, we can assume as well that the hydrophobic pyrene group would try to have most of its surface in contact with the walls of SWCNTs. Therefore, if we put pyrene in van der Waals contact with SWCNTs, with the long axis of the molecule running along the carbon nanotube length, we get Figure A.

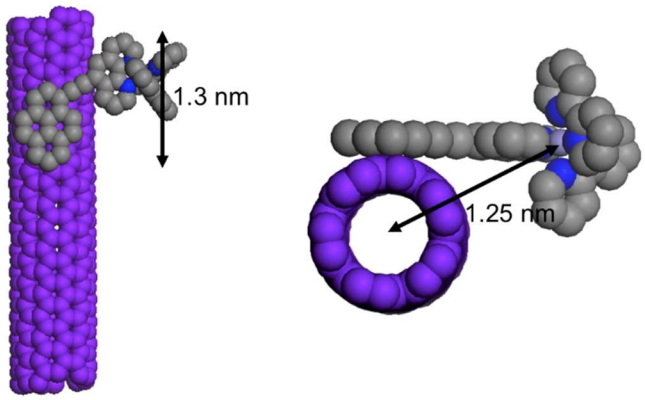

Figure S14. Structural model of the interaction between RuPy 1 and a (6,5) SWNCT. The distance from the ruthenium polypyridyl complex and the center of the SWCNT is about 1.25 nm.

The calculated lifetime of RuPy1 is 665 μs. If we calculate R_0, then the rate of FRET can be calculated at different distances. Our experiments show that the quantum yield of RuPy1 is nitrogen purged acetonitrile is 0.027 and the refractive

index of the medium was 1.3. To calculate J we need to have an idea of the extinction coefficient of SWCNTs. Hertel et al. calculated an extinction coefficient for the S_2 transition of (6,5) SWCNTs (band at ca. 991 nm) of 4400 M^{-1} cm^{-1} per carbon atom. From Figure A, we can estimate that the projection of RuPy1 on the SWCNTs is about 1.3 nm. Therefore, if a (6,5) carbon nanotube has 88 carbons per nm, there are 114 C atoms per RuPy1 length. If FRET is going to occur, it will occur to these carbon atoms close to the ruthenium center rather than carbon atoms farther away. With this information, we calculated an extinction coefficient for the 991 nm transition of (6,5) carbon nanotubes of 501600 $M^{-1}s^{-1}$. The calculation of R_0 is done by normalizing the value of the 991 nm transition to this value and using the spectrum to calculate the overlap integral (*J*). The calculated R_0 is 51.8 Å, and with it, the rate of FRET was calculated using FRETView.[42] The results are shown in Table 1.

Table S4. FRET parameters for the interaction of **RuPy 1** and (6,5) SWCNTs.

r (Å)	E	k_{FRET} (s^{-1})	$\tau_{acceptor}$
8	1	1.10E+08	9.04 ns
9	1	5.50E+07	18.27 ns
10	1	2.90E+07	34.4 ns
11	1	1.60E+07	60.96 ns
12	1	9.70E+06	102.78 ns

13	1	6.00E+06	166.12 ns
14	1	3.90E+06	259.11 ns
15	0.999	2.60E+06	391.89 ns
16	0.999	1.70E+06	577 ns
17	0.999	1.20E+06	829.84 ns
18	0.998	8.50E+05	1.17 us
19	0.998	6.20E+05	1.62 us
20	0.997	4.50E+05	2.2 us
21	0.996	3.40E+05	2.94 us
22	0.994	2.60E+05	3.88 us
23	0.992	2.00E+05	5.06 us
24	0.99	1.50E+05	6.51 us
25	0.988	1.20E+05	8.3 us
26	0.984	9.40E+04	10.47 us
27	0.98	7.50E+04	13.07 us
28	0.976	6.00E+04	16.18 us
29	0.97	4.90E+04	19.86 us
30	0.964	4.00E+04	24.18 us
31	0.956	3.30E+04	29.21 us
32	0.947	2.70E+04	35.01 us
33	0.937	2.20E+04	41.67 us
34	0.926	1.90E+04	49.24 us
35	0.913	1.60E+04	57.78 us

36	0.899	1.30E+04	67.34 us
37	0.883	1.10E+04	77.96 us
38	0.865	9.60E+03	89.67 us
39	0.846	8.30E+03	102.46 us
40	0.825	7.10E+03	116.33 us
41	0.803	6.10E+03	131.24 us
42	0.779	5.30E+03	147.14 us
43	0.753	4.60E+03	163.95 us
44	0.727	4.00E+03	181.58 us
45	0.699	3.50E+03	199.91 us
46	0.671	3.10E+03	218.82 us
47	0.642	2.70E+03	238.16 us
48	0.612	2.40E+03	257.8 us
49	0.583	2.10E+03	277.58 us
50	0.553	1.90E+03	297.35 us
51	0.523	1.70E+03	316.99 us
52	0.494	1.50E+03	336.34 us
53	0.466	1.30E+03	355.31 us
54	0.438	1.20E+03	373.78 us
55	0.411	1.00E+03	391.66 us
56	0.385	9.40E+02	408.88 us
57	0.36	8.50E+02	425.39 us
58	0.337	7.60E+02	441.14 us

59	0.314	6.90E+02	456.1 us
60	0.293	6.20E+02	470.27 us
61	0.273	5.60E+02	483.65 us
62	0.254	5.10E+02	496.23 us
63	0.236	4.60E+02	508.03 us
64	0.219	4.20E+02	519.08 us
65	0.204	3.90E+02	529.39 us
66	0.189	3.50E+02	539.02 us
67	0.176	3.20E+02	547.97 us
68	0.163	2.90E+02	556.3 us
69	0.152	2.70E+02	564.03 us
70	0.141	2.50E+02	571.2 us
71	0.131	2.30E+02	577.85 us
72	0.122	2.10E+02	584.01 us
73	0.113	1.90E+02	589.72 us
74	0.105	1.80E+02	595 us
75	0.098	1.60E+02	599.89 us
76	0.091	1.50E+02	604.41 us
77	0.085	1.40E+02	608.59 us
78	0.079	1.30E+02	612.46 us
79	0.074	1.20E+02	616.04 us
80	0.069	1.10E+02	619.36 us

3.6 Acknowledgments

A. A. M. thanks the Welch foundation, grant C-1743 for financial support. We acknowledge Leonie Wibmer (Friedrich-Alexander-Universität Erlangen-Nürnberg) for recording Raman spectra.

3.7 Contributions

I synthesized the starting materials **1**, **3**, and **4** and perfected the conditions. When more samples were needed, I synthesized more of the starting materials.

3.8 References

1. Iijima, S. Helical Microtubules of Graphitic Carbon. *Nature* **1991**, *354*, 56-58.

2. Bartelmess, J.; Ballesteros, B.; de la Torre, G.; Kiessling, D.; Campidelli, S.; Prato, M.; Torres, T.; Guldi, D. M. Phthalocyanine-Pyrene Conjugates: A Powerful Approach toward Carbon Nanotube Solar Cells. *J. Am. Chem. Soc.* **2010**, *132*, 16202-16211.

3. Jung, Y.; Li, X.; Rajan, N. K.; Taylor, A. D.; Reed, M. A. Record High Efficiency Single-Walled Carbon Nanotube/Silicon P–N Junction Solar Cells. *Nano Lett.* **2013**, *13*, 95-99.

4. Tune, D. D.; Shapter, J. G. The Potential Sunlight Harvesting Efficiency of Carbon Nanotube Solar Cells. *Energy & Environ. Sci.* **2013**, *6*, 2572-2577.

5. Lau, R. H.; Takei, K.; Wang, C.; Ju, Y.; Kim, J.; Yu, Z.; Takahashi, T.; Cho, G.; Javey, A. Fully Printed, High Performance Carbon Nanotube Thin-Film Transistors on Flexible Substrates. *Nano Lett.* **2013**, *13*, 3864-3869.

6. Xu, F.; Wu, M.-Y.; Safron, N. S.; roy, S. S.; Jacobberger, R. M.; Bindi, D. J.; Seo, J.-H.; Chang, T.-H.; Ma, Z.; Arnold, M. S. Highly Stretchable Carbon Nanotube Transistors with Ion Gel Gate Dielectrics. *Nano Lett.* **2014**, *14*, 682-686.

7. Nasibulin, A. G.; Kaskela, A.; Mustonen, F.; Anisimov, A. S.; Ruiz, V.; Kivistö, S.; Rackauskas, S.; Timmermans, M. Y.; Pudas, M.; Aitchison, B.; Kauppinen, M.; Brown, D. P.; Okhotnikov, O. G.; Kauppinen, E. I. Multifunctional Free-Standing Single-Walled Carbon Nanotube Films. *ACS Nano* **2011**, *5*, 3214-3221.

8. Saha, A.; Ghosh, S.; Weisman, R. B.; Martí, A. A. Films of Bare Single-Walled Carbon Nanotubes from Superacids with Tailored Electronic and Photoluminescence Properties. . *ACS Nano* **2012**, *6*, 5727-5734.

9. Rösner, B.; Guldi, D. M.; Chen, J.; Minett, A. I.; Fink, R. H. Dispersion and Characterization of Arc Discharge Single-Walled Carbon Nanotubes – Towards Conducting Transparent Films *Nanoscale* **2014**, *6*, 3695-3703.

10. Behabtu, N.; Young, C. C.; Tsentalovich, D. E.; Kleinerman, O.; Wang, X.; Ma, A. W. K.; Bengio, A.; ter Waarbeek, R. F.; de Jong, J. J.; Hoogerwerf, R. E.; Fairchild, S. B.; Ferguson, J. B.; Maruyama, B.; Kono, J.; Talmon, Y.; Cohen, Y.; Otto, M. J.; Pasquali, M. Strong, Light, Multifunctional Fibers of Carbon Nanotubes with Ultrahigh Conductivity. *Science* **2013**, *339*, 182-186.

11. Jiang, C.; Saha, A.; Young, C. C.; Hashim, D. P.; Ramirez, C. E.; Ajayan, P. M.; Pasquali, M.; Martí, A. A. Macroscopic Nanotube Fibers Spun from Single-Walled Carbon Nanotube Polyelectrolytes. *ACS Nano* **2014**, *8*, 9107-9112.

12. Leonard, A. D.; Hudson, J. L.; Fan, H.; Booker, R.; Simpson, L. J.; O'Neill, K. J.; Parilla, P. A.; Heben, M. J.; Pasquali, M.; Kittrell, C.; Tour, J. M. Nanoengineered Carbon Scaffolds for Hydrogen Storage. *J. Am. Chem. Soc.* **2009**, *131*, 723-728.

13. Guldi, D. M.; Rahman, G. M. A.; Jux, N.; Tagmatarchis, N.; Prato, M. Integrating Single-Wall Carbon Nanotubes into Donor–Acceptor Nanohybrids. *Angew. Chem. Int. Ed.* **2004**, *43*, 5526-5530.

14. Jiang, C.; Saha, A.; Changsheng, X.; Young, C.; Tour, J. M.; Pasquali, M.; Martí, A. A. Increased Solubility, Liquid-Crystalline Phase, and Selective Functionalization of Single-Walled Carbon Nanotube Polyelectrolyte Dispersions. *ACS Nano* **2013**, *7*, 4503-4510.

15. Saha, A.; Ghosh, S.; Behabtu, N.; Pasquali, M.; Martí, A. A. Single-Walled Carbon Nanotubes Shell Decoration Porous Silicate Materials: A General Platform for Studying the Interaction of Carbon Nanotubes with Photoactive Molecules. *Chem. Sci.* **2011**, *2*, 1682-1687.

16. Jain, D.; Saha, A.; Martí, A. A. Non-Covalent Ruthenium Polypyridyl Complexes-Carbon Nanotubes Composites: An Alternative for Functional Dissolution of Carbon Nanotubes in Solution. *Chem. Commun.* **2011**, *47*, 2246-2248.

17. Chen, Z.; Kobashi, K.; Rauwald, U.; Booker, R.; Fan, H.; Hwang, W.-F.; Tour, J. M. Soluble Ultra-Short Single-Walled Carbon Nanotubes. *J. Am. Chem. Soc.* **2006**, *128*, 10568-10571.

18. Hof, F.; Bosch, S.; Eigler, S.; Hauke, F.; Hirsch, A. New Basic Insight into Reductive Functionalization Sequences of Single Walled Carbon Nanotubes (Swcnts). *J. Am. Chem. Soc.* **2013**, *135*, 18385-18395.

19. Zhao, Y.-L.; Stoddart, J. F. Noncovalent Functionalization of Single-Walled Carbon Nanotubes. *Acc. Chem. Res.* **2009**, *42*, 1161-1171.

20. Romero-Nieto, C.; García, R.; Herranz, M. A.; Ehli, C.; Ruppert, M.; Hirsch, A.; Guldi, D. M.; Martín, N. Tetrathiafulvalene-Based Nanotweezers—Noncovalent Binding of Carbon Nanotubes in Aqueous Media with Charge Transfer Implications. *J. Am. Chem. Soc.* **2012**, *134*, 9183-9192.

21. Olson, E. J. C.; Hu, D.; Hörmann, A.; Jonkman, A. M.; Arkin, M. R.; Stemp, E. D. A.; Barton, J. K.; Barbara, P. F. First Observation of the Key Intermediate in the "Light-Switch" Mechanism of $[Ru(Phen)_2dppz]^{2+}$. *J. Am. Chem. Soc.* **1997**, *119*, 11458-11467.

22. Olofsson, J.; Önfelt, B.; Lincoln, P.; Nordén, B.; Matousek, P.; Parker, A. W.; Tuite, E. Picosecond Kerr-Gated Time-Resolved Resonance Raman Spectroscopy of the $[Ru(Phen)_2dppz]^{2+}$ Interaction with DNA. *J. Inorg. Biochem.* **2002**, *91*, 286-297.

23. Monro, S.; Scott, J.; Chouai, A.; Lincoln, R.; Zong, R.; Thummel, R. P.; McFarland, S. A. Photobiological Activity of Ru(Ii) Dyads Based on (Pyren-1-Yl)Ethynyl Derivatives of 1,10-Phenanthroline. *Inorg. Chem.* **2010**, *49*, 2889-2900.

24. Gómez, F. J.; Chen, R. J.; Wang, D.; Waymouth, R. M.; Dai, H. Ring Opening Metathesis Polymerization on Non-Covalently Functionalized Single-Walled Carbon Nanotubes *Chem. Commun.* **2003**, 190-191.

25. Ehli, C.; Rahman, G. M. A.; Jux, N.; Balbinot, D.; Guldi, D. M.; Paolucci, F.; Marcaccio, M.; Paolucci, D.; Melle-Franco, M.; Zerbetto, F.; Campidelli, S.; Prato, M. Interactions in Single Wall Carbon Nanotubes/Pyrene/Porphyrin Nanohybrids. *J. Am. Chem. Soc.* **2006**, *128*, 11222-11231.

26. Zhao, Y.-L.; Hu, L.; Stoddart, J. F.; Grüner, G. Pyrenecyclodextrin-Decorated Single-Walled Carbon Nanotube Field-Effect Transistors as Chemical Sensors. *Adv. Mater.* **2008**, *20*, 1910-1915.

27. D'Souza, F.; Sandanayaka, A. S. D.; Ito, O. Swnt-Based Supramolecular Nanoarchitectures with Photosensitizing Donor and Acceptor Molecules. *J. Phys. Chem. Lett.* **2010**, *1*, 2586-2593.

28. Yu, M.; Zu, S.-Z.; Chen, Y.; Liu, Y.-P.; Han, B.-H.; Liu, -. Y. Spatially Controllable DNA Condensation by a Water-Soluble Supramolecular Hybrid of Single-Walled Carbon Nanotubes and B-Cyclodextrin-Tethered Ruthenium Complexes. *Chem. Eur. J.* **2009**, *16*, 1168-1174.

29. Ji, S.; Wu, W.; Wu, W.; Song, P.; Han, K.; Wang, Z.; Liu, S.; Guo, H.; Zhao, J. Tuning the Luminescence Lifetimes of Ruthenium(Ii) Polypyridine Complexes and Its Application in Luminescent Oxygen Sensing. *J. Mater. Chem.* **2010**, *20*, 1953-1963.

30. Ji, S.; Wu, W.; Wu, W.; Guo, H.; Zhao, J. Ruthenium(Ii) Polyimine Complexes with a Long-Lived 3il Excited State or a 3mlct/3il Equilibrium: Efficient Triplet Sensitizers for Low-Power Upconversion. *Angew. Chem. Int. Ed.* **2011**, *50*, 1626-1629.

31. Kalyanasundaram, K. Photophysics, Photochemistry and Solar Energy Conversion with Tris(Bipyridyl)Ruthenium(Ii) and Its Analogues. *Coord. Chem. Rev.* **1982**, *46*, 159-244.

32. Kalyanasundaram, K. *Photochemistry of Polypyridine and Phorphyrin Complexes*. Academic Press: London, 1992.

33. McClenaghan, N. D.; Leydet, Y.; Maubert, B.; Indelli, M. T.; Campagna, S. Excited-State Equilibration: A Process Leading to Long-Lived Metal-to-Ligand Charge Transfer Luminescence in Supramolecular Systems. *Coord. Chem. Rev.* **2005**, *249*, 1336-1350.

34. Hissler, M.; Harriman, A.; Khatyr, A.; Ziessel, R. Intramolecular Triplet Energy Transfer in Pyrene ± Metal Polypyridine Dyads: A Strategy for Extending the Triplet Lifetime of the Metal Complex. *Chem. Eur. J.* **1999**, *5*, 3366-3381.

35. Tyson, D. S.; Henbest, K. B.; Bialecki, J.; Castellano, F. N. Excited State Processes in Ruthenium(Ii)/Pyrenyl Complexes Displaying Extended Lifetimes. *J. Phys. Chem. A* **2001**, *105*, 8154-8161.

36. Wilson, G. J.; Launikonis, A.; Sasse, W. H. F.; Mau, A. W.-H. Excited-State Processes in Ruthenium(Ii) Bipyridine Complexes Containing Covalently Bound Arenes. *J. Phys. Chem. A* **1997**, *101*, 4860-4866.

37. Lefebvre, J.; Finnie, P. Photoluminescence and Förster Resonance Energy Transfer in Elemental Bundles of Single-Walled Carbon Nanotubes. *J. Phys. Chem. C* **2009**, *113*, 7536-7540.

38. Torrens, O. N.; Milkie, D. E.; Zheng, M.; Diddawa, J. M. Photoluminescence from Intertube Carrier Migration in Single-Walled Carbon Nanotube Bundles. *Nano Lett.* **2006**, *6*, 2864-2867.

39. Khairoutdinov, R. F.; Doubova, L. V.; Haddon, R. C.; Saraf, L. Persistent Photoconductivity in Chemically Modified Single-Wall Carbon Nanotubes. *J. Phys. Chem. B* **2004**, *108*, 19976-19981.

40. Jang, S.-R.; Vittal, R.; Kim, K.-J. Incorporation of Functionalized Single-Wall Carbon Nanotubes in Dye-Sensitized Tio_2 Solar Cells. *Langmuir* **2004**, *20*, 9807-9810.

41. Zhao, Y.-L.; Hu, L.; Grüner, G.; Stoddart, J. F. A Tunable Photosensor. *J. Am. Chem. Soc.* **2008**, *130*, 16996-17003.

42. Stevens, N.; Dyer, J.; Marti, A. A.; Solomon, M.; Turro, N. J. Fretview: A Computer Program to Simplify the Process of Obtaining Fluorescence Resonance Energy Transfer Parameters. *Photochem. Photobiol. Sci.* **2007**, *6*, 909-911.

43. Soler, M.; McCusker, C. E. Distinguishing between Dexter and Rapid Sequential Electron Transfer in Covalently Linked Donor−Acceptor Assemblies. *J. Am. Chem. Soc.* **2008**, *130*, 4708-4724.

44. Yoon, K. B. Electron- and Charge- Transfer Reactions within Zeolites. *Chem. Rev.* **1993**, *93*, 321-339.

45. Youngblood, W. J.; Lee, S.-H. A.; Maeda, K.; Mallouk, T. E. Visible Light Water Splitting Using Dye-Sensitized Oxide Semiconductors. *Acc. Chem. Res.* **2009**, *42*, 1966-1973.

46. Hissler, M.; Connick, W. B.; Geiger, D. K.; McGarrah, J. E.; Lipa, D.; Lachicotte, R. J.; Eisenberg, R. Platinum Diimine Bis(Acetylide) Complexes: Synthesis, Characterization, and Luminescence Properties. *Inorg. Chem.* **2000**, *39*, 447-457.

47. Huang, K.; Martí, A. A. Optimizing the Sensitivity of Photoluminescent Probes Using Time-Resolved Spectroscopy: A Molecular Beacon Case Study. *Anal. Chem.* **2012**, *84*, 8075-8082.

48. Chu, P.-L. E.; Wang, L.-Y.; Khatua, S.; Kolomeisky, A. B.; Link, S.; Tour, J. M. Synthesis and Single-Molecule Imaging of Highly Mobile Adamantane-Wheeled Nanocars. *ACS Nano* **2012**, *7*, 35-41.

49. Chiang, I. W.; Brinson, B. E.; Huang, A. Y.; Willis, P. A.; Bronikowski, M. J.; Margrave, J. L.; Smalley, R. E.; Hauge, R. H. Purification and Characterization of Single-Wall Carbon Nanotubes (Swnts) Obtained from the Gas-Phase Decomposition of Co (Hipco Process). *J. Phys. Chem. B* **2001**, *105*, 8297-8301.

CHAPTER 4

Cyclodextrin Wheeled Nanocars

4.1 Introduction

4.1.1 Cyclodextrins and their Applications

Cyclodextrins (CD) are a class of compounds composed of several glucose units (n > 5) linked together to form a circular structure. The most common unmodified CDs includes α-CD (n = 6), β-CD (n = 7) and γ-CD (n = 8) shown in Figure 4.1.

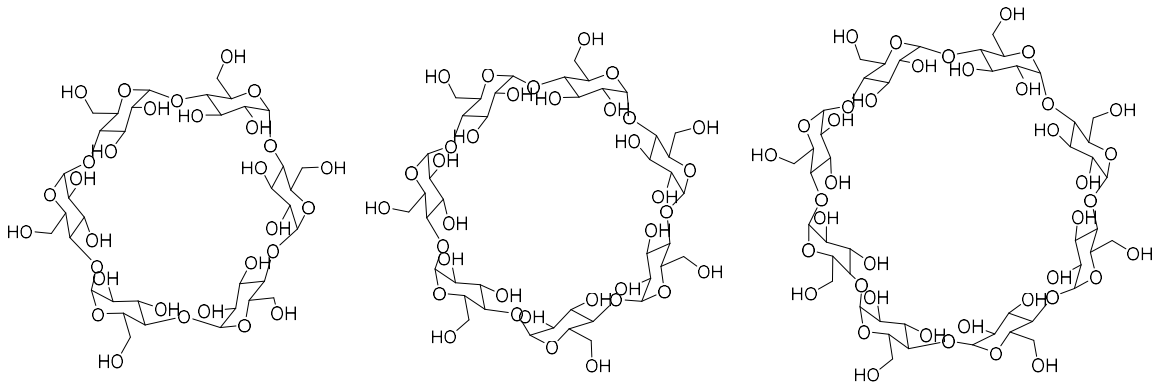

Figure 4.1. Left to right, α-CD, β-CD and γ-CD, with 6, 7 and 8 glucose units, respectively.

Larger CDs are known, but are of relatively low industrial or scientific relevance.[1] CDs can be seen as having a toroidal truncated cone shape, with secondary hydroxyl groups on the narrow rim and primary hydroxyl groups on the wide rim (Figure 4.2).[2]

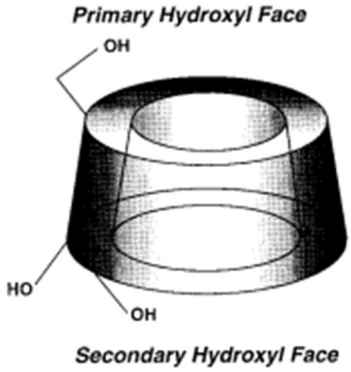

Figure 4.2. Hydroxyls on the rims of cyclodextrin. (Reprinted with permission from the American Chemical Society, 1998).[2]

In contrast the inner cavity is lined with hydrogen and ether oxygen. This unique orientation of the functional groups makes the outer region of CDs hydrophilic; although the inner cavity is not hydrophobic, it is considerably less hydrophilic than the outer region. The orientation of the functional groups and the lack of structural freedom imparts the ability of CDs to accommodate small organic molecules as guests, while lending water solubility to the guest molecules.[3]

Due to the CDs' ability to form host/guest complexes and dramatically improving the water solubility of guest molecules, they are widely applied in pharmaceuticals as a drug delivery method to enhance water solubility of hydrophobic drugs.[4] Hundreds of modified CDs have been synthesized and researched, but only those containing hydroxypropyl,

methyl, and sulfobutyl ether have been commercially used as drug delivery candidates.[5, 6] The advantages of cyclodextrin-complexed drugs are as follows:

1. *Increased aqueous solubility*: When CDs are complexed with poorly-soluble drugs, the resulting complex hides most of the apolar or hydrophobic functional groups in the interior cavity of the CDs, while the hydrophilic exterior rim is exposed to the environment, creating a net effect of aqueous solubility.[7] Although there are many hydroxyl groups on a CD molecule, unmodified CDs are not particularly soluble in water compared to sugars or organic acids and alcohols. Unmodified CDs are also extremely insoluble in most organic solvents (Table 4.1)[8]
2. *Enhanced bioavailability*: Aside from the fact that CDs increases the water solubility of drugs, hence increased oral or rectal absorption, CDs also prevent crystallization of drug molecules by complexation so they can no longer self-assemble into a crystalline lattice[6, 9]
3. *Improvement of stability*: Drugs are often heat or oxygen sensitive. When encapsulated within the cavity of CDs in a solid state, the barrier that the CD molecule makes it harder for reactants such as

oxygen to reach the guest and for chemical reactions to take place[6, 10, 11]

% cosolvent	MeOH	EtOH	dmso	CH_3CN	thf
0	1.60	1.60	1.8	1.60	1.60
10	1.00	1.82	2.0	3.11	2.10
20	0.71	2.01	2.1	3.70	2.20
30	0.50	2.20	2.2	2.60	1.88
40	0.40	1.80	2.7	1.80	1.30
50	0.34	1.30	6.3	0.88	0.90
60	0.26	0.80	16.0	0.30	0.50
65.7			47.0		
70	0.10	0.29		0.10	0.20
72.4			76.5		
80	0.05	0.10		0.05	0.19
81.5			75.0		
90	0.00	0.05	74.5	0.00	0.05
96			73.0		
100	0.00	0.00	50.0	0.00	0.00

Table 4.1. Solubility (g/100 mL) of β-CD with various organic solvents as cosolvents. The solubility of β-CD in pure water with no cosolvent is only 1.6 g/100 mL. (Reprinted with permission from the American Chemical Society, 1992)[8]

4.1.2 Rotoxanes and Pseudorotoxanes

A rotoxane is a mechanically locked architecture consisting of a dumbbell shaped molecule which is threaded through macrocycles such as cyclodextrins,[12] cucurbiturils,[13] and calixarenes.[14] The two ends of the dumbbell which are usually bulky substituents act as stoppers and prevents the macrocycle from falling out and further leading the assembly to dissociate.

A pseudorotoxane is identical to a rotoxane but the two ends of the axis are not sterically designed to prevent the macrocycle from falling off, so instead of a permanent architecture, it is a dynamic one. There are two common ways to synthesize a rotoxane (Figure 4.3):[15]

1. With the macrocycle in solution, it would allow the axis molecule to thread through the macrocycle and then perform a coupling reaction that caps both ends of the axis with a bulky substituent
2. The macrocycle is threaded through the dumbbell, called "slippage" and this process mostly forms pseudorotoxanes

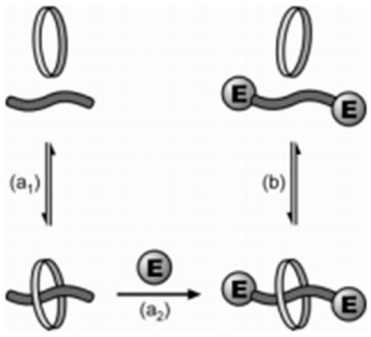

Figure 4.3. Reaction scheme for synthesizing rotoxanes: (a_1) threading the axis molecule; (a_2) capping the ends via coupling reactions; (b) by slippage. E = end group.[15] (Reprinted with permission from the American Chemical Society, 2006)

Being a macrocycle, cyclodextrin has been used by many researchers as a constituent of a rotoxane.[3, 12, 15] One example is shown in Figure 4.4.

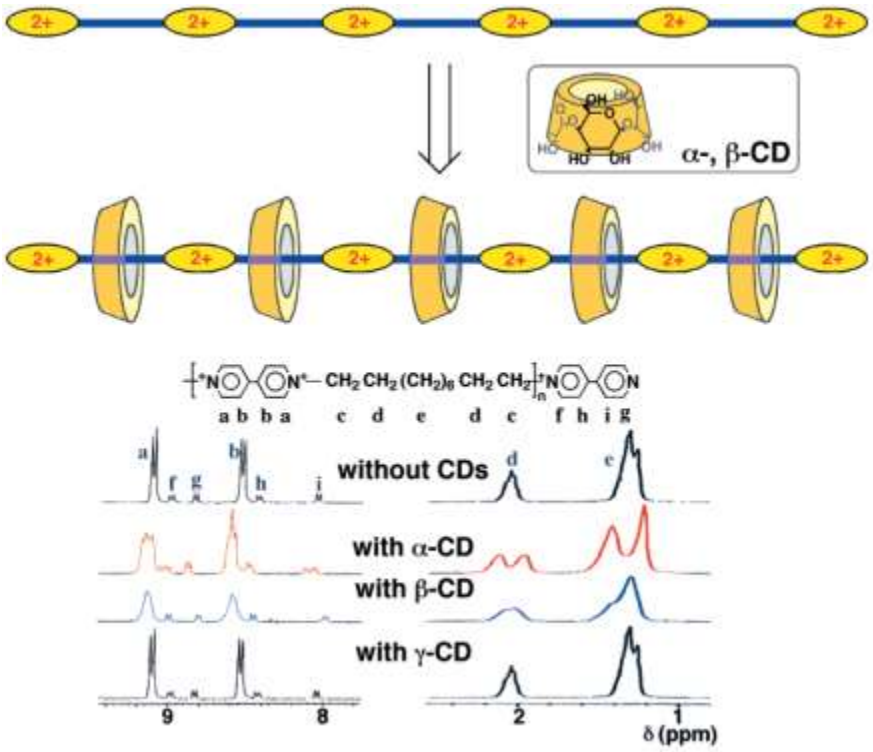

Figure 4.4 A cyclodextrin polypseudorotoxane. Without CD, the aromatic region of the NMR is sharp and resolved. With α-CD added, the bipyridyl (viologen) peaks starts to merge and broaden, while the broad peak of the alkyl region splits, implying the α-CD moves between the viologen and alkyl region, creating different environments. When β-CD is added, the viologen peaks merge and broaden even more, and the alkyl region merges back into two broad peaks, suggesting the β-CD moves between the two regions even faster. γ-CD has no effect, which might mean either no complexation occurred or the ring size is too large to affect the axis' protons on the

NMR.[12] (Reprinted with permission from the American Chemical Society, 2001)

4.2 Cyclodextrin Application on Nanocars

We have previously synthesized adamantane-wheeled fluorescent nanocar **1** (Figure 4.5) and studied its performance on glass with single molecule fluorescent microscopy (SMFM).[16] We compared the diffusion constant of nanocar **1** with nanocar **2** and found an increase in both mobility and diffusion constant. We attributed this increase to the adamantane wheels of nanocar **1** having less surface interaction with the hydrophilic glass surface while the *p*-carborane wheels of nanocar **2** are somewhat polarized to form a pseudo-hydrogen bond with the glass.[17] This is further confirmed by changing the glass surface from as-obtained glass to amine-terminated Vectabond glass, with nanocar **2** decreasing its average diffusion constant by a factor of 4.

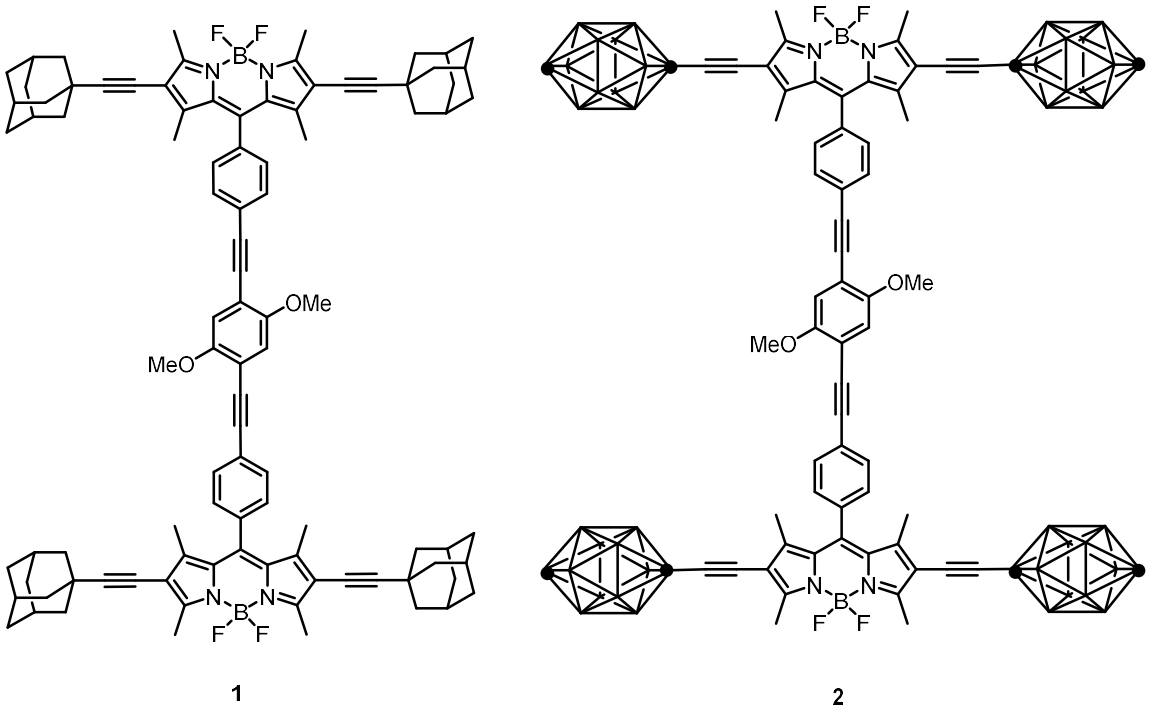

Figure 4.5. Fluorescent nanocar **1** with adamantane wheels, and fluorescent nanocar **2** with *p*-carborane wheels.

With these data from previous experiments in hand, we wondered if we could provide supplementary justification for the wheel-surface interaction claim by synthesizing a nanocar with extremely polar wheels. These polar wheels would interact with normal glass very strongly and yield very low mobility and diffusion constant, yet an increase in mobility and diffusion constant could be seen when the glass surface is functionalized with chemicals such as alkyl siloxanes to become more hydrophobic.

We selected cyclodextrin as the wheel because it meets two requirements:

1. Round or spherical shape needed to mimic a wheel
2. Extremely polar exterior region that contacts the glass surface

4.3 Routes for Synthesizing a Cyclodextrin-Wheeled Nanocar

A direct attachment of CD to the nanocar's axle was considered. The problem with this method is there is no way of properly connecting the two since there is no bond to the center of the CD since it is hollow, and attaching a bond to the rim would produce an off-centered and asymmetrical (Figure 4.6) nanocar.

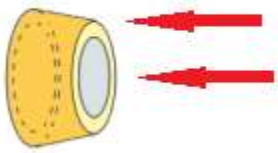

Figure 4.6. Connecting a direct bond from the nanocar to cyclodextrin is not practical.

The next idea is to synthesize a rotoxane with the CD as a macrocyle, but this option was explored by Dr. Jason Guerrero from our lab, and he

could not obtain the rotoxane in any significant yield (Scheme 4.1). In order for a rotoxane to be formed, the constituent and catalyst must be soluble in water, which is not an easy task for rigid rod-like alkynylaromatics.

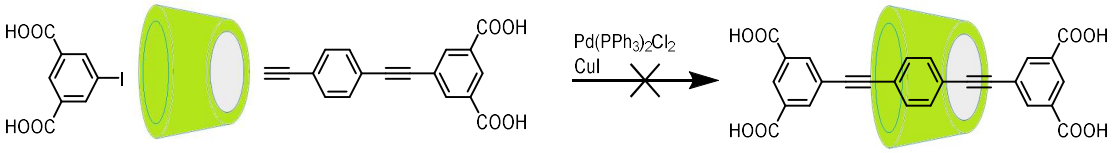

Scheme 4.1. Failed attempt to synthesize a CD containing rotoxane.

We decided that the best route would be to synthesize a nanocar bearing functional groups where the wheels should be, with the functional groups having a strong affinity to CD so it could form a pseudorotoxane.

Adamantane has long been known to form inclusion complexes with β-CD,[18-21] and it makes sense to try nanocar **1** first since it has already been synthesized. Unfortunately, we could not find a cosolvent system that would dissolve both the β-CD and nanocar **1** for the complexation to occur. The BODIPY core in nanocar **1** is already very hydrophobic, plus the four adamantane wheels make the entire process extremely difficult. We next investigated nanocar **2**. Harada and Takahashi have shown that *o*-carborane forms a 1:1 inclusion complex with α-CD using a water/isopropanol

cosolvent system.[22] We subjected nanocar **2** to the same conditions but no complex is observed to be formed.

We presumed that the strongly hydrophobic BODIPY core of the fluorescent nanocars **1** and **2** is the main reason why they would not form complexes with α-CD. In order to increase the solubility of the BODIPY core, we elected to use a benzene sulfonate group. This functional group would not only serve to make the BODIPY more soluble in water, it will also serve as the guest to complex with cyclodextrin to produce a wheel (Figure 4.7).

It would be tempting to follow Scheme 5.2 and synthesize the 4-((trimethylsilyl)ethynyl)benzenesulfonic acid **4** directly,[23] but as sulfonic acids are notoriously hard to purify by column chromatography, and there are quite a few requisite subsequent steps, we decided to use an alcohol as the protection group to form a sulfonate ester (Scheme 4.3).

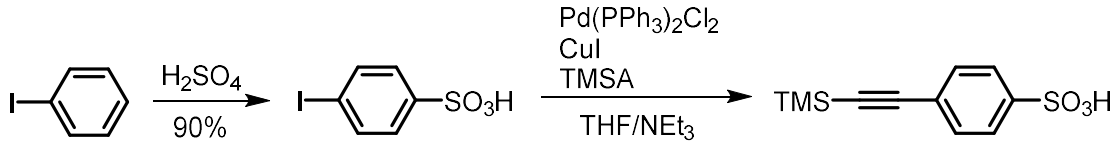

3 **4**

Scheme 4.2. The synthesis of **4** through reaction of iodobenzene leading to **3** is shown.[23]

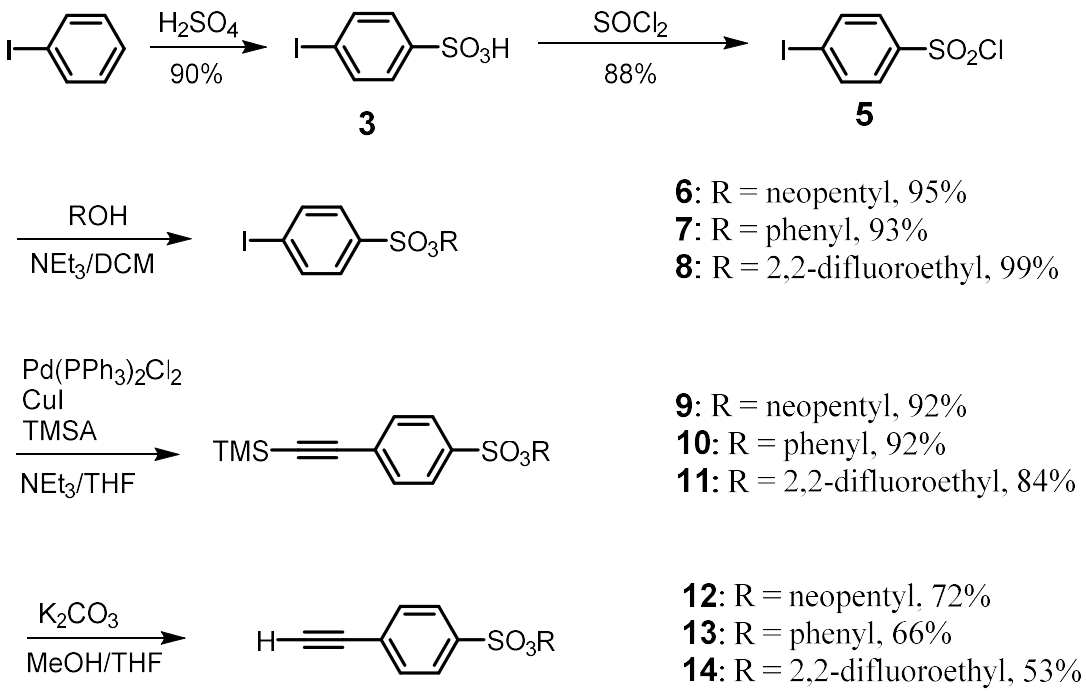

Scheme 4.3. The synthesis of acid chloride **5** has been reported.[24] The protecting groups chosen were neopentyl, phenyl, and 2,2-difluoroethyl groups. 2,2-Difluoroethyl protected sulfonate esters generally have lower yields in subsequent reactions due to the instability of the ester.

Before we coupled **12**, **13**, and **14** to the previously synthesized diiodo-BODIPY **15** (Figure 4.7), we tested the deprotection of the esters on a model compound. We synthesized model compounds **16**, **17** and **18**, which have a hydrophobic naphthalene moiety coupled to the esters (Scheme 4.4).

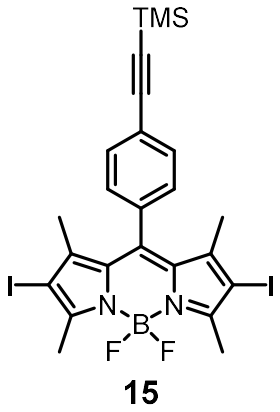

15

Figure 4.7. The diiodo-BODIPY **15.**

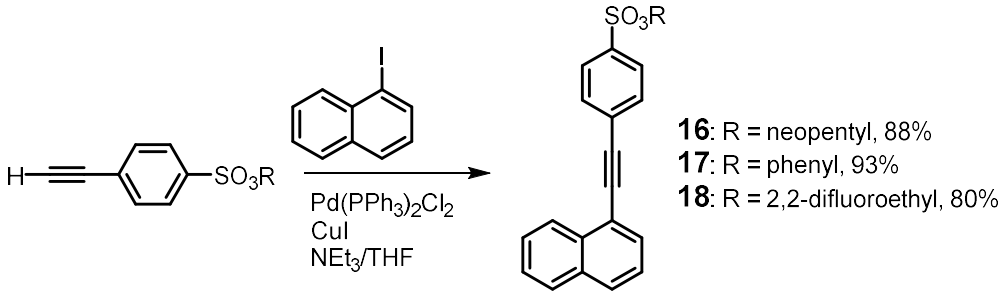

Scheme 4.4. Synthesis of the model compounds **16**, **17** and **18**.

We explored the options of deprotecting the relatively bulky group on **16**. According to the literature, complete cleavage of the neopentyl group can be achieved by reaction with BBr_3 (Scheme 4.5).[25]

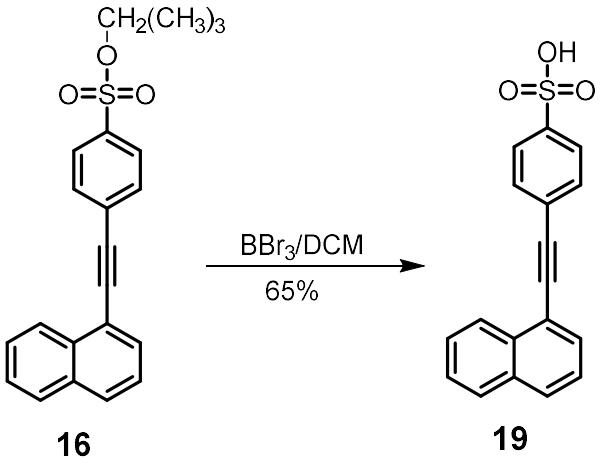

Scheme 4.5. Reaction of **16** with BBr_3 to form deprotected **19**.

We found the yield to be 65% crude, with inseparable impurities and a significant amount of decomposition. We also found the BBr_3 to be incompatible with BODIPYs as we used a stable BODIPY test compound **20** (Figure 4.8), and observed immediate decomposition when **20** was in contact with BBr_3.

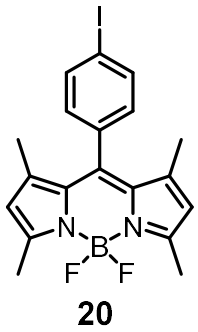

Figure 4.8. Test compound BODIPY **20**.

The phenyl protecting group is known to cleave when subjected to a 0.1 M solution of NaOH in a 1:10 mixture of methanol and dichloromethane.[25] We tested this with the model compound **17** and found it gave quantitative yields of **19** (Scheme 4.6).

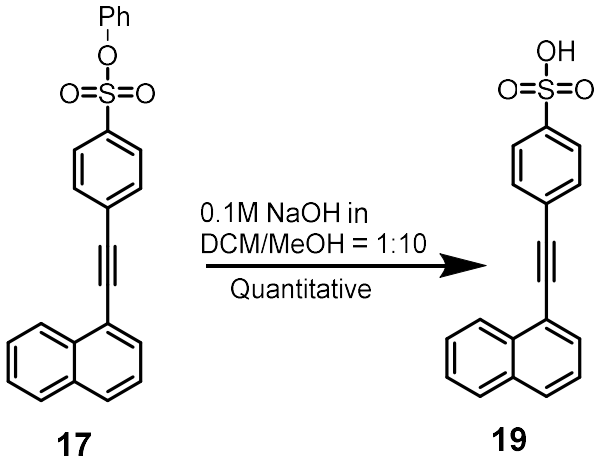

Scheme 4.6. High yielding deprotection of phenyl protection group. **19** was obtained as the sodium salt of the sulfonic acid.

When test compound **20** was subjected to the same conditions, we saw complete decomposition of **20**. It is known that the boron core of BODIPYs is base sensitive, and would dissociate from the dipyrromethene but could sometimes be restored following an acid workup.[26] This is not the case with **20** as no amount of acid workup yielded the intact BODIPY.

The 2,2'-difluoroethanyl (DFE) protecting group is known to be the most labile group and could be cleaved from protected sulfonate esters using a variety of methods.[25] Piperidine (20% in DMF) is a basic nucleophile that readily cleaved the DFE from **19** after prolonged reaction time in a quantitative yield (Scheme 4.7). But when subjected to test compound **20** complete decomposition was observed.

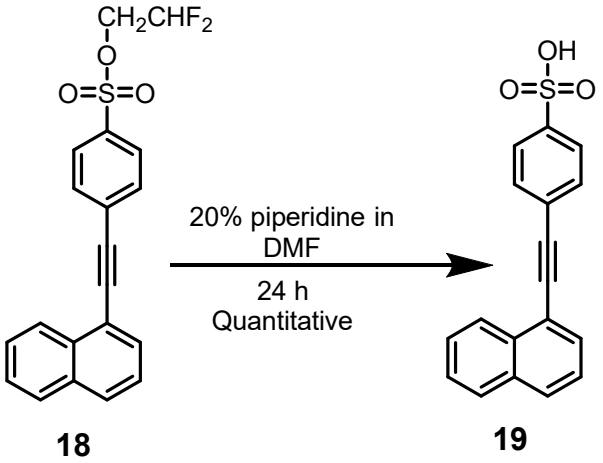

Scheme 4.7. High yielding deprotection of DFE protection group.

It is clear that we need to choose a deprotection method that does not involve basic reactants to avoid decomposition of the BODIPYs. Sodium iodide in refluxing acetone is a nonbasic nucleophile that can be used to deprotect butyl-, isobutyl-, isopropyl-, and DFE- sulfonate esters.[25] Although DFE showed greater stability to cleavage among this group, it nonetheless

succumbed under conditions commonly used in the Finkelstein reaction (Scheme 4.8).

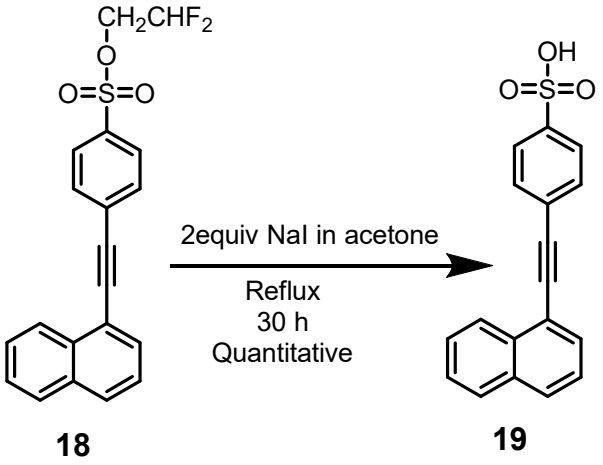

Scheme 4.6. Deprotection of DFE protection group in Finkelstein reaction conditions. **19** is obtained as the sodium salt of the sulfonic acid.

Test compound **20** was subjected to sodium iodide in refluxing acetone, and only partial decomposition was observed after prolonged periods (36 h). We synthesized half nanocar **21**, and subjected it to the Finkelstein reaction conditions to produce half nanocar **22** (Scheme 4.7).

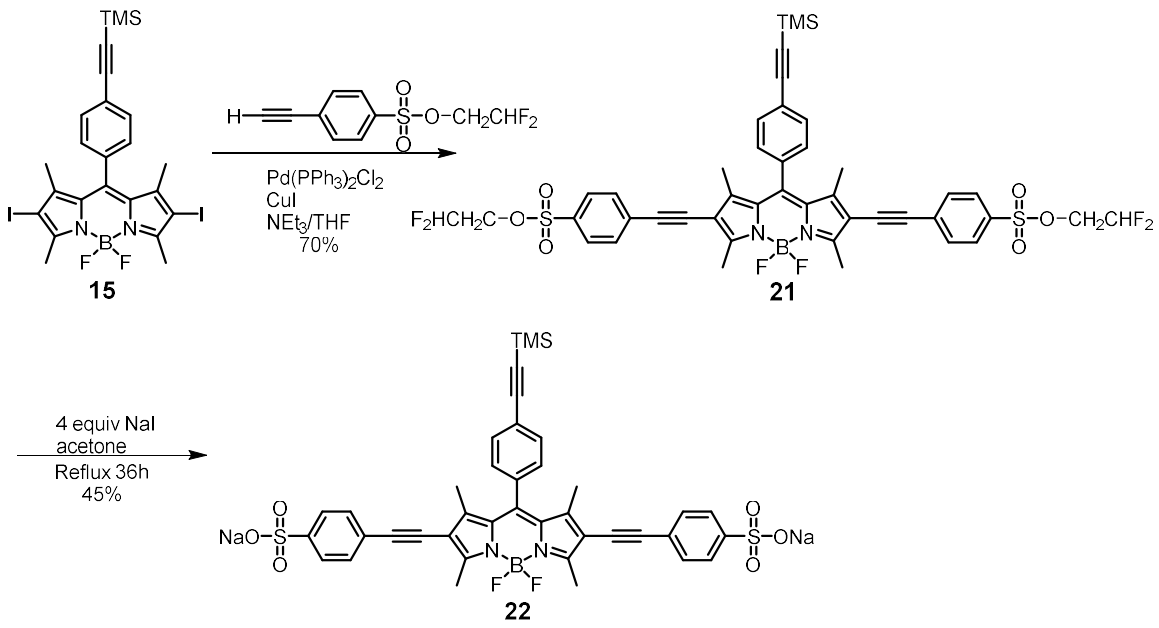

Scheme 4.7. Synthesis of half nanocar **21** and **22**. When synthesizing **22** it is crucial to add NaI to the solution in parts every 6 h to minimize decomposition.

4.4 Cyclodextrin Complexation

Since the cleavage of sulfonate esters on BODIPY is a harder task than we imagined, we decided to just synthesize a half car, and stop at half nanocar **22**. The next step is to complex CDs to the sulfonate groups on **22**. Similar to previous syntheses, before we attempted to do any reactions on our target molecule, we first tested complexation conditions on model

compound **19**. We tried complexing with α- and β-CD; we did not consider γ-CD because of the excessive size of the cavity.

As previously stated, unmodified CDs are not very water soluble, and are nearly insoluble in organic solvents. Because of this, we opted to use methyl-β-cyclodextrin (mβ-CD) as our complexation host, since it is soluble in a variety of organic solvents including methanol, DCM and hexanes. We varied the ratio of **19** and mβ-CD and found NMR evidence of complexation as aromatic peaks starts to shift and merge (Figure 4.9). The H(a) peaks are the shifted the most, and this might be due to that it is in the closest proximity with the hydroxyl groups on the outer rim of CD when complexation occurs.

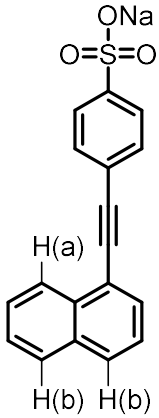

19

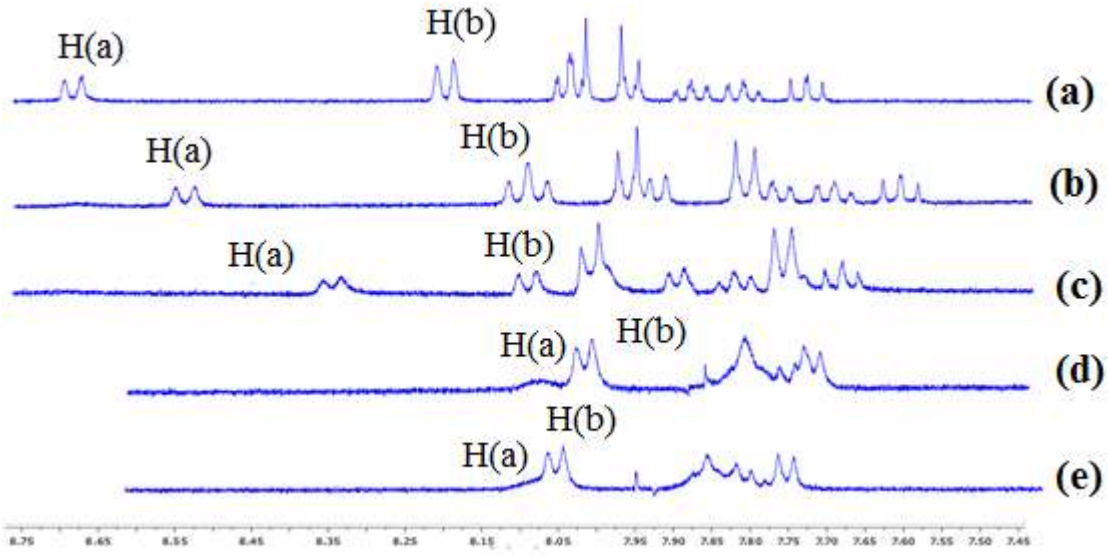

Figure 4.9. (a) 0 equiv mβ-CD to **19**. (b) 0.25 equiv mβ-CD to **19**. (c) 0.5 equiv mβ-CD to **19**. (d) 0.75 equiv mβ-CD to **19**. (b) 1.0 equiv mβ-CD to **19**. The aromatic peaks merge and shift through interaction with the mβ-CD. mβ-CD region is not show as it is a mixture with no significant identifying peaks.

The same effect is reported in the literature as shown in Figure 5.4. When the same experiment is done on half nanocar **22**, we encountered problems as **22** is not soluble in aqueous solutions, and forms aggregates when we tried to dissolve it in water. This phenomenon on sulfonated BODIPYs has been reported.[27] We could not do the same titration experiment with **22**, as **22** did not dissolve in water with 0.25 to 1.5 equiv of mβ-CD. However, if we use a 20% MeOH/water cosolvent system and add in 2 equiv of mβ-CD, we could carefully remove the MeOH via vacuum without half nanocar **22** precipitating. The comparison of **22** and the complex is shown in Figure 4.10. All of the protons indicated showed shifts and changes, suggesting the complexation is not selective to the benzene sulfonate sites, but also the top part of half nanocar **22** that has a trimethyl(phenylethynyl)silane group. The trimethylsily groups seems bulky, but is actually smaller than adamantane , which is known to form host/guest complex with CD.

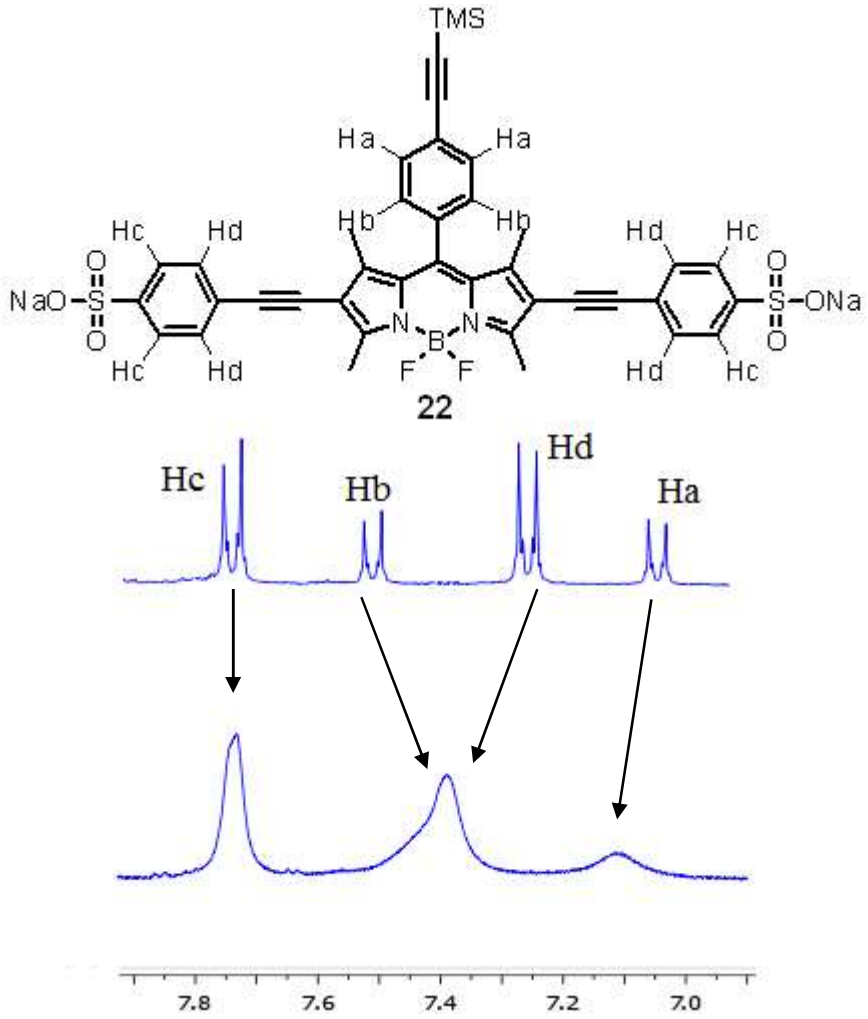

Figure 4.10. The aromatic region of **22** with and without mβ-CD.

A more visual representation is show in Figure 4.11, where a solution of half nanocar **22** in methanol (0.01 M) was dripped into water, methanol and water with an excess of mβ-CD. The mβ-CD associates with **22** and disrupts its ability to form aggregates, producing a water soluble complex.

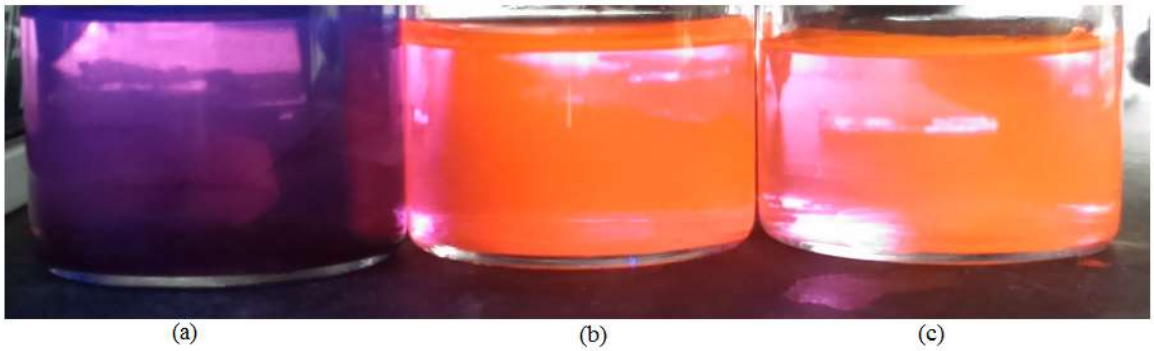

Figure 4.11. (a) Methanol solution of **22** dripped into water; aggregates formed a thin film. (b) Methanol solution of **22** dripped into methanol. (c) Methanol solution of **22** dripped into a 1 M solution of mβ-CD in water.

4.5 Conclusion

In conclusion, we synthesized the BODIPY-based half nanocar **22** that could be complexed with mβ-CD through deprotection of the sulfonate esters at the last step. The complexation site on the half nanocar is not selective. When the benzene sulfonic acid groups on **22** are complexed with mβ-CD, we would expect **22** to have little or no motion on untreated glass slides.

4.6 Experimental Section

General Methods. ^{1}H NMR and ^{13}C NMR spectra were recorded at 400 or 500 and 100 or 125 MHz, respectively. Chemical shifts (δ) are reported in ppm from TMS. FTIR spectra were recorded using a FT-IR Infrared Microscope with ATR objective with 2 cm^{-1} resolution. All glassware was oven-dried overnight prior to use. Reagent grade tetrahydrofuran (THF) was distilled from sodium benzophenoneketyl under N_2 atmosphere. Triethylamine (NEt_3), dichloromethane (CH_2Cl_2) and *N*,*N*-dimethylformamide (DMF) were distilled from calcium hydride (CaH_2) under an N_2 atmosphere. The reactions were performed under N_2 unless otherwise noted. All chemicals were purchased from commercial suppliers and used without further purification unless otherwise noted. Flash column chromatography was performed using 230-400 mesh silica gel from EM Science. Thin layer chromatography (TLC) was performed using glass plates pre-coated with silica gel 40 F_{254} 0.25 mm layer thickness.

General procedure for the synthesis of 9, 10, and 11 by Sonogashira coupling. An oven dried 10 mL Schlenk-tube or screw-cap tube equipped with a stir bar was charged inside a dry-box with sulfonate ester (1.0 equiv), $Pd(PPh_3)_2Cl_2$ (0.05 equiv), and CuI (0.1 equiv) to which were added Et_3N (5 mL), THF (10 mL), and TMSA (1.2 equiv), the Schlenk-tube or screw-cap

tube was sealed, then removed from the dry-box, and the reaction mixture was stirred at 60 °C for 12 h. After cooling to rt, the reaction was quenched with saturated $NH_4Cl_{(aq)}$ (20 mL) and extracted with CH_2Cl_2 (30 mL). The organic phase was washed with water (30 mL), dried over anhydrous $MgSO_4$, filtered, and the filtrate was concentrated under vacuum. The crude product was purified by column chromatography (silica gel, 10% to 20% EtOAc in hexanes).

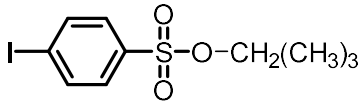

6

Sulfonate Ester 6. An oven-dried 100 mL round bottom flask equipped with a stir bar was charged with sulfonyl chloride **5** (1.00 g, 3.31 mmol), neopentyl alcohol (0.43 g, 4.96 mmol) to which were added dichloromethane (30 mL) and Et_3N (10 mL). The reaction mixture was stirred at room temperature overnight. The mixture was quenched with water (20 mL) and extracted with dichloromethane (60 mL). The organic phase was washed with water (30 mL), dried over anhydrous $MgSO_4$, filtered, and the filtrate was concentrated under vacuum. The crude product was purified by column chromatography (silica gel, 20% EtOAc in hexanes) to yield **6** as

a white solid (1.10 g, 95%). m.p. 48-50 °C. FTIR (neat) 3081, 2964, 1575, 1482, 1354, 1178, 1097 cm^{-1}. ^{1}H NMR (500 MHz; $CDCl_3$): δ 7.92 (d, *J* = 8.7 Hz, 2H), 7.61 (d, *J* = 8.7 Hz, 2H), 3.69 (s, 2H), 0.91 (s, 9H). ^{13}C NMR (125 MHz; CDCl3): δ 138.5, 135.7, 129.2, 101.4, 80.0, 31.7, 26.0. HRMS (APCI) *m/z* calcd for $[M+H]^+$ $C_{11}H_{15}IO_3S$ 354.9865, found 354.9847.

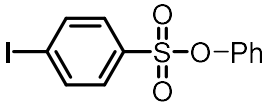

7

Sulfonate Ester 7. An oven-dried 100 mL round bottom flask equipped with a stir bar was charged with sulfonyl chloride **5** (1.00 g, 3.31 mmol), phenol (0.5 g, 5.29 mmol) to which were added dichloromethane (30 mL) and Et_3N (10 mL). The reaction mixture was stirred at room temperature overnight. The mixture was quenched with water (20 mL) and extracted with dichloromethane (60 mL). The organic phase was washed with water (30 mL), dried over anhydrous $MgSO_4$, filtered, and the filtrate was concentrated under vacuum. The crude product was purified by column chromatography (silica gel, 10% EtOAc in hexanes) to yield **7** as a dark yellow oil (1.11 g, 93%). FTIR (neat) 3677, 2976, 2894, 1552, 1494, 1354, 1143, 1061, 1015 cm^{-1}. ^{1}H NMR (500 MHz; $CDCl_3$): δ 7.88 (d, *J* = 8.7 Hz, 2H), 7.52 (d, *J* = 8.7 Hz, 2H), 7.33-7.26 (m, 3H), 6.99 (dd, *J* = 8.5, 1.3 Hz, 2H). ^{13}C NMR

(125 MHz; CDCl3): δ 149.4, 138.5, 135.0, 129.81, 129.72, 127.4, 122.3, 102.3. HRMS (APCI) *m/z* calcd for $[M+H]^+$ $C_{12}H_9IO_3S$ 360.9395, found 360.9388.

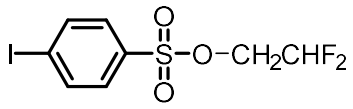

8

Sulfonate Ester 8. An oven-dried 100 mL round bottom flask equipped with a stir bar was charged with sulfonyl chloride **5** (1.00 g, 3.31 mmol), 2,2'-difluoroethanol (0.34 mL, 5.29 mmol) to which were added dichloromethane (30 mL) and Et_3N (10 mL). The reaction mixture was stirred at room temperature overnight. The mixture was quenched with water (20 mL) and extracted with dichloromethane (60 mL). The organic phase was washed with water (30 mL), dried over anhydrous $MgSO_4$, filtered, and the filtrate was concentrated under vacuum. The crude product was purified by column chromatography (silica gel, 20% EtOAc in hexanes) to yield **8** as a light yellow solid (1.14 g, 99%). m.p. 40-42 °C. FTIR (neat) 3677, 3081, 2988, 2894, 2357, 1926, 1564, 1365, 1178, 10731015 cm^{-1}. ^1H NMR (500 MHz, $CDCl_3$) δ 7.88 (d, *J* = 8.7 Hz, 2H), 7.55 (d, *J* = 8.7 Hz, 2H), 5.86 (tt, *J* = 54.5, 3.9 Hz, 1H), 4.14 (td, *J* = 12.8, 4.0 Hz, 2H). ^{13}C NMR (125 MHz;

CDCl3): δ 138.8, 134.7, 129.2, 111.8, 102.5, 66.9. HRMS (APCI) *m/z* calcd for $[M+H]^+$ $C_8H_7F_2IO_3S$ 348.9207, found 348.9231.

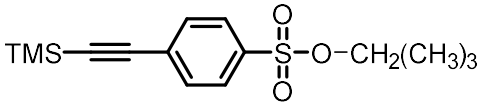

9

Sulfonate Ester 9. An oven-dried 25 mL Schlenk tube equipped with a stir bar was charged with sulfonate ester **6** (500 mg, 1.41 mmol), $Pd(PPh_3)_2Cl_2$ (49.5 mg, 70.6 μmol), and CuI (26.8 mg, 141 μmol) to which were added Et_3N (5 mL), THF (10 mL) and TMSA (0.24 mL, 1.69 mmol). The reaction mixture was stirred at 50 °C overnight. The mixture was quenched with saturated NH_4Cl (20 mL) and extracted with dichloromethane (50 mL). The organic phase was washed with water (50 mL), dried over anhydrous $MgSO_4$, filtered, and the filtrate was concentrated under vacuum. The crude product was purified by column chromatography (silica gel, 10% EtOAc in hexanes) to yield **9** as a brown solid (422 mg, 92%). m.p. 65-67 °C. FTIR (neat) 2941, 2357, 2170, 1599, 1471, 1354, 1260, 1178, 1085 cm^{-1}. ^1H NMR (500 MHz; $CDCl_3$): δ 7.84 (d, *J* = 8.7 Hz, 2H), 7.62 (d, *J* = 8.7 Hz, 2H), 3.66 (s, 2H), 0.89 (s, 9H), 0.27 (s, 9H). ^{13}C NMR (125 MHz; CDCl3): δ 135.3,

132.5, 128.8, 127.8, 102.8, 99.3, 79.9, 31.7, 26.0, 0.3. HRMS (APCI) *m/z* calcd for $[M+H]^+$ $C_{16}H_{24}O_3SSi$ 325.1294, found 325.1277.

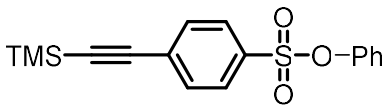

10

Sulfonate Ester 10. An oven-dried 25 mL Schlenk tube equipped with a stir bar was charged with sulfonate ester **7** (500 mg, 1.39 mmol), $Pd(PPh_3)_2Cl_2$ (48.7 mg, 69.4 μmol), and CuI (26.4 mg, 139 μmol) to which were added Et_3N (5 mL), THF (10 mL) and TMSA (0.24 mL, 1.69 mmol). The reaction mixture was stirred at 50 °C overnight. The mixture was quenched with saturated NH_4Cl (20 mL) and extracted with dichloromethane (50 mL). The organic phase was washed with water (50 mL), dried over anhydrous $MgSO_4$, filtered, and the filtrate was concentrated under vacuum. The crude product was purified by column chromatography (silica gel, 10% EtOAc in hexanes) to yield **10** as a dark brown oil (422 mg, 92%). FTIR (neat) 3677, 2964, 2894, 2369, 2158, 1576, 1494, 1377, 1202, 1132, 1085 cm^{-1}. ^1H NMR (500 MHz; $CDCl_3$): δ 7.55 (d, *J* = 8.8 Hz, 2H), 7.38 (d, *J* = 8.8 Hz, 2H), 7.11-7.06 (m, 3H), 6.77 (dd, *J* = 8.4, 1.4 Hz, 2H), 0.08 (s, 9H). 13C NMR (125 MHz; CDCl3): δ 150.0, 135.0, 132.9, 130.2, 129.9, 128.9, 127.8, 122.8,

103.2, 100.3, 0.2. HRMS (APCI) *m/z* calcd for $[M+H]^+$ $C_{17}H_{18}O_3SSi$ 331.0824, found 331.0829.

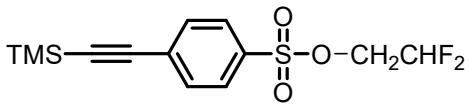

11

Sulfonate Ester 11. An oven-dried 25 mL Schlenk tube equipped with a stir bar was charged with sulfonate ester **8** (500 mg, 1.39 mmol), $Pd(PPh_3)_2Cl_2$ (48.7 mg, 69.4 μmol), and CuI (26.4 mg, 139 μmol) to which were added Et_3N (5 mL), THF (10 mL) and TMSA (0.24 mL, 1.69 mmol). The reaction mixture was stirred at 50 °C overnight. The mixture was quenched with saturated NH_4Cl (20 mL) and extracted with dichloromethane (50 mL). The organic phase was washed with water (50 mL), dried over anhydrous $MgSO_4$, filtered, and the filtrate was concentrated under vacuum. The crude product was purified by column chromatography (silica gel, 10% EtOAc in hexanes) to yield **11** as a light yellow solid (384 mg, 84%). m.p. 63-65 °C. FTIR (neat) 3689, 2976, 2894, 2369, 2147, 1587, 1377, 1248, 1167, 1073, 1015 cm^{-1}. ^1H NMR (500 MHz, $CDCl_3$) δ 7.78 (d, *J* = 8.7 Hz, 2H), 7.57 (d, *J* = 8.7 Hz, 2H), 5.86 (tt, *J* = 54.5, 3.9 Hz, 1H), 4.12 (td, *J* = 12.9, 3.9 Hz, 2H), 0.20 (s, 9H). ^{13}C NMR (125 MHz; CDCl3): δ 134.1, 132.6, 129.6, 127.8,

111.7, 102.5, 99.9, 66.8, -0.4. HRMS (APCI) *m/z* calcd for $[M+H]^+$ $C_{13}H_{16}F_2O_3SSi$ 319.0636, found 319.0611.

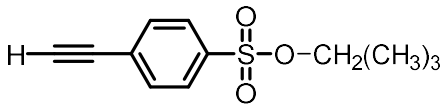

12

Sulfonate Ester 12. An oven-dried 50 mL round bottom flask equipped with a stir bar was charged with **9** (300 mg, 0.926 mmol) and K_2CO_3 (650 mg, 4.63 mmol), to which were added MeOH (10 mL) and THF (10 mL). The reaction mixture was stirred at room temperature for 90 min. The mixture was quenched with water and extracted with dichloromethane (60 mL). The organic phase was washed with water (50 mL), dried over anhydrous $MgSO_4$, filtered, and the filtrate was concentrated under vacuum. The crude product was purified by column chromatography (silica gel, 15% EtOAc in hexanes) to yield **12** as a yellow oil (167 mg, 72%). FTIR (neat) 3268, 2953, 2345, 2113, 1576, 1459, 1354, 1167, 1097 cm^{-1}. ^1H NMR (500 MHz; $CDCl_3$): δ 7.86 (d, *J* = 8.7 Hz, 2H), 7.65 (d, *J* = 8.6 Hz, 2H), 3.68 (s, 2H), 3.29 (s, 1H), .90 (s, 9H). ^{13}C NMR (125 MHz; CDCl3): δ 135.9, 132.8, 127.85, 127.83, 81.8, 81.3, 80.0, 31.7, 26.0. HRMS (APCI) *m/z* calcd for $[M+H]^+$ $C_{13}H_{16}O_3S$ 253.0898, found 253.0914.

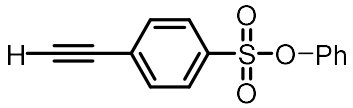

13

Sulfonate Ester 13. An oven-dried 50 mL round bottom flask equipped with a stir bar was charged with **10** (400 mg, 1.21 mmol) and K_2CO_3 (850 mg, 6.04 mmol), to which were added MeOH (10 mL) and THF (10 mL). The reaction mixture was stirred at room temperature for 90 min. The mixture was quenched with water and extracted with dichloromethane (60 mL). The organic phase was washed with water (50 mL), dried over anhydrous $MgSO_4$, filtered, and the filtrate was concentrated under vacuum. The crude product was purified by column chromatography (silica gel, 10% EtOAc in hexanes) to yield **13** as a reddish oil (206 mg, 66%). FTIR (neat) 3674, 2981, 2892, 1565, 1494, 1354, 1167, 1073, 1015. ^{1}H NMR (500 MHz; CD_2Cl_2): δ 7.75 (d, *J* = 8.8 Hz, 2H), 7.62 (d, *J* = 8.7 Hz, 2H), 7.32-7.25 (m, 3H), 6.96 (dd, *J* = 8.4, 1.4 Hz, 2H), 3.38 (s, 1H). ^{13}C NMR (125 MHz; CD2Cl2): δ 149.5, 135.1, 132.7, 129.8, 128.44, 128.36, 127.4, 122.2, 81.50, 81.49. HRMS (APCI) *m/z* calcd for $[M+H]^+$ $C_{14}H_{10}O_3S$ 259.0429, found 259.0422.

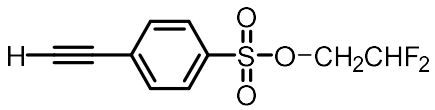

14

Sulfonate Ester 14. An oven-dried 50 mL round bottom flask equipped with a stir bar was charged with **11** (300 mg, 0.94 mmol) and K_2CO_3 (650 mg, 4.72 mmol), to which were added MeOH (10 mL) and THF (10 mL). The reaction mixture was stirred at room temperature for 90 min. The mixture was quenched with water and extracted with dichloromethane (60 mL). The organic phase was washed with water (50 mL), dried over anhydrous $MgSO_4$, filtered, and the filtrate was concentrated under vacuum. The crude product was purified by column chromatography (silica gel, 15% EtOAc in hexanes) to yield **14** as a light reddish oil (123 mg, 53%). FTIR (neat) 3665, 3292, 2953, 2883, 2369, 1587, 1354, 1167, 1073, 1015 cm^{-1}. ^1H NMR (500 MHz, $CDCl_3$) δ 7.89 (d, *J* = 8.7 Hz, 2H), 7.68 (d, *J* = 8.7 Hz, 2H), 5.93 (tt, *J* = 54.5, 4.0 Hz 1H), 4.21 (td, *J* = 12.7, 4.0 Hz, 2H), 3.33 (s, 1H). ^{13}C NMR (125 MHz; CDCl3): δ 138.9, 134.7, 132.2, 129.2, 111.8, 93.6. 91.6 66.7. HRMS (APCI) *m/z* calcd for $[M+H]^+$ $C_{10}H_8F_2O_3S$ 247.0240, found 247.0251.

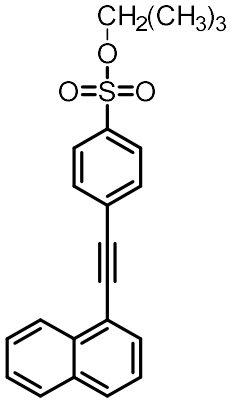

16

Model compound 16. An oven-dried 25 mL Schlenk tube equipped with a stir bar was charged with 1-iodonaphthalene (100 mg, 0.394 mmol), **12** (120 mg, 0.473 mmol), $Pd(PPh_3)_2Cl_2$ (13.8 mg, 19.7 μmol), and CuI (7.5 mg, 39.4 μmol) to which were added Et_3N (3 mL) and THF (10 mL). The reaction mixture was stirred at 70 °C overnight. The mixture was quenched with saturated NH_4Cl (20 mL) and extracted with dichloromethane (60 mL). The organic phase was washed with water (30 mL), dried over anhydrous $MgSO_4$, filtered, and the filtrate was concentrated under vacuum. The crude product was purified by column chromatography (silica gel, 20% EtOAc in hexanes) to yield **16** as a red solid (131 mg, 88%). m.p. 118-120 °C. FTIR (neat) 2964, 2345, 2205, 1587, 1459, 1365, 1155, 1085 cm^{-1}. ^1H NMR (500 MHz; $CDCl_3$): δ 8.39 (d, J = 7.8 Hz, 1H), 7.95-7.92 (m, 2H), 7.91 (d, J = 4.5 Hz, 1H), 7.90 (d, J = 4.3 Hz, 1H), 7.82-7.79 (m, 3H), 7.63 (ddd, J = 8.3, 6.9, 1.4 Hz, 1H), 7.57 (ddd, J = 8.1, 6.8, 1.3 Hz, 1H), 7.50 (dd, J = 8.3, 7.2 Hz,

1H), 3.72 (s, 2H), 0.93 (s, 9H). ^{13}C NMR (125 MHz; CDCl3): δ 135.2, 133.19, 133.16, 132.2, 131.1, 129.8, 129.2, 128.5, 128.0, 127.1, 126.7, 125.9, 125.3, 119.8, 92.4, 91.7, 79.9, 31.7, 26.0. HRMS (APCI) *m/z* calcd for $[M+H]^+$ $C_{23}H_{22}O_3S$ 379.1368, found 379.1352.

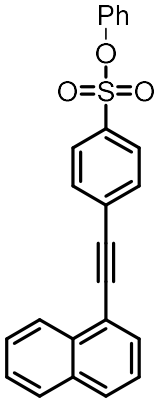

17

Model compound 17. An oven-dried 25 mL Schlenk tube equipped with a stir bar was charged with 1-iodonaphthalene (100 mg, 0.394 mmol), **13** (132 mg, 0.512 mmol), $Pd(PPh_3)_2Cl_2$ (13.9 mg, 19.7 μmol), and CuI (7.6 mg, 39.4 μmol) to which were added Et_3N (3 mL) and THF (10 mL). The reaction mixture was stirred at 70 °C overnight. The mixture was quenched with saturated NH_4Cl (20 mL) and extracted with dichloromethane (60 mL). The organic phase was washed with water (30 mL), dried over anhydrous $MgSO_4$, filtered, and the filtrate was concentrated under vacuum. The crude product was purified by column chromatography (silica gel, 10% EtOAc in hexanes) to yield **17** as a white or off-white solid (128 mg, 85%). m.p. 115-

117 °C. FTIR (neat) 3689, 2988, 2894, 2346, 2205, 1576, 1482, 1377, 1190, 1143, 1073 cm^{-1}. ^{1}H NMR (500 MHz; $CDCl_3$): δ 8.38 (d, *J* = 8.7 Hz, 1H), 7.89 (dd, *J* = 8.2, 5.1 Hz, 2H), 7.83 (d, *J* = 8.7 Hz, 2H), 7.79 (dd, *J* = 7.1, 1.1 Hz, 1H), 7.74 (d, *J* = 8.7 Hz, 2H), 7.62 (ddd, *J* = 8.3, 6.9, 1.4 Hz, 1H), 7.56 (ddd, *J* = 8.1, 6.9, 1.3 Hz, 1H), 7.48 (dd, *J* = 8.3, 7.2 Hz, 1H), 7.33-7.25 (m, 3H), 7.02-7.00 (m, 2H). ^{13}C NMR (125 MHz; CDCl3): δ 149.6, 134.4, 133.20, 133.15, 132.0, 131.1, 129.89, 129.79, 129.78, 128.62, 128.55, 127.36, 127.20, 126.7, 125.9, 125.3, 122.4, 119.7, 92.34, 92.23. HRMS (APCI) *m/z* calcd for $[M+H]^+$ $C_{24}H_{16}O_3S$ 385.0898, found 385.0888.

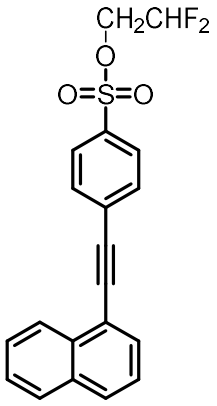

18

Model compound 18. An oven-dried 25 mL Schlenk tube equipped with a stir bar was charged with 1-iodonaphthalene (80 mg, 0.315 mmol), **14** (93 mg, 0.378 mmol), $Pd(PPh_3)_2Cl_2$ (11.1 mg, 15.76 μmol), and CuI (6.08 mg, 31.5 μmol) to which were added Et_3N (5 mL) and THF (10 mL). The reaction mixture was stirred at 70 °C overnight. The mixture was quenched

with saturated NH_4Cl (20 mL) and extracted with dichloromethane (60 mL). The organic phase was washed with water (30 mL), dried over anhydrous $MgSO_4$, filtered, and the filtrate was concentrated under vacuum. The crude product was purified by column chromatography (silica gel, 20% EtOAc in hexanes) to yield **18** as a light yellow solid (74 mg, 80%). m.p. 110-112 °C. FTIR (neat) 3677, 2976, 2918, 2357, 2194, 1587, 1365, 1167, 1073,1003 cm^{-1}. ^1H NMR (500 MHz, $CDCl_3$) δ 8.38 (ddt, *J* = 8.4, 1.3, 0.8 Hz, 1H), 7.98 – 7.93 (m, 2H), 7.90 (ddd, *J* = 7.5, 4.2, 3.4 Hz, 2H), 7.82 (ddd, *J* = 7.0, 4.3, 0.9 Hz, 3H), 7.64 (ddd, *J* = 8.3, 6.9, 1.4 Hz, 1H), 7.57 (ddd, *J* = 8.1, 6.9, 1.3 Hz, 1H), 7.50 (dd, *J* = 8.3, 7.2 Hz, 1H), 5.96 (tt, *J* = 54.5, 4.0 Hz, 1H), 4.24 (td, *J* = 12.7, 4.1 Hz, 2H). ^{13}C NMR (125 MHz, $CDCl_3$) δ 134.0, 133.2, 133.1, 132.3, 131.1, 130.1, 129.9, 128.5, 128.1, 127.2, 126.7, 125.8, 125.3, 119.6, 111.8, 92.4, 92.1, 66.8. HRMS (APCI) *m/z* calcd for $[M+H]^+$ $C_{20}H_{14}F_2O_3S$ 373.0710, found 373.0702.

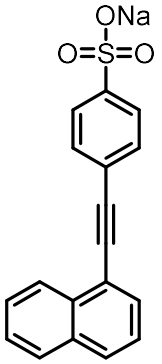

19

Model compound 19.

From 17. An oven-dried 25 mL Schlenk tube equipped with a stir bar was charged with **17** (50 mg, 0.13 mmol) and NaOH (40 mg, 1 mmol) to which were added MeOH (1 mL) and DCM (10 mL). The reaction mixture was stirred at rt overnight. The white precipitate that formed was filtered out, washed with water (10 mL) and allowed to dry with no further purification to yield **19** as a white solid (43 mg, 99%)

From 18. An oven-dried 25 mL Schlenk tube equipped with a stir bar was charged with **18** (50 mg, 0.134 mmol) and NaI (40 mg, 0.268 mmol) to which were added acetone (10 mL). The reaction mixture was stirred at rt for 30 h. The solvent is then removed under vacuum and the resulting solid is washed with water (20 mL) and allowed to dry to yield **19** as a white solid (44 mg, 99%). m.p. 105-107 °C. FTIR (neat) 3467, 3058, 2976, 1587, 1424, 1400, 1190, 1120, 1026 cm^{-1}. ^{1}H NMR (500 MHz, MeOD) δ 8.44 (d, J = 8.3 Hz, 1H), 7.96 (d, J = 8.1 Hz, 2H), 7.93 (d, J = 8.2 Hz, 2H), 7.81 (d, J = 7.0 Hz, 1H), 7.76 (d, J = 7.9 Hz, 2H), 7.68 (t, J = 7.2 Hz, 1H), 7.60 (t, J = 7.1 Hz, 1H), 7.58 – 7.49 (m, 1H). ^{13}C NMR (125 MHz; MeOD): δ 133.3, 133.0, 131.1, 130.3, 128.9, 128.1, 126.7, 126.3, 125.9, 125.5, 125.2, 125.0, 120.1, 99.8, 92.9, 88.4. MS (ESI, negative mode) *m/z* calcd for $[M\text{-}Na]^-$ $C_{18}H_{11}O_3S$ 307.04, found 307.22.

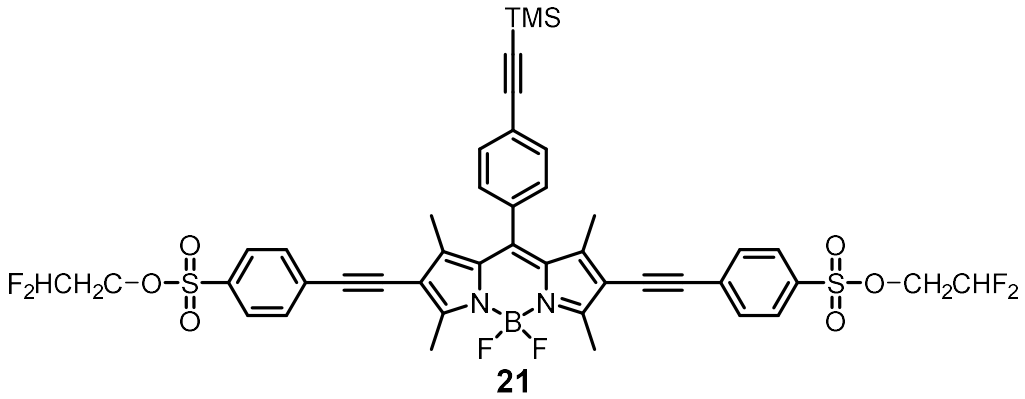

21

Half Nanocar 21 An oven-dried 10 mL Schlenk tube equipped with a stir bar was charged with diiodo-BODIPY **15** (50 mg, 74.5 μmol), $Pd(PPh_3)_2Cl_2$ (5.2 mg, 7.45 μmol), and CuI (2.8 mg, 14.9 μmol) to which were added Et_3N (1 mL) and THF (3 mL). The reaction mixture was stirred at 40 °C overnight. The mixture was quenched with saturated NH_4Cl (10 mL) and extracted with dichloromethane (20 mL). The organic phase was washed with water (20 mL), dried over anhydrous $MgSO_4$, filtered, and the filtrate was concentrated under vacuum. The crude product was purified by column chromatography (silica gel, 8% EtOAc in hexanes) to yield **21** as a dark purple solid (47 mg, 70%). m.p. 150-152 °C (decomposition). FTIR (neat) 3677, 2988, 2906, 2357, 1377, 1237, 1061 cm^{-1}. ^1H NMR (500 MHz, $CDCl_3$) δ 7.88 (d, *J* = 8.8 Hz, 4H), 7.67 (d, *J* = 8.5 Hz, 2H), 7.62 (d, *J* = 8.8 Hz, 4H), 7.26 (d, *J* = 8.5 Hz, 2H), 5.93 (tt, *J* = 54.6, 4.1 Hz, 2H), 4.21 (td, *J* = 12.7, 4.1 Hz, 4H), 2.73 (s, 6H), 1.56 (s, 6H), 0.30 (s, 9H). ^{13}C NMR (100 MHz, $CDCl_3$) δ 157.0, 145.1, 140.3, 134.7, 134.1, 132.9, 132.6, 131.1,

129.7, 127.82, 127.80, 124.5, 111.7, 103.8, 102.5, 100.1, 96.4, 96.5, 66.7, 17.1, 16.0, -0.2. HRMS (APCI) *m/z* calcd for $[M+H]^+$ $C_{44}H_{39}BF_6N_2O_6S_2Si$ 909.2094, found 909.2071.

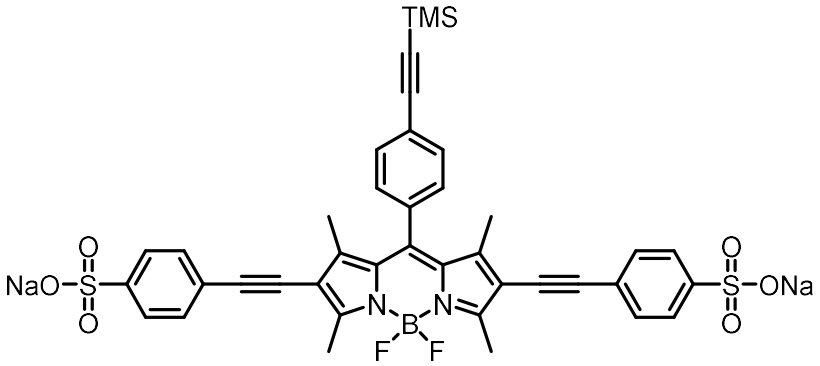

22

Half Nanocar 22 An oven-dried 10 mL Schlenk tube equipped with a stir bar was charged with **21** (40 mg, 44 μmol) to which were added acetone (10 mL). NaI (26 mg, 0.176 mmol) was split into four portions and each portion is added every 6 h. The reaction mixture was stirred at rt for 30 h. The solvent is then removed under vacuum. The crude product is purified by reverse phase column chromatography (C18 silica gel, 0 to 15% MeOH in water) to yield **22** as a dark blue solid (16 mg, 45%). m.p. 142-145 °C (decomposition). FTIR (neat) 3690, 2976, 2894, 2345, 2158, 1517, 1400, 1342, 1190, 1120, 1003 cm^{-1}. ^1H NMR (500 MHz, $CDCl_3$) δ 7.84 (d, J = 8.7 Hz, 4H), 7.71 (d, J = 8.5 Hz, 2H), 7.56 (d, J = 8.7 Hz, 4H), 7.44 (d, J = 8.5 Hz, 2H), 2.72 (s, 6H), 1.66 (s, 6H), 0.31 (s, 9H). ^{13}C NMR (100 MHz, $CDCl_3$) δ 158.1, 143.0, 140.7, 138.0, 135.0, 132.8, 130.6, 129.4, 128.1,

127.1, 125.1, 124.1, 122.7, 116.9, 106.0, 104.2, 96.0, 94.0, 92.5, 0.5 MS (ESI, negative mode) *m/z* calcd for $[M-2Na]^{2-}$ $C_{40}H_{33}BF_2N_2O_6S_2Si$ 389.08, found 389.10.

4.7 Contributions

I designed and devised all the synthetic route to **22** and developed the correct reaction conditions for **19**, which this deprotection method is crucial in the success of making **22**.

4.8 Acknowledgements

J. M. T. acknowledges support from the National Science Foundation (CHE-1007483). We thank Drs. I. Chester of FAR Research, Inc. and R. Awartari of Petra Research, Inc. for providing trimethylsilyacetylene.

4.9 References

1. Larsen, K. L. Large Cyclodextrins. *J. Inclusion Phenom. Macrocyclic Chem.* **2002**, *43*, 1-13.

2. Uekama, K.; Hirayama, F.; Irie, T. Cyclodextrin Drug Carrier Systems. *Chem. Rev.* **1998**, *98*, 2045-2076.

3. Szejtli, J. Introduction and General Overview of Cyclodextrin Chemistry. *Chem. Rev.* **1998**, *98*, 1743-1753.

4. Becket, G.; Schep, L. J.; Tan, M. Y. Improvement of the in Vitro Dissolution of Praziquantel by Complexation with Alpha-, Beta- and Gamma-Cyclodextrins. *Int. J. Pharm.* **1999**, *179*, 65-71.

5. Nagase, Y.; Hirata, M.; Wada, K.; Arima, H.; Hirayama, F.; Irie, T.; Kikuchi, M.; Uekama, K. Improvement of Some Pharmaceutical Properties of Dy-9760e by Sulfobutyl Ether Beta-Cyclodextrin. *Int. J. Pharm.* **2001**, *229*, 163-172.

6. Tiwari, G.; Tiwari, R.; Rai, A. K. Cyclodextrins in Delivery Systems: Applications. *J Pharm Bioallied Sci* **2010**, *2*, 72-79.

7. Archontaki, H. A.; Vertzoni, M. V.; Athanassiou-Malaki, M. H. Study on the Inclusion Complexes of Bromazepam with Beta- and Beta-Hydroxypropyl-Cyclodextrins. *J. Pharm. Biomed. Anal.* **2002**, *28*, 761-769.

8. Chatjigakis, A. K.; Donze, C.; Coleman, A. W.; Cardot, P. Solubility Behavior of Beta-Cyclodextrin in Water Cosolvent Mixtures. *Anal. Chem.* **1992**, *64*, 1632-1634.

9. Arima, H.; Yunomae, K.; Miyake, K.; Irie, T.; Hirayama, F.; Uekama, K. Comparative Studies of the Enhancing Effects of Cyclodextrins on the Solubility and Oral Bioavailability of Tacrolimus in Rats. *J. Pharm. Sci.* **2001**, *90*, 690-701.

10. Arima, H.; Miyaji, T.; Irie, T.; Hirayama, F.; Uekama, K. Enhancing Effect of Hydroxypropyl-B-Cyclodextrin on Cutaneous Penetration and Activation of Ethyl 4-Biphenylyl Acetate in Hairless Mouse Skin. *Eur. J. Pharm. Sci.* **1998**, *6*, 53-59.

11. Shimada, K.; Fujikawa, K.; Yahara, K.; Nakamura, T. Antioxidative Properties of Xanthan on the Autoxidation of Soybean Oil in Cyclodextrin Emulsion. *J. Agric. Food Chem.* **1992**, *40*, 945-948.

12. Harada, A. Cyclodextrin-Based Molecular Machines. *Acc. Chem. Res.* **2001**, *34*, 456-464.

13. Eelkema, R.; Maeda, K.; Odell, B.; Anderson, H. L. Radical Cation Stabilization in a Cucurbituril Oligoaniline Rotaxane. *J. Am. Chem. Soc.* **2007**, *129*, 12384-+.

14. Talotta, C.; Gaeta, C.; Neri, P. Stereoprogrammed Direct Synthesis of Calixarene-Based [3]Rotaxanes. *Org. Lett.* **2012**, *14*, 3104-3107.

15. Wenz, G.; Han, B. H.; Muller, A. Cyclodextrin Rotaxanes and Polyrotaxanes. *Chem. Rev.* **2006**, *106*, 782-817.

16. Chu, P. L. E.; Wang, L. Y.; Khatua, S.; Kolomeisky, A. B.; Link, S.; Tour, J. M. Synthesis and Single-Molecule Imaging of Highly Mobile Adamantane-Wheeled Nanocars. *ACS Nano* **2013**, *7*, 35-41.

17. Khatua, S.; Godoy, J.; Tour, J. M.; Link, S. Influence of the Substrate on the Mobility of Individual Nanocars. *J. Phys. Chem. Lett.* **2010**, *1*, 3288-3291.

18. Granadero, D.; Bordello, J.; Perez-Alvite, M. J.; Novo, M.; Al-Soufi, W. Host-Guest Complexation Studied by Fluorescence Correlation Spectroscopy: Adamantane-Cyclodextrin Inclusion. *Int J Mol Sci* **2010**, *11*, 173-188.

19. Harrison, J. C.; Eftink, M. R. Cyclodextrin Adamantanecarboxylate Inclusion Complexes - a Model System for the Hydrophobic Effect. *Biopolymers* **1982**, *21*, 1153-1166.

20. Jaime, C.; Redondo, J.; Sanchezferrando, F.; Virgili, A. Beta-Cyclodextrin Inclusion Complex with Adamantane Intermolecular H-1(H-1) Noe Determinations and Molecular Mechanics Calculations. *J. Mol. Struct.* **1991**, *248*, 317-329.

21. Paolino, M.; Ennen, F.; Lamponi, S.; Cernescu, M.; Voit, B.; Cappelli, A.; Appelhans, D.; Komber, H. Cyclodextrin-Adamantane Host-Guest Interactions on the Surface of Biocompatible Adamantyl-Modified Glycodendrimers. *Macromolecules* **2013**, *46*, 3215-3227.

22. Harada, A.; Takahashi, S. Preparation and Properties of Inclusion Complexes of 1,2-Dicarbadodecaborane(12) with Cyclodextrins. *J Chem Soc Chem Comm* **1988**, 1352-1353.

23. Yusubov, M. S.; Yusubova, R. Y.; Nemykin, V. N.; Maskaev, A. V.; Geraskina, M. R.; Kirschning, A.; Zhdankin, V. V. Potassium 4-Iodylbenzenesulfonate: Preparation, Structure, and Application as a Reagent for Oxidative Iodination of Arenes. *Eur. J. Org. Chem.* **2012**, 5935-5942.

24. Guan, Z. J.; Chai, X. Y.; Yu, S. C.; Hu, H. G.; Jiang, Y. Y.; Meng, Q. G.; Wu, Q. Y. Synthesis, Molecular Docking, and Biological Evaluation of Novel Triazole Derivatives as Antifungal Agents. *Chem. Biol. Drug Des.* **2010**, *76*, 496-504.

25. Miller, S. C. Profiling Sulfonate Ester Stability: Identification of Complementary Protecting Groups for Sulfonates. *J. Org. Chem.* **2010**, *75*, 4632-4635.

26. Yang, L.; Simionescu, R.; Lough, A.; Yan, H. Some Observations Relating to the Stability of the Bodipy Fluorophore under Acidic and Basic Conditions. *Dyes Pigm.* **2011**, *91*, 264-267.

27. Niu, S.; Ziessel, R.; Ulrich, G. Advanced Water Soluble Bodipy Dyes Synthesis and Application. *Thesis. Thèse De Doctorat: Chimie: Strasbourg* **2011**.

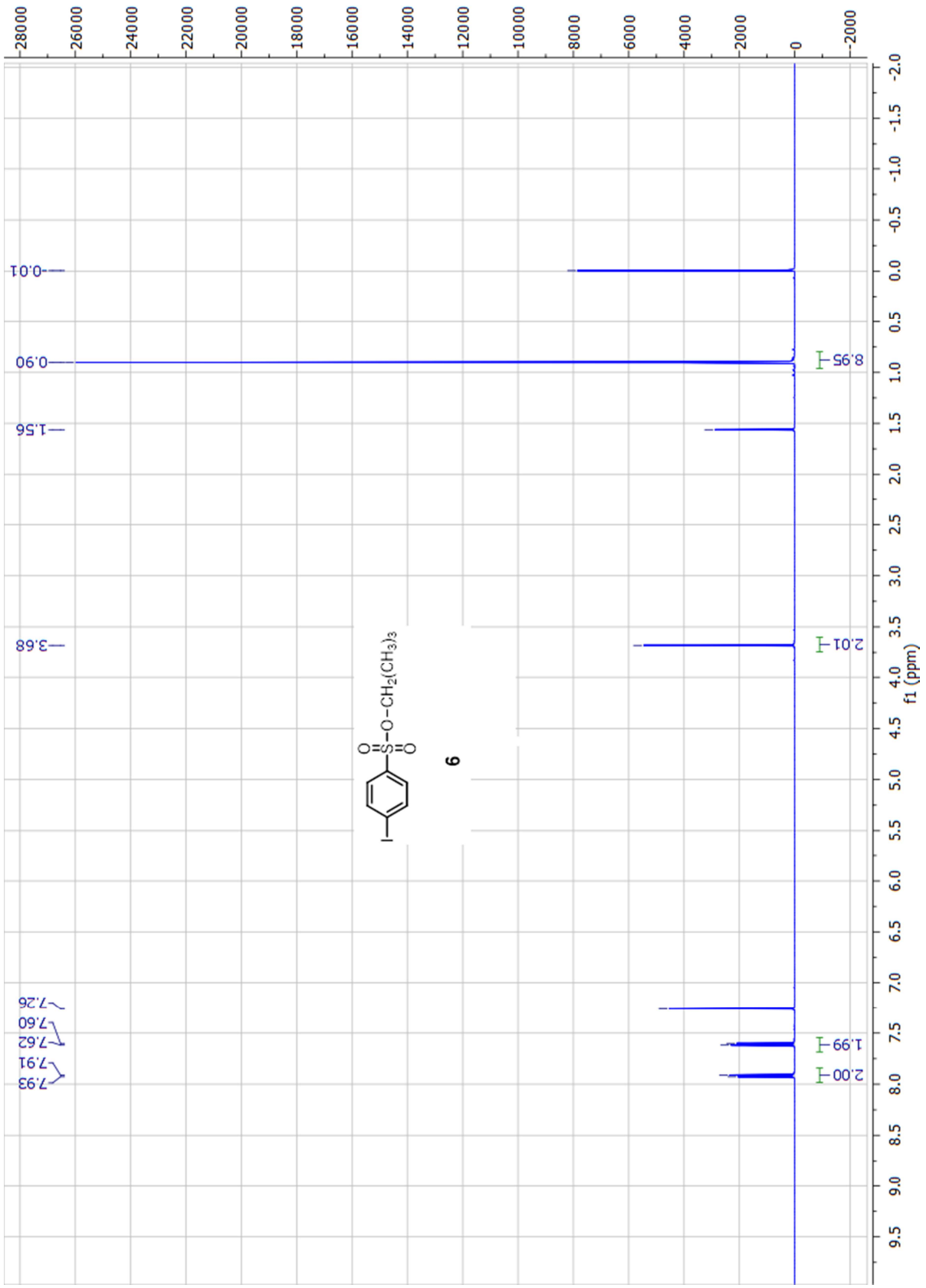
0.01
0.90
1.56
3.68
7.26
7.60
7.62
7.91
7.93
8.95
2.01
1.99
2.00
6
f1 (ppm)

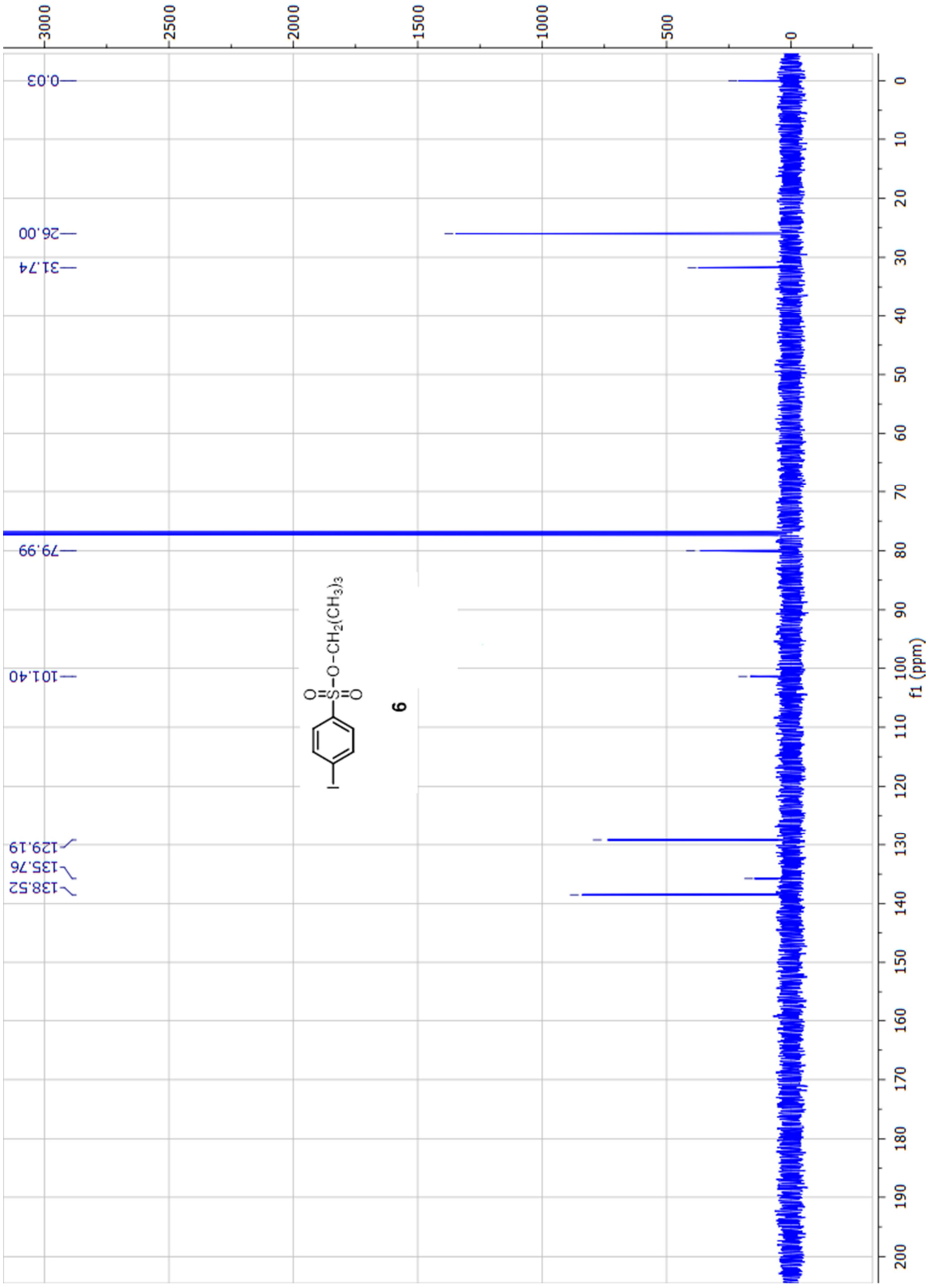
0.03
26.00
31.74
79.99
101.40
129.19
135.76
138.52
6
f1 (ppm)

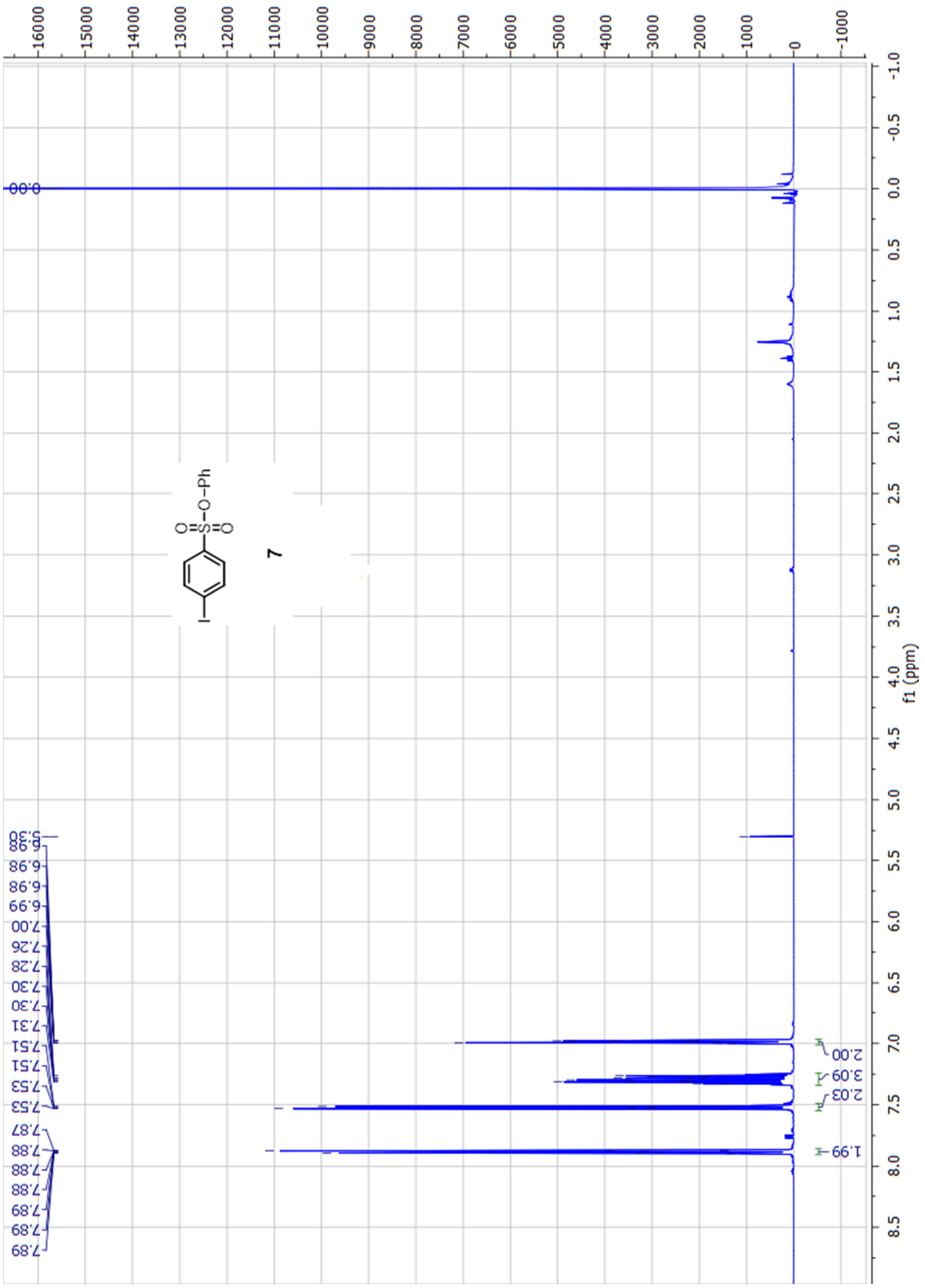
7
f1 (ppm)
2.00
3.09
2.03
1.99

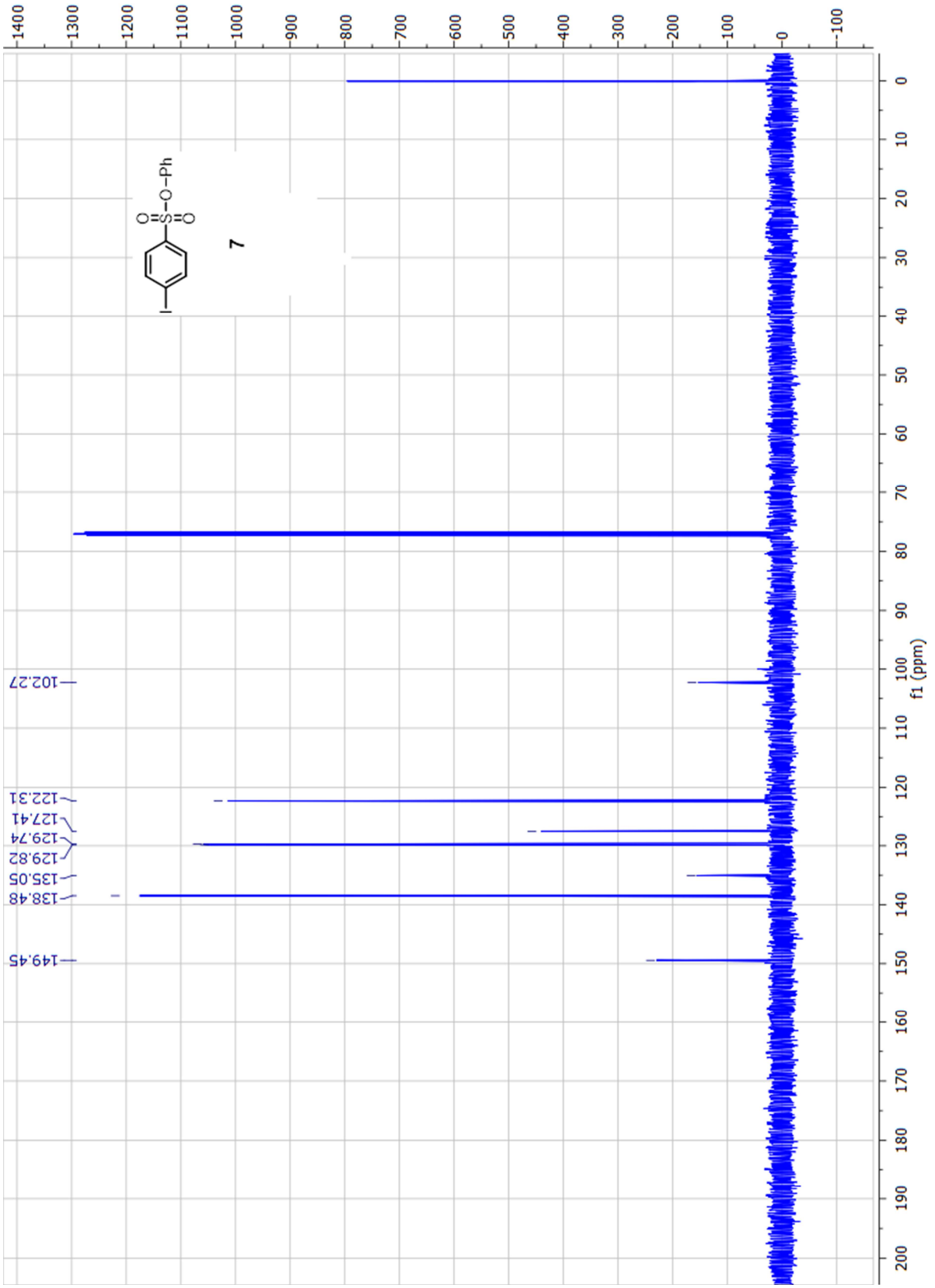
7
102.27
122.31
127.41
129.74
129.82
135.05
138.48
149.45
f1 (ppm)

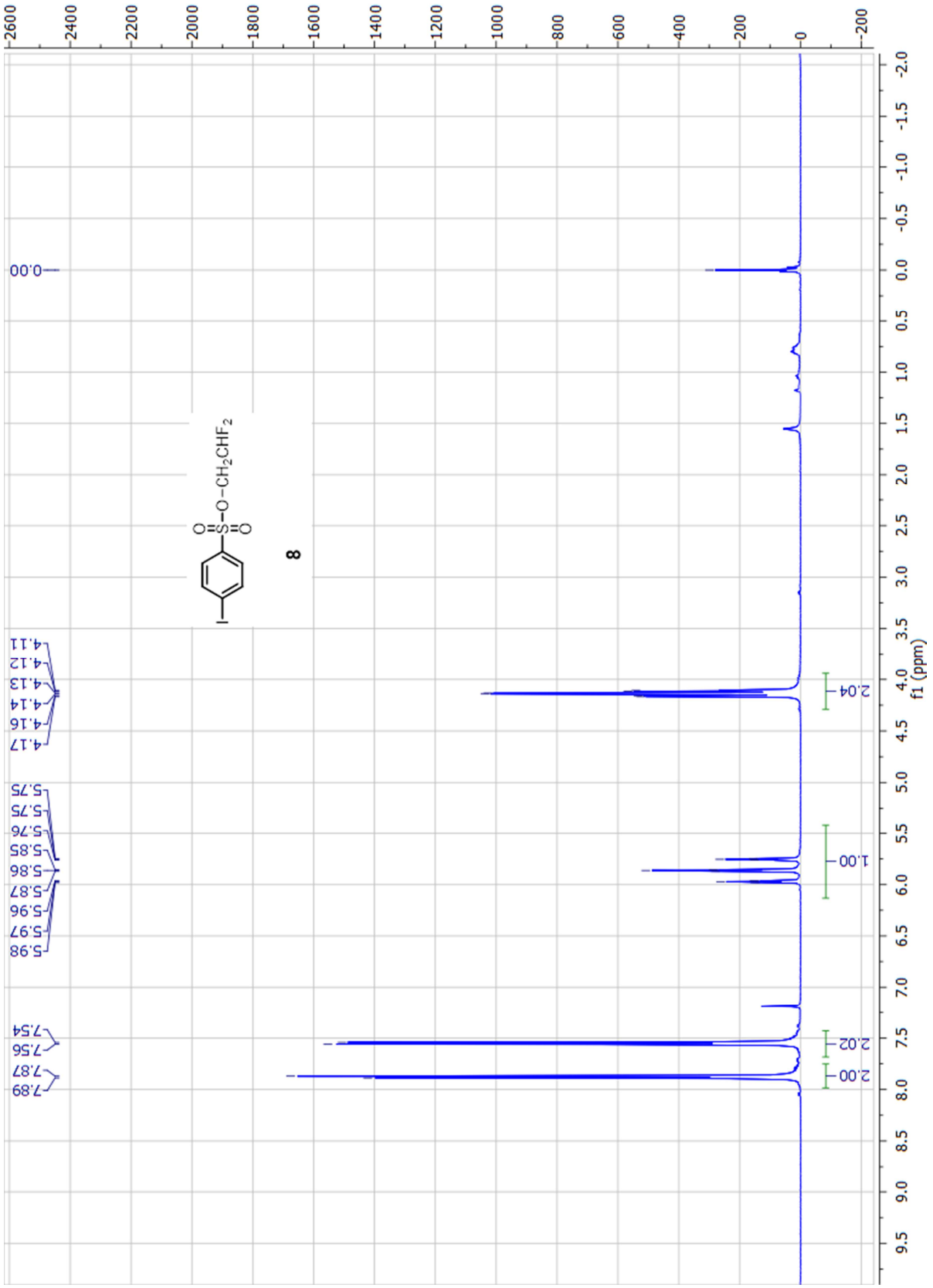
8
0.00
4.11
4.12
4.13
4.14
4.16
4.17
5.75
5.75
5.76
5.85
5.86
5.87
5.96
5.97
5.98
7.54
7.56
7.87
7.89
2.04
1.00
2.02
2.00
f1 (ppm)

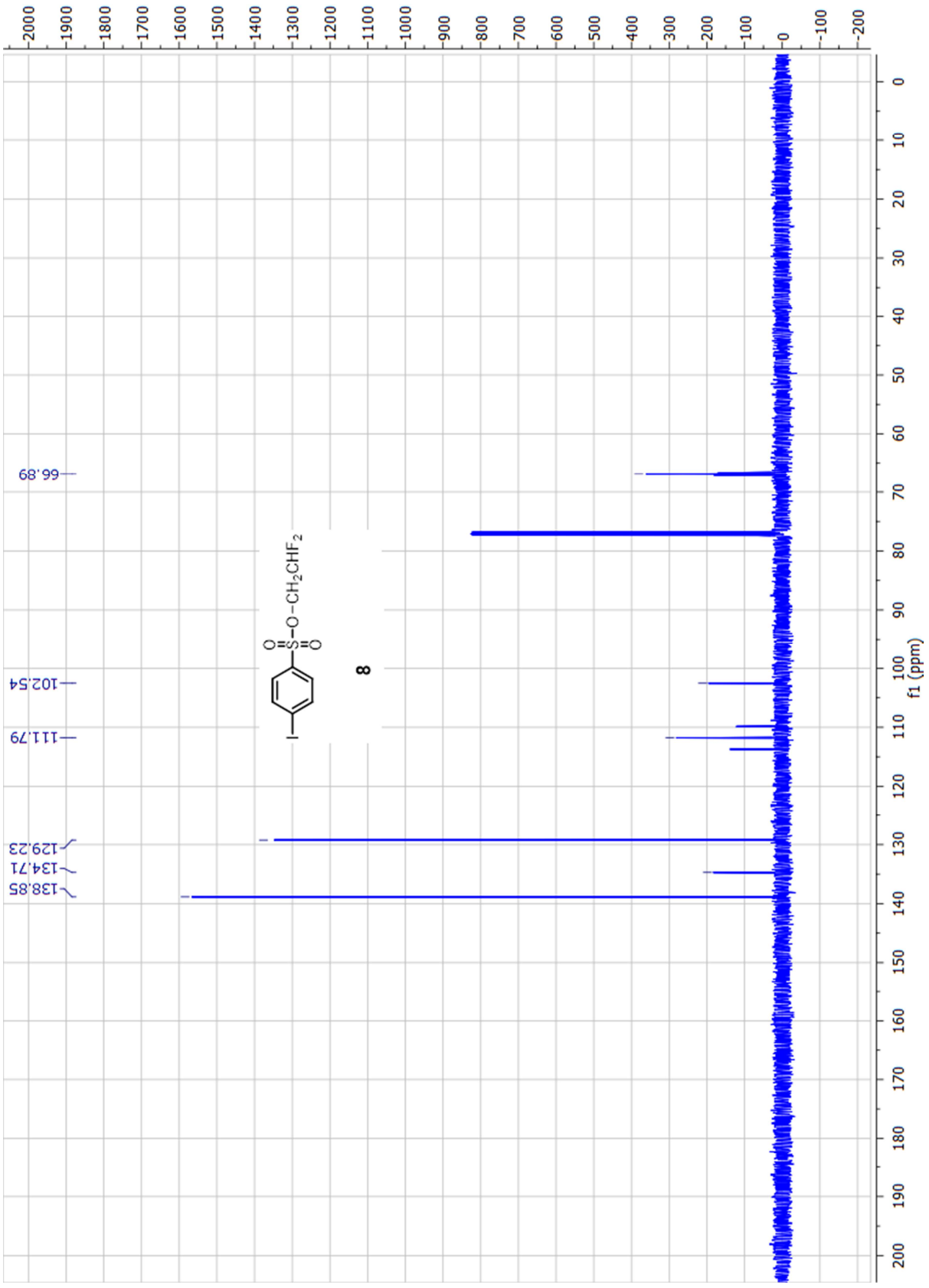
66.89
102.54
111.79
129.23
134.71
138.85
8
f1 (ppm)

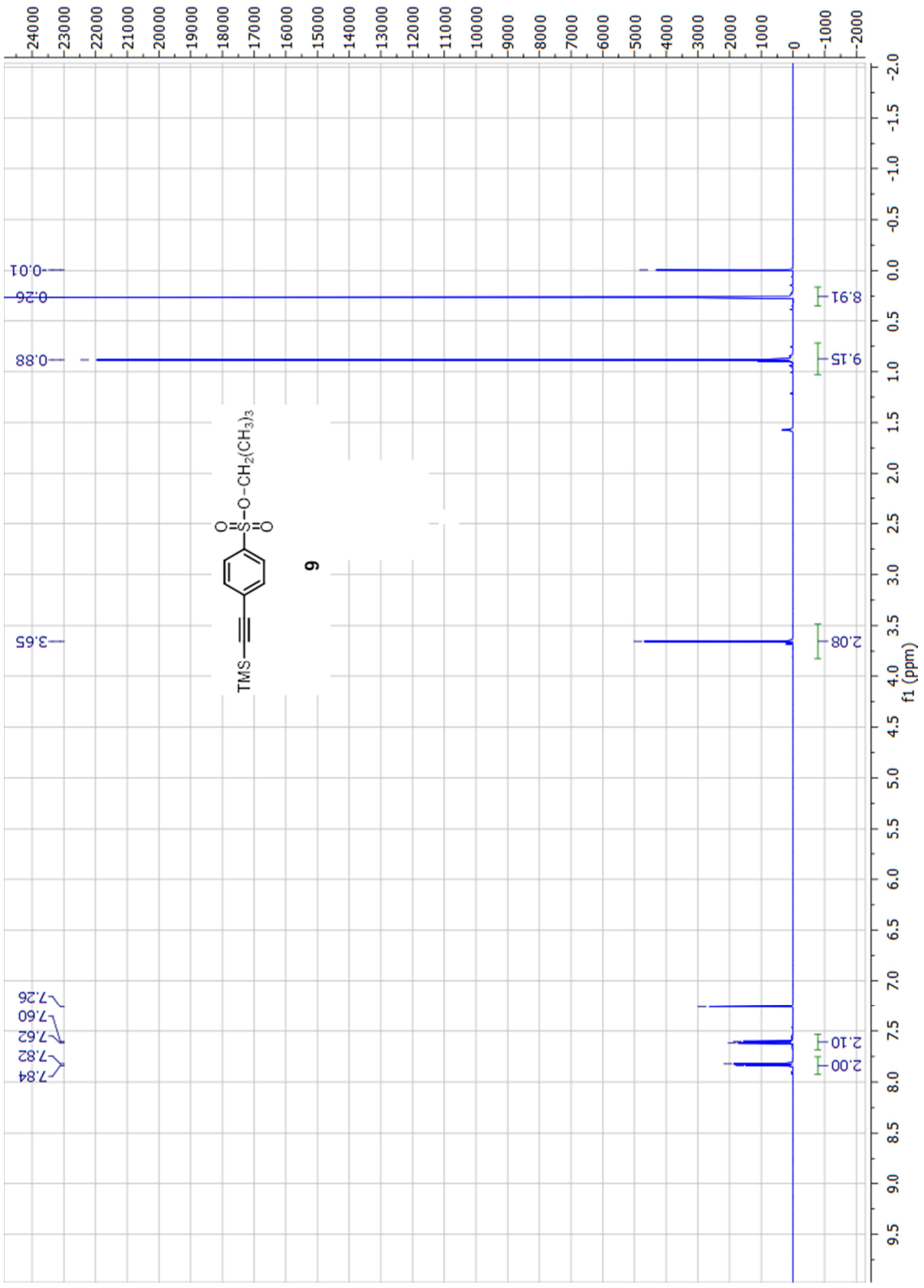
TMS
O
S
O
O
CH2(CH3)3
9
0.01
0.26
0.88
3.65
7.26
7.60
7.62
7.82
7.84
8.91
9.15
2.08
2.10
2.00
f1 (ppm)

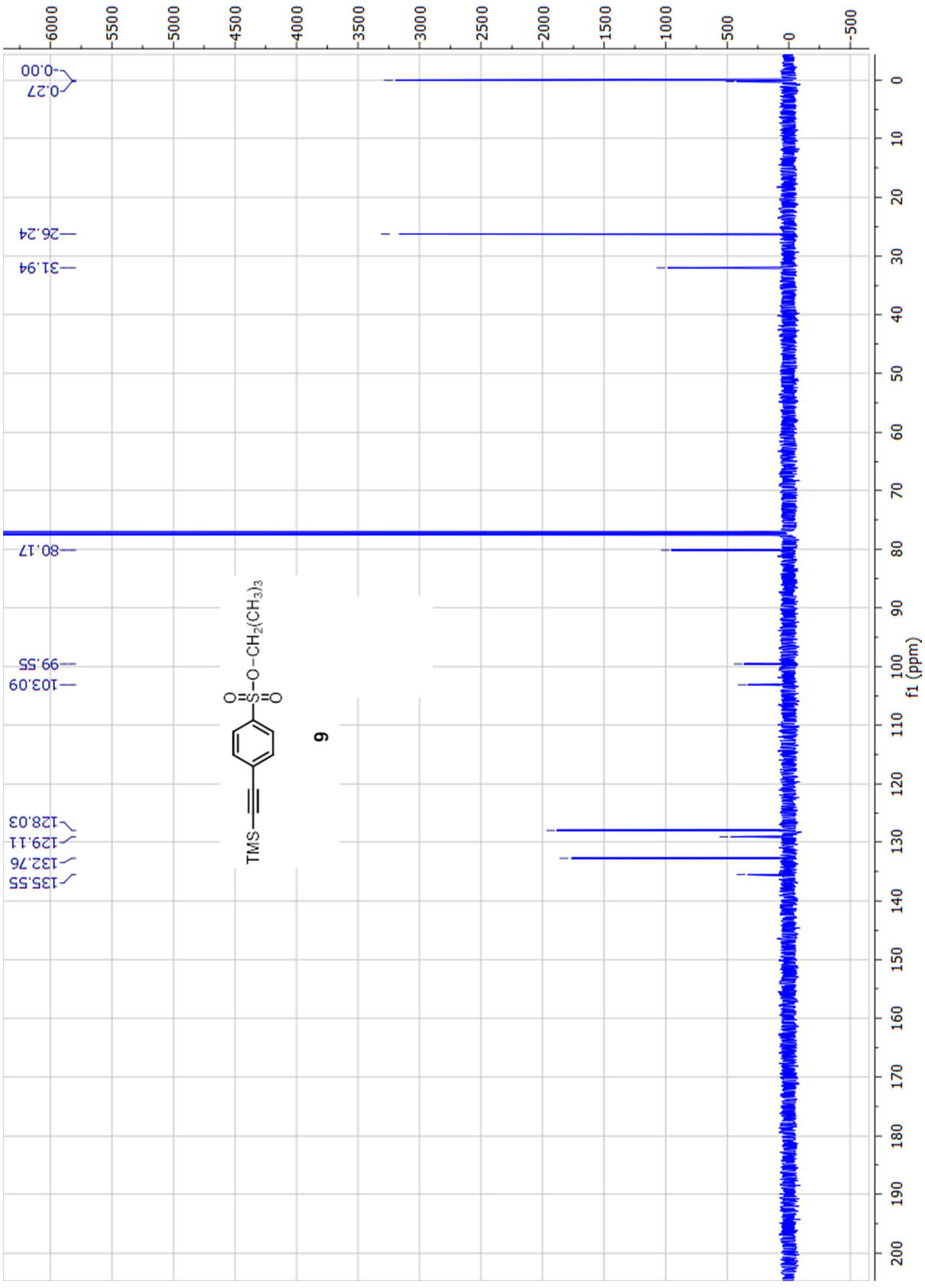
0.27
0.00
26.24
31.94
80.17
99.55
103.09
128.03
129.11
132.76
135.55
TMS
O
S
O
O–CH2(CH3)3
9
f1 (ppm)

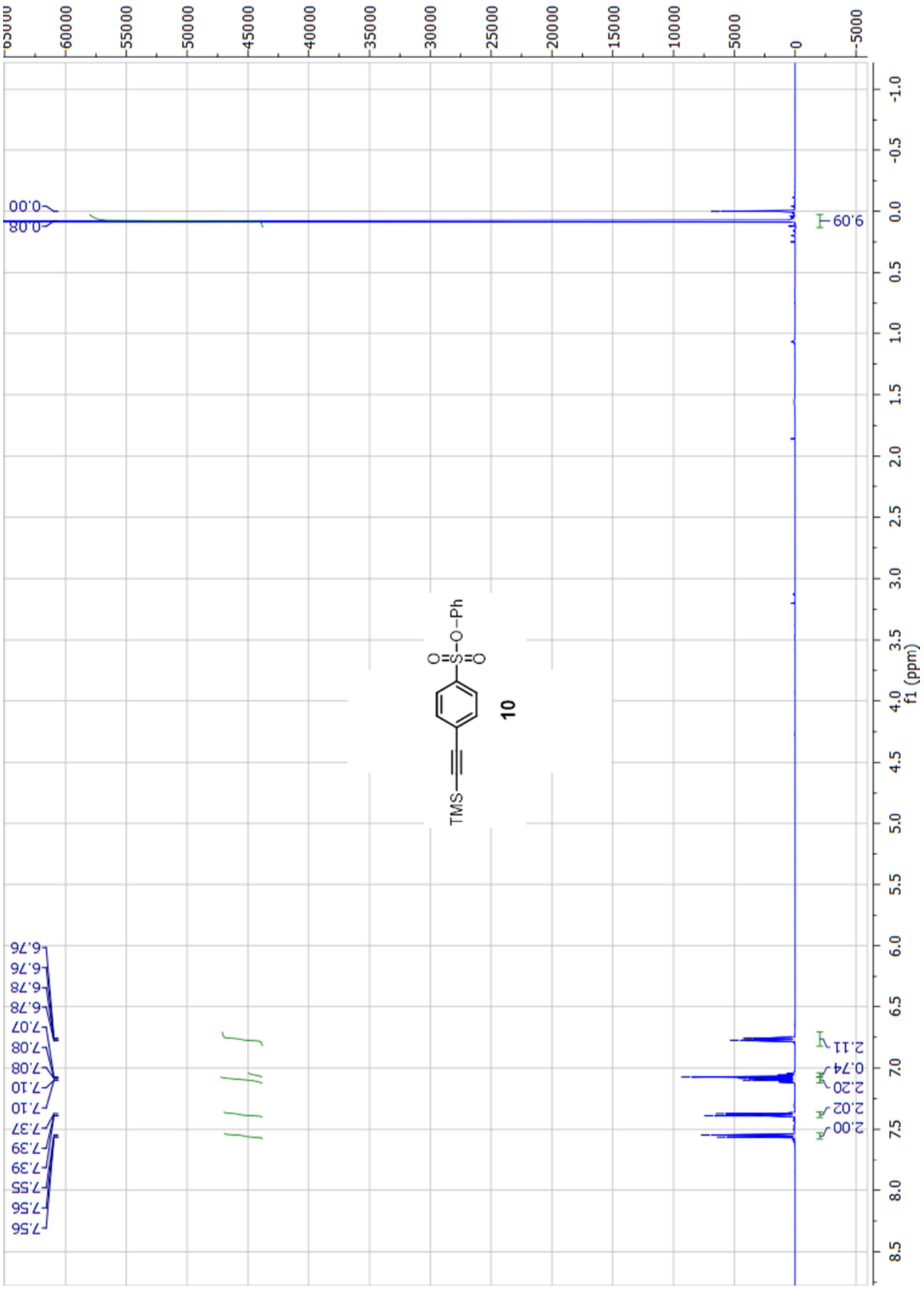
TMS
O
S
O
O–Ph
10
f1 (ppm)

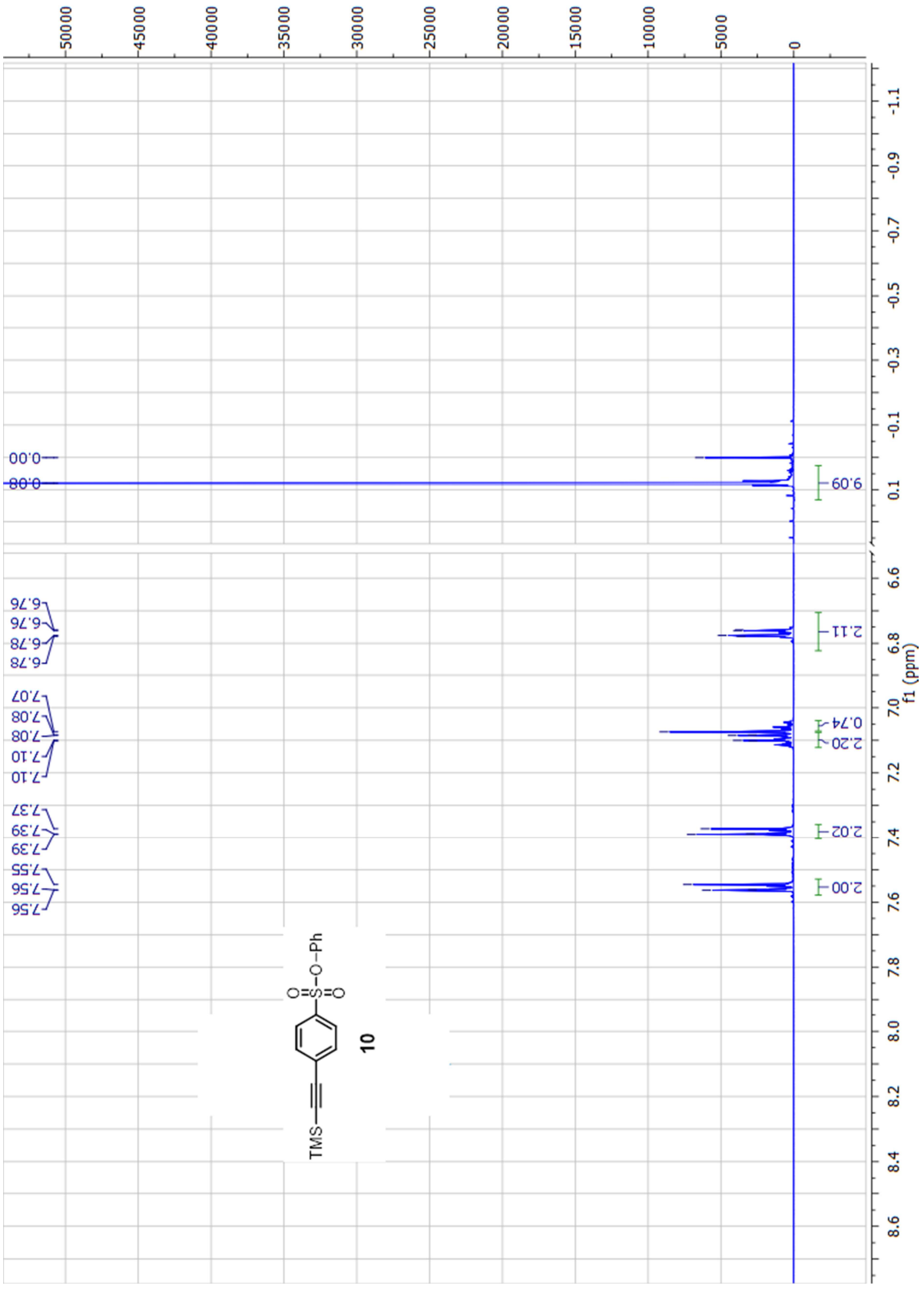
0.00
0.08
9.09
6.76
6.76
6.78
6.78
7.07
7.08
7.08
7.10
7.10
7.37
7.39
7.39
7.55
7.56
7.56
2.11
0.74
2.20
2.02
2.00
f1 (ppm)
TMS
O
S
O
O
O
Ph
10

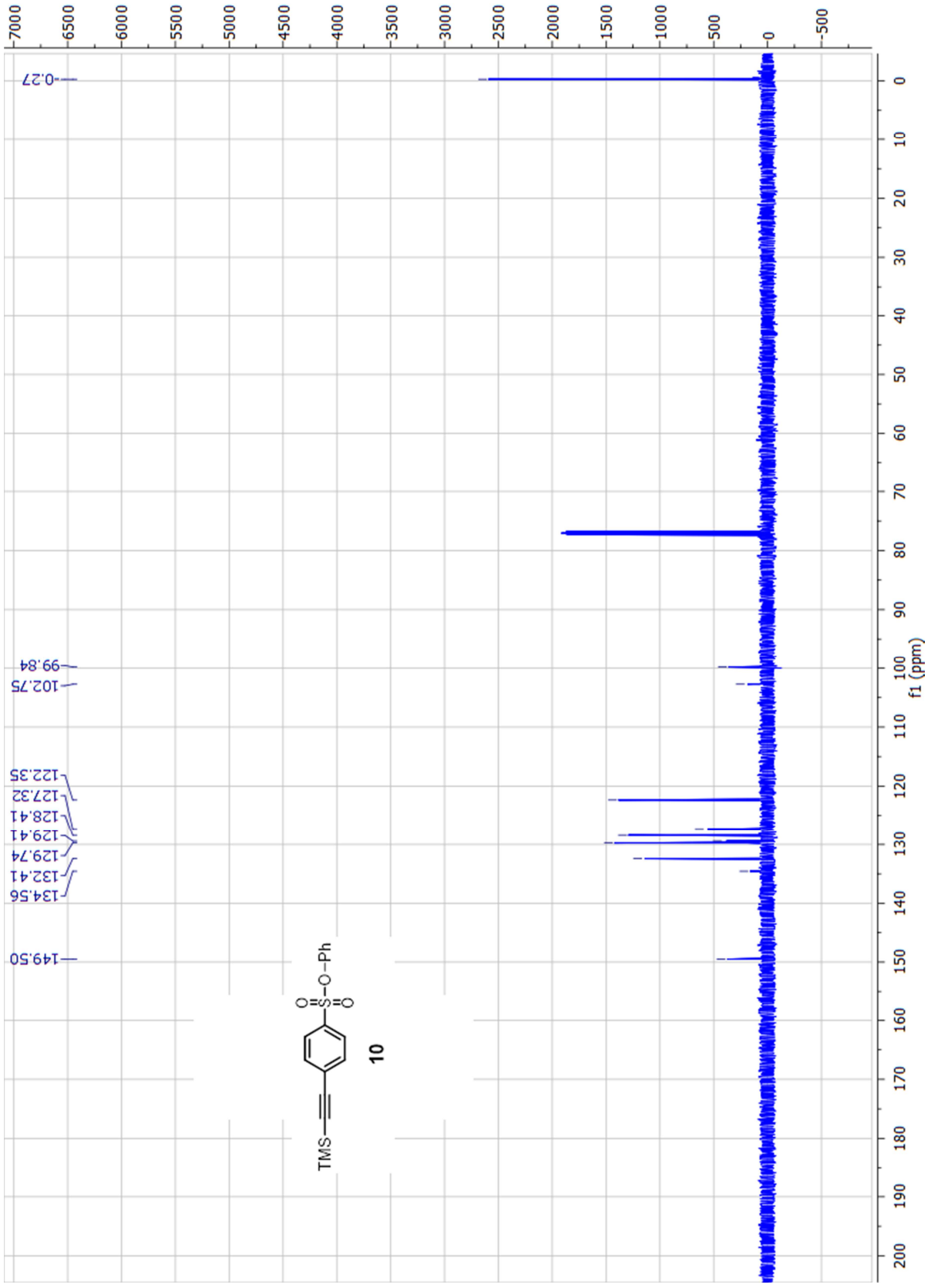
-0.27
99.84
102.75
122.35
127.32
128.41
129.41
129.74
132.41
134.56
149.50
TMS
O=S=O
O-Ph
10
f1 (ppm)

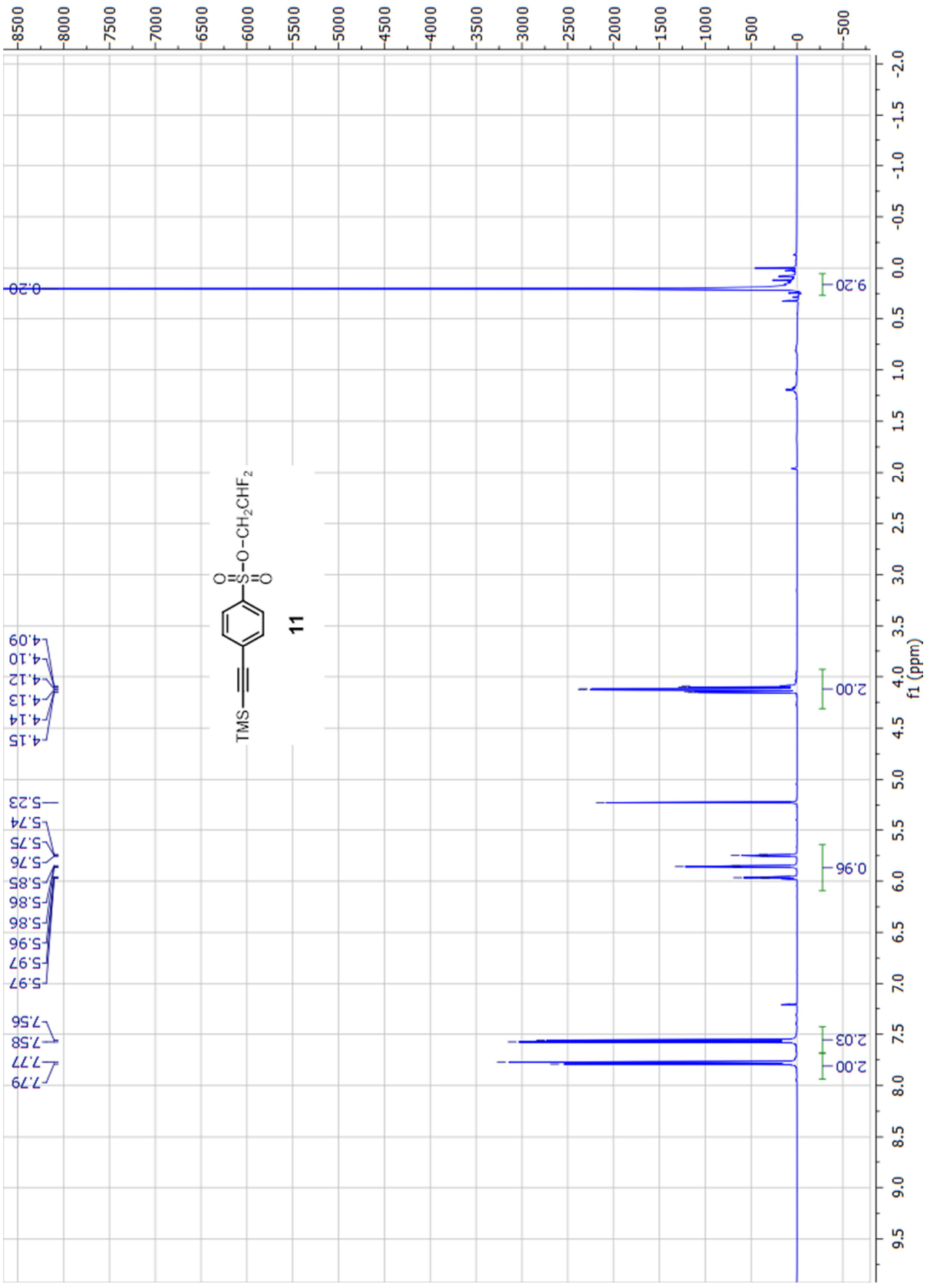
0.20
4.09
4.10
4.12
4.13
4.14
4.15
5.23
5.74
5.75
5.76
5.85
5.86
5.86
5.96
5.97
5.97
7.56
7.58
7.77
7.79
9.20
2.00
0.96
2.03
2.00
TMS
O
S
O
O
O–CH2CHF2
11
f1 (ppm)

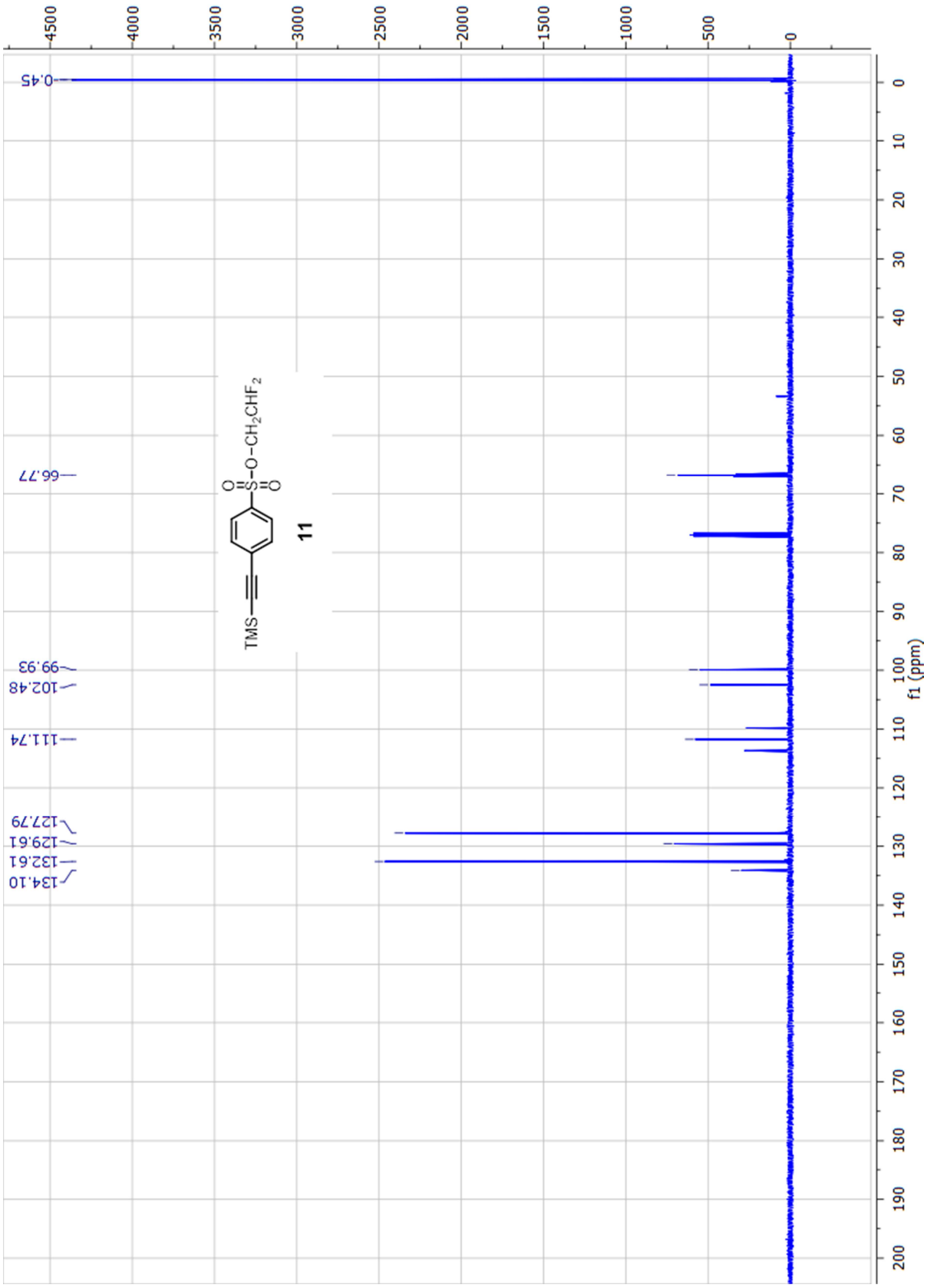
0.45
66.77
99.93
102.48
111.74
127.79
129.61
132.61
134.10
TMS
O
S
O
O
CH2CHF2
11
f1 (ppm)

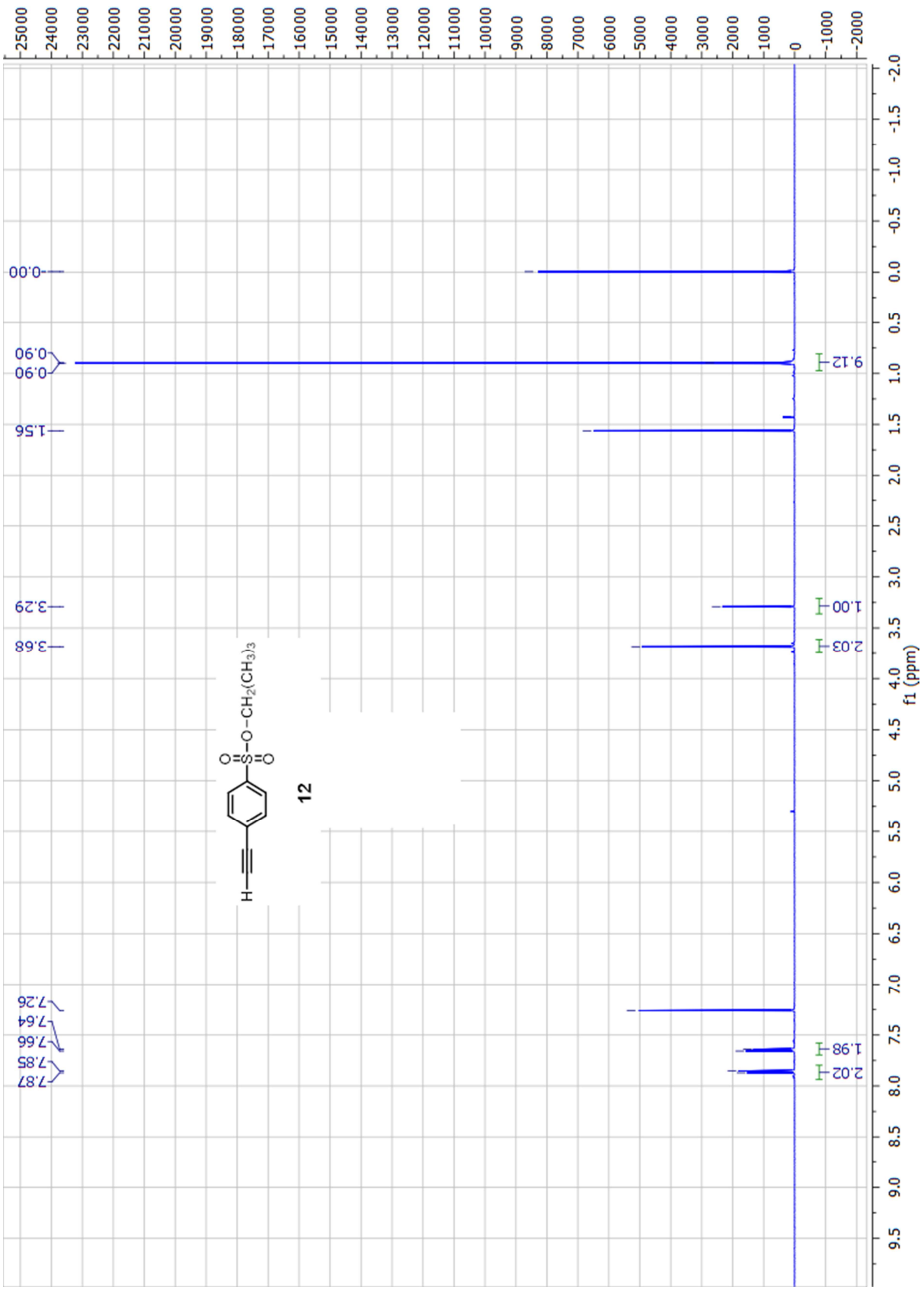
12
f1 (ppm)
0.00
0.90
0.90
1.56
3.29
3.68
7.26
7.64
7.66
7.85
7.87
9.12
1.00
2.03
1.98
2.02

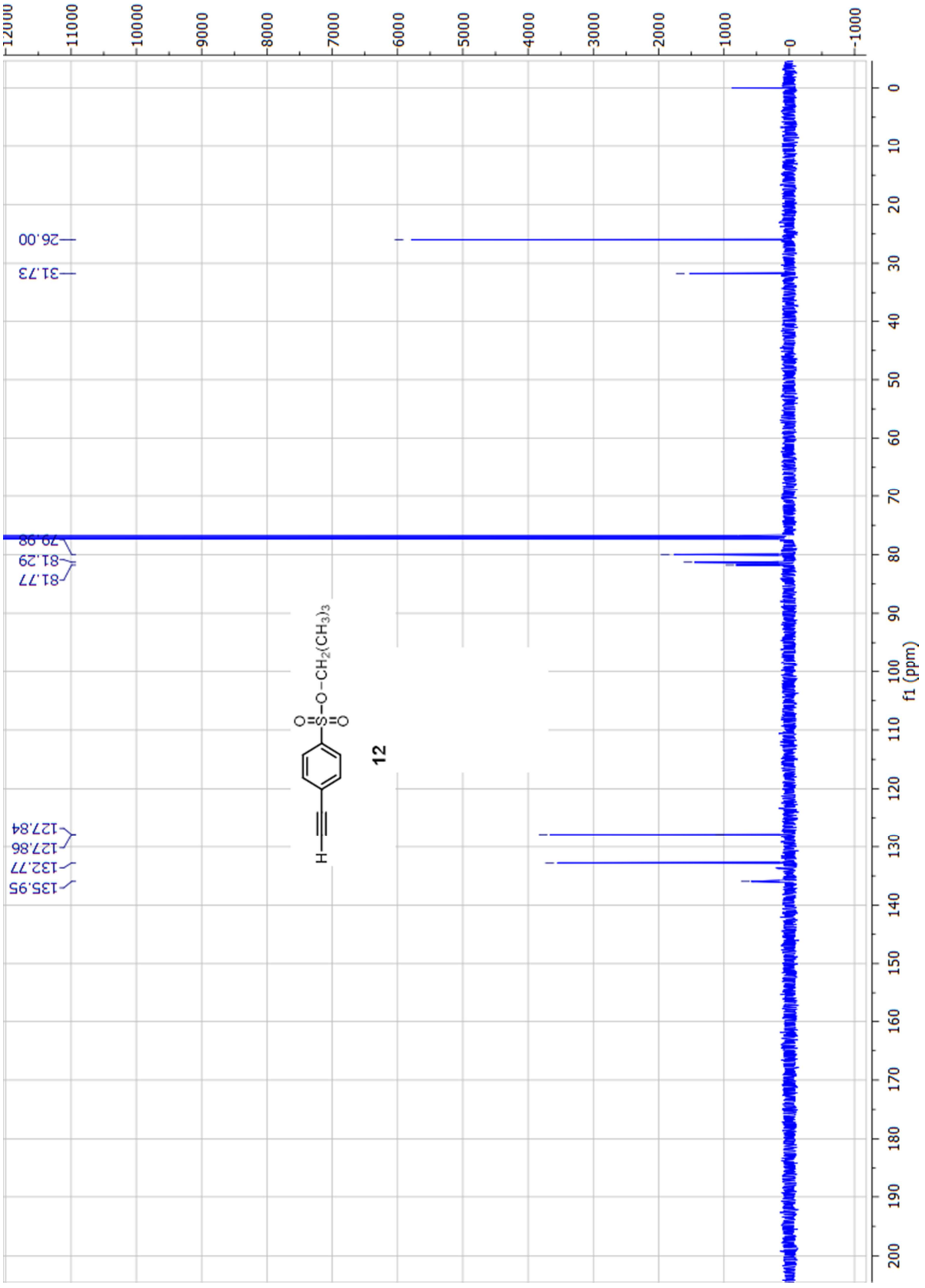
135.95
132.77
127.86
127.84
81.77
81.29
79.98
31.73
26.00
12
f1 (ppm)

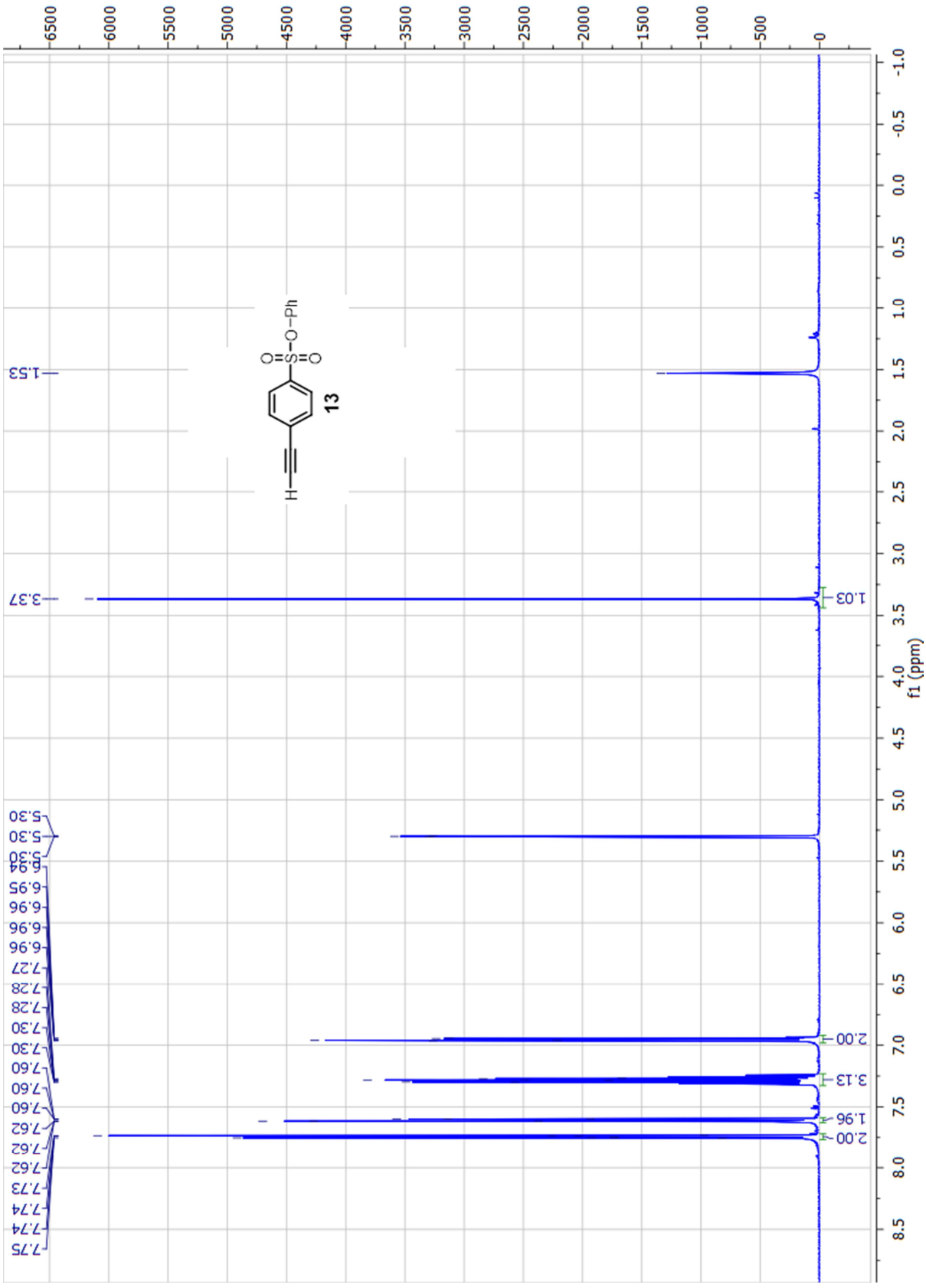
13
f1 (ppm)

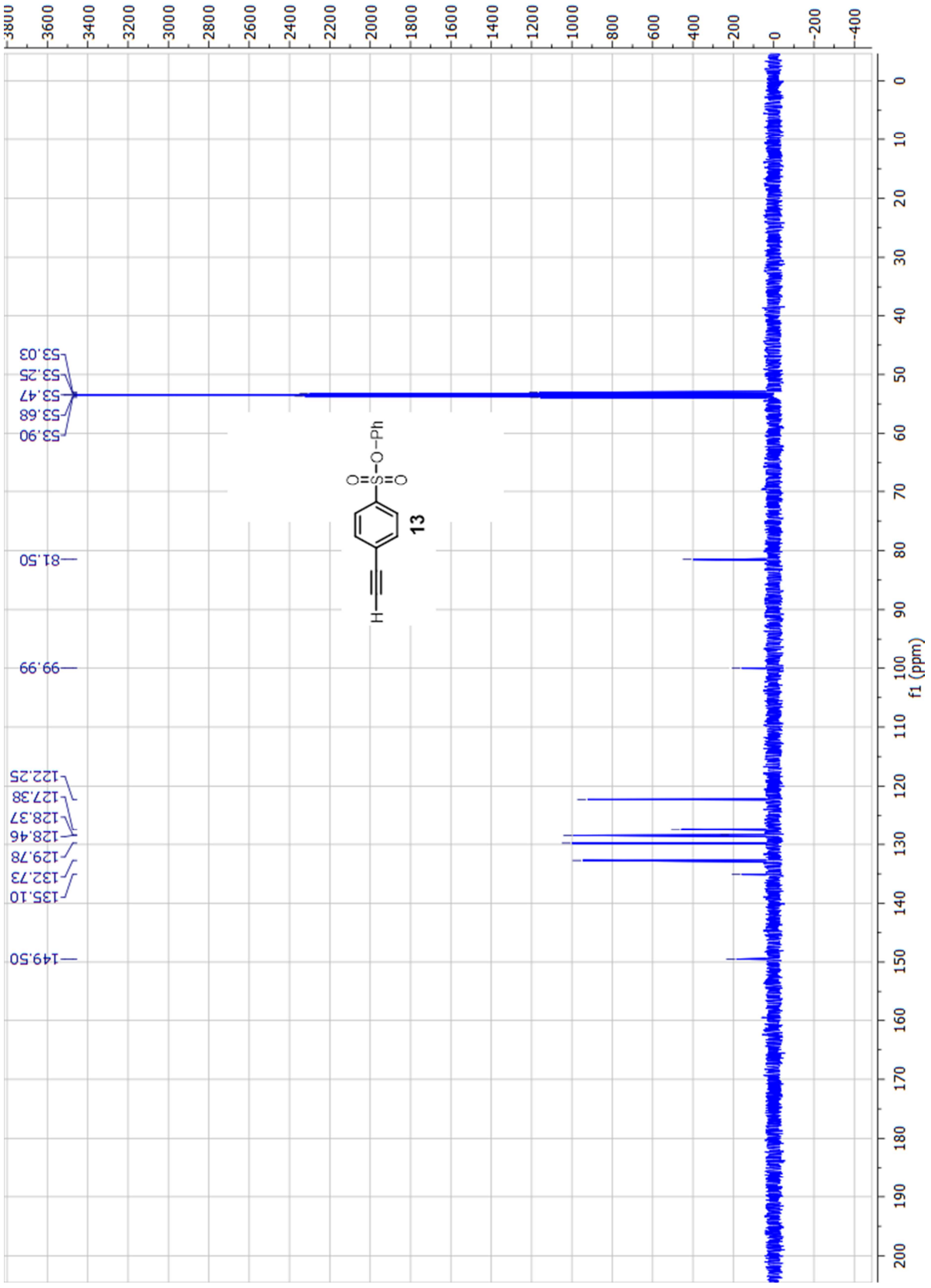
53.03
53.25
53.47
53.68
53.90
81.50
99.99
122.25
127.38
128.37
128.46
129.78
132.73
135.10
149.50
13
f1 (ppm)

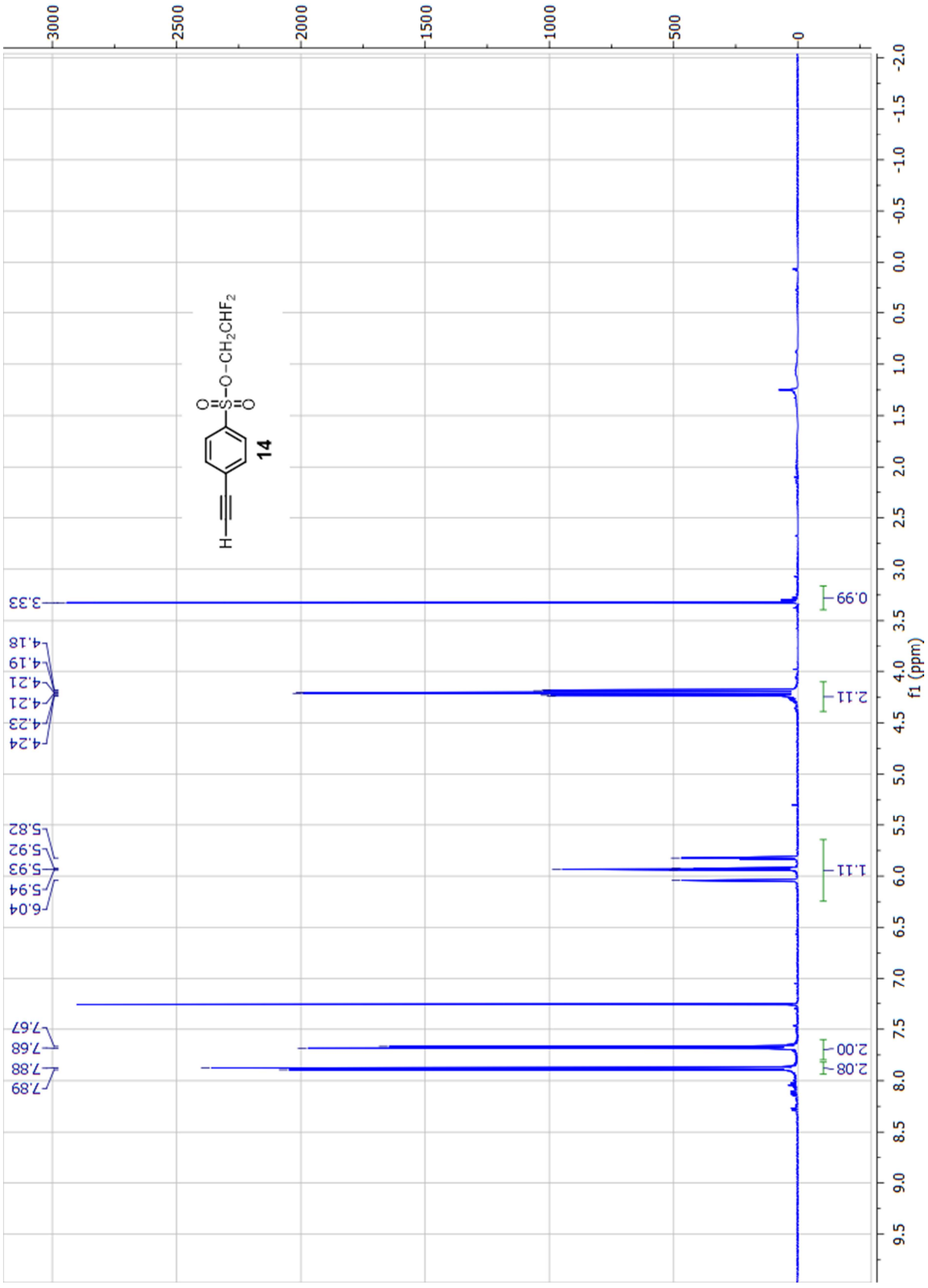
14
3.33
4.18
4.19
4.21
4.21
4.23
4.24
5.82
5.92
5.93
5.94
6.04
7.67
7.68
7.88
7.89
0.99
2.11
1.11
2.00
2.08
f1 (ppm)

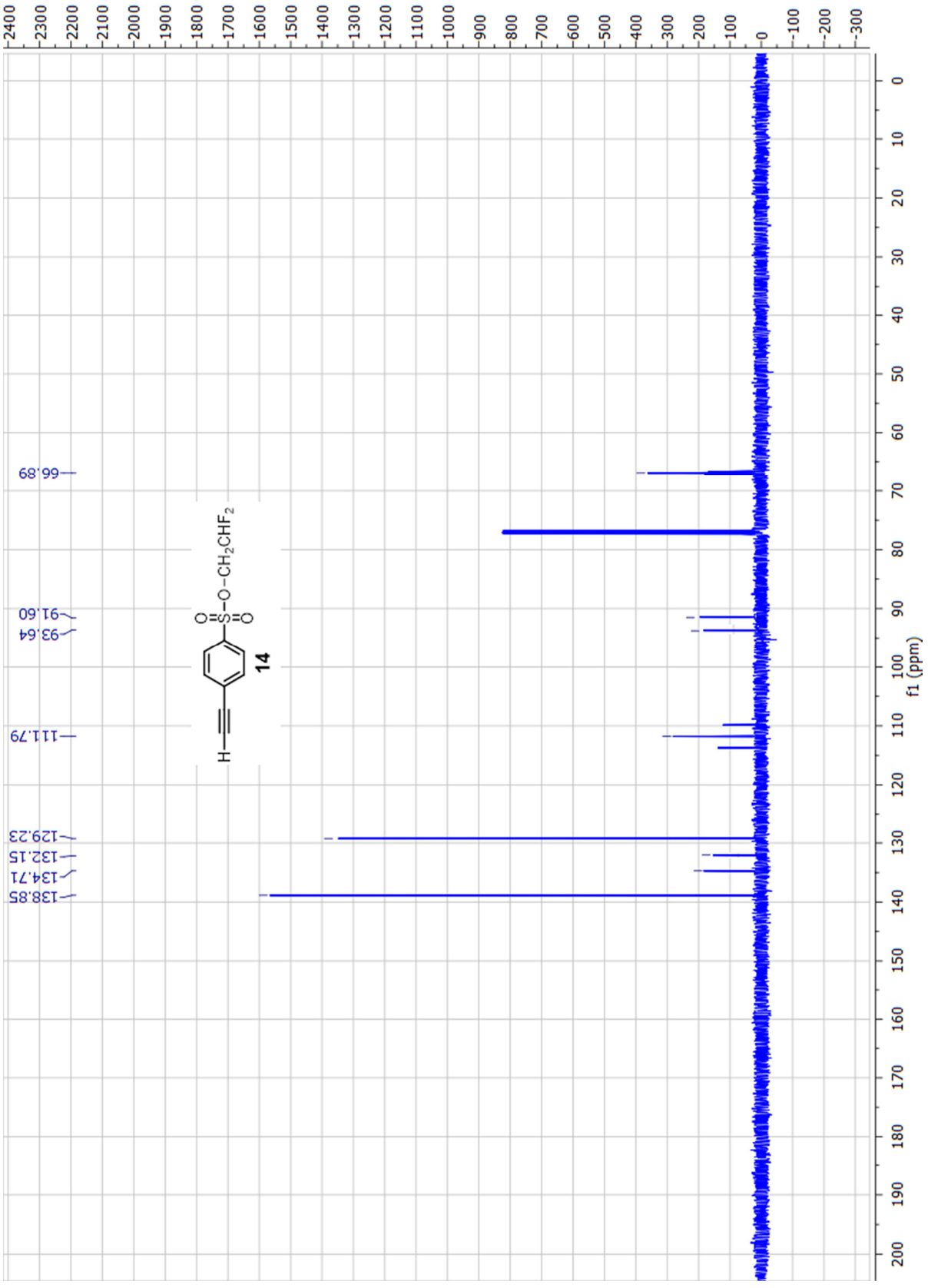
66.89
91.60
93.64
111.79
129.23
132.15
134.71
138.85
14
f1 (ppm)

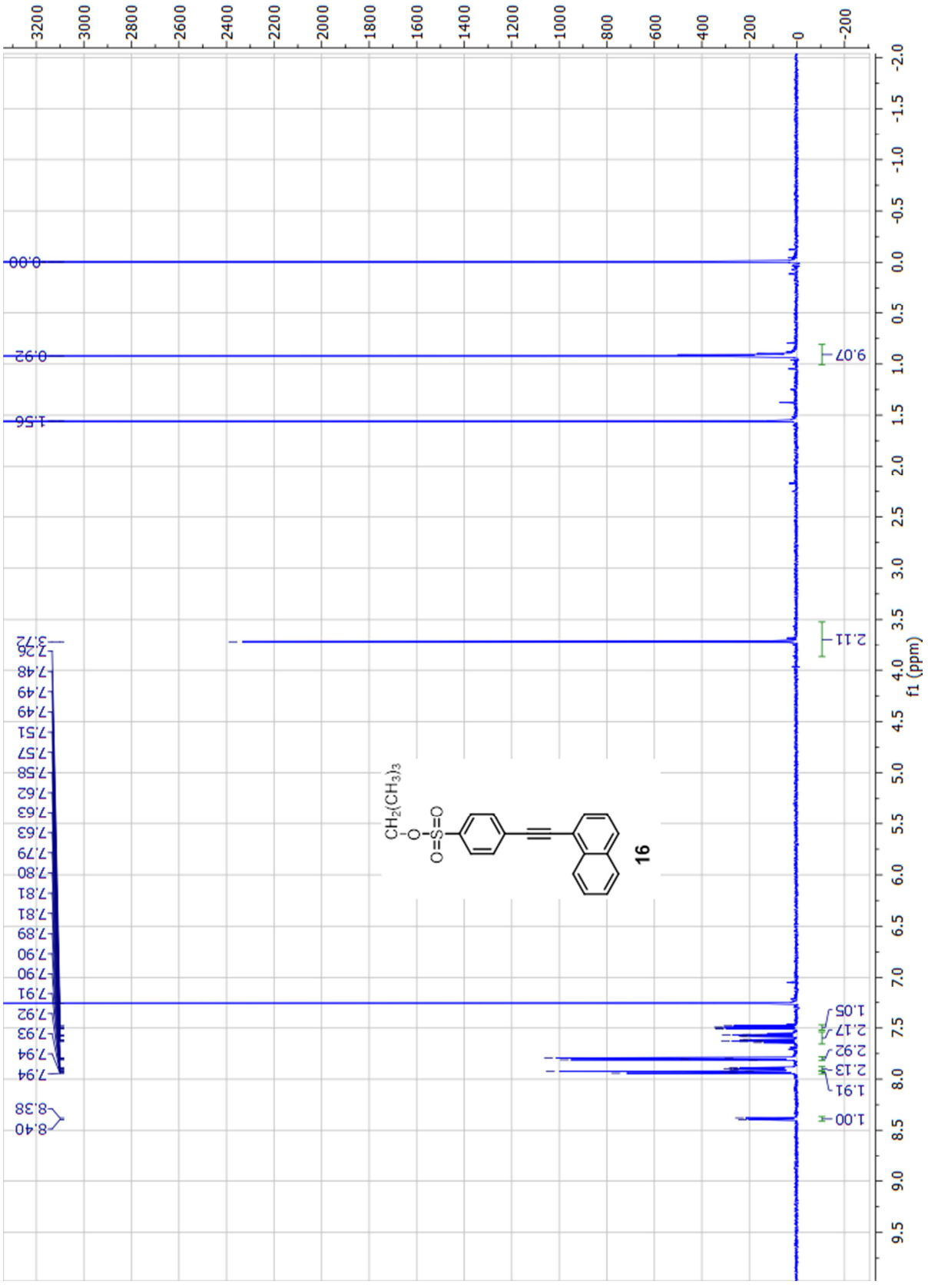
0.00
0.92
1.56
3.72
7.26
7.48
7.49
7.49
7.51
7.57
7.58
7.62
7.63
7.63
7.79
7.80
7.81
7.81
7.89
7.90
7.90
7.91
7.92
7.93
7.94
7.94
8.38
8.40
9.07
2.11
1.05
2.17
2.92
2.13
1.91
1.00
CH2(CH3)3
O
O=S=O
16
f1 (ppm)

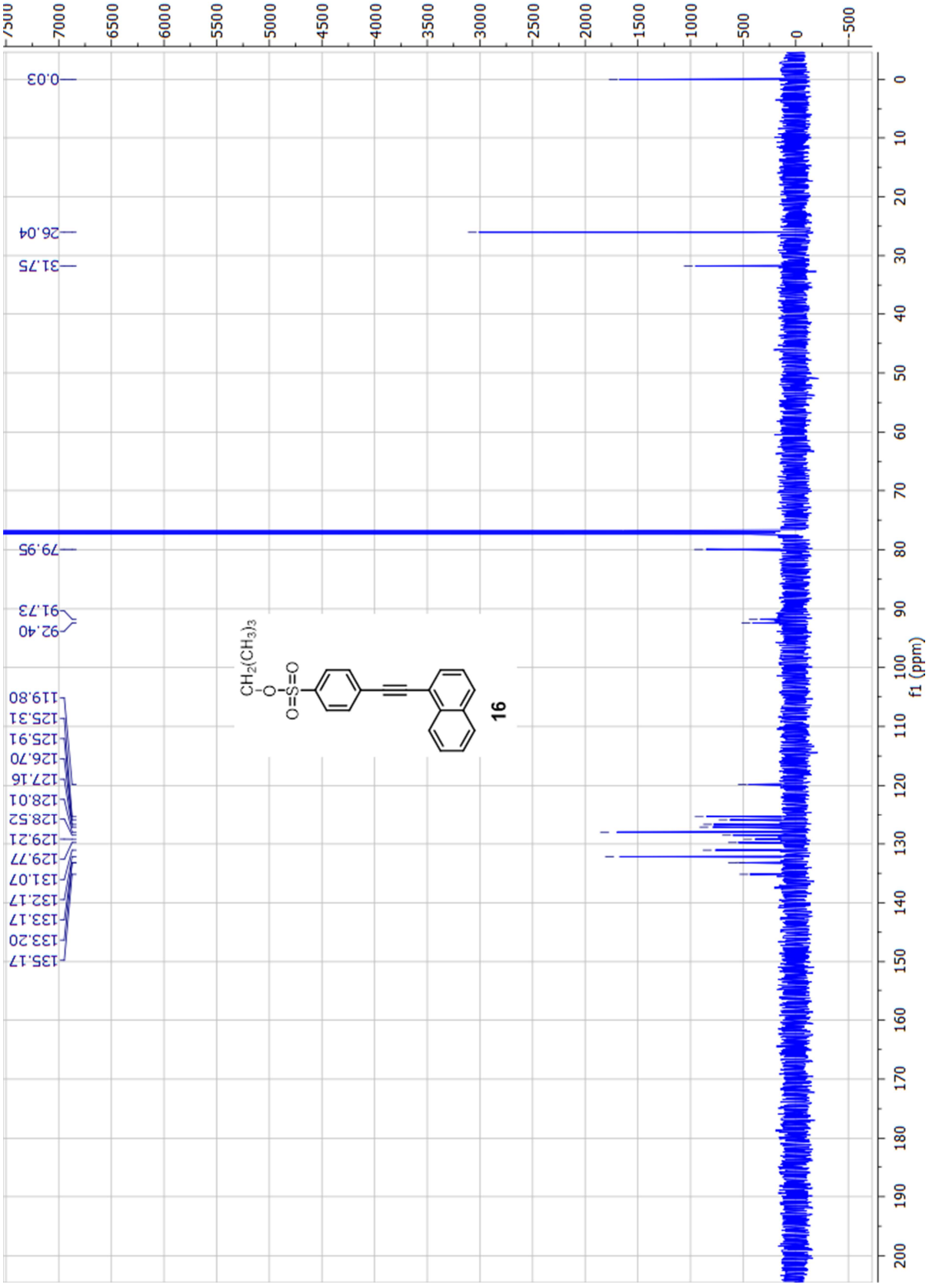
0.03
26.04
31.75
79.95
91.73
92.40
119.80
125.31
125.91
126.70
127.16
128.01
128.52
129.21
129.77
131.07
132.17
133.17
133.20
135.17
CH2(CH3)3
O
O=S=O
16
f1 (ppm)

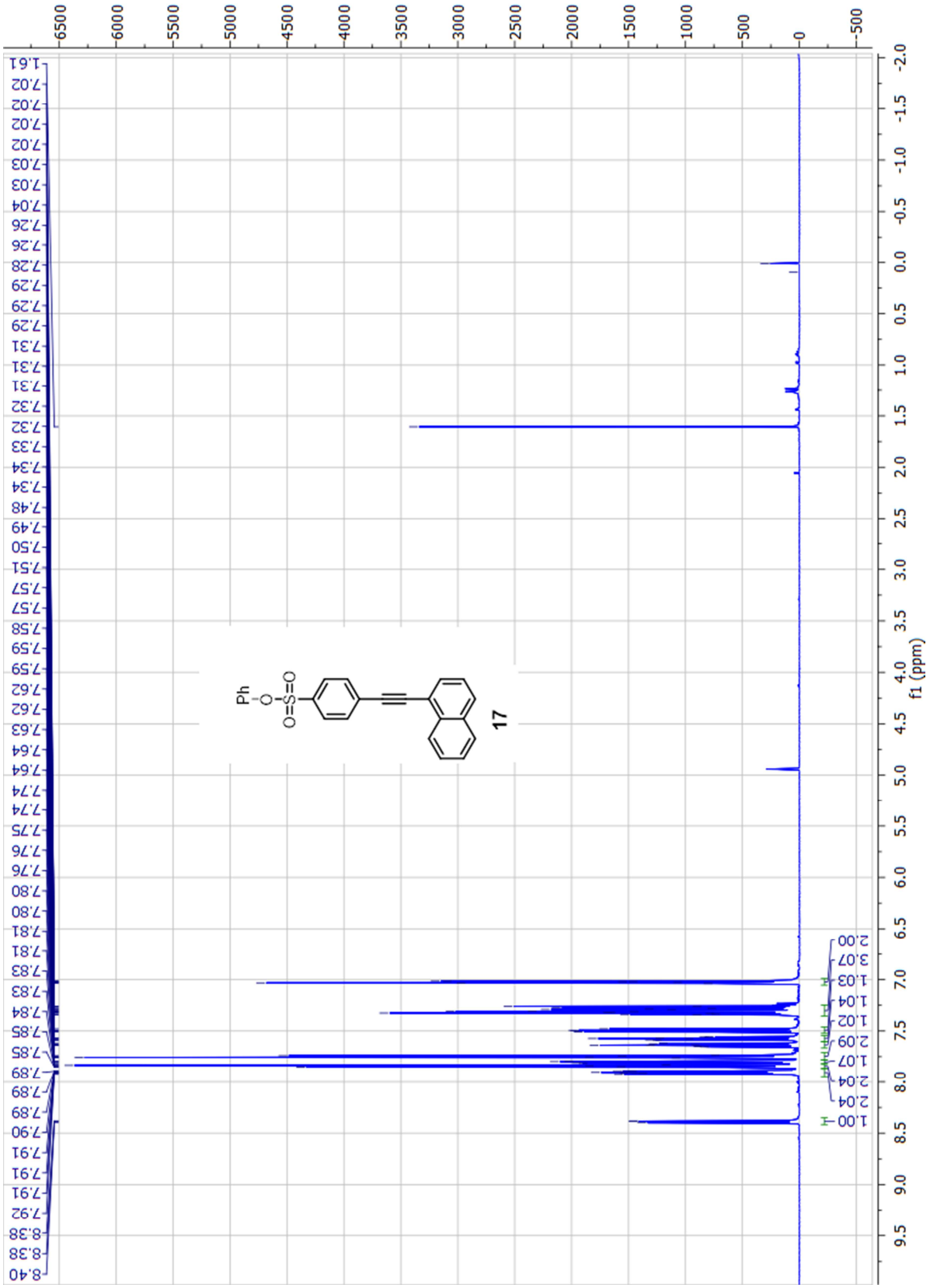
Ph
O
O=S=O
17
f1 (ppm)

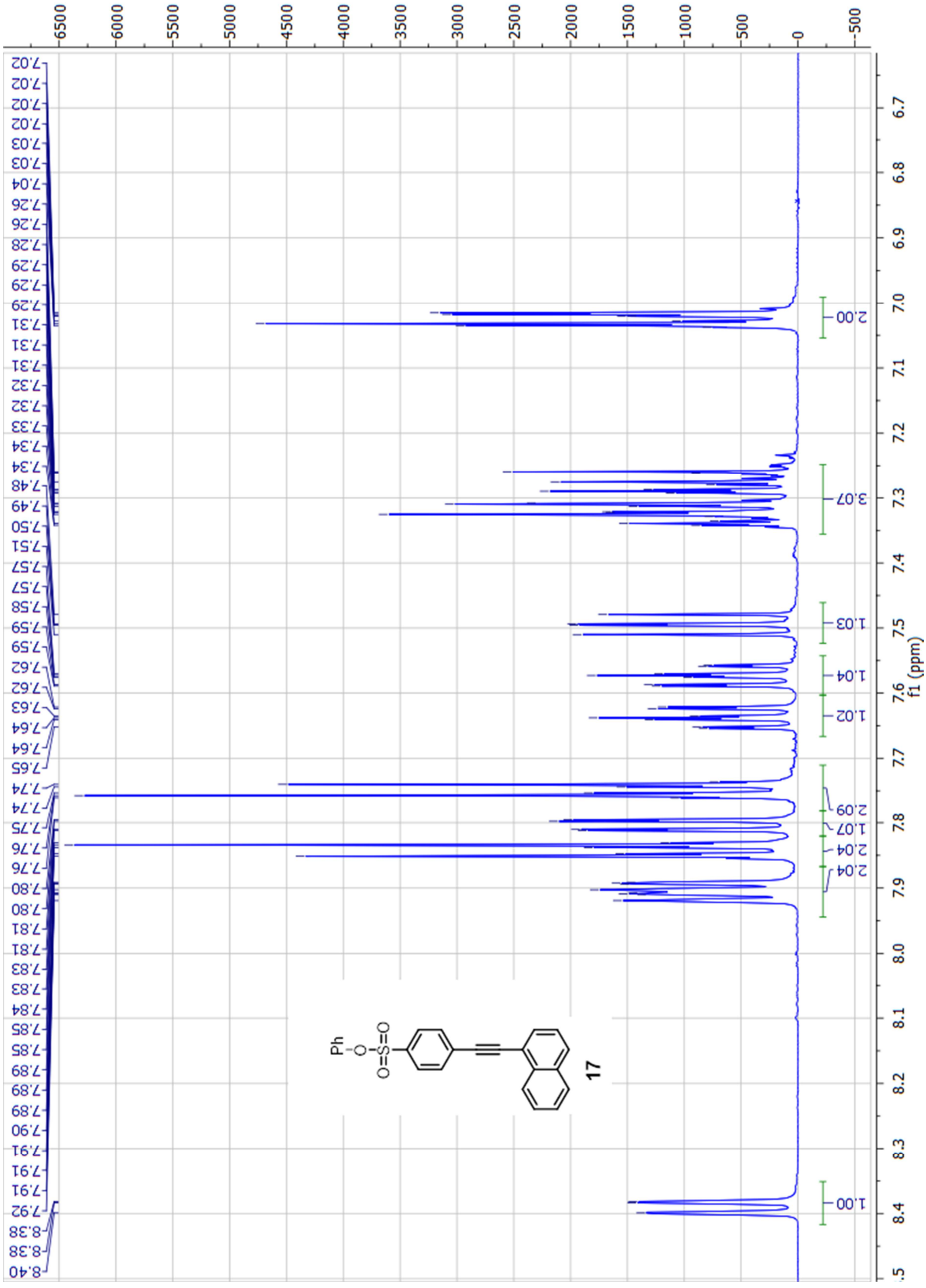
Ph
O
S
O
O
17
2.00
3.07
1.03
1.04
1.02
2.09
1.07
2.04
2.04
1.00
f1 (ppm)

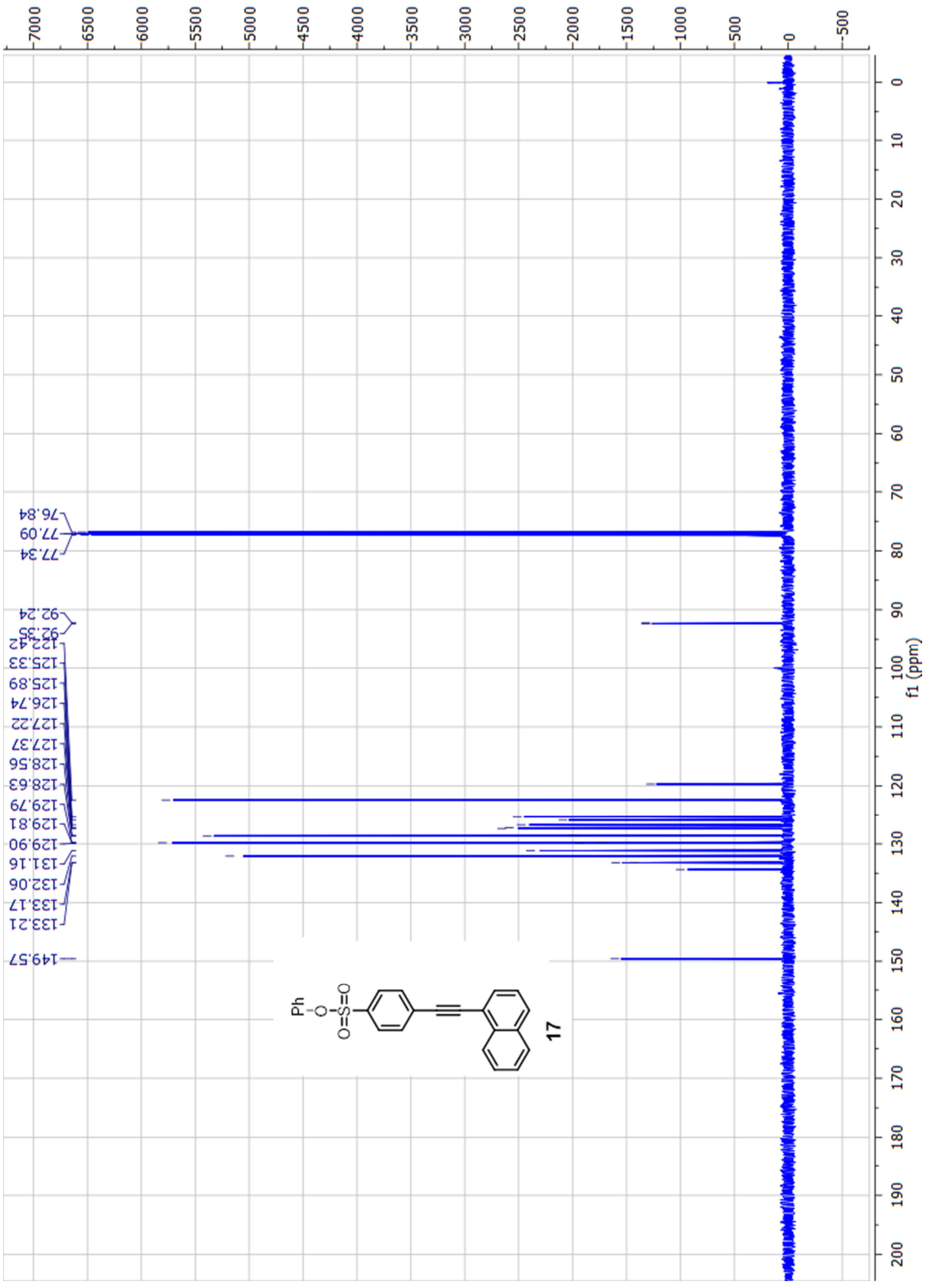
149.57
133.21
133.17
132.06
131.16
129.90
129.81
129.79
128.63
128.56
127.37
127.22
126.74
125.89
125.33
122.42
92.35
92.24
77.34
77.09
76.84
Ph
O
O=S=O
17
f1 (ppm)

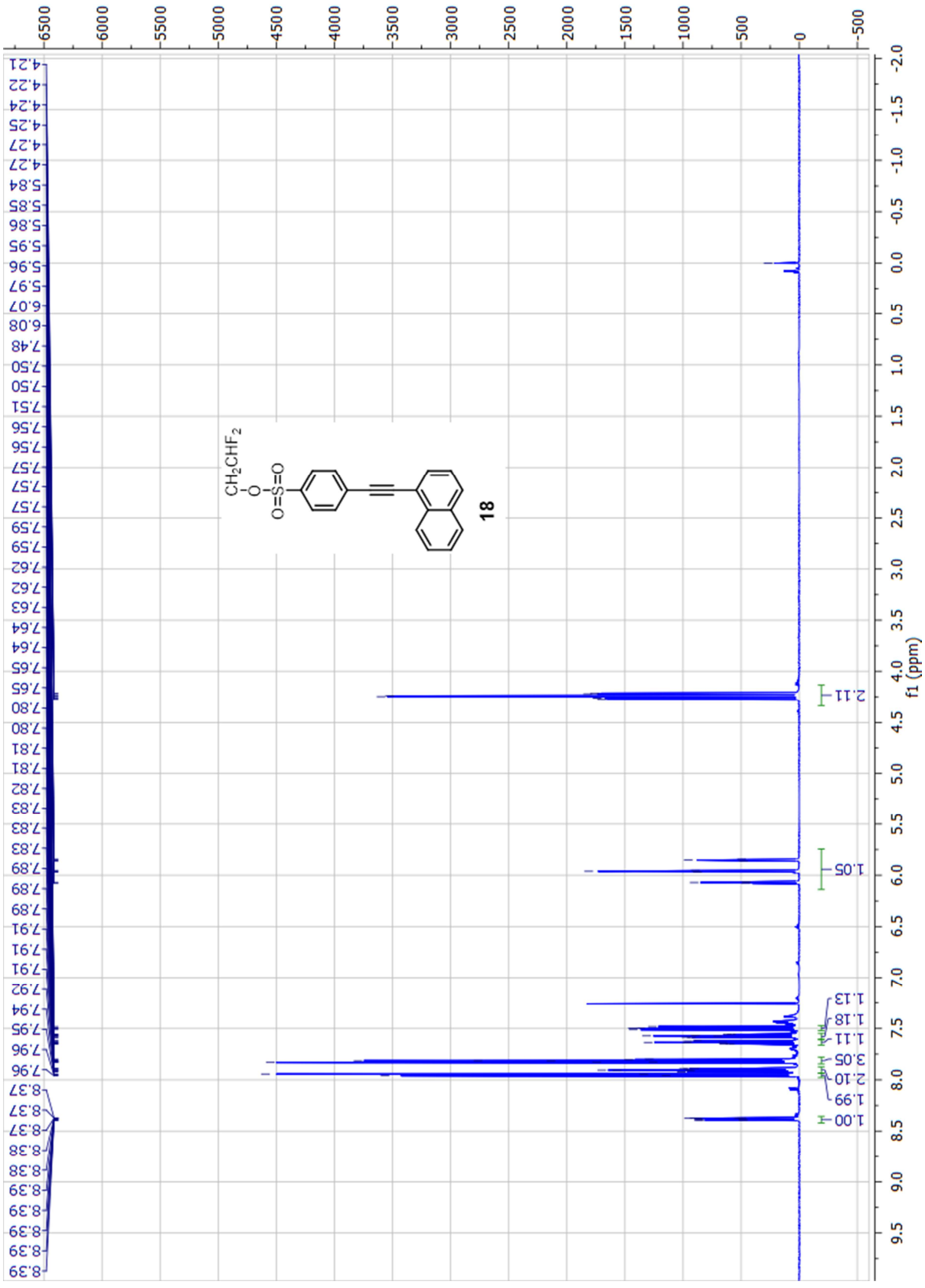
CH2CHF2
O
O=S=O
18
2.11
1.05
1.13
1.18
1.11
3.05
2.10
1.99
1.00
f1 (ppm)

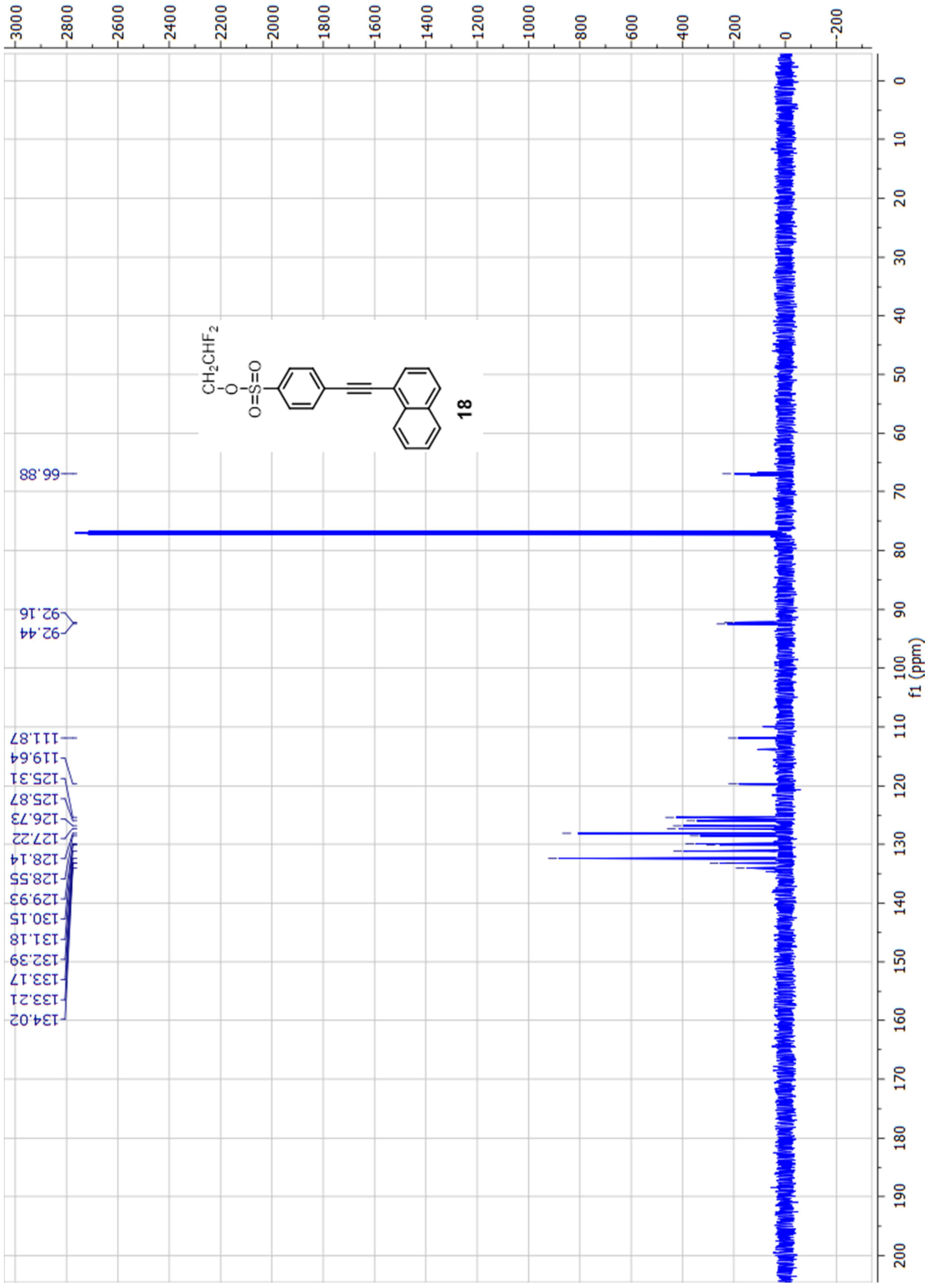
CH2CHF2
O
O=S=O
18
66.88
92.44
92.16
111.87
119.64
125.31
125.87
126.73
127.22
128.14
128.55
129.93
130.15
131.18
132.39
133.17
133.21
134.02
f1 (ppm)

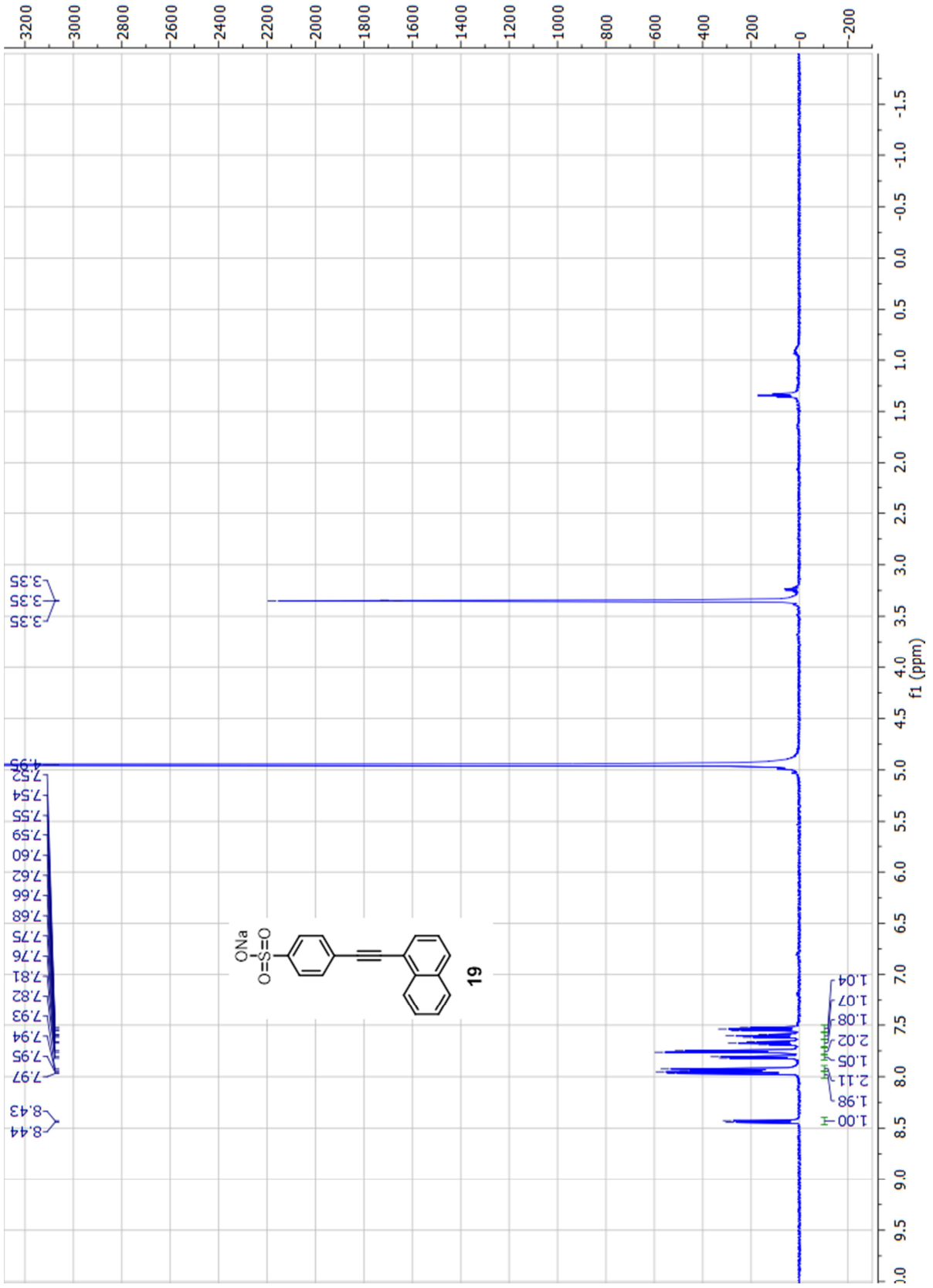
ONa
O=S=O
19
f1 (ppm)

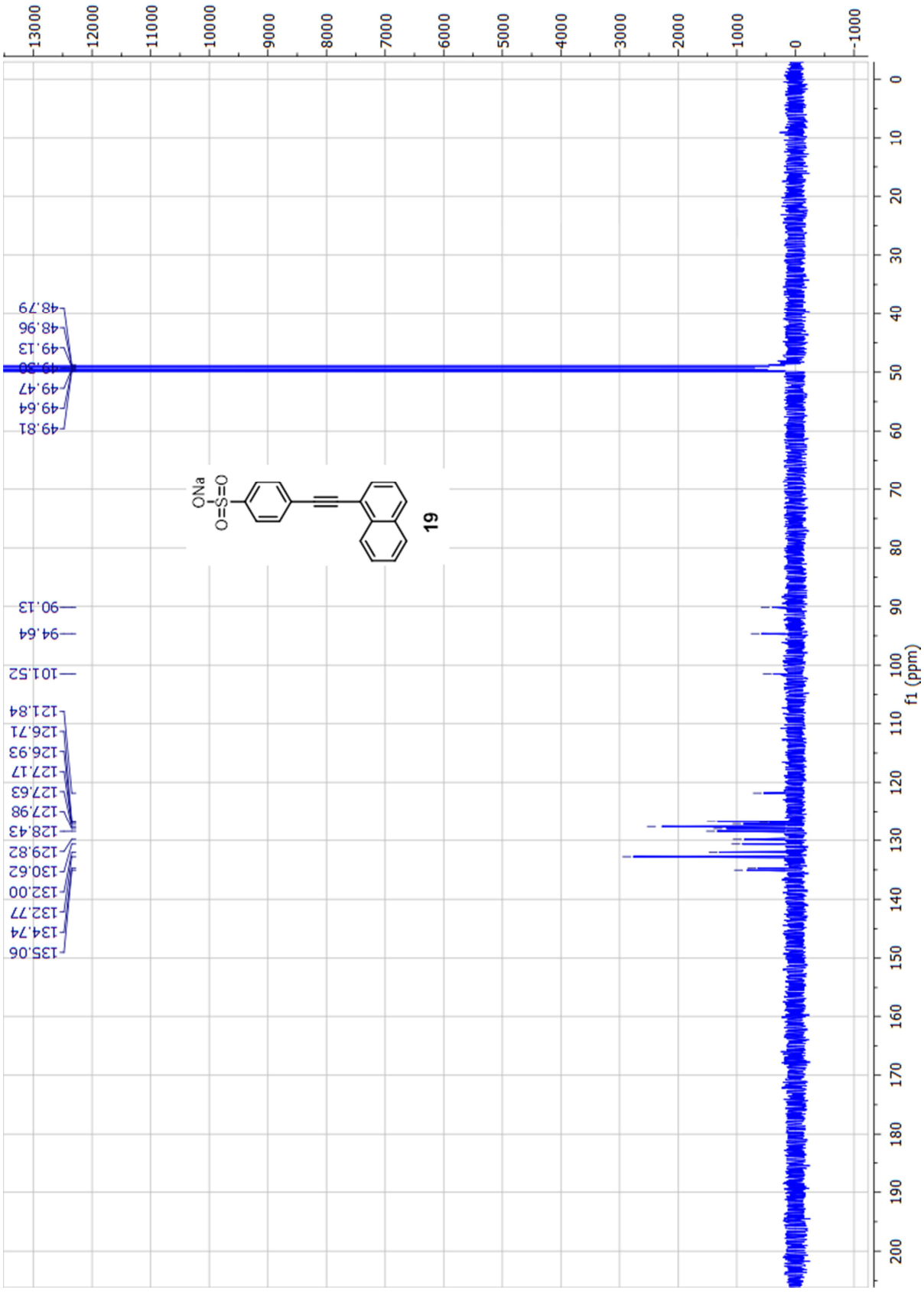
ONa
O=S=O
19
f1 (ppm)

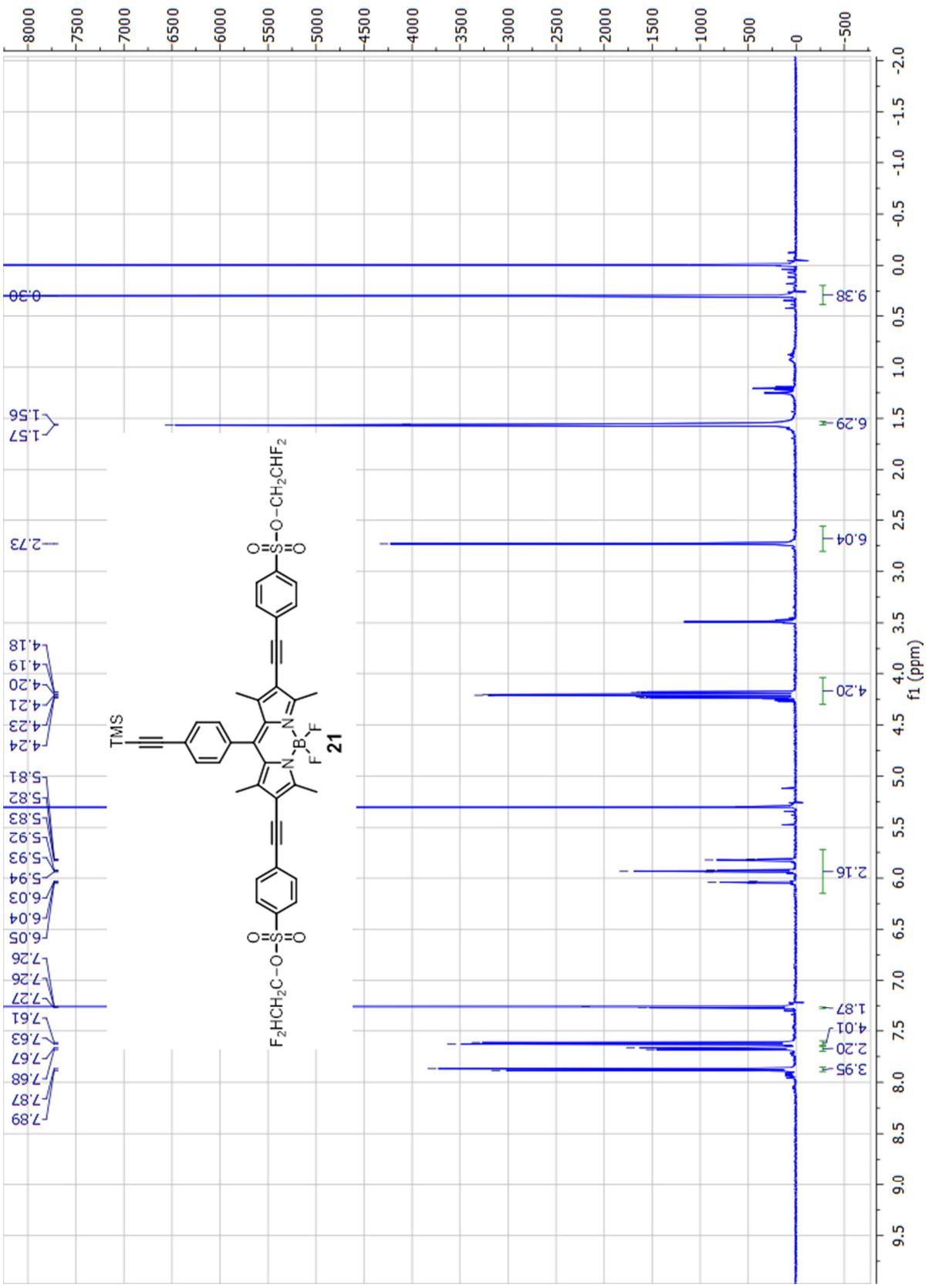
TMS
21
F2HCH2C–O–S(=O)(=O)–
–S(=O)(=O)–O–CH2CHF2
f1 (ppm)

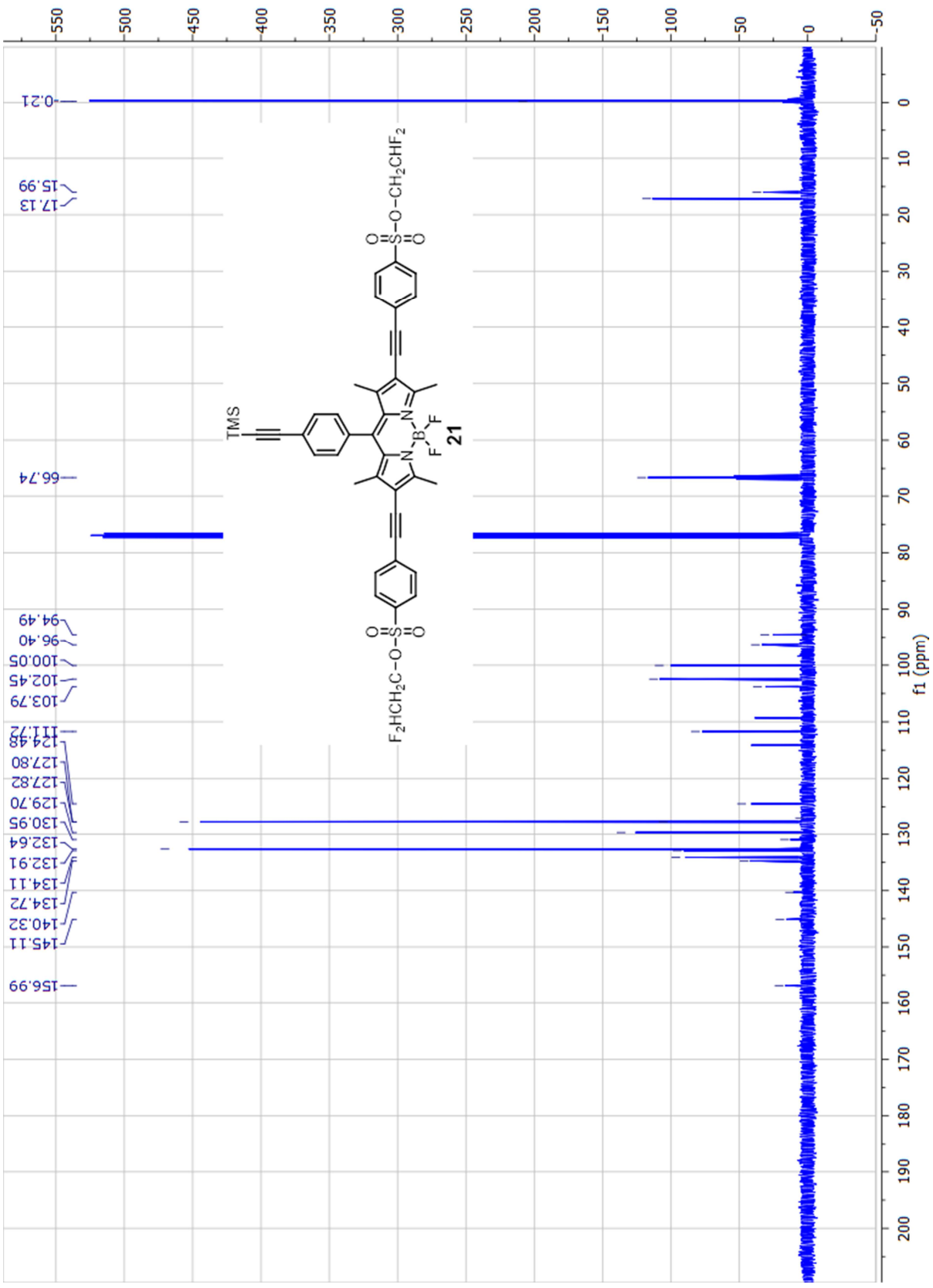
0.21
15.99
17.13
66.74
94.49
96.40
100.05
102.45
103.79
111.72
124.48
127.80
127.82
129.70
130.95
132.64
132.91
134.11
134.72
140.32
145.11
156.99
TMS
21
f1 (ppm)

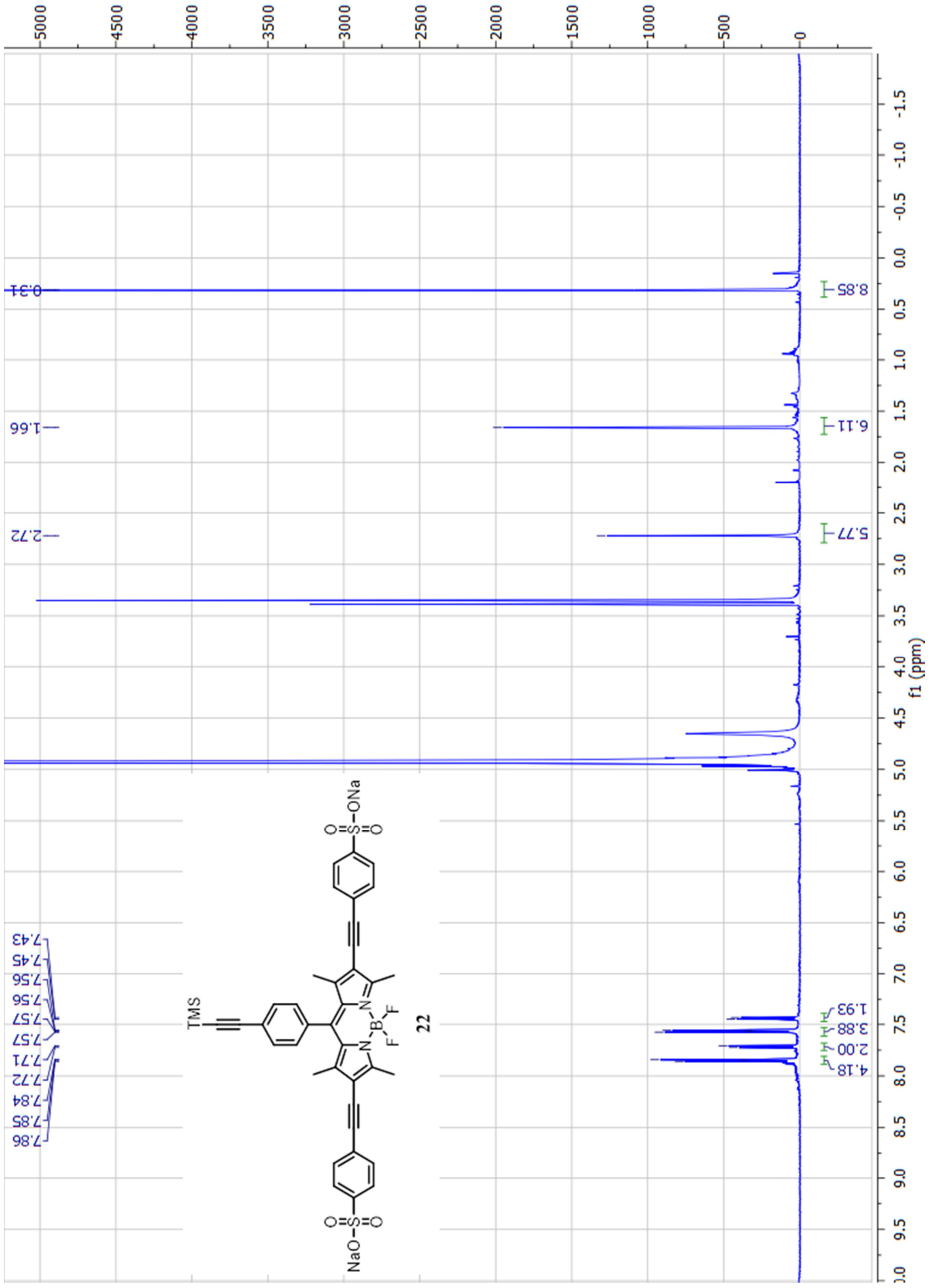
TMS
NaO
O
S
O
O
N
B
F
F
22
0.31
1.66
2.72
8.85
6.11
5.77
1.93
3.88
2.00
4.18
7.86
7.85
7.84
7.72
7.71
7.57
7.57
7.56
7.56
7.45
7.43
f1 (ppm)

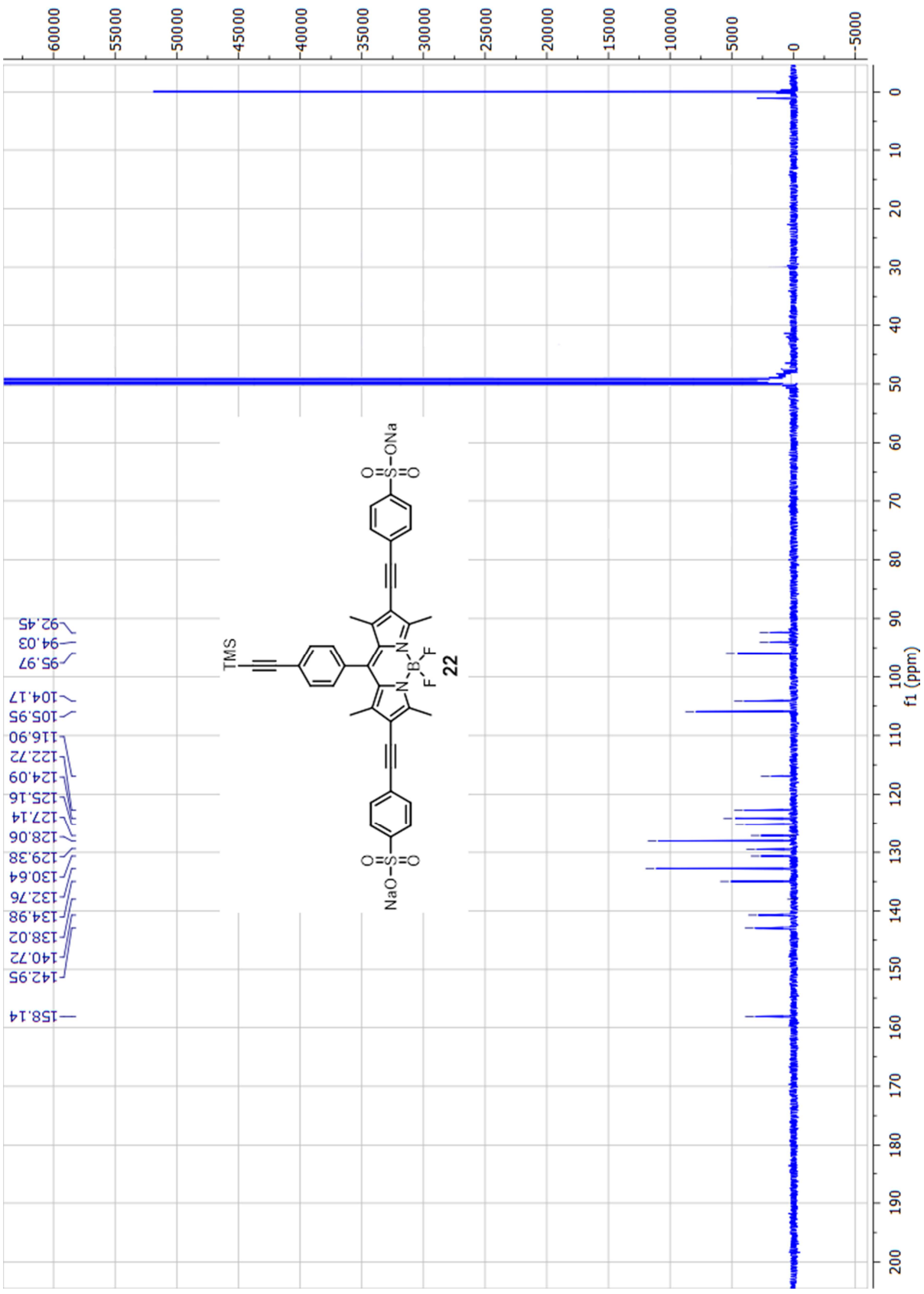
158.14
142.95
140.72
138.02
134.98
132.76
130.64
129.38
128.06
127.14
125.16
124.09
122.72
116.90
105.95
104.17
95.97
94.03
92.45
TMS
22
f1 (ppm)